

**“STUDY OF STRUCTURE AND DIELECTRIC PROPERTIES OF  
1:2 TYPE MODIFIED BARIUM NIOBATES IN BULK AND THIN  
FILM FORMS”**

**A**

**THESIS**

**Submitted for the award of the degree of**

**Doctor of philosophy**

**In**

**Physics**

**By**

**Ms. BHAGWANTI BEN S BISHNOI**

**UNDER THE SUPERVISION OF**

**Dr. PRASHANT K MEHTA**



**DEPARTMENT OF PHYSICS, FACULTY OF SCIENCE  
THE MAHARAJA SAYAJIRAO UNIVERSITY OF BARODA  
VADODARA 390 002, INDIA  
JUNE 2012**

*DEDICATED TO*  
*.....MY BELOVED PARENTS*

## **DECLARATION BY THE CANDIDATE**

I hereby declare that this thesis entitled “*Study of Structure and Dielectric properties of 1:2 modified Barium niobates in Bulk and Thin films forms.*” is the result of the investigations carried out by me at Department of Physics, The Maharaja Sayajirao University of Baroda, Vadodara under the supervision of Dr. Prashant K Mehta. The work is approved by Council of Post-Graduate Studies and Research. Further, I have put in research work for requisite number of terms as required by the University. This thesis has not been submitted for the award of any degree, diploma, associateship, fellowship etc. of any university or institute.

**Ms. Bhagwanti Ben S Bishnoi**

**(Candidate)**

**Date:**

## **CERTIFICATE**

This is to certify that the thesis entitled “*Study of Structure and Dielectric properties of 1:2 modified Barium niobates in Bulk and Thin films forms.*”. Submitted to Department of Physics, The Maharaja Sayajirao University of Baroda, Vadodara contains the bonafide record of the work carried out by **Ms.Bhagwanti Ben S Bishnoi**, who has completed the necessary work for her degree of **Doctor of Philosophy in Physics of Maharaja Sayajirao University (M.S.University), Vadodara, Gujarat** and it is complete and satisfactory in all respects. The work was carried out and presented in this thesis by the candidate under my supervision and guidance at **M.S.University Vadodara, Gujarat**. This work has not been submitted anywhere for any degree or diploma.

### **Forwarded through**

Dr. Prashant K Mehta  
Associate Professor  
Department of Physics  
The M. S. University of Baroda  
Vadodara 390 002  
Gujarat, (India)

Date :

Prof A C Sharma  
Professor and Head  
Department of Physics  
The M. S. University of Baroda  
Vadodara 390 002  
Gujarat, (India)

## ACKNOWLEDGEMENTS

We all have certain objectives in our life to accomplish and hence, follow a path. However, one is fortunate who has blessings by teachers around them to guide the path. I am one of the privileged who enjoyed the educating criticism, precious discussion and friendly environment from my guide **Dr. Prashant K. Mehta**. It does not always feel good when things come to an end, but to think about someone who stand out and make the things work our way to reach is really pleasant. This thesis would have not been in proper configuration without immeasurable contributions from a large number of people. Though it may be simple to name all of them, it is very tough to thank each of them to the required extent.

At this juncture of fulfilling my desire of satisfactory completion of the present work, I bow before Almighty God to express my deep gratitude for the divine grace. I prostrate to my most affectionate parents and express my deepest sense of gratitude for their blessings, external inspiration, care and love without that I would not have been able to venture into this work.

My sincere gratitude and thanks to Prof. Nikhil Desai, Dean, Faculty of Science, The Maharaja Sayajirao University of Baroda for all the valuable support. I am thankful to Prof. A.C. Sharma, Head, Department of Physics, The Maharaja Sayajirao University of Baroda for all the help during my stay in the department. I am also thankful to Dr. D. G. Rathod, Prof P. K. Jha, Prof N. L. Singh, Prof C. F. Desai, Dr. Mitiesh Sarkar and Mr. N. V. Patel for their kind cooperation that they had extended to me while I was in the M. S. University of Baroda.

I would like to thank each and every non-teaching staff of my Physics department for their timely help. I am also thankful to faculty office staff for all the help.

Valuable suggestions and constant support are greatly acknowledged and appreciated which I had during the discussions with Dr. Chetan Panchal and Dr. M. D Desai, Applied Physics Department, The M.S. University of Baroda.

I thank Director Inter University Accelerator Centre (IUAC), Dr Amit Roy for encouragement and financial support during my work and stay at the centre. I would like to express special gratitude and thanks to Prof. Ravi Kumar and his group for constant support extended to me during experimental work carried out at IUAC, New Delhi.

I thank all the scientists and staff members of IUAC for their support. In particular Dr. D. Kanjilal, Dr. D. K. Avasthi, Dr. Sandip Chopra, Dr. Fouran Singh, Dr. K. Asokan, Mr. Pawan Kulariya, Mrs. Indra Sulania, Dr. Ambuj Tripathi, for their support and cooperation during the whole period. My gratitude goes for the Pelletron group of IUAC. I also thank Mr. Rajesh and his canteen team for their co-operation during my stay at IUAC.

I would like to thank Dr. Ajay Gupta, Center Director, IUC-UGC-CSR, Indore and Dr. V. Ganesan, Dr. D. M. Phase, Dr. Ram Janay Choudhary, Dr. T Shripati, Dr N. P. Lulla, and Dr. V .Reddy, for providing laboratory facility. I would like to thank Prof. R. V. Upadhyaya, Department of Physics, Bhavnagar University, Bhavnagar for the XRD Measurements of some of the samples.

UGC-DRS laboratory, Physics Department is greatly acknowledged for providing instrument facilities for measurements.

I would also like to appreciate the help of my seniors at IUAC, who taught me several experimental techniques and data analysis methods. To name few Dr. Shalendra Gautum, Dr. Abhinav Pratap Singh, Dr. D. K. Shukla, Mr. Aditya Sharma, Dr. J P Singh, Dr. N. E. Rajeevan, , Mr. Jai Prakash and Dr Preetam Singh.

No work is accomplished without appreciation and healthy environment we receive from friends and well-wishers. I wish to record my deep gratitude to my colleague Mr. D. G. Shah, Mr. Nishant Barot, Dr. (Mrs.)Sejal Shah, Mrs. Chaitali Gavade, Mr.Yogesh Kumar, Dr. (Mrs.) Anju Dhillon, Mrs. Mumtaz Oswal, Mrs. Sharan Saini, Dr. Feroz, Dr (Mrs) Abida, Dr. (Mrs.) Dolly Singh, Ms. Sangeeta Kishore, Mrs. Poonam Sharma, Dr. (Mrs.) Meenakshi Pant, Ms. Kavita Sharma, Dr. Sagar Ambavale, Mr. Manish, Mr. Naveen and many others.

I am very much grateful for the moral support of my parents throughout the period of my research work. I am very indebted to them without whose help I could not have finished my work. I thank each and every family member for their moral support and constant encouragement. I am short of words to express my deep gratitude to my Father (Shri Surendralal S Bishnoi) and my dearest and most loving Mother (Late Mrs Tulsi Devi Bishnoi) brothers (Mr.Amarjeet Singh Bishnoi and Mr.Virendra Singh Bishnoi) along with my dear and loving bhabhi's (Mrs. Shakti Bishnoi and Mrs Nirma Bishnoi) for their constant support throughout my thesis work and encouraged me to complete my work.

I also express deep gratitude to my in-laws and sister-in-law's family who also stood beside me in all hardships. I therefore would like to thank them from the bottom of my heart. I am very much thankful to my Husband (Mr. Anuj Kumar Vishnoi) whose constant support and encouragement has led me to complete my thesis. Finally I thank again to the almighty for giving such a supportive and loving family being with us in all the ups and downs of life.

Bhagwanti Ben S Bishnoi

Date:

## PREFACE

In view of the processing and environmental issues pertaining to lead based ferroelectric materials, investigations on lead free ferroelectrics are carried intensively in recent years. These materials are interesting because, they are flexible with respect to structural changes and functional properties. These materials have potential device applications such as capacitors, sensors, actuators, and memory storage and microwave devices. This thesis is an attempt to elucidate the effect of substitution of isovalent ions (Sr, Ca) at the 'A' site of Hexagonal structured Barium Magnesium Niobate  $\text{Ba}(\text{Mg}_{1/3}\text{Nb}_{2/3})\text{O}_3$  (BMN) as well as effect of simultaneous substitution of divalent ions ( $\text{Co}^{2+}$  and  $\text{Cu}^{2+}$ ) on the 'B'-site' of  $\text{Ba}(\text{Mg}_{1/3}\text{Nb}_{2/3})\text{O}_3$  (BMN) and  $\text{Sr}(\text{Mg}_{1/3}\text{Nb}_{2/3})\text{O}_3$  (SMN). Their structural, morphological, dielectric, impedance and optical properties are investigated. The XRD study on the ceramic compositions (SMN) showed single phase monoclinic hexagonal perovskite structure at room temperature. The SEM micrograph shows that the grains are uniformly distributed throughout the surface and the average grain size decreases with the substitution of divalent ion doping in  $\text{Sr}(\text{Mg}_{1/3}\text{Nb}_{2/3})\text{O}_3$  ceramic. The diffusivity of ceramics increases with increase in divalent ions substitution. The dielectric study confirmed that the relaxor nature is introduced in the Barium Niobate on replacement by other divalent ions at the A- or B'-site. Among various compositions in  $\text{Sr}(\text{Cu}_{1/3}\text{Nb}_{2/3})\text{O}_3$  we obtained most promising dielectric properties. The impedance and modulus spectroscopy were employed to evaluate the different electrical properties of the grain and grain boundary of the ceramics. Ac Conductivity shows the two types of hopping conduction mechanism in frequency exponent vs temperature plots after the divalent ions replacement. The optical band gaps were calculated from UV –Visible spectroscopy ceramic suggested the presence of intermediately energy levels within the band gap.

The single phase thin films of various compositions with A- and B'-site substitutions were successfully made using Pulsed laser deposition technique. Over all properties of films are identical to the respective bulk compositions except for some of the samples which exhibited relaxor behaviour only in the film form. Compared to  $\text{O}^{7+}$  irradiation the  $\text{Ag}^{15+}$  irradiation due to type of defects it created is more effective in reducing lattice strain induced dielectric losses along with marginal loss of dielectric constant. Significant increase in dielectric constant with



low loss, on  $O^{7+}$  as well as  $Ag^{15+}$  ion irradiation, may enhance the electro-optical properties which in turn increase compounds tuneability for device applications.

*Keywords: Ferroelectrics, Relaxor ferroelectrics, Diffuse phase transition, Dielectric relaxation, Impedance spectroscopy, UV-vis absorption spectroscopy.*

# **CONTENTS**

<b>TITLE</b>	<b>PAGE NO.</b>
<b>CERTIFICATE</b>	
<b>ACKNOWLEDGEMENT</b>	<b>i</b>
<b>PREFACE</b>	<b>iv</b>
<b>CONTENT</b>	<b>vi</b>
<b>LIST OF TABLES</b>	<b>xii</b>
<b>LIST OF FIGURES</b>	<b>xiii</b>
<b>INTRODUCTION</b>	<b>1</b>
<b>CHAPTER 1</b>	
<b><i>INTRODUCTION AND MOTIVATION</i></b>	<b>2</b>
1.0    Introduction	<b>2</b>
1.1    Perovskite Structure	<b>2</b>
1.2    Classification of Ferroelectricity Crystals	<b>5</b>
1.2.1    Ferroelectrics	<b>5</b>
1.2.2    Relaxor Ferroelectrics	<b>8</b>
1.2.3    Diffuse Phase Transition	<b>12</b>
1.3    Literature Survey	<b>14</b>
1.4    Aim of the work	<b>16</b>
1.5    Objective and Scope of the Work	<b>17</b>
References	<b>21</b>
<b>CHAPTER 2</b>	
<b><i>EXPERIMENTAL AND CHARACTERIZATION TECHNIQUES</i></b>	<b>25</b>
2.1    Introduction	<b>26</b>
2.1.1    Synthesis methods	<b>26</b>

2.2	Thin Film Deposition	29
2.2.1	Pulsed laser Deposition Technique (PLD)	29
2.3	Characterization Technique	32
2.3.1	X-ray diffraction	32
2.3.2	Scanning electron microscopy	34
2.3.3	Atomic force microscopy	37
	2.3.3.1 Contact Mode AFM	37
	2.3.3.1 Tapping Mode AFM	38
2.3.4	Optical Studies	39
	2.3.4.1 UV-Vis Spectroscopy	39
2.3.5	Dielectric Measurements	41
2.3.6	Impedance Spectroscopy	43
2.4	Swift Heavy Ion Irradiation	45
2.4.1	Pelletron Accelerator	45
2.4.2	Material Science Beam Line	47
2.4.3	Ion-Solid Interaction	49
	2.4.3.1 Thermal Spike Model	50
	2.4.3.2 Coulomb Model	51
	References	51

### CHAPTER 3

#### ***EFFECT OF A-SITE SUBSTITUTION ON THE COMPLEX PEROVSKITES [Ba(Mg<sub>1/3</sub>Nb<sub>2/3</sub>)O<sub>3</sub>] BULK SAMPLES***

3.1	Introduction	55
3.2	Results and Discussions	59
3.2.1	X-Ray Diffraction Measurement	59
3.2.2	Scanning Electron Microscopy Analysis	61
3.2.3	Dielectric Measurement	63
	3.2.3.1 Frequency dependence dielectric properties	63
	3.2.3.2 Temperature dependence dielectric properties	65

3.2.4	Modulus Spectroscopy Analysis	66
3.2.5	Conductivity Studies	72
3.2.6	Uv-Vis Spectroscopy Analysis	74
3.3	Conclusion	76
	References	77

## CHAPTER 4

### ***REPLACEMENT AT B'-SITE BY DIVALENT IONS IN STRONTIUM SERIES Sr(Mg<sub>1/3</sub>Nb<sub>2/3</sub>)O<sub>3</sub> AND ITS IMPACTS ON STRUCTURAL, MICROSTRUCTURAL, DIELECTRIC, COMPLEX IMPEDANCE, CONDUCTIVITY AND OPTICAL STUDIES***

80

4.1	Introduction	81
4.2	Results and Discussions	82
4.2.1	X-Ray Diffraction Measurement	82
4.2.2	Scanning Electron Microscopy Analysis	84
4.2.3	Dielectric Measurement	85
	4.2.3.1 Frequency dependence dielectric properties	85
	4.2.3.2 Temperature dependence dielectric properties	87
4.2.4	Diffuse Phase Transition	89
4.2.5	Impedance Spectroscopy Studies	91
4.2.6	Modulus Spectroscopy Analysis	98
4.2.7	Conductivity Studies	103
	4.2.7.1 Frequency dependence conductivity	103
	4.2.7.2 Temperature dependence conductivity	106
4.2.8	Uv-Vis Spectroscopy Analysis	107
4.3	Conclusion	109
	References	111

## CHAPTER 5

### ***EFFECT AT RELACEMENT B'-SITE BY DIVALENT IONS IN BARIUM NIOBATES AND ITS IMPACT ON STRUCTURAL, MICROSTRUCTURE, DIELECTRIC, COMPLEX IMPEDANCE AND CONDUCTIVITY STUDIES***

113

5.1	Introduction	114
5.2	Results and Discussions	115
5.2.1	X-Ray Diffraction Measurement	115
5.2.2	Scanning Electron Microscopy Analysis	116
5.2.3	Dielectric Measurement	117
5.2.3.1	Frequency dependence dielectric properties	117
5.2.3.2	Temperature dependence dielectric properties	120
5.2.4	Diffuse Phase Transition	121
5.2.5	Impedance Spectroscopic Studies	123
5.2.6	Modulus Spectroscopy Analysis	125
5.2.7	Conductivity Studies	128
5.2.7.1	Frequency dependence conductivity	128
5.2.7.2	Temperature dependence conductivity	130
5.3	Conclusion	131
	References	133

## CHAPTER 6

### ***A COMPARATIVE STUDY OF CRYSTAL STRUCTURE, MICROSTRUCTURE, DIELECTRIC AND CONDUCTIVITY PROPERTIES OF BULK AND THINFILMS OF $Ba(B'_{0.33}Nb_{0.67})O_3$ , WHERE B' STANDS FOR $(Mg^{2+}, Co^{2+})$***

#### **PART -A**

#### **i) STUDIES ON UN-IRRADIATED THIN FILMS OF $Ba(B'_{0.33}Nb_{0.67})O_3$ , WHERE B' STANDS FOR $(Mg^{2+}, Co^{2+})$**

135

6.1	Introduction	136
-----	--------------	-----

6.2	Deposition Conditions for the PLD	138
6.3	Results and Discussions	138
6.3.1	X-Ray Diffraction Measurement	138
6.3.2	Atomic Force Microscopy Analysis	141
6.3.3	Dielectric Measurement	144
6.3.3.1	Frequency dependence of dielectric properties	144
6.3.3.2	Temperature dependence of dielectric properties	147

**ii) STUDIES OF IRRADIATED THIN FILMS OF  $Ba(B'_{0.33}Nb_{0.67})O_3$ , WHERE B' STANDS FOR  $(Mg^{2+}, Co^{2+})$**  **150**

6.4	Introduction	150
6.5	Irradiation Effects of 200 MeV $Ag^{15+}$ and 100 MeV $O^{7+}$ on $Ba(Mg_{0.33}Nb_{0.67})O_3$ [BMN] and $Ba(Co_{0.33}Nb_{0.67})O_3$ [BCoN] thin films on dielectric properties.	151
6.5.1	Dielectric Properties of BMN	151
6.5.2	Dielectric Properties of BCoN	152
6.5.2.1	Frequency dependence of dielectric properties	152
6.5.2.2	Temperature dependence of dielectric properties	153
6.6	Conclusion	156

**PART –B**

**A COMPARITIVE STUDY OF CRYSTAL STRUCUTRE MICRO STRUCTURE, DIELECTRIC AND CONDUCTIVITY PROPERTIES OF THIN FILMS OF  $Sr(Mg_{0.33}Nb_{0.67})O_3$**  **158**

6.7	Introduction	159
6.8	Deposition Conditions for the PLD	159
6.9	Results and Discussions	159
6.9.1	X-Ray Diffraction Measurement	159
6.9.2	Atomic Force Microscopy Analysis	160

6.9.3	Dielectric Measurement	161
6.9.4	Conductivity Studies	163
6.10	Conclusion	164
	References	165
 <b>CHAPTER 7</b>		
	<b><i>SUMMARY AND FUTURE SCOPE</i></b>	<b>167</b>
7.1	Summary of the present work	168
7.2	Future scope of the work	170
	 <b><i>LIST OF PUBLICATION IN JOURNALS</i></b>	 <b>171</b>
	 <b><i>LIST OF PUBLICATION IN CONFERNCES AND PROCEEDINGS</i></b>	 <b>172</b>

## LIST OF TABLES

<b>Table No</b>	<b>Table Description</b>	<b>Page No</b>
Table 1.1	A Partial list of ferroelectric systems.	6
Table 3.1	Structure, the lattice Constant and Unit cell Volume for $A(\text{Mg}_{0.33}\text{Nb}_{0.67})\text{O}_3$	60
Table 3.2	The observed indirect band Gap values of BMN, SMN and CMN.	76
Table 4.1	Structure, Lattice parameters and Tolerance of $\text{Sr}(\text{B}'_{1/3}\text{Nb}_{2/3})\text{O}_3$ ( $\text{B}'=\text{Mg}^{2+}, \text{Co}^{2+}, \text{Cu}^{2+}$ ).	84
Table 4.2	Variations of electrical parameters (bulk and grain boundary) as a function of temperature.	96
Table 4.3	Calculated Activation energies from different formalisms.	97
Table 4.4	Conductivity values for grain and grain boundary calculated from Table 4.2.	97
Table 4.5	The Indirect band Gap values of SMN, SCoN and SCuN.	109
Table 5.1	Structure, lattice parameters and Unit Cell Volume for $\text{Ba}(\text{B}'_{1/3}\text{Nb}_{2/3})\text{O}_3$ ( $\text{B}'=\text{Mg}^{2+}, \text{Co}^{2+}, \text{Cu}^{2+}$ ).	116
Table 6.1	XRD peak and AFM analysis of BMN films on Si, MgO and ITO coated glass substrates.	140



## List of Figures

Figure No	Figure Description	Page No
Figure 1.1	A Partial list of ferroelectric systems.	3
Figure1.2	A cubic $\text{ABO}_3$ , perovskite type unit cell.	3
Figure 1.3	The Complex Perovskite Structure of $\text{A}(\text{B}^{2+}_{1/3}\text{B}^{5+}_{2/3})\text{O}_3$	4
Figure 1.4	A Polarization vs. Electric Field (P-E) hysteresis loop for a typical ferroelectric crystal.	7
Figure1.5	$\text{ABO}_3$ structure of relaxor ferroelectrics $[\text{Pb}(\text{Mg}_{1/3}\text{Nb}_{2/3})\text{O}_3]$ .	10
Figure 1.6	Contrast between the properties of normal ferroelectrics and relaxor ferroelectrics.	11
Figure 2.1	Flow chart for the preparation of bulk samples.	28
Figure 2.2	A schematic view of Pulsed Laser Deposition Technique.	31
Figure 2.3	A representation of x-ray diffraction.	33
Figure 2.4	X-ray diffractometer (UGC-DAE CSR Indore).	34
Figure 2.5	Schematic diagram of Scanning Electron Microscope (SEM) (UGC-DAE CSR Indore).	36
Figure 2.6	Schematic diagram of Atomic Force Microscope (AFM).	38
Figure2.7	Schematic View of UV-Vis Spectroscopy.	40
Figure 2.8	Dielectric measurement set up Physics department (The M.S. University of Baroda).	42
Figure 2.9	(a) The impedance plot for a circuit of a resistor and a capacitor in parallel. (b) The corresponding equivalent circuit.	45

Figure 2.10	(a) The impedance plot for an ideal polycrystalline sample and (b) The corresponding equivalent circuit.	45
Figure 2.11	Schematics of the 15 UD Pelletron at IUAC, New Delhi, India.	47
Figure 2.12	An overview of (a) Experimental chamber and (b) materials science beam line at Inter-University Accelerator Center, New Delhi, India.	49
Figure 3.1	X- ray powder diffraction patterns of BMN, SMN, and CMN samples.	61
Figure 3.2	SEM Micrograph of (a) BMN, (b) SMN, (c) CMN.	62
Figure 3.3	(a-c) Angular Frequency dependence of the real part ( $\epsilon'$ ) of the electrical permittivity for different compositions.	63
Figure 3.4	Dielectric losses ( $\tan\delta$ ) versus frequency plots (a) for SMN and (b) for CMN.	64
Figure 3.5	The Arrhenius plot for the $\tan\delta_{max}$ with inverse of temperature.	65
Figure 3.6	Temperature dependence of the real part ( $\epsilon'$ ) of the electrical permittivity for different frequencies.	66
Figure 3.7 (a)	Variation of real part of modulus, and imaginary part of modulus of SMN with different frequency at different temperatures.	67
Figure 3.7 (b)	Variation of real part of modulus, and imaginary part of modulus of CMN with different frequency at different temperatures.	68
Figure 3.8	The Arrhenius plots of relaxation frequency ( $\omega_{max}$ ) for SMN and CMN as a function of temperature where the crosses are the experimental points and the solid line is the least- square straight line-fit.	69
Figure 3.9	The Arrhenius plots of dc conductivity ( $\sigma_{dc}$ ) for SMN and CMN as a function of temperature where the crosses are the	70

experimental points and the solid line is the least- square straight line-fit.

Figure 3.10	The Scaling behaviour of $M''_{max}$ for SMN and CMN as a function of temperatures.	71
Figure 3.11	The Scaling behaviour of $\tan\delta_{max}$ for SMN and CMN as a function of temperatures.	72
Figure 3.12	(a) Frequency dependence of ac conductivity of SMN at different temperatures. (b) Frequency dependence of ac conductivity of CMN at different temperatures.	73
Figure 3.13	(a-c) UV- Vis Absorption Spectra of (a) BMN, (b) SMN, (c) CMN samples.	75
Figure 4.1	X-ray powder diffraction pattern of SMN, SCoN, SCuN samples.	83
Figure 4.2	SEM Micrograph of (a) SMN (b) SCoN, (c) SCuN samples.	85
Figure 4.3	Dielectric Constant as a function of Frequency of SMN, SCoN, SCuN samples from (RT – 350 <sup>0</sup> C).	86
Figure 4.4	Dielectric Loss ( $\tan\delta$ ) vs. Frequency of SMN, SCoN, SCuN samples from (RT – 350 <sup>0</sup> C).	87
Figure 4.5	Temperature dependence of Dielectric Constant for SMN, SCoN and SCuN ceramics in full frequency range (100-32MHz).	88
Figure 4.6	Temperature dependence of Dielectric loss ( $\tan\delta$ ) for SMN, SCoN and SCuN ceramics in full frequency range (100-32MHz).	89
Figure 4.7	Variation of $\ln(1/\epsilon - 1/\epsilon_{max})$ with $\ln(T - T_m)$ at 10 kHz.	90
Figure 4.8	Cole-Cole graphs of SMN, SCoN and SCuN at three different temperatures 100, 200, 300 deg.	92
Figure 4.9	The Temperature dependence of the Cole-Cole parameter, which indicates the width of the relaxation time distribution.	93

Figure 4.10	Variation of grain boundary resistance ( $R_{gb}$ ) as a function of temperature for SCoN sample.	94
Figure 4.11	Variation of frequency independent conductivity due to grain (bulk) and grain boundary effects as a function of temperature for SCoN sample.	95
Figure 4.12	(a) Variation of real part of modulus, and imaginary part of modulus of SMN with different frequency at different temperatures and (inset) is the Arrhenius plot of $\log \omega_{max}$ with inverse temperature.	100
Figure 4.12	(b) Variation of real part of modulus, and imaginary part of modulus of SCoN with different frequency at different temperatures and (inset) is the Arrhenius plot of $\log \omega_{max}$ with inverse temperature.	101
Figure 4.12	(c) Variation of imaginary part of modulus of SCuN with different frequency at different temperatures.	101
Figure 4.13	(a) Scaling behaviour of $M''_{max}$ at various temperatures for [SMN] (b) Scaling behaviour of $M''_{max}$ at various temperatures for [SCoN].	102
Figure 4.14	(a) Frequency dependence of normalized peaks, $Z''/Z''_{max}$ and $M''/M''_{max}$ for SMN ceramic at 190°C. (b) Frequency dependence of normalized peaks, $Z''/Z''_{max}$ and $M''/M''_{max}$ for SCoN ceramic at 150°C.	102
Figure 4.15	The frequency response of the conductivity for (a) SMN, (b) SCoN, and (c) SCuN at different temperature ranges from 30°C to 350°C with an interval of 10°C.	103
Figure 4.16	The room temperature values of the frequency exponents as a function of the frequency, obtained using the derivative curves.	105
Figure 4.17	The peak values of the frequency exponents vs. the absolute	106

temperature T.

Figure 4.18	(a-c) UV- Vis Absorption Spectra of (a) SMN, (b) SCoN, (c) SCuN samples	108
Figure 5.1	X-ray powder diffraction pattern of BMN, BCoN, BCuN samples.	115
Figure 5.2	SEM Micrograph of (a) BMN (b) BCoN, (c) BCuN.	117
Figure 5.3	Dielectric Constant as a function of Frequency of BMN, BCoN, BCuN samples from (RT – 350 <sup>0</sup> C).	117
Figure 5.4	Dielectric Loss (tan $\delta$ ) vs. Frequency of BCoN, BCuN samples from (RT–350 <sup>0</sup> C).	119
Figure 5.5	Temperature dependence of Dielectric Constant for BMN, BCoN and BCuN ceramics.	120
Figure 5.6	Temperature dependence of Dielectric loss (Tan $\delta$ ) for BMN, BCoN and BCuN ceramics.	121
Figure 5.7	Variation of $\ln (1/\epsilon - 1/\epsilon_{\max})$ with $\ln (T - T_m)$ at 10 kHz.	122
Figure 5.8	Cole-Cole graphs of BCoN and BCuN at two different temperatures 200, 300 deg.	124
Figure 5.9	The Temperature dependence of the Cole-Cole parameter, which indicates the width of the relaxation time distribution.	125
Figure 5.10	Variation of imaginary part of modulus at different frequencies and at different temperatures.	127
Figure 5.11	Scaling behavior of $M''_{\max}$ at various temperatures for [BCuN].	127
Figure 5.12	The frequency response of the conductivity for BCoN and BCuN at different temperature ranges from 30 <sup>0</sup> C to 350 <sup>0</sup> C with an interval of 10 <sup>0</sup> C.	128
Figure 5.13	The room temperature values of the frequency exponent 's' as a	129

function of the frequency, obtained using the derivative curves.

Figure 5.14	The peak values of the frequency exponent 's' vs. the absolute temperature T.	131
Figure 6.1	X-ray diffraction pattern of un-irradiated BMN bulk, Si, MgO and ITO coated glass substrates.	139
Figure 6.2	X-ray diffraction patterns of BCoN bulk, and un-irradiated thin film on ITO coated glass.	141
Figure 6.3	AFM images of BMN on different substrates (a) Pt-Si (1.0 $\mu$ m), (b) MgO (001)(1.0 $\mu$ m), (c) Si (111) (100nm) (d) ITO (100nm).	142
Figure 6.4	AFM images of BCoN pristine thin films.	144
Figure 6.5	Variation of Dielectric Constant and Dielectric loss vs Frequency at room temperature of BMN (a) Bulk sample and (b) thin film sample.	145
Figure 6.6	Variation of Dielectric Constant and Dielectric loss vs Frequency at room temperature of BCoN (a) Bulk sample and (b) thin film sample.	146
Figure 6.7	(a) Dielectric Constant and Loss of BMN-Bulk sample. (b) Dielectric Constant and Loss of BMN- Pristine Film.	148
Figure 6.8	(a) Dielectric Constant and loss for the BCoN-Bulk sample. (b) Dielectric Constant and loss for the BCoN-Thin Film.	149
Figure 6.9	(a) Variation of dielectric constant vs. temperature at 300 KhZ for un-irradiated as well as Ag <sup>15+</sup> and O <sup>7+</sup> irradiated BMN films. (b) Variation of tan $\delta$ vs. temp at 300 KHz for pristine as well as Ag <sup>15+</sup> and O <sup>7+</sup> irradiated BMN films.	152
Figure 6.10	Variation of dielectric constant and loss vs. frequencies for un-irradiated, Ag <sup>15+</sup> and O <sup>7+</sup> irradiated BCoN films at room temperature. Inset in (b) shows frequency dependence of	153

dielectric loss in un-irradiated BCoN film.

Figure 6.11	(a)Shows the temperature dependence of dielectric loss ( $\tan \delta$ of) $\text{Ag}^{15+}$ and $\text{O}^{7+}$ irradiated BCoN films at highest fluence at different frequencies. (b) Shows the temperature dependence of dielectric constant ( $\epsilon'$ ) of $\text{Ag}^{15+}$ and $\text{O}^{7+}$ irradiated films at highest fluence. Inset in (b) shows temperature dependence of dielectric loss and dielectric constant in un-irradiated BCoN film.	155
Figure 6.12	Variation of conductivity vs. temperature for un-irradiated, Ag irradiated and oxygen irradiated BCoN films at 300 kHz frequency.	156
Figure 6.13	X-ray diffraction pattern of Bulk (red) and thin film (black) of SMN.	160
Figure 6.14	AFM images of SMN pristine thin film.	160
Figure 6.15	Variation of $\epsilon'$ and $\tan \delta$ with temperature at different frequencies.	161
Figure 6.16	Variation of the real ( $\epsilon'$ ) and complex part of permittivity ( $\epsilon''$ ) with frequencies at different temperatures.	162
Figure 6.17	Variation of Ac Conductivity with frequency at measured temperatures.	163
Figure 6.18	Arrhenius Plot of $\text{Ln} \zeta_{ac}$ vs. $1000/T$ (K) for SMN thin film.	164

### Chapter 1

#### Introduction

This chapter presents a brief description of the origin of perovskite structure exhibiting dielectric and ferroelectric properties. The phenomenon behind the relaxor behaviour is discussed. An overview is given highlighting various published work on prominent systems based on general formula  $A(B'_{1/3}B''_{2/3})O_3$ . It also outlines the contradictions and deficiencies in the reported work. This has provided the motivation and Aim to the present thesis work.



## INTRODUCTION AND MOTIVATION

### 1.0 Introduction

Never-ending thirst of man to improve his living, kept him working for the advancement of technology. He is always in hunt of better and smarter materials to meet these technological endeavours. For the use of a material in a particular application, it is mandatory to understand the fundamental concepts behind the observed physical phenomena. The perovskites materials have long attracted interest and continue to do so, because properties suitable for the applications can be found in compounds with this or closely related structures.

The family of compounds with general formula  $ABO_3$  is generally called perovskites oxides, as their structure is similar to naturally obtained mineral  $CaTiO_3$ . The mineral perovskite ( $CaTiO_3$ ) is named after a Russian mineralogist, Count Lev Aleksevich von Perovski. It was discovered and named by Gustav Rose in 1839 when he found compound in the Ural Mountains. The study on compounds of this family is important as they find several applications in non-linear optics, memory devices, pyroelectric, piezoelectric sensors, wireless communications systems, as well as microwave dielectric materials. Further, they show outstanding and tuneable dielectric properties in number of compositions as well as they have academic importance due to flexibility they show in their physical properties. The well-known examples are  $BaTiO_3$ ,  $PbZrO_3$ ,  $PbTiO_3$  etc. Since then considerable attention has been paid to the perovskite family of compositions. The perovskite is a true engineering ceramic material with a plethora of applications spanning energy production (SOFC technology), environmental containment (radioactive waste encapsulations) and communication (dielectric resonator materials). More exotic applications include  $LaGaO_3$ ,  $PrGaO_3$  and  $NdGaO_3$  being considered as substrates for epitaxy of high  $T_c$  superconductors.

### 1.1 Perovskite structure

The perovskite structure has the general stoichiometry  $ABO_3$ , where “A” and “B” are cations and “O” is an anion. The “A” and “B” cations can have a variety of charges and in the original Perovskite mineral ( $CaTiO_3$ ) the A cations is divalent and the B cation is tetravalent. The ions occupying the A and B lattice sites are detailed in Figure 1.1

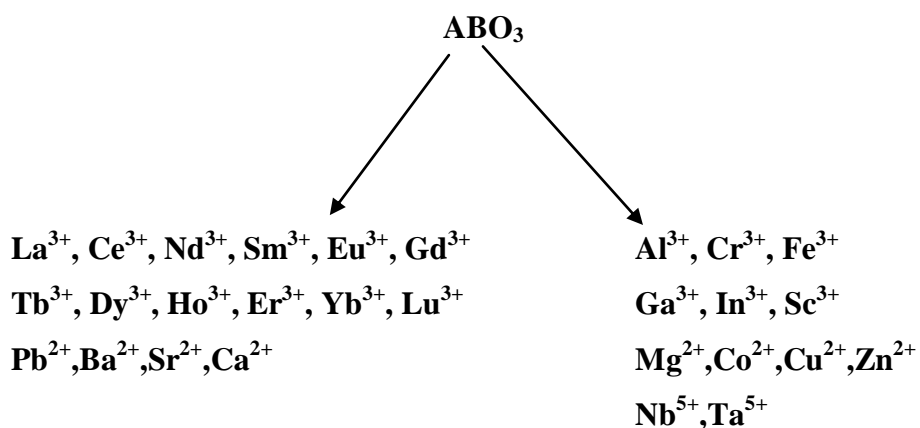


*Figure 1.1* Various combinations of A and B Site cations

The ideal perovskite structure is cubic with the general formula  $A^{2+}B^{4+}O_3^{2-}$ , where in most of the cases  $O^{2-}$  occupies the anion site (Figure 1.2).

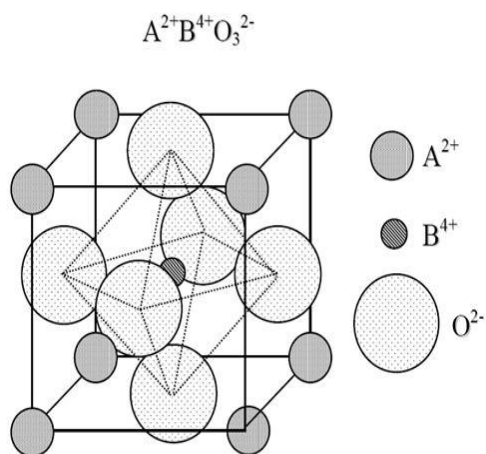


*Figure 1.2* A cubic ABO<sub>3</sub>, perovskite type unit cell

This structure is called „simple“ perovskite. However, there are non-oxide perovskite-type materials, e.g. the fluoride perovskites, having  $F^-$  on the anion site such as  $NaMgF_3$  where  $Na^+$  and  $Mg^{2+}$  ensure the charge balance of the system. This example highlights the advantage of the perovskite-type structure: it allows for a vast variety of compositions,

including the possibility for mixed-cation sites, leading to many outstanding physical properties such as giant magnetoresistance, ferroelectricity, and superconductivity. The structure becomes „complex“ if two ions are of different valency and size at A as well as B sites. This structure is called complex perovskite with the general formula  $(A''A''')(B''B''')O_3$ . First attempt on the synthesis of complex perovskite was reported by Galasso and Pyle [1], and Galasso and Pinto [2] with the modification in B-site. The structure is formed only when there is perfect ordering in B-site with divalent and pentavalent ions in one set of compounds and trivalent & pentavalent ions in another set of compounds, shown in Figure 1.3. This is the system we have worked on in present thesis.

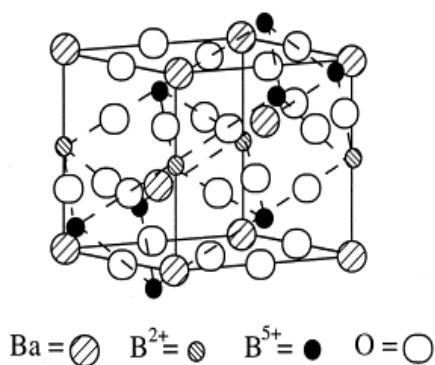


**Figure 1.3 The Complex Perovskite Structure of  $A(B^{2+}_{1/3}B^{5+}_{2/3})O_3$**

Some of the well known complex perovskites are  $Ba(Zn_{1/3}Nb_{2/3})O_3$  [BZN],  $Sr(Zn_{1/3}Nb_{2/3})O_3$  [SZN] [3-4]. The nature of dielectric response of these compounds find many applications such as  $Pb^{2+}$  based relaxor ferroelectrics transducers, actuators, multilayers capacitors and  $Ba^{2+}$  based Dielectric resonator (DR) and microwave band gap structures. As will be discussed later, ferroelectricity is mostly observed in certain temperature regions delineated by transition (or Curie temperature,  $T_C$ ) points above which the crystals are no longer ferroelectric. In 1945 Barium Titanate ( $BaTiO_3$ ) became the first ceramic material in which ferroelectric behaviour was observed, [5]. With its much simpler structure (perovskite), better ferroelectric properties, chemical and mechanical stability, Barium Titanate (BT) became one of the most extensively studied ferroelectric materials [6].  $BaTiO_3$  was considered not only as a model system for ferroelectricity, but also used for practical applications. Added to the chemical and mechanical stability, it exhibits

ferroelectric properties at and above room temperature ( $\sim 125^\circ\text{C}$ ) and can be easily prepared and used in polycrystalline form [7]. By the 1950s the solid solution system  $\text{Pb}(\text{Zr,Ti})\text{O}_3$  (PZT), which also possess the perovskite structure, was found to be ferroelectric. PZT compositions are now the most widely exploited of all piezoelectric ceramics both in research and industry. An up to date brief description of BT and PZT systems can be found in the literature [8-9]. Although the ideal perovskite structure is cubic, the real structure often deviates from the cubic structure. The degree of distortion in the perovskite materials is determined by the Goldschmidt tolerance factor ( $t$ ) given as

$$t = \frac{r_a + r_o}{\sqrt{2} (r_b + r_o)} \quad (1.1)$$

Where  $r_a$ ,  $r_b$  and  $r_o$  are the ionic radii of A, B and O ions respectively. For ideally packed perovskite structure,  $t$  is one. In most of the cases,  $t$  varies from 0.8 to 1. Under topological and geometrical constraints three structural degrees of freedom of distortion from the ideal perovskite structure are considered to be possible: i) displacement of A-site and B-site cations from the centers of the polyhedra, ii) distortions of the anion octahedra and iii) tilting of the  $\text{BO}_6$  octahedra [10-11]. The displacement of the cations and the distortion of the octahedra are usually correlated and driven by electronic instability of the metal cations. The Jahn-Teller distortion in  $\text{KCuF}$  [12] and the cation displacement in  $\text{PbZrO}$  [13] are the typical examples. Octahedral tilting is a more common distortion mechanism that can be realized by tilting the rigid  $\text{BO}_6$  octahedra while maintaining their corner sharing connectivity [14-16]. This type of distortion is generally observed when the A-site cation is too small for the cubic  $\text{BO}_6$  corner sharing octahedral network.

## 1.2 Classification of Ferroelectric Crystals

### 1.2.1 Ferroelectrics

Ferroelectrics are the materials that display an electric polarization in the absence of the externally applied electric field, together with the property that the direction of the polarization may be reversed by an electric field. To understand the dielectric response of these ferroelectric compounds, one has to probe the microstructure details [17]. For

ferroelectrics the dielectric relaxation mechanisms are very sensitive to factors such as temperature, electric field, ionic substitutions, and structural defects etc. In one set of the perovskite systems, the ions displace from their equivalent positions and lead to net dipole moment in the unit cell. The compounds exhibiting this type of permanent dipole moment are called ferroelectrics. The displacement of ions is cooperative i.e., in the same direction for one set of unit cells. This results in formation of domains [18]. The ferroelectrics are characterized by well-defined domain structure. Within a domain, all the electric dipoles are aligned in the same direction. The domain structure results in certain unique properties to these systems. The properties are discussed below.

**Table 1.1 A Partial List of early Ferroelectric systems (Jona et al 1962, M. E. Lines 1977) [6, 7]**

<b>Name and Chemical Formula</b>	<b>Curie Temperature, <math>T_c</math> (<math>^{\circ}\text{C}</math>)</b>	<b>Spontaneous Polarization <math>P_s</math> (<math>\mu\text{C}/\text{cm}^2</math>)</b>
Rochelle salt $\text{NaKC}_4\text{H}_4\text{O}_6 \cdot \text{H}_2\text{O}$	23	0.25
Potassium Dihydrogen Phosphate (KDP) $\text{KH}_2\text{PO}_4$	-150	4
Potassium Dihydrogen Arsenate $\text{KH}_2\text{AsO}_4$	-177	5
Potassium Dideuterium Phosphate $\text{KD}_2\text{PO}_4$	-60	5.5
Barium Titanate $\text{BaTiO}_3$	120	26
Lead Titanate $\text{PbTiO}_3$	490	>50
Potassium Nibonate $\text{KNbO}_3$	415	30
Lead Zirconate Titanate (PZT) $\text{Pb}(\text{Zr}_x\text{Ti}_{1-x})\text{O}_3$	~350	>40

The well-defined domain structure in ferroelectrics is the distinctive characteristic of ferroelectrics which results in square hysteresis loop, large coercive fields, large remanent polarization ( $P_R$ ) and spontaneous polarization ( $P_S$ ).

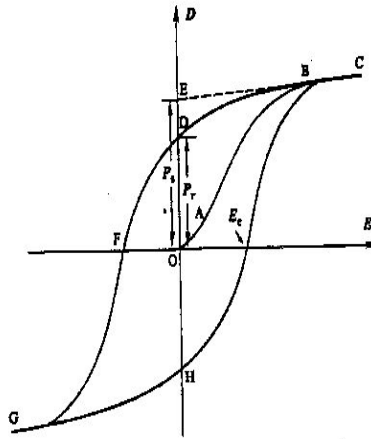


**Figure 1.4 A Polarization vs. Electric Field (P-E) hysteresis loop for a typical ferroelectric crystal.**

Figure 1.4 shows the P-E loop for a typical ferroelectric crystal. A net spontaneous polarization exists even after the electric field is turned off. Above the Curie temperature we have the paraelectric phase where the material has higher symmetry and behaves like a normal dielectric. Here the polarization vanishes and no Hysteresis is observed. The transition from paraelectric to ferroelectric phase is sharp in the dielectric response curve. Some ferroelectrics have additional ferroelectric-ferroelectric transitions (usually to lower symmetry) below the Curie temperature and some even undergo a transition back to a paraelectric state. The ability of ferroelectrics to change their atomic structure under the influence of electric fields gives rise, in some cases, to extremely high values of permittivity, and hence dielectric constant. For example, lead magnesium niobate in single crystal form has a dielectric constant just over 30,000 with the actual maximum depending on measurement frequency and temperature. Two of the most significant recent applications involve incorporating ferroelectrics into silicon devices. The high dielectric constant materials are being developed for increased charge storage in a smaller area in memory chips. The ability of ferroelectrics to exist in two different polarizations in the absence of a

field is being used for non-volatile ferroelectric memories. The temperature dependence of  $\epsilon_r$  obeys Curie-Weiss law above  $T_c$  and thermal hysteresis is observed in the dielectric response. No dispersion is observed in radio frequency region, i.e., it is independent of frequency. Dispersion is observed in microwave frequency region due to domain wall motion. The transition involves changes in macroscopic symmetry, which is evident from the appearance of the shoulders or splitting of certain lines indicating lowering of symmetry. Ferroelectric transition can be thermodynamically the first order or second order transition.

Some materials may not have a well defined domain structure due to reasons discussed later on. One set of such compounds are called as relaxor ferroelectrics. Relaxor ferroelectrics are the materials which are similar to the normal ferroelectrics but it have randomness with one or more atoms of the unit cell. Relaxor behavior is observed in normally in ferroelectric materials with compositionally induced disorder or frustration. This behavior has been observed and studied most extensively in disordered  $ABO_3$  perovskites ferroelectrics and is also seen in mixed crystals of hydrogen-bonded ferroelectrics and anti-ferroelectrics, the protonic glasses [19-20]. The silent features of relaxor ferroelectrics are explained in the following section.

### 1.2.2 Relaxor Ferroelectrics

Relaxor materials are of interest due to unusual properties and they are useful materials from the technological point of view. Relaxor ferroelectrics differ from normal ferroelectrics by three distinct phenomena [21, 22]

- (1) The relaxor ferroelectrics exhibit broad maximum and a significant frequency dispersion of the dielectric permittivity, with the temperature of the maximum dielectric constant ( $T_{max}$ ) increasing and its magnitude ( $\epsilon_{max}$ ) decreasing with increasing frequency.
- (2) No macroscopic phase transition into the ferroelectric state takes place around  $T_{max}$ , not even a „diffuse“ one.
- (3) The local polarization and nanopolar domains appear below a temperature  $T_d$  far above that of maximum permittivity  $T_{max}$ , while the (induced) macro polarization vanishes at a temperature well below  $T_{max}$ .

The effect of chemical ordering on the relaxor ferroelectric properties were initially studied in  $\text{Pb}(\text{Sc}_{1/2}\text{Ta}_{1/2})\text{O}_3$  by Stenger [23-25] and Setter and Cross [26,27] and since then it has been extensively investigated [28-30]. Relaxor ferroelectrics are characterized by diffuse phase transition. In the  $\text{ABO}_3$  oxides substituting ions of different sizes, valences, and polarizability at both the A and B lattice sites produces dipolar defects and can introduce a sufficiently high degree of disorder so as to break translational symmetry and prevent the formation of a long-range ordered state. Instead, the dipolar motion in such systems freezes into a glass-like state on cooling below a dynamic transition temperature,  $T_m$ . In these highly polarisable host lattices, the presence of a dipolar impurity on a given site can induce dipoles in a number of adjacent unit cells within a correlation length of that site. We expect the dipolar motion within this correlation length to be correlated, leading to the formation of polar nanodomains. Indeed, such nanodomains have been observed in many  $\text{ABO}_3$  relaxors at temperatures far above the peak in  $\varepsilon'(T)$ , and their occurrence is now considered to be crucial to the understanding of the properties of relaxors. We picture a distribution of sizes of such nanodomains in which the orientational degrees of freedom are correlated within each domain, but uncorrelated across the various domains. At sufficiently low temperatures, the dipolar motion within each domain freezes, resulting in the formation of an orientational glass (relaxor) state. Such a state is characterized by a distribution of relaxation times related to the sizes of the nanodomains. Two important characteristics of this relaxor state that distinguish it from simple dipolar glasses or spin glasses are the predominant existence of the dipolar nanodomains (vs. largely individual dipoles or spins) and the presence of some degree of cooperative freezing of the orientational degrees of freedom. Evidence of this cooperative effect comes from the observation of some remanent polarization in electric field hysteresis loops. It should be noted, however, that such evidence is also seen in systems of random dipoles in low polarizability hosts for doped alkali halides with sufficiently high concentration of dipoles. The atomic structure of relaxor ferroelectric [PMN] is shown in figure 1.5



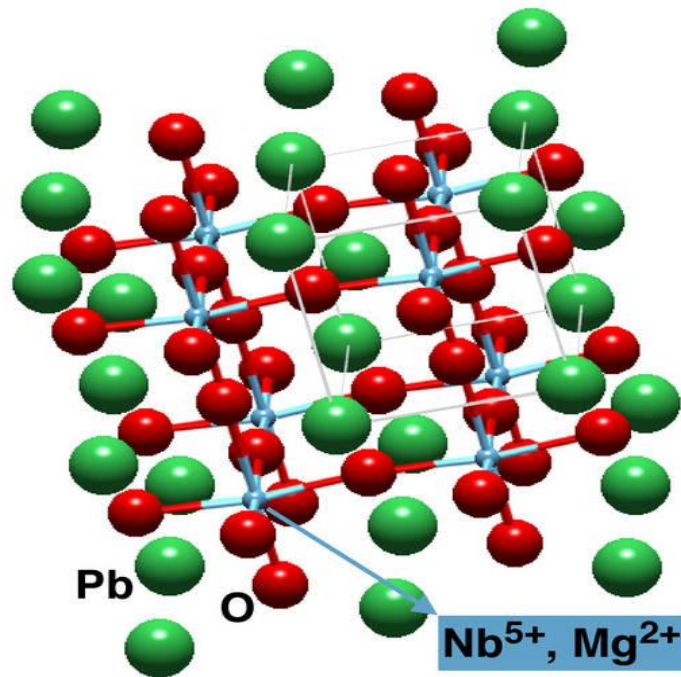


*Figure 1.5 ABO<sub>3</sub> structure of relaxor ferroelectrics [Pb(Mg<sub>1/3</sub>Nb<sub>2/3</sub>)O<sub>3</sub>]*

In order to understand the properties of relaxors it is useful to contrast the properties of relaxors with normal ferroelectrics materials. We do so with the help of Figure 1.6. The contrast is as follows, The P-E hysteresis loop is the signature of a ferroelectric in the low temperature ferroelectric (FE) phase. The large remanent polarization,  $P_R$ , is a manifestation of the cooperative nature of the ferroelectric FE phenomenon. A relaxor, on the other hand, exhibits a so-called slim-loop. For sufficiently high electric fields the nanodomains of the relaxor can be oriented with the field leading to large polarization; however, on removing the field most of these domains reacquire their random orientations resulting in a small  $P_R$ . The small  $P_R$  is evidence for the presence of some degree of cooperative freezing of dipolar (or nanodomain) orientations.

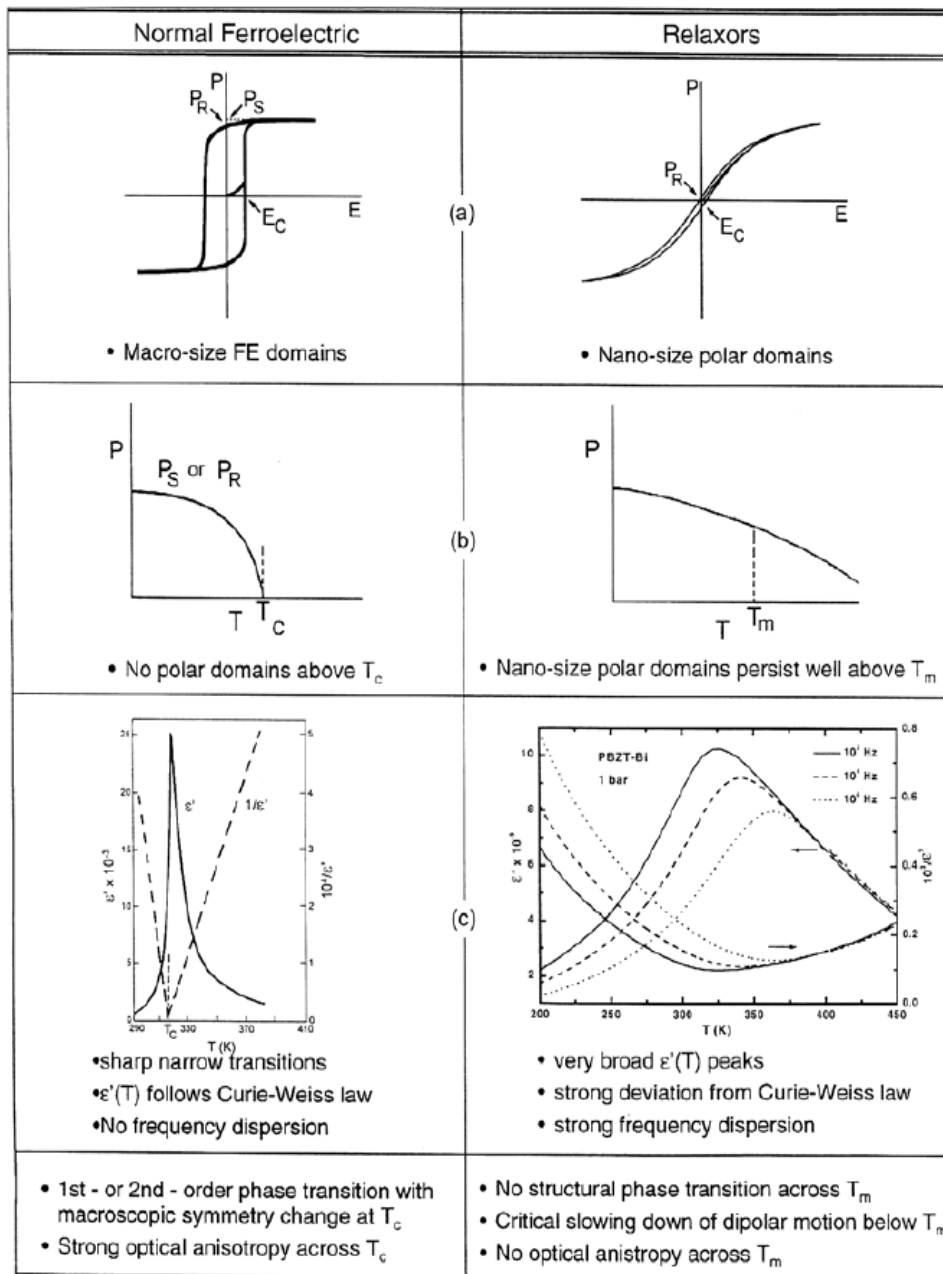


**Figure 1.6 Contrast between the properties of normal ferroelectrics and relaxor ferroelectrics or relaxors (Matthew Delgado, December 13, 2005) [69].**

The saturation and remanent polarizations of a ferroelectric decrease with increasing temperature and vanish at the FE transition temperature ( $T_c$ ). The vanishing of  $P$  at  $T_c$  is continuous for a second-order phase transition and discontinuous for a first-order transition. No

polar domains exist above  $T_c$ . By contrast, the field induced polarization of a relaxor decreases smoothly through the dynamic transition temperature  $T_m$  and retains finite values to rather high temperatures due to the fact that nano-size domains persist to well above  $T_m$ .

By contrast, a relaxor exhibits a very broad  $\varepsilon'(T)$  peak and strong frequency dispersion in the peak temperature ( $T_m$ ) and in the magnitude of  $\varepsilon'$  below  $T_m$ . The conventional wisdom has been that the broad  $\varepsilon'(T)$  peak, also referred to as a “diffuse phase transition,” is associated with compositional fluctuations leading to many micro FE regions with different compositions and  $T_c$ 's. The breadth of the peak is simply a manifestation of the dipolar glass-like response of these materials. The temperature dependence of  $\varepsilon'$  of a ferroelectric obeys a Curie-Weiss law,

$$\varepsilon = c / (T - T_c) \quad (1.2)$$

Above,  $T_c$  could be shown by the linear  $1/\varepsilon'$  vs.  $T$  response. By contrast  $\varepsilon'(T)$  for a relaxor, exhibits strong deviation from this law in the temperature range of many 10s to a few 100s degrees above  $T_m$ .

### 1.2.3 Diffuse Phase Transition

Ferroelectric materials with diffuse phase transition (DPT) characteristics and/or relaxor properties have been studied extensively due to interesting properties. Many phase transitions in macroscopic homogeneous materials are characterized by the fact that the transition temperature is not sharply defined. In these, so-called diffuse phase transition temperature (DPT), the transition is smeared out over a certain temperature interval, resulting in a gradual change of physical properties in this temperature region. Though this phenomenon is observed in several types of materials, however, the most remarkable examples of DPT are found in ferroelectric materials. Ferroelectrics diffuse phase transitions (FDPT) are first mentioned in the literature in the early 1950's [31]. The Diffuse Phase Transition in ferroelectrics are characterized by (a) extending the phase transition in wide temperature interval around the temperature ( $T_m$ ) where the dielectric permittivity assumes its maximum value ( $\varepsilon'_m$ ) (b) gradual decrease of spontaneous and remanent polarizations with rising temperature, (c) transition temperatures obtained by different techniques which do not coincide, (d) relaxation character of the dielectric properties in

transition region and (e) no Curie-Weiss behavior in certain temperature intervals above the transition temperature. The diffuseness of the phase transition is assumed to be due to the occurrence of fluctuations in a relatively large temperature interval around the transition. Usually two kinds of fluctuations are considered: (a) compositional fluctuation and (b) polarization (structural) fluctuation. From the thermodynamic point of view, it is clear that the compositional fluctuation is present in ferroelectric solids-solutions and polarization fluctuation is due to the small energy difference between high and low temperature phases around the transition. This small entropy difference between ferroelectric and paraelectric phase will cause a large probability of fluctuation. Kanzing [31] has observed from X-ray diffraction that in a narrow temperature range around the transition BaTiO<sub>3</sub> single crystal splits up into FE and PE micro regions. According to Fritsberg [32] substances of less stability are expected to have a more diffuse transition. For relaxor as well as other FDPT the width of the transition region is mainly important for practical applications. Smolensky [33] and Rolov [34] have introduced a model calculation, based on the concept of Gaussian distribution for both the compositional and polarization fluctuation, from which the diffuseness parameter can be calculated.

Complex perovskite type ferroelectrics with distorted cation arrangements show DPT which is characterized by a broad maximum for the temperature dependence of dielectric constant ( $\epsilon'$ ) and dielectric dispersion in the transition region (Smolensky, [35]). For DPT  $\epsilon'$  follows modified temperature dependence.

$$\frac{1}{\epsilon} - \frac{1}{\epsilon_m} = (T - T_m)^{\gamma/C'} \quad (1.3)$$

where  $T_m$  is the temperature at which  $\epsilon$  reaches maximum,  $\epsilon_m$  is the value of  $\epsilon'$  at  $T_m$ ,  $C'$  is the modified Curie Weiss like constant and: is the critical exponent, explains the diffusivity of the materials, which lies in the range  $1 < \gamma < 2$  [36]. The smeared out  $\epsilon'$  vs  $T$  response has generally been attributed [37] to the presence of micro regions with local compositions varying from the average composition over length scale of 100 to 1000 Å. Different micro regions in a macroscopic sample are assumed to transfer at different temperature, so-called Curie range, leading DPT which is due to compositional fluctuations [21]. The dielectric and mechanical properties of FE system below their  $T_C$  are functions of the state of polarization and stress. So

ferroelectrics have major application today because of their characteristic electro-optic, dielectric and hysteresis properties. For many practical applications, it is desired to use the very large property maxima in the vicinity of the ferroelectric phase transition, to move the transition into the temperature range of interest and to broaden and diffuse the very large sharp peak values. In DPT the dielectric maxima is now much rounder and polarization persists for a short range of temperature above  $T_m$ .

In reflecting on the occurrence of relaxor behavior in perovskite, there appears to be three essential ingredients: the existence of lattice disorder [38], evidence for the existence of polar nanodomains at temperatures much higher than  $T_m$  and these domains existing as islands in a highly polarizable (soft-mode) host lattice [39]. Various physical models such as super paraelectric model [21], Dipolar Glassy Model [40], Random Field Frustrated Model [41,42], Re-oriented polar clusters model [43,44] have been proposed to explain the behavior of Relaxor Ferroelectric Electrics (RFEs).

### 1.3 Literature Survey

Internationally lots of efforts are being carried out to prepare new compositions of relaxor dielectrics, exhibiting broad temperature and frequency dependent maxima in dielectric parameter, as well as study its structural and dielectric behaviour. The process will enhance the understanding towards origin of observed Relaxor behaviour and its optimization to choose appropriate composition for the devices in thin film as well as in bulk form. No clarity has still emerged regarding spin and dipole glass like temperature dependent conductivity behaviour. Further, it is known that weak changes in grain size, composition, electric field, local strain, etc., can completely modify the physical properties of ferroelectric compounds. These effects are of uttermost importance for industrial applications of these compounds in the form of thin films or in the form of bulk ceramics. For practical applications in devices, optimization of dielectric relaxation and transport behaviour is of immense importance.

Some of the well-known complex perovskites are  $\text{Ba}(\text{Zn}_{1/3}\text{Nb}_{2/3})\text{O}_3$ ,  $\text{Sr}(\text{Zn}_{1/3}\text{Nb}_{2/3})\text{O}_3$  [3-4],  $\text{Pb}(\text{Fe}_{1/2}\text{Nb}_{1/2})\text{O}_3$  (PFN),  $\text{Pb}(\text{Yb}_{1/2}\text{Nb}_{1/2})\text{O}_3$  (PYN) [45],  $\text{Pb}(\text{Sc}_{1/2}\text{Nb}_{1/2})\text{O}_3$  (PSN),  $\text{Pb}(\text{Sc}_{1/2}\text{Ta}_{1/2})\text{O}_3$  (PST) [46],  $\text{Pb}(\text{Mg}_{1/2}\text{W}_{1/2})\text{O}_3$  (PMW),  $\text{Pb}(\text{Fe}_{1/2}\text{W}_{1/2})\text{O}_3$  (PFW),  $\text{Pb}(\text{Fe}_{1/2}\text{Ta}_{1/2})\text{O}_3$  (PFT) [47], as well as  $\text{Pb}(\text{Lu}_{1/2}\text{Nb}_{1/2})\text{O}_3$  (PLN),  $\text{Pb}(\text{Lu}_{1/2}\text{Ta}_{1/2})\text{O}_3$  (PLT) [48]. In the prominent 1: 2 family it is

reported that system is unable to sustain a macroscopic polarization below the dielectric maximum but local polarization does exist till higher temperatures. The nature of dielectric response of these compounds find many applications such as  $\text{Pb}^{2+}$  based relaxor ferroelectric transducers, actuators and multilayer capacitors and  $\text{Ba}^{2+}$  based dielectric resonators (DR) and microwave band gap structure materials. In one kind of perovskite systems the ions displace from their equivalent positions and lead to net dipole moment in the unit cell. The compounds exhibiting this kind of permanent dipole moment are called as Ferroelectrics. There are some materials which do not show well-define domains structure. These kinds of compounds are called relaxor ferroelectrics [19]. Relaxor behavior is observed normally in ferroelectric materials with compositionally induced disorder or frustration. This behavior has been observed and studied most extensively in disordered  $\text{ABO}_3$  perovskite ferroelectrics and also seen in mixed crystals of hydrogen-bonded ferroelectrics and anti-ferroelectrics, the protonic glasses.

A lot of work has been reported on Lead based Iron Niobate or Magnesium Niobate but little work has been reported on Barium, Strontium, Calcium or Bismuth based layered Perovskite Structures, an environmentally friendly material. Many researchers have moved towards environmentally friendly materials and these materials show good promising dielectric/relaxor ferroelectric properties also [49-54]. Barium iron niobate ( $\text{BaFe}_{1/2}\text{Nb}_{1/2}\text{O}_3$ ) (BFN) is a relaxor ferroelectric material that has a diffuse phase transition (DPT) with a broad maximum in the temperature dependence of the dielectric constant. This ceramic is useful for high voltage capacitors and other applications. The plot of dielectric constant as a function of temperature exhibited the broad curve with the highest value of dielectric constant ( $\epsilon_r$ ) of about 50,000 at 300 °C [55]. Dielectric spectra of  $\text{Sr}(\text{Fe}_{1/2}\text{Nb}_{1/2})\text{O}_3$  [SFN] ceramics show two dielectric relaxations with strong frequency dispersion is observed with giant dielectric constant. The high temperature relaxor like dielectric peak is assigned to be a defect ordering induced relaxor behavior, while the low temperature dielectric relaxation was proposed to stem from the electronic ferroelectricity [56]. Strontium copper niobate  $\text{Sr}(\text{Cu}_{1/3}\text{Nb}_{2/3})\text{O}_3$  [SCN] is a ferroelectric material with Curie temperature of 390°C. Progressive addition of Lanthanum at A-site causes a lowering of transition temperature  $T_c$ , dielectric maxima  $\epsilon_{max}$  is also reduced, but increased the dielectric constant. This manifests significant change in the conductivity properties of the sample [57].

Recently there has been overwhelming research on the ferroelectric thin films on account of its potential use in high charge storage devices, non volatile ferroelectric random access memories (NV-FERAM's), tuneable microwave devices, systems (MEMS). The integration of ferroelectric thin films onto the semiconductors in the recent years has given a boost to the development of memory devices for a wide range of applications. As part of the process of miniaturization, it must be recognized that the properties of materials at small scales are often different from those of bulk. The most studied materials for this purpose are the lead based perovskite, such as  $\text{Pb}(\text{Zr}_{0.53}\text{Ti}_{0.47})\text{O}_3$  (PZT). Although, they show good ferroelectric properties, but suffer from severe fatigue problems [58,59]. The other groups of materials which overcome above problems are Strontium, Calcium and Bismuth based Complex Perovskite compounds [60-62].  $\text{Ba}(\text{Zn}_{1/3}\text{Ta}_{2/3})\text{O}_3$  (BZT) films prepared by sol-gel process possess low dielectric constant and high dielectric loss compared to bulk ceramics [63]. The  $\text{Ca}(\text{Zr}_{0.05}\text{Ti}_{0.95})\text{O}_3$  (CZT) thin films prepared by soft chemical method on Pt-Si substrates has shown room temperature ferroelectric properties. The dielectric constant and dielectric loss ( $\tan \delta$ ) at 100 kHz and 1MHz were 212 and 0.032, respectively, and found to be lead free ferroelectric material with possible applications in random access memory [58].

SHI irradiation provides several interesting and unique aspects in understanding of structural damage, material modification and production of controlled defects in the oxide materials. [64-68]. The SHI irradiation is known to generate strain/stress field in oxide materials. It is evident that electronic energy loss,  $S_e$ , due to inelastic collision is able to generate point/cluster of defects, if  $S_e$  is less than the threshold value of electronic energy loss ( $S_e^{\text{th}}$ ). If  $S_e$  is greater than the  $S_e^{\text{th}}$ , then the energetic ions can create columnar amorphization.

### 1.4 Aim of the work

The aim of the present work is to develop understanding as well as produce new relaxor dielectric/ferroelectric material which has tuneability and scope of improvement in its dielectric properties. It is understood from above literature survey that till date there are very few known Lead free relaxor dielectric/ferroelectric thin film materials and its irradiated studies. The development of such type of material, which has exotic ferroelectric/relaxor ferroelectric properties, will be a milestone for the modern technology. These materials have potential

applications in the memory devices where one can write Ferro electrically and read magnetically or vice versa.

Further, the interest in the swift heavy ion (SHI) irradiation on spinel oxides has shown the effect of irradiation on the super exchange interactions, which are highly sensitive to any disorder in the ferrite materials. The multifunctional properties of the magnetoelectric materials (ferroelectric or ferromagnetic properties) are known to be tunable by introducing some defects. The swift heavy ion irradiation is known to create the controlled defects in the materials depending on the choice of ion and its energy. SHI has been widely used to understand the damage structure and the modification in the physical properties of the materials. Moreover, SHI has been proved a good source to produce a wide variety of defects which can create structural strain and disorder in oxide materials, responsible for modifying the physical properties of materials. This motivated us to further extend our studies on thin films to SHI irradiation to attain tuneable dielectric properties.

### 1.5 Objective and Scope of the Work

The current trend in electronic industry has been towards miniaturization. In the case of capacitor as a component and multilayer ceramic capacitor (MLCC) one desires high volume efficiency, low fabrication cost, and high reliability. The materials having a diffuse phase transition (DPT) received the most attention due to their temperature dependence broad maximum in dielectric constant. High dielectric constants allow smaller capacitive components, thus offering the opportunity to decrease the size of the electronic devices. The  $\epsilon'$  (dielectric constant) value of these oxides exhibits only small variation with change in temperature and frequency, which is desirable for technological applications.

In the present work we have studied the effect of A site and B<sup>''</sup>-site substitutions in the Barium and Strontium based [1:2] niobates. The full replacement of A and B site have drastically modified the structural and dielectric properties. Full replacement of  $\text{Mg}^{2+}$  by  $\text{Co}^{2+}$  and  $\text{Cu}^{2+}$  at B<sup>''</sup>- site in Barium and Strontium based [1:2] niobate have induced the Jahn-Teller distortions and gave excellent dielectric properties (high dielectric constant and low dielectric losses) mandatory for devices miniaturization. Motivated by the observed promising modifications to the basic properties we have extended our studies to thin film form. The films of these



compositions are prepared by Physical Vapour Deposition i.e Pulsed Laser Deposition technique. We have grown barium based films on different substrates (Pt-Si, MgO (001), Si(111)) but due to non-conducting nature of these base as well as poor grain growth these substrates were not finalized. Good quality thin films were finally deposited on Indium- Tin oxide (ITO) coated glass substrate. The grain growth was of nano size and polycrystalline films are grown. These well characterized films were put through Swift Heavy Ion Beam Irradiation at Inter University Accelerator Centre (IUAC), New Delhi.

The investigation involves the synthesis, structural and dielectric studies of polycrystalline Barium and Strontium based complex perovskite niobate in bulk and thin film forms as well as the irradiation studies of some of these compounds. The compositions studied are-

- [A]  $A(\text{Mg}_{0.33}\text{Nb}_{0.67})\text{O}_3$  where A stands for  $\text{Ba}^{2+}$ ,  $\text{Sr}^{2+}$  and  $\text{Ca}^{2+}$ .
- [B]  $\text{Ba}(\text{B}'_{0.33}\text{Nb}_{0.67})\text{O}_3$  where B' stands for  $\text{Mg}^{2+}$ ,  $\text{Co}^{2+}$  and  $\text{Cu}^{2+}$ .
- [C]  $\text{Sr}(\text{B}'_{0.33}\text{Nb}_{0.67})\text{O}_3$  where B' stands for  $\text{Mg}^{2+}$ ,  $\text{Co}^{2+}$  and  $\text{Cu}^{2+}$ .

The polycrystalline samples are synthesized using conventional solid state reaction technique and these polycrystalline bulk samples are characterized using X-ray diffraction technique, microstructure analysis(SEM), dielectric properties (temperature and frequency dependent), Conductivity studies and Optical studies. The work is aimed at understanding of A and B'-site substitution and its effect on structural and dielectric properties.

The A and B'-site substitutions are done on the basis of different factors.

- (a) Tolerance Factor
- (b) Ionic Radii
- (c) Charge balancing at (B' and B'') to make it equal to  $4^+$ .

The work that has been done on Barium Magnesium Niobates [BMN] involves replacement of Barium by smaller ionic radii (Sr, Ca) and analysis its structural and dielectric properties. Further, we made Strontium based Series by replacing B- site ( $\text{Mg}^{2+}$ ) by  $\text{Co}^{2+}$  and  $\text{Cu}^{2+}$ . Here  $\text{Co}^{2+}$  and  $\text{Cu}^{2+}$  were used because they may exhibit partial or complete Jahn-Teller Effect. The

Strontium Cobalt Niobate [SCoN] showed good promising dielectric properties in comparison to Strontium Magnesium Niobate [SMN]. Structure wise both SMN and SCoN are same but the dielectric properties were different because of weak Jahn-Teller Effect. Further, when the  $\text{Co}^{2+}$  was again replaced by  $\text{Cu}^{2+}$  forming Strontium Copper Niobate [SCuN] showed excellent dielectric properties. It is proposed to be a direct influence of strong Jahn-Teller Distortions in  $\text{CuO}_6$  octahedra.

These compositions were studied in detail and were further fabricated into thin film from using Physical Vapour Deposition technique i.e Pulsed laser deposition. Detailed studies of these fabricated thin films were carried out using X-ray diffractogram, Microstructure (AFM/SEM), Dielectric studies and conductivity studies. These well characterized films were subjected to Swift Heavy Ion Irradiation at Inter University Accelerator centre (IUAC) to investigate radiation effects on it by two different beams of different energies and different fluencies.

### **Proposed content of the thesis**

#### **Chapter 1**

The first chapter of the thesis will introduce the basic concepts of dielectric, ferroelectricity and relaxor ferroelectricity. A brief introduction about the classification of dielectrics and theory of dielectric classification, theory of the dielectric polarization phenomenon are presented. The phenomenon of ferroelectricity and relaxor ferroelectricity are discussed in detail. The basic understanding of the perovskite structure is elaborated and systems that possess this structure are discussed. The summary of few models explaining relaxor behaviour are presented and finally, the objective of the present work is highlighted.

#### **Chapter 2**

The second chapter of the thesis contains details of the experimental techniques used for preparation of bulk samples, thin films. Detailed of Swift Heavy Ion Irradiation Technique and the characterization Techniques for Structural measurement, Microstructure studies like SEM/AFM, dielectric and impedance studies and optical measurements are explained in detail.

### Chapter 3

The third chapter of the thesis deals with the bulk studies of A site variation in  $A(\text{Mg}_{0.33}\text{Nb}_{0.67})\text{O}_3$  where A stands for  $[\text{Ba}^{2+}, \text{Sr}^{2+} \text{ and } \text{Ca}^{2+}]$  and based on the presence of elements in the composition coding is done as [BMN], [SMN] or [CMN]. The phase formation of polycrystalline  $A(\text{Mg}_{0.33}\text{Nb}_{0.67})\text{O}_3$  , ceramics were done with the help of X-ray diffraction. The micro structural study was carried out through Scanning Electron Microscope. The dielectric study of  $A(\text{Mg}_{0.33}\text{Nb}_{0.67})\text{O}_3$ , reveals that the composition exhibiting relaxor behaviour. The impedance study  $A(\text{Mg}_{0.33}\text{Nb}_{0.67})\text{O}_3$  in case of BMN does not show any semi circular arc in the temperature range (Room temperature -400deg) where as [SMN, CMN] shows two semicircle arcs within the above mentioned studied temperature range. The variation of DC conductivity with temperature follows Arrhenius behaviour. The optical studies show that these compounds are wide band gap semiconductor material.

### Chapter 4

The fourth chapter of the thesis deals with the bulk studies of B'-site variation in Strontium based complex perovskite.  $\text{Sr}(\text{B}'_{0.33}\text{Nb}_{0.67})\text{O}_3$  where  $\text{B}' [ \text{Mg}^{2+}, \text{Co}^{2+}, \text{Cu}^{2+})$  and explains the phase formation of polycrystalline  $\text{Sr}(\text{B}'_{0.33}\text{Nb}_{0.67})\text{O}_3$  ceramics The details structural study of  $\text{Sr}(\text{B}'_{0.33}\text{Nb}_{0.67})\text{O}_3$  ceramics were done by the X-ray diffraction. The micro structural study was done through scanning electron microscope. The dielectric study of  $\text{Sr}(\text{B}'_{0.33}\text{Nb}_{0.67})\text{O}_3$  reveals that the composition shows relaxor behaviour with high magnitude in dielectric constant and low loss tangent. The impedance data shows two semicircles in Nyquist plot within the study temperature indicating the distinct contribution of grain and grain boundary to the total impedance. The variation of imaginary part of impedance and modulus with frequency shows asymmetric peaks and the peak maximum shifts towards higher frequencies with increase in temperature indicating a non-Debye type of relaxation behaviour in the investigated system. The variation of DC conductivity with temperature follows Arrhenius behaviour.

### Chapter 5

The fifth chapter of the thesis deals with the bulk studies of B'-site variation in Barium based complex perovskite.  $\text{Ba}(\text{B}'_{0.33}\text{Nb}_{0.67})\text{O}_3$  where B' stands for (  $\text{Mg}^{2+}, \text{Co}^{2+}, \text{Cu}^{2+})$  and explains the phase formation of polycrystalline  $\text{Ba}(\text{B}'_{0.33}\text{Nb}_{0.67})\text{O}_3$  ceramics. The details structural study of  $\text{Ba}(\text{B}'_{0.33}\text{Nb}_{0.67})\text{O}_3$ , ceramics was done by the help of X-ray diffraction. The

micro structural study was done by scanning electron microscope. The dielectric study of  $\text{Ba}(\text{B}'_{0.33}\text{Nb}_{0.67})\text{O}_3$ , reveals that the composition shows relaxor behaviour with high magnitude in dielectric constant and low loss tangent. The variation of imaginary part of impedance and modulus with frequency shows asymmetric peaks and the peak maximum shifts towards higher frequencies with increase in temperature indicating a non-Debye type of relaxation behaviour in the investigated system. The variation of DC conductivity with temperature follows Arrhenius behaviour

### Chapter 6

The sixth chapter of the thesis contains the thin films studies of  $\text{Ba}(\text{B}'_{0.33}\text{Nb}_{0.67})\text{O}_3$  where B' stands for ( $\text{Mg}^{2+}$ ,  $\text{Co}^{2+}$ ) and  $\text{Sr}(\text{Mg}_{0.33}\text{Nb}_{0.67})\text{O}_3$  prepared from respective bulk samples. The structural, micro structural, dielectric studies and conductivity studies are presented here. Further the swift heavy ion irradiation studies of the thin films of  $\text{Ba}(\text{B}'_{0.33}\text{Nb}_{0.67})\text{O}_3$  where B' stands for ( $\text{Mg}^{2+}$ ,  $\text{Co}^{2+}$ ) and its structural, microstructure, dielectric studies and conductivity analysis are carried out.

**Chapter 7** presents the summary of the research work and major conclusion drawn after in depth discussion in individual chapters. A brief report on the scope for future work is mentioned. At the end list of publications are presented.

### References

- [1] F Galasso, and J. Pyle, *Inorg Chem* **2**, 482, 1962.
- [2] F Galasso, and J. Pinto, *Nature* **207**, 70, 1965.
- [3] M Onada, J. Kuwata, K Kaneeta, K. Toyama, and S Nomura, *Jpn. J. Appl. Phys* **21**, 1707, 1982.
- [4] E L Colla, I. M. Reaney, and N. Setter, *J. Appl. Phys.* **74**, 3414, 1993.
- [5] Wul. B, Goldman. I.M, C. R. Acad. Sci. U.R.S.S., **46**, 177, 1945.
- [6] M E Lines, A M Glass, "Principles and Applications of Ferroelectrics and Related Materials", Clarendon Press, Oxford, 1977.
- [7] F Jona, G Shirane, "Ferroelectric Crystals", Pergamon Press, Oxford, 1962

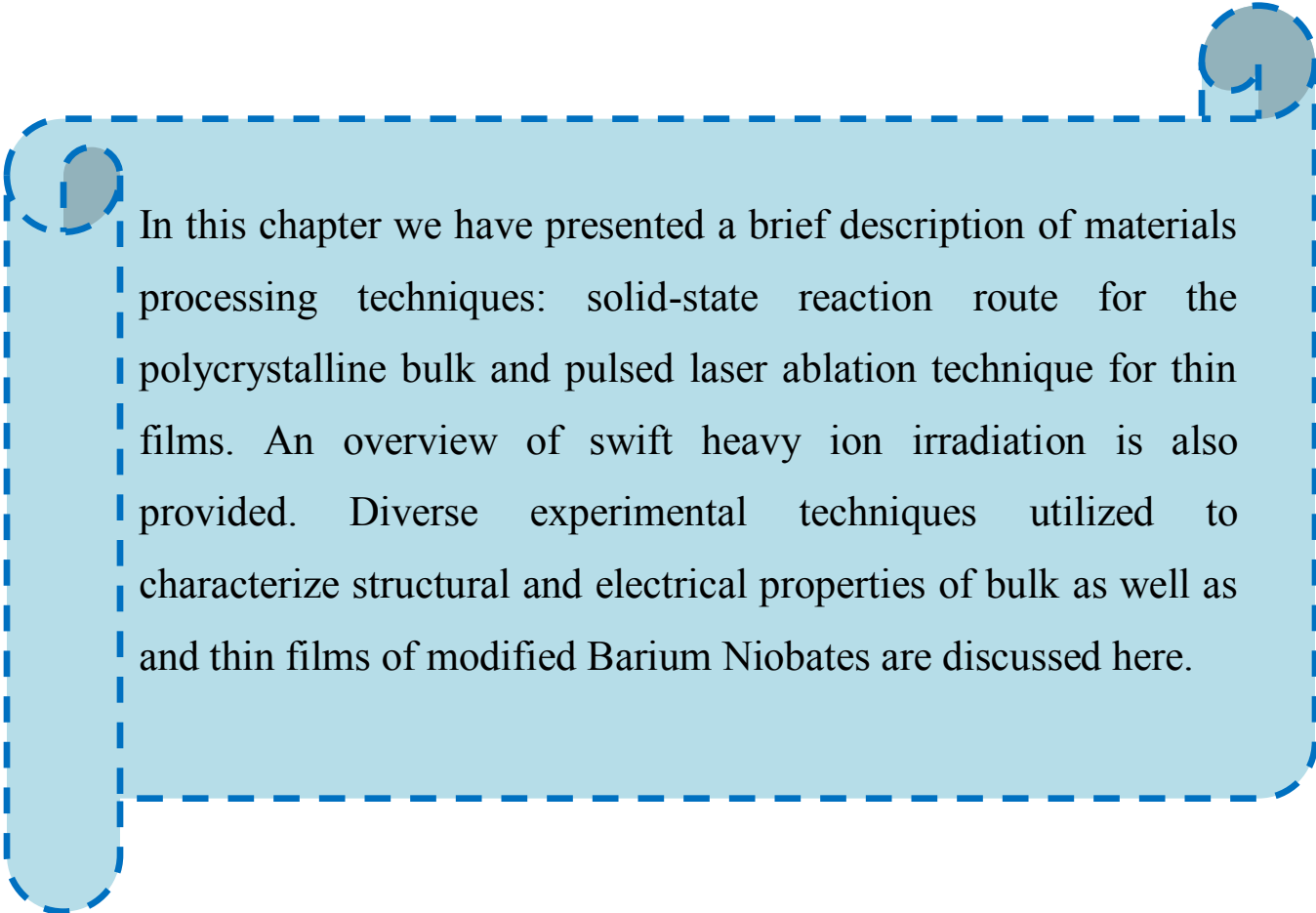
- [8] B Jaffe, W R Cook, H Jaffe, “Piezoelectric Ceramics”, Academic Press, London and New York, 1971.
- [9] A J Moulson, J M Herbert, “Electroceramics”, Chapman and Hall Ltd., London, 1990.
- [10] K S Knight, *Solid State Ionics*, **74**, 109, 1994.
- [11] J H Yang, W K Choo, J H Lee, C H Lee, *Acta Cryst.* **B55**, 348, 1999.
- [12] A Okazaki, Y Suemune, *J. Phys. Soc. Jp*, **16**, 176, 1961.
- [13] D L Corker, A. M. Glazer, J. Dec, K. Roleder and R. W. Whatmore, *Acta Cryst.* **B53**, 135, 1997.
- [14] H D Megaw, Darlington. C.N.W, *Acta Cryst.* **A31**, 161, 1975.
- [15] A M Glazer, *Acta Cryst* **B28**, 3384, 1972.
- [16] A M Glazer, *Acta Cryst.* **A31**, 756, 1975.
- [17] N W Thomas, *J. Appl. Chem Solids* **51**, 1419, 1990.
- [18] E Fatuzzo, and W. J. Merz, *Ferroelectricity*, North Holland publishing company- Amsterdam, 1967.
- [19] L. E. Cross, *Ferroelectrics* **151**, 305, 1994.
- [20] G A Samara, *Solid State Physics* **56**, 239, 2001, G. A. Samara and E. L. Venturini, *Phase Transitions*, **79(1–2)**, 21, 2006.
- [21] L. E. Cross, *Ferroelectrics* **76**, 241, 1987.
- [22] Z.-G. Ye, *Key Engg.Mater*, **81**,155, 1998.
- [23] C. G. Stenger, F. L. Scholten and A. G. Burgraaf, *Solid State Communication* **32**, 989, 1979.
- [24] C. G. Stenger and A. G. Burgraaf *Phys. Stat Sol (a)*, **61**, 275, 1980.
- [25] C. G. Stenger and A. G. Burgraaf *Phys. Stat Sol (a)*, **61**, 653, 1980.
- [26] N. Setter and L. E. Cross *J. Mater Sci*, **15**, 2478, 1980.
- [27] N. Setter and L. E. Cross, *J. Appl Phys*, **51(8)**, 4356, 1980.
- [28] D Vieland and J. F. Li. *J. Appl Phys*, **75(3)**, 1705, 1994.
- [29] F. Chu, N. Setter and A. K. Tagantsev *J. Appl Phys*, **74(8)**, 5129, 1993.
- [30] A. A. Bokov., *Ferroelectrics*,**183** 65, 1996.
- [31] W Kanzig. “Ferroelectrics and Antiferroelectrics”, Academic Press, New York, 1957.
- [32] J Fritesberg “Proc. 4th Int. Meeting on Ferroelectricity”, Leningrad, 1977.

- [33] G A Smolenskii. *J. Phys. Soc. Jp* **28**, 26, 1970.
- [34] B N Rolov, *Soviet Phys. Solid state*, **6**, 1676, 1965.
- [35] G Smolensky *Ferroelectricity*, **53**, 129, 1984.
- [36] S V Tiwari, D Pandey. *J.Am Ceram Soc.II*, **77**, 1819, 1994.
- [37] V V Kirillov, A V Isupov *Ferroelectrics*, **5**, 3, 1973.
- [38] Shashank Priya, Hyeoung Woo Kim Jungho Ryu, Kenji Uchino, Dwight Viehland *Appl Phys Lett*, **80**, 1625, 2002.
- [39] Surya M Gupta, Dwight Viehland, *J. of App Phys* **80**, 5875, 1996.
- [40] D. Viehland, S. J. Jang, L. E. Cross and M Wuttig *J. Appl Phys*, **68(6)**, 2916, 1990, *Physical Rev B* **46** 8003, 1992.
- [41] V. Westphal, W. Kleemann, and M. D. Glinchuk, *Phys. Rev. Lett.* **68**, 847, 1992.
- [42] A. K. Tagantsev and A. E. Glazounov, *J. Korean Phys. Soc.* **32**, S951, 1998.
- [43] B. E. Vugmeister and H. Rabitz, *Phys. Rev. B* **57**, 7581, 1998.
- [44] B. E. Vugmeister and H. Rabitz, cond-mat/9906403 unpublished.
- [45] G. A. Smolenskii, A. I. Agranovskaya, S. N. Popov, and V. A. Isupov, *Zhurnal TekhnicheskoiFiziki*, **28**, 2152 1958 (in Russian).
- [46] G. A. Smolenskii, V. A. Isupov, and A. I. Agranovskaya, *FizikaTverdogoTela*, **1**, 170 1959 (in Russian).
- [47] G. A. Smolenskii, A. I. Agranovskaya, and V. A. Isupov, *FizikaTverdogoTela*, **1**, 990 1959 (in Russian).
- [48] V. A. Isupov and N. N. Krainik, *Fizika Tverdogo Tela*, **6**, 3713 1964 (in Russian).
- [49] T.R. Shrout and A. Halliyal, *Am. Ceram. Soc. Bull.*, **66** 704, 1987.
- [50] G. Smolenski and A. Agranovska, *Fiz. TverdogoTela (Leningrad)* **1**, 1562, 1959. *Sov.Phys.Sol. Stat.* **1**, 1429, 1960.
- [51] V.A. Bokov, I.E. Mylnikova and G.A. Smolensky, *Sov.Phys. JEPT*, **15** 447, 1962.
- [52] SonaliSaha and T.P. Sinha, *Phys. Rev. B***65**, 134103, 2002.
- [53] S.B. Bajaj, R.L. Raibagkar and L.J. Raibagkar, *DAE-Solid State Physics Symposium* **46**, 721, 2003.
- [54] Z.Wang, X. M. Chen, L. Ni, and X. Q. Liu *Appl Phy Let* **90**, 022904, 2007.

- [55] S. Eitssayeam, U. Intatha, K. Pengpat, T. Tunkasiri *Current Applied Physics* **6**, 316, 2006.
- [56] Y. Y. Liu, X. M. Chen, X. Q. Liu, and L. Li *ApplPhys Let* **90**, 192905, 2007.
- [57] K. Sarnbasiva Rao, P.S. Jagga Rao and K. Rarna Rao *Ferroelectrics Letters*, **16** 195, 1993.
- [58] L.S. Cavalcante, A.Z. Simoes, L.P.S. Santos, M.R.M.C. Santos, E. Longo, J.A. Varela *Journal of Solid State Chemistry* **179** 3739, 2006.
- [59] Xinhua Zhu, Shengguo Lu, Chung-Loong Choy, Helen Lai-Wah Chan, and Kin-hung Wong *Integrated Ferroelectrics*. **36**,73,2001.
- [60] Xinhua Zhu Nui Chong, Helen Lai-Wah Chan, Chung-Loong Choy, and Kin-Hung Wong Zhiguo Liu, and Naiben Ming *Appl Phys Lett* **80**, 3376, 2002.
- [61] Basavaraj Angadi, P. Victor, V.M. Jali, M. T. lagare, Ravi Kumar, S. B. Krupanidhi, *Mat Science Engg.* **B100**, 93, 2003.
- [62] J.T. Evans, R. Womak, *IEEE J. Solid-State Circuits SSC* **23**, 1171, 1988.
- [63] Zhou Ji, D J Barber *J of Mat Sci Let* **16**, 1426, 1997.
- [64] Jean-Marc Costantini, Francis Studer, Jean-Claude Peuzin, *J. Appl. Phys.* **90**,126, 2001.
- [65] J.M. Costantini, F. Brisard, J.L. Flament, D. Bourgault, L. Sinopoli, J.L. Uzureau, *Nucl. Instr and Meth.* **B 59–60** 600, 1991.
- [66] S. Meillon, F. Studer, M. Hervieu, H. Pascard, *Nucl. Instr. and Meth.* **B 107** 363, 1996.
- [67] F. Studer, M. Toulemonde, *Nucl. Instr. and Meth.* **B 65**, 560, 1992.
- [68] S. Furuno, N. Sasajima, K. Hojou, K. Izui, H. Otsu, T. Muromura, T. Matsui, *Nucl. Instr. and Meth.* **B 127–128**, 181, 1997.
- [69] Matthew Delgado, Phase Transition in Relaxor Ferroelectrics, December 13, 2005.

## Chapter 2

### Experimental and Characterization Techniques



In this chapter we have presented a brief description of materials processing techniques: solid-state reaction route for the polycrystalline bulk and pulsed laser ablation technique for thin films. An overview of swift heavy ion irradiation is also provided. Diverse experimental techniques utilized to characterize structural and electrical properties of bulk as well as and thin films of modified Barium Niobates are discussed here.



## 2.1 Introduction

This chapter outlines the complex perovskites  $A(\text{Mg}_{1/3}\text{Nb}_{2/3})\text{O}_3$  where  $A = \text{Ba}^{2+}$ ,  $\text{Sr}^{2+}$  and  $\text{Ca}^{2+}$  and  $\text{Sr}(\text{B}'_{1/3}\text{Nb}_{2/3})\text{O}_3$  where  $\text{B}' = [\text{Mg}^{2+}, \text{Co}^{2+}, \text{Cu}^{2+}]$  sample preparation details in bulk as well as in thin film form used in our present study. The working principle of accelerators and various techniques used for bulk measurements, off line analysis of pristine and irradiated thin film are also discussed.

This chapter on the whole describes the experimental techniques used during the course of present research work. It is divided in to two parts (I) synthesis of sample in bulk and thin films forms and (II) characterization techniques employed for evaluating various properties of these samples.

### 2.1.1 Synthesis of Bulk Materials

There are various methods known for the synthesis of relaxor ferroelectric bulk materials such as solid state reaction [1-6], sol gel [7] and co precipitation [8-9]. In the present thesis, the bulk target materials for thin film deposition of A- site variation in  $A(\text{Mg}_{1/3}\text{Nb}_{2/3})\text{O}_3$  (where  $A = \text{Ba}^{2+}$ ,  $\text{Sr}^{2+}$  and  $\text{Ca}^{2+}$ ) and B'- site variation in  $\text{Sr}(\text{B}'_{1/3}\text{Nb}_{2/3})\text{O}_3$  (where  $\text{B}' = \text{Mg}^{2+}$ ,  $\text{Co}^{2+}$  and  $\text{Cu}^{2+}$ ) based dielectric/relaxor ferroelectric materials have been synthesized by solid state reaction technique. This route of bulk preparation, which is also acknowledged as ceramic method, has superiority due to easiness of the process involved in the technique. This process involves various steps, for instance (i) mixing the required oxide/carbonate powders in appropriate proportion, (ii) calcinations, (iii) pelletization and (iv) sintering of the polycrystalline bulk.

#### (i) Mixing of Powders

For the preparation of  $A(\text{Mg}_{1/3}\text{Nb}_{2/3})\text{O}_3$  (where  $A = \text{Ba}^{2+}$ ,  $\text{Sr}^{2+}$  and  $\text{Ca}^{2+}$ ) and B'- site variation in  $\text{Sr}(\text{B}'_{1/3}\text{Nb}_{2/3})\text{O}_3$  (where  $\text{B}' = \text{Mg}^{2+}$ ,  $\text{Co}^{2+}$  and  $\text{Cu}^{2+}$ ) samples, the high purity fine powders of  $\text{BaCO}_3$ ,  $\text{SrCO}_3$ ,  $\text{CaCO}_3$ ,  $\text{MgO}$ ,  $\text{Nb}_2\text{O}_5$ ,  $\text{CuO}$ ,  $\text{Co}_3\text{O}_4$ , were weighed and mixed in appropriate proportions were thoroughly mixed and ground in highly pure acetone using a mortar and pestle. This process is carried out for several hours in order to accomplish the homogeneity of the mixed powder. The physical uniformity and the chemical homogeneity of the mixtures are of significant importance especially for the doped samples.

**(ii) Calcinations**

The decomposition of the mixed powder by heating below its melting point is known as calcinations. Mixed powders are kept in crucible/boats and heated in box furnace in ambient environment. The course of calcinations entails heating the homogenously mixed powder to an intermediate high temperature, roughly 600<sup>0</sup>-800<sup>0</sup>C lower than the final sintering temperature. The intention of calcinations procedure is to establish the course of nucleation for the grain growth and facilitates the decomposition of the substituent oxides/carbonates. The rationale for this process is the concentration gradient and high temperature. This step crafts a seed for the chemically and crystallographic ally uniform growth of the structure. For A(Mg<sub>1/3</sub>Nb<sub>2/3</sub>)O<sub>3</sub> and Sr(B'<sub>1/3</sub>Nb<sub>2/3</sub>)O<sub>3</sub> samples, the samples were calcinated at 600<sup>0</sup>-800<sup>0</sup>C. Calcination was repeated 2-3 times with intermediate grinding and every time calcinations temperature was kept same as in the previous step.

**(iii) Pelletization**

In order to make use of these ceramic materials, the calcinated powders must be brought into the required shapes and densities before the final sintering process. This is achieved by using dye-press technique in which a dye of proper shape was filled with calcinated powder and pressed using hydraulic pressure. In our case, pelletization is done in a dye of circular shape of 12mm diameter. The thickness of the pellets was ~1.4mm.

**(iv) Sintering**

After pelletization of the fine calcinated powder, sintering of the pellet is done at relatively higher temperature and for longer duration used during calcinations. This is followed by slow cooling with a suitable predefined rate, which is an essential and important process as it favors the required oxygen content in the materials. For A(Mg<sub>1/3</sub>Nb<sub>2/3</sub>)O<sub>3</sub> bulk pellet, the final sintering temperature was kept at 1150<sup>0</sup>C for 48 hours followed by natural cooling. For Sr(B'<sub>1/3</sub>Nb<sub>2/3</sub>)O<sub>3</sub> bulk pellets, the sintering temperature was maintained at 1250<sup>0</sup>C for 48 hours followed by natural cooling. Figure 2.1 shows the flow chart used for the preparation of bulk samples.

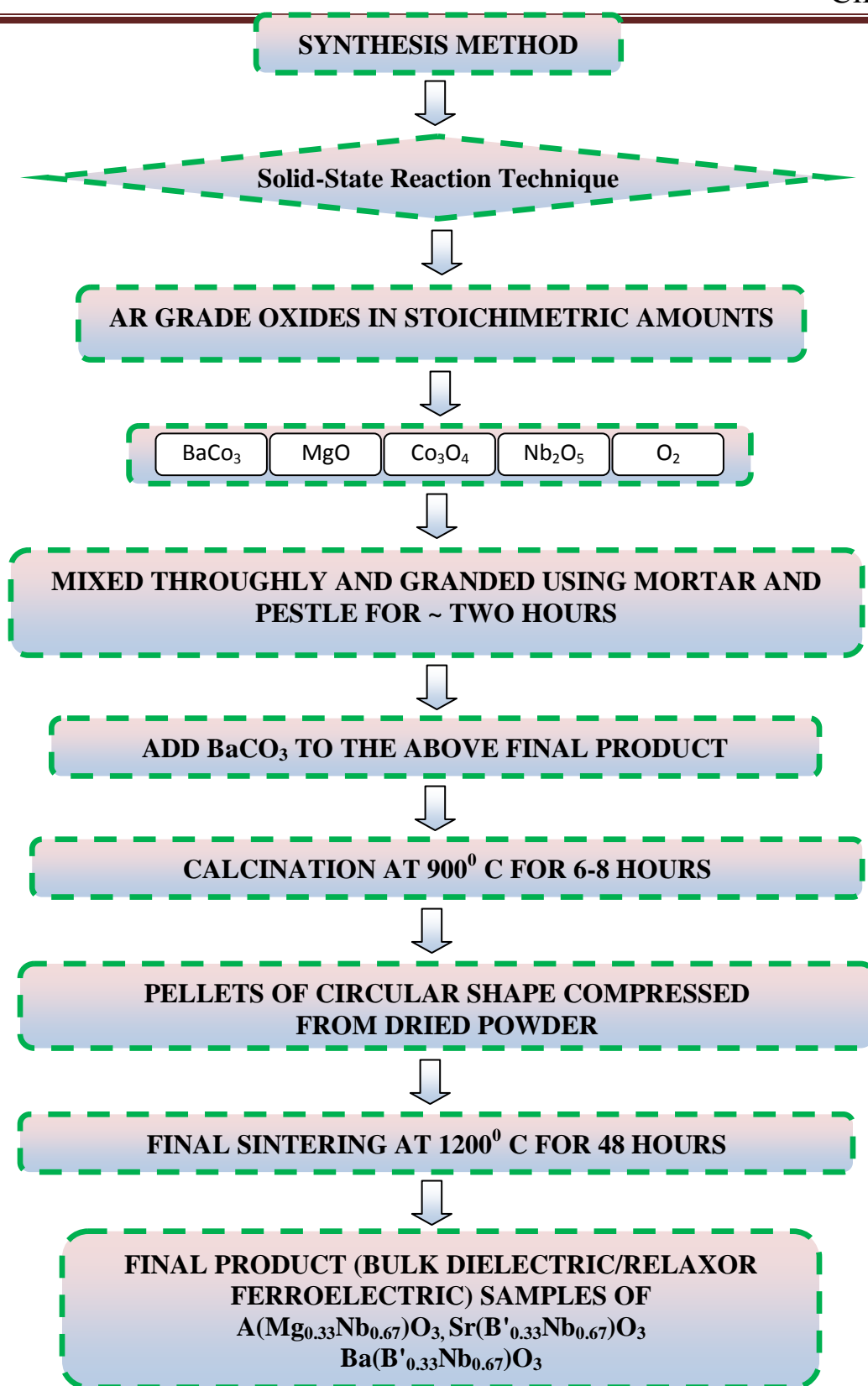


Figure 2.1 Flow chart for the preparation of bulk samples

## 2.2 Thin Film Deposition

### Pulsed laser Deposition (PLD) Technique

Pulsed laser deposition had several characteristic that made it remarkably competitive in the complex oxide thin-film research arena as compared to other film growth techniques these principle attractive features were stoichiometric transfer, excited oxidizing species, and simplicity in initial setup and in the investigation of arbitrary oxide compounds. One could rapidly investigate thin-film deposition of nearly and oxide compound regardless of the complexity of the crystal chemistry.

The applicability and acceptance of pulsed laser deposition in thin-film research rests largely in its simplicity in implementation. There are many deposition techniques for thin film preparation, such as Pulsed laser deposition (PLD) is a physical vapour deposition process,[1-9], chemical vapour deposition (CVD), metal organic chemical vapour deposition (MOCVD) [10-16], DC and RF sputtering [17-21], molecular beam epitaxy (MBE) [22] thermal evaporation [23] sole gel [24] etc. Among the various techniques as mentioned above for thin film deposition; PLD is one of the most commonly used for thin film growth of multicomponent materials. A pulsed laser is focused onto a target of the material to be deposited, for sufficiently high laser energy density, each laser pulse vaporizes or ablates a small amount of the material creating a plasma plume, and the ablated material is ejected from the target in a highly forward-directed plume. The ablation plume provides the material flux for film growth. Matrix has been investigated.

#### (a) Principles of Excimer PLD

Excimer lasers such as XeF ( $\lambda = 352\text{nm}$ ); XeCl ( $\lambda = 308\text{nm}$ ); Krf ( $\lambda = 222\text{nm}$ ); ArF ( $\lambda = 193\text{nm}$ ); and F<sub>2</sub> ( $\lambda = 157\text{nm}$ ) are commercially available and can be used for thin film deposition. It uses a pulsed laser beam, usually but not necessarily, from an ultraviolet excimer laser with pulse energy of about 1J. The typical duration of the laser pulse is a few tens of nanosecond. Because of such a short duration of pulse, tremendous power ( $\sim 10 - 100 \text{ MW/pulse}$ ) is delivered to the target. This is because of the non equilibrium nature of PLD, in the sense that the absorption of energy and ablation takes place in a very short time, usually within a nanosecond, before thermodynamic equilibrium is reached. Typical schematic of the pulsed laser deposition technique is shown in Figure 2.2.

The generality of the materials used for PLD research has a very high absorption coefficient in this wavelength region. The shorter the wavelength of the excimer laser, the higher the absorption. The importance of this feature is that it minimizes the interaction time between the laser radiation and the target material, hence making it possible to deposit nanolayers of the target materials during PLD.

The basic components of an excimer PLD system include a vacuum system equipped with a target and substrate holder as well as deposition monitoring systems. The evaporating source is a high-power laser located outside of the vacuum chamber. An optical system (lenses and mirrors) is used to focus the high-power laser beam on the substrate. The mechanism of PLD leading to material transfer to the substrate involves many stages, although it depends mainly on the type of laser, optics, and properties of the target used. First, a target is heated by short, concentrated burst of laser radiation and when the laser radiation is absorbed by the solid surface, electromagnetic energy is converted first into electronic excitation and then into thermal and the material is ablated. Subsequently, the evaporants form a plume which consists of a mixture of high-energy species including atoms, molecules, electrons, ions, clusters, and even micron-sized particulates. The plume that is formed propagates through a background of working gas toward the substrate. The plume is characterized by numerous collisions that may affect the velocities and the mean-free paths of the ablated atoms and ions as well as initiating reactions, the reduction of the mean-free path caused by collision leads to the fast expansion of the plume from the target surface to form narrow forward angular distributions of the evaporants. During this process, some material is redeposited onto the target or chamber walls, but most reaches the substrate where nucleation and growth occur. The eventual formation of the film is not only governed by the ablation and plume propagation but also by the substrate properties such as structure and topography, working gas, and the laser power [25].

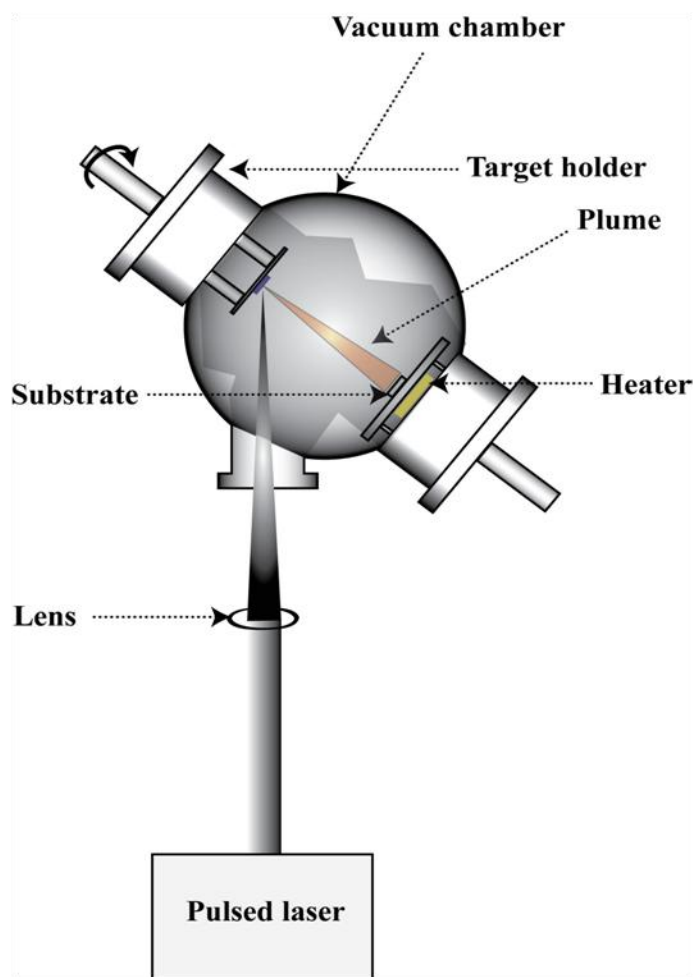


*Figure 2.2*     **A schematic view of Pulsed Laser Deposition Technique.**

In the Present work thin films were prepared by pulsed laser deposition (PLD) technique from a single-phase bulk target of basic compositions of  $\text{Ba}(\text{Mg}_{1/3}\text{Nb}_{2/3})\text{O}_3[\text{BMN}]$  and  $\text{Sr}(\text{Mg}_{1/3}\text{Nb}_{2/3})\text{O}_3[\text{SMN}]$  (20-25mm diameter) onto ITO substrate. The target was processed by conventional solid-state reaction technique. For deposition, a KrF excimer laser (model Lambda Physik,  $\lambda = 248\text{nm}$ ) see at 20ns pulse duration, 10hz repetition rate and a home-made stainless stell vacuum chamber were used. The thin film deposition was done at UGC-DAE Consortium for Scientific Research, Indore, India. The target was mounted at an angle of  $45^\circ$  to laser beam inside vacuum chamber, where a base pressure of  $2 \times 10^{-5}\text{mTorr}$  was achieved through a turbo-mechanical pump. The substrate (10mm  $\times$  10mm) was attached to a stainless steel holder at a distance of 40 mm from the target and is placed parallel to it inside the heater assembly, which is

capable to heating the substrate up to 650<sup>0</sup>C. The target material was rotated at about 10rpm and the deposition was carried out in an O<sub>2</sub> partial pressure of 200mTorr by keeping the substrate temperature to 450<sup>0</sup>C. The deposition was performed for ~ 20 min. after the deposition; the thin film was cooled slowly to room temperature by turning down the power to the substrate heater and maintaining the oxygen pressure in the chamber to 200 m Torr. The film thickness was measured by profilometer with 0.5 nm resolution.

### **2.3 Characterization Techniques**

The following characterizing tools are used to study the structural, microstructural, dielectric, impedance and optical study of ceramics.

#### **2.3.1 X-Ray Diffraction Measurement**

X-ray powder diffraction is used to determine the atomic structure of crystalline materials without the need for large (~100μm) single crystals. “Powder” can be a misnomer; the technique is applicable to polycrystalline phases such as cast solids or films grown on a substrate. X-ray powder diffraction can be useful in a wide variety of situations.

X-ray diffraction (XRD) technique is used for the realization of structural property and can be employed exclusively to categorize the crystalline phase in the sample [26]. This technique is suitable for both form of samples i.e. thin film as well as bulk and can yield the information regarding the crystallinity of the material, nature of the phase present, lattice parameter, grain size, out of plane orientation and relative in plane orientation between the film and substrate. In case of thin film, the change in lattice parameter with respect to the bulk gives the idea of nature of strain present in the film.

The following information is obtained from the X-ray diffractogram

- (i) Quality and confirmation of the prepared samples,
- (ii) The interplanar spacing  $d$  of the reflections,
- (iii) The intensities of the reflections, and
- (iv) The unit cell dimensions and lattice type.

The fundamental of XRD is best explained by the Bragg's equation which places the condition for the constructive interference for the scattered X-ray from the successive atomic planes formed by the crystal lattice of the material. The Bragg's condition is formulated by

$$2 d \sin \theta = n \lambda \quad (2.1)$$

Where  $\lambda$  is the wavelength of the incident X-ray,  $d$  is the interplanar distance,  $\theta$  is the scattering angle and  $n$  is an integer- the order of diffraction.

In thin films, X-rays are diffracted by the oriented crystallites at a particular angle to satisfy the Bragg's condition. Having known the value of  $\theta$  and  $\lambda$ , once can calculate the interplanar spacing which is shown in Figure 2.3.

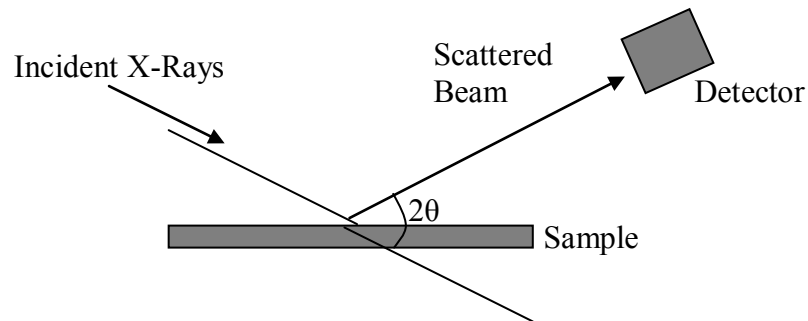


**Figure 2.3 A representation of x-ray diffraction**

The XRD can be taken in various modes such as  $\theta$  -  $2\theta$  scan mode,  $\theta$  -  $2\theta$  rocking curve, and  $\Phi$  scan. In the  $\theta$  -  $2\theta$  scan mode, a monochromatic beam of X-ray is incident on the sample at an angle of  $\theta$  with the sample surface. The detector motion is coupled with the X-ray source in such a way that it always makes an angle  $2\theta$  with the incident direction of the X-ray beam (Figure 2.3). The resulting spectrum is a plot between the intensity recorded by the detector versus  $2\theta$ .





*Figure 2.4*     **X-ray diffractometer (UGC-DAE CSR Indore)**

The crystalline quality of the oriented samples can be estimated by using it in rocking curve mode wherein a single Bragg peak is measured as the sample is tilted within the diffraction plane. In this arrangement the position of the detector is kept fixed at  $2\theta$  value corresponding to a particular  $d$  value and sample is rocked around the  $\theta$  value. The resulting spectrum is a plot between the intensity and  $\theta$ . The full width at half maximum (FWHM) of the plot estimates the mis orientation of the grains in the film with respect to the sample normal.

In the present work, Bruker D8 Advanced Diffractometer (see Figure 2.4) with Cu-K $\alpha$  ( $\lambda = 1.542 \text{ \AA}$ ) was used for the phase detection of bulk powders and thin films at UGC-DAE Consortium of Scientific Research, Indore. The angle  $2\theta$  was varied from 10 to 110 steps of  $0.05^\circ$ . The lattice spacing “ $d$ ” was calculated using Bragg’s equation (see eqn. 2.1) which is further utilized to calculate lattice constant. The analysis of the XRD pattern was done using Powder-X software [27] at room temperature.

### **2.3.2 Scanning Electron Microscopy**

The Scanning Electron Microscopy (SEM) is one of the most widely used instruments in materials research laboratories and is common in various forms in fabrication plants. Scanning electron microscopy is central to microstructural analysis and therefore important to any

investigation relating to the processing, properties, and behaviour of materials that involves their microstructure [28]. The SEM provides information relating to topographical features, morphology, phase distribution, compositional differences, crystal structure, crystal orientation, and the presence and location of electrical defects. The SEM is also capable of determining elemental composition of micro-volumes with the addition of an x-ray or electron spectrometer and phase identification through analysis of electron diffraction patterns. The strength of SEM lies in its inherent versatility due to the multiple signals generated, simple image formation process, wide magnification range, and excellent depth of field.

Lenses in the SEM are not a part of the image formation system but are used to demagnify and focus the electron beam onto the sample surface. This gives rise to two of the major benefits of the SEM: range of magnification and depth of field in the image. Depth of field is that property of SEM images where surfaces at different distances from the lens appear in focus, giving the image three-dimensional information. The SEM has more than 300 times the depth of field of the light microscope. Another important advantage of the SEM over the optical microscope is its high resolution. Resolution of 1 nm is now achievable from an SEM with a field emission (FE) electron gun. As a consequence, TEM sample preparation of bulk materials is tedious and time consuming, compared to the ease of SEM sample preparation, and may damage the microstructure. The SEM is relatively easy to operate and affordable and allows for multiple operation modes, corresponding to the collection of different signals.

The SEM electron beam is a focused probe of electrons accelerated to moderately high energy and positioned onto the sample by electromagnetic fields. A secondary electron (SE) is a low-energy (2- to 5 eV) electron ejected from the outer shell of a sample atom after an inelastic interaction. Backscattered electrons (BSEs) are electrons from the incident probe that undergo elastic interactions with the sample, change trajectory, and escape the sample.

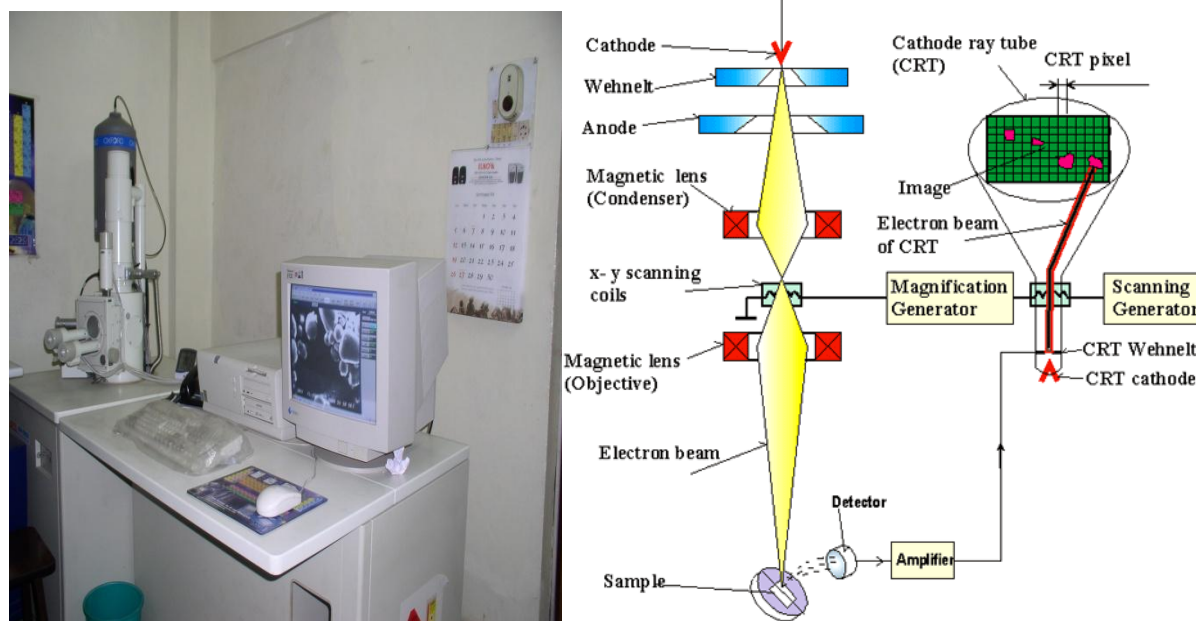


**Figure 2.5 Schematic diagram of scanning electron microscope (SEM) (UGC-DAE CSR Indore)**

Image construction in a SEM is accomplished by mapping intensity of one of these signals (usually SE and /or BSE) from the specimen onto a viewing screen or film. The region on the specimen from which information is transferred to a single pixel of the image is called a picture element. The size of the picture element is determined by the length of the scan on the specimen divided by the number of pixels in a line of the image. A common digital resolution for the SEM is  $1024 \times 1024$ , and thus the picture element width for the  $100\times$  image would be  $0.98\mu\text{m}$ . The picture element width would be  $0.098\mu\text{m}$  at  $1000\times$  and  $0.0098\mu\text{m}$  at  $10,000\times$ . The SEM image will appear in focus if the sampling volume is smaller in diameter than this picture element size. The SEM image conveys three-dimensional information due to the depth of field in the image. Modern SEM's with field emission electron guns (FESEMs) are capable of resolutions near  $1\text{nm}$  on appropriate samples using the SE signal.

In the present thesis work, Scanning electron microscope measurement has been done using FModel JEOL JSM 5600 with resolution of  $3.5\text{ nm}$  shown in (Figure 2.5). Magnification is 18 to 300,000 (in 136 steps) Accelerating Voltage 0.5 to 30 kV (53 steps) Displayed image  $640 \times 480$  pixel Image memory is  $1280 \times 960$  pixels with optional Attachment of Energy Dispersive X-ray spectrometer(EDS)

### 2.3.3 Atomic Force Microscopy

The atomic force microscope (AFM) is one of the most widely used techniques for studying the surface morphology [28, 29]. It consists of piezoelectric scanner to control the scanning motion, the optical head to vibrate the cantilever and sense the cantilever deflection and a base to support the scanner and head. In this technique, an atomically sharp tip placed at the end of a cantilever is scanned over a surface with feedback mechanisms that facilitate the piezoelectric scanners to sustain the tip at a constant force (to obtain height information), or height (to obtain force information) above the sample surface. Tips are typically made from  $\text{Si}_3\text{N}_4$  or Si. The cantilever bends in response to the force between the tip and the sample. A representative view of the function of AFM is shown in Figure 2.6.

The tip approaches the surface of the sample and interacts with it via Van der Waals forces. The interaction translates in a cantilever deflection or a change in the cantilever's oscillating frequency, depending on the operational mode of the AFM: contact or tapping. The deflection or the frequency changes of the cantilever are detected by an optical system consisting of a laser beam, which is reflected on the cantilever. The vertical and the horizontal deflections are measured using a split photodiode detector that analyses the reflected beam. The displacement of the cantilever on the three directions is done by means of a piezoelectric scanner, combining independently operated piezo-electrodes, for X, Y and Z direction into a single tube. The two operating modes that have been used, contact-AFM and tapping-AFM, are described in more detail in the following text.

#### 2.3.3.1 Contact Mode AFM

As we have mentioned the changes in the cantilever's deflection are monitored with a split photodiode detector as the tip is scanning the sample surface [30]. A feedback loop maintains a constant deflection between the cantilever and the sample by vertically moving the scanner at each data point to maintain a „set-point“ deflection. By maintaining a constant cantilever deflection, the force between the tip and the sample remains constant. The force  $F$  is calculated from Hook's law;  $F = -kx$ , where  $k$  is the spring constant and  $x$  is the deflection. Spring constants usually range from 0.01 to 1.0N/m, resulting in forces ranging from  $n\text{N}$  to  $\mu\text{N}$ .

The distance that scanner moves vertically at each point (x,y) is stored by the computer to form the topographic image of the surface.

### 2.3.3.2 Tapping Mode AFM

In tapping mode, the cantilever is oscillated near its resonance frequency with the amplitude ranging typically from 20 to 100 nm. The tip lightly „taps“ the surface while scanning, contacting the surface at the bottom of its swing. The feedback loop maintains constant oscillation amplitude by maintaining a constant RMS of the oscillation signal acquired by the split photodiode detector. In order to maintain constant oscillation amplitude the scanner has to move vertically at each point (x, y). The vertical position of the scanner is stored by the computer, to form the topographic image of the sample surface. In the present work, to study topographic and morphology of the thin films, Atomic Force Microscopy (AFM) measurements have been carried out using Nanoscope III a (Digital Instruments) at UGC-DAE consortium of Scientific Research, Indore.

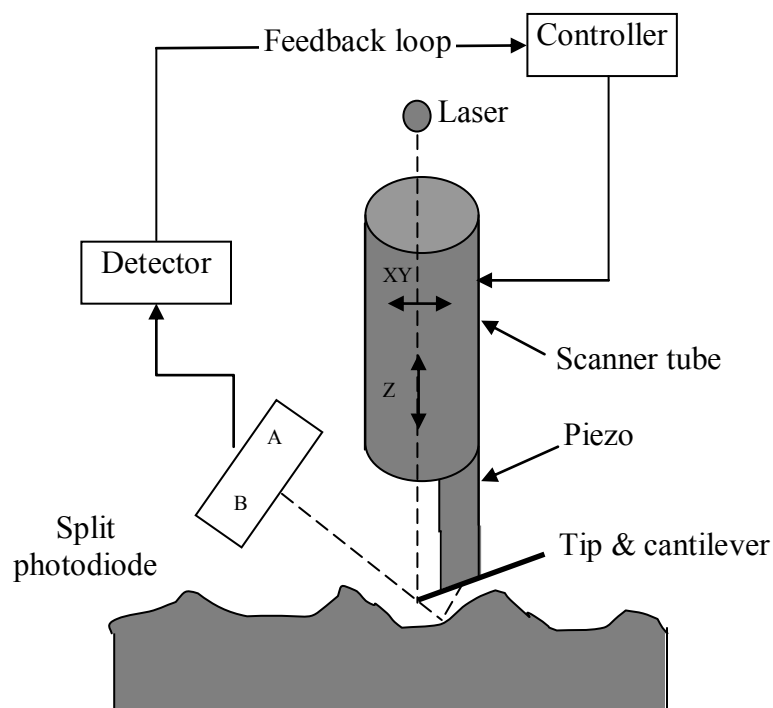


*Figure 2.6*      **Schematic diagram of Atomic Force Microscope (AFM)**

### 2.3.4 Optical Studies

#### 2.3.4.1 Ultraviolet and Visible Absorption Spectroscopy (UV-Vis)

Ultraviolet and visible (UV-Vis) absorption spectroscopy is the measurement of the attenuation of a beam of light after it passes through a sample or after reflection from a sample surface. Ultraviolet-visible spectroscopy is one of the most ubiquitous analytical and characterization techniques in science. There is a linear relationship between absorbance and absorber concentration, which makes UV-Vis spectroscopy especially attractive for making quantitative measurements. Ultraviolet and visible photons are energetic enough to promote electrons to higher energy states in molecules and materials. UV-Vis spectroscopy is useful to the exploration of the electronic properties of the materials and materials precursors in basic research and in the development of applied materials. Materials that can be characterized by UV-Vis spectroscopy include semiconductors for electronics, lasers, and detectors; transparent or partially transparent optical components; solid-state laser hosts; optical fibres, waveguides, and amplifiers for communication; fibres, waveguides, and amplifiers for communication; and materials for solar energy conversion. The UV-Vis range also spans the range of human visual acuity of approximately 400 to 750nm, making UV-Vis spectroscopy useful in characterizing the absorption, transmission, and reflectivity of a variety of technologically important materials, such as pigments, coatings, windows, and filters.

When an atom or molecule absorbs energy, electrons are promoted from their ground state to an excited state. UV-visible spectroscopy provides direct evidence about electron energy jumps between the two distinct energy levels.

In the present study UV-Vis spectrometer (Perkin Elmer lambda 25) has been used to study the optical properties of bulk as well as polycrystalline thin films. Figure 2.7 shows the schematic diagram of the components of UV-Vis spectrometer. The optical components are coated with silica for durability and a holographic concave grating with 1053 lines/mm in the center is used in the monochromator. Two radiation sources, deuterium lamp and a tungsten halogen lamp cover the working wavelength range from 200-1100nm of the spectrum. During the operation in the visible range, mirror  $M_1$  reflects the radiation from the halogen lamp onto source mirror  $M_2$  and at the same time  $M_1$  blocks the radiation from the deuterium lamp. While in UV range mirror  $M_1$  is raised to permit radiation from the deuterium lamp to strike source

mirror  $M_2$ . The radiation source and filter change is automatic during monochromator slewing. Radiation from the source lamp is reflected from source mirror  $M_2$  through an optical filter on the filter wheel assembly that has been driven by a stepping motor in synchronization with the monochromator. Depending on the wavelength being produced, the appropriate optical filter is located in the beam path to prefilter the radiation before it enters the monochromator. From optical filter the radiation passes through entrance slit ( $S_1$ ) of the monochromator grating. The radiation is dispersed at the grating to produce a spectrum. The rotational position of the grating effectively selects a segment of the spectrum, reflecting the segment through the exit slit ( $S_2$ ) to mirror  $M_3$ . The exit slit restricts the spectrum segment to a near monochromatic radiation beam. The slit provide spectral band pass of 1 nm. From mirror  $M_3$  the radiation is reflected onto a beam splitter which allows

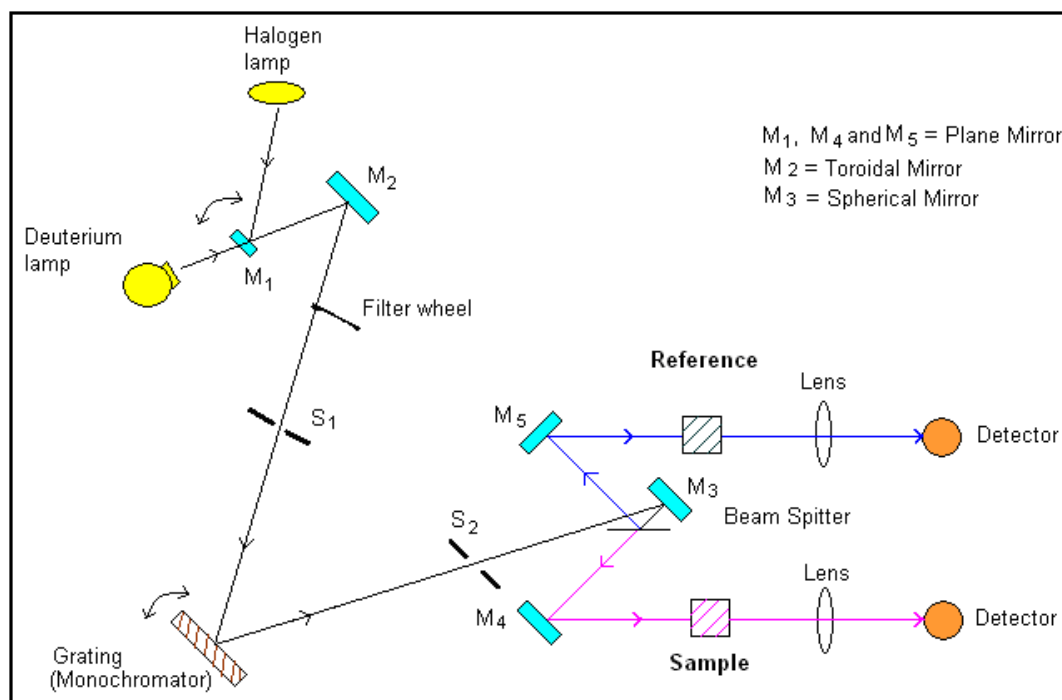


**Figure 2.7 Schematic View of UV-Vis Spectroscopy**

50% of the radiation to pass onto plane mirror  $M_4$ , and reflects 50% of the radiation onto plane mirror  $M_5$ . Mirror  $M_4$  focus the radiation beam in the sample cell. Mirror  $M_5$  focuses the radiation beam in the reference cell and the beam then passes through a convex lens onto the photodiode detector. The intensity of the reference beam, which should have suffered little or no light absorption, is defined as  $I_0$ . The intensity of the sample beam is defined as  $I$ . Over a short

period of time, the spectrometer automatically scans all the component wavelengths in the manner described above. If the sample compound does not absorb light of a given wavelength then  $I = I_0$ . However, if the sample compound absorbs light then  $I$  is less than  $I_0$  and this difference may be plotted on a graph as a function of wavelength. Absorption may be presented as transmittance ( $T = I/I_0$ ) or absorbance ( $A = \log I_0/I$ ). If no absorption has occurred then  $T = 1.0$  and  $A = 0$ . Most spectrometers display absorbance on the vertical axis and the commonly observed range is from 0 (1% transmittance) to 2 (100% transmittance). The wavelength of maximum absorbance is a characteristic value. Different compounds may have very different absorption maxima and absorbance.

### 2.3.5 Dielectric Measurement

#### 2.3.5.1 Electroding

The selection of suitable electrode for the test materials is important. In our case the contacting, conducting thin film electrode method is adopted because (i) it causes minimum error caused by air gap between the electrode and surface of the test material, which is more in case of contacting rigid metal electrode method, and (ii) procedure to measure dielectric constant are simple, which are relatively complex in non-contacting electrode method. In our case, all the ceramic bodies after sintering were polished well and coated on both sides with conducting silver paste. For organic removal printed disks were kept on an alumina plate and fired at 300°C for 60 minutes. This procedure is repeated twice for better electroding.

The main objective behind the development of automated dielectric setup is to study the behaviour of dielectric constant of different type of materials such as magnetic materials, ferroelectric and multiferroic materials etc. Such types of materials require accurate measurements of dielectric constant as a function of temperature and frequency. The dielectric constant as a function of temperature measures the unique property of the materials such as ferroelectric property and the transition temperature etc. The dielectric measurement setup was developed to study the temperature dependence of dielectric constant at various frequencies.

The dielectric constant for the bulk sample was calculated by measuring the capacitance of the material. The capacitance as a function of frequency and temperature was measured using Solatron 1260 LCR meter (for bulk sample) shown in Figure 2.8 and Agilent 4284A precision LCR meter (for thin films). Shielded test leads were used for the electrical connections from the



analyser to the sample in order to avoid any parasitic impedance. The samples were made in the form of circular pellets by applying a pressure of 5 tons. The surface of the disks were polished and coated with silver paste that acts as a good contact for measuring dielectric properties. Before starting the measurement the samples were heated at 300 deg for 1 hour, so as to homogenize the charge carries and to remove the moisture content, if any.



*Figure 2.8*      **Dielectric measurement set up Physics department (MSU Baroda)**

The measured capacitance was then converted into dielectric constant using the following formula:

$$C = \epsilon_0 \epsilon_r \frac{A}{d} \quad (2.5)$$

$$\epsilon_r = \frac{C \times d}{\epsilon_0 \times A} \quad (2.6)$$

where,  $C$  : Capacitance in farad ( $F$ )

$\epsilon$  : Permittivity of free space in farad per meter ( $8.85 \times 10^{-12} F/m$ )

$\epsilon_r$ : Dielectric constant or relative permittivity of the sample.

$A$  : Area of each plane electrode in square meters ( $m^2$ )

$d$  : Separation between the electrodes in meters ( $m$ )

The imaginary component of dielectric constant ( $\epsilon''$ ) is calculated using the formula;

$$\epsilon'' = \epsilon' \tan \delta \quad (2.8)$$

Where  $\tan \delta$  is loss tangent, proportional to the „loss“ of energy from the applied field into the sample (in fact this energy is dissipated into heat) and therefore denoted as dielectric loss. The ac conductivity is calculated from the data of dielectric constant and loss tangent ( $\tan \delta$ ) using the relation

$$\sigma_{ac} = \epsilon' \epsilon_0 \omega \tan \delta \quad (2.9)$$

Where  $\omega = 2\pi f$

### 2.3.6 Impedance spectroscopy Studies

The complex impedance spectroscopy is a powerful tool to investigate the electrical properties of the complex perovskite oxides. The main advantages of the techniques, i) it involves relatively simple electrical measurements that can readily be automated ii) the measurements can be implemented by using arbitrary electrodes iii) the results can be often correlated with the properties such as composition, microstructure, defects, dielectric properties, chemical reaction etc. of the sample iv) the resistance of the grain boundaries and that of grains can be easily separated in most of the polycrystalline samples. AC measurements are often made with a Wheatstone bridge type of apparatus (Impedance analyzer or LCR meter) in which the resistance  $R$  and capacitance  $C$  of the sample are measured and balanced against variable resistors and capacitors. The impedance  $|Z|$  and the phase difference ( $\theta$ ) between the voltage and current are measured as a function of frequency for the given sample and the technique is called impedance spectroscopy. Analysis of the data is carried out by plotting the imaginary part of the impedance  $Z'' = |Z| \cos \theta$  against the real part  $Z' = |Z| \sin \theta$  on a complex plane called the impedance plot. An impedance plot with linear scale is used to analyze the equivalent circuit as follows. Impedance plot of a pure resistor is a point on real axis and that of pure capacitor is a straight

line coinciding with the imaginary axis. The impedance of a parallel  $RC$  combination is expressed by the following relation,

$$Z^* = Z' - jZ'' = \frac{R}{1 + j\omega RC} \quad (2.10)$$

After simplification, one gets

$$\left( Z' - \frac{R}{2} \right)^2 + Z''^2 = \left( \frac{R}{2} \right)^2 \quad (2.11)$$

which represents the equation of a circle with radius  $R/2$  and center at  $(R/2, 0)$ . Thus, a plot of  $Z'$  vs.  $Z''$  (as parametric function of) will result in a semicircle of radius  $R/2$  as shown in Figure 2.9 (a) and the equivalent circuit is shown in Figure 2.9 (b). (This plot is often called a Nyquist plot). The time constant of the simple circuit is defined as  $t = RC = 1/\omega_m$ .

This corresponds to the relaxation time of the sample and the characteristic frequency lies at the peak of the semi-circle. In an ideal polycrystalline sample, the impedance plot exhibits an arc at high frequency corresponds to the bulk property of the sample, an arc at low frequency corresponds to the grain boundary behaviour and a spike at the lowest frequency corresponds to the electrode effect. Figure 2.10 (a) shows a typical impedance plot for a polycrystalline sample and Figure 2.10 (b) represented the equivalent circuit. In the present thesis work, impedance measurements for bulk samples have been performed using Solatron 1260 Impedance Analyser (1Hz-32MHz) in the temperature range (Room Temperature to 450°C). And for the thin films we have used the Agilent 4284A precision LCR meter.

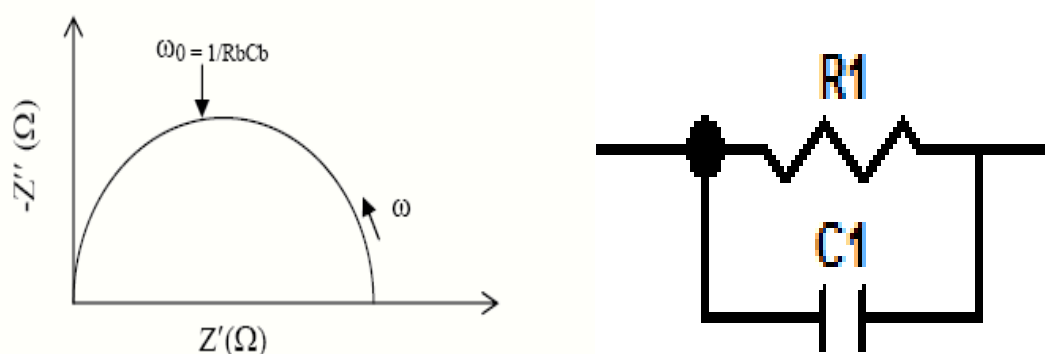


*Figure 2.9* (a) The impedance plot for a circuit of a resistor and a capacitor in parallel.  
(b) The corresponding equivalent circuit.

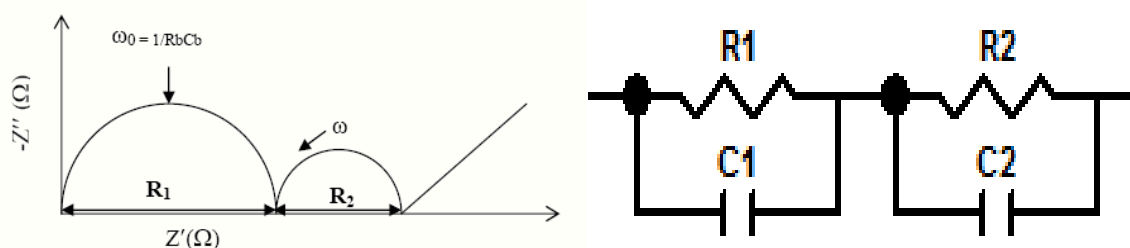


*Figure 2.10* (a) The impedance plot for an ideal polycrystalline sample and  
(b) The corresponding equivalent circuit.

## 2.4 Swift Heavy Ion Irradiation

To understand the swift heavy ion irradiation induced modifications of thin films, we have used Pelletron accelerator and materials science beam line at IUAC, New Delhi.

### 2.4.1 Pelletron Accelerator

The 15UD Pelletron, as shown in Figure 2.11, is a versatile tandem type of electrostatic heavy ion accelerator. This is installed in a vertical configurations in an insulating tank of 26.5 meter height an 5.5 meter in diameter, in this machine negative ions are produced and pre-accelerated to 300keV by the cesium sputter ion source known as SNICS( Source of Negative

Ions by Cesium Sputtering) (Now it has been replaced by MCSINCS (Multi Cathode SNICS). The pre-accelerated ions are injected into strong electrical field inside and accelerator tank filled with SF<sub>6</sub> insulating gas maintained at a pressure of 6-7 atmospheres. The ion beam is selected by injector magnet, which selects the mass of the ion using mass spectroscopy. The ions are mass analysed by a ions then enter in the strong electrical filed inside the accelerator. A terminal shell of about 1.52 meter in diameter and 3.61 meter in height is located at the centre of the tank, which can be charged to a high voltage (15MV) by a pellet charging system. The negative ions on traversing through the accelerating tubes from the column top of the tank to the positive terminal get accelerated. On the reaching the terminal they pass through the stripper (foil or gas), which removes electrons from the negative ions and transforms the negative ions into positive ions with high charge state. For very heavy ions ( $A > 50$ ), the lifetime of the carbon foils used in the stripper are limited to a few hours due to radiation damage. Therefore a gas filled canal or a combination of the gas stripper followed by a foil stripper is used for heavy ions. The transformed positive ions are then repelled away from the positively charged terminal and are accelerated towards ground potential to bottom of the tank. In this way same terminal potential is used twice to accelerate the ion in tandem. Hence, the name given to this accelerator is a Tandem Pelletron Accelerator. The final energy of the emerging ions from the accelerator is given by,

$$E_i = [ E_{decpot} + (1 + q_i) V ] \quad (2.11)$$

Where  $E_i$  is the energy of the ions having a charge state  $q_i$  after stripping,  $V$  is the terminal potential in MV and  $E_{decpot}$  is the deck potential of the SNICS source. On exciting from the tank, the ions are bent into horizontal plane using analysing magnet. This magnet works as an energy analyser and depending on the dipole magnetic field, ions of particular energy travel in the horizontal direction. The switching magnet diverts the high-energy ion beam into selected beam line of the beam hall. The ion beam kept centered and focused using steering magnets and quadruple triplet magnets. The beam line of the accelerator is in ultra high vacuum (UHV) conditions (10<sup>-10</sup> mbar). The beam is monitored by beam profile meter (BPM) and the current is observed using Faraday cups. The entire machine is computer controlled and is operated from the control room. The accelerator can accelerate ions from proton to uranium from a few MeV to hundreds of MeV (200MeV) depending upon the ion.

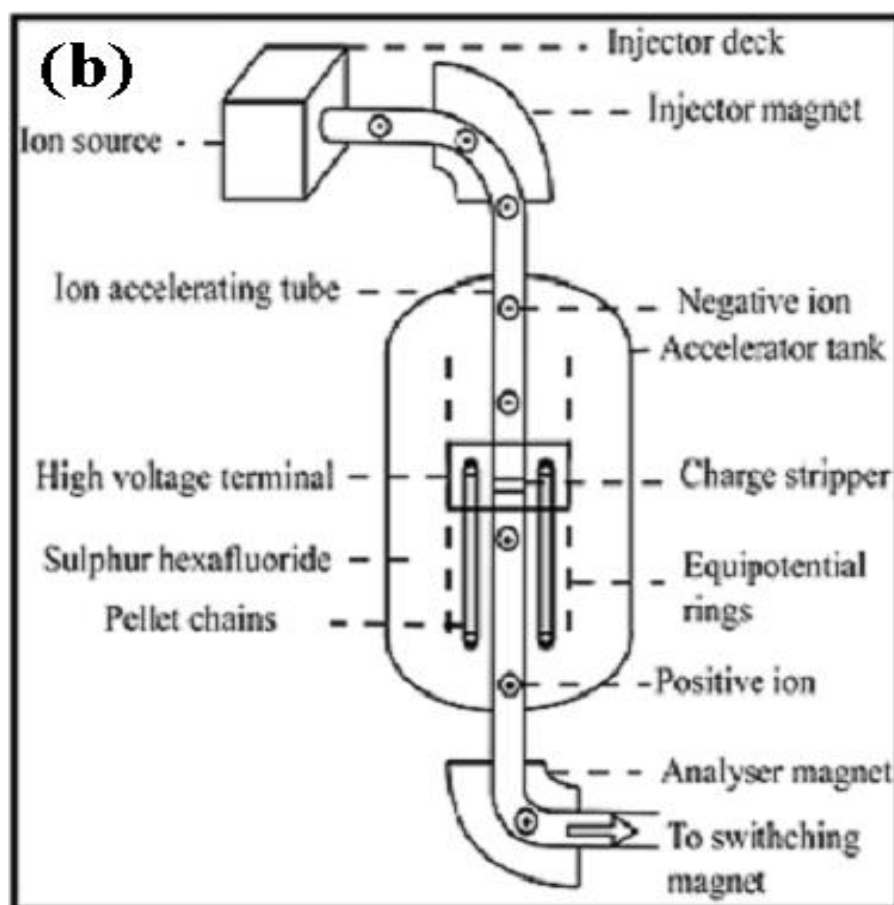


Figure 2.11 Schematics of the 15 UD Pelletron at IUAC, New Delhi, India

## 2.4.2 Material Science Beam Line

The accelerated beam from the Pelletron accelerator is brought to the beam hall and can be switched to any of the seven beam lines by using the switching magnet. Materials Science beam line is at  $15^\circ$  to the right w.r.t. the zero degree beam line. This beam line has three chambers-high vacuum chambers, ultra high vacuum chamber and goniometry chamber. The high vacuum chamber is a cylindrical shaped multiport stainless steel chamber. A view of the high vacuum chamber is shown in Figure 2.12 (a). The irradiation experiments were performed in high vacuum chamber ( $\sim 10^{-6}$  mbar) at room temperature in materials science beam line (see Figure 2.12(b)). The sample to be irradiated was mounted on the four sides of the target ladder (on copper block). The whole body of the ladder is made of stainless steel and a perforated square copper block is brazed at the end of the ladder. The target ladder is mounted through a

Wilson seal from the top flange of the chamber. This top flange is connected to the chamber through a flexible bellow that can be expanding up to 11cm from its minimum positions. A stepper motor in conjunction with suitable mechanical assembly is used to control the up and down motion of the ladder. The beam on the ladder can be observed by observing the luminescence of the beam on the quartz crystal mounted on all sides of the ladder. After the observation of the beam on the quartz, the sample to be irradiated is brought to the same position as that of the quartz by moving the ladder in the desirable position. A CCD camera is attached to one of the ports of the chamber for viewing the sample and the quartz position. The positions can be monitored using close circuit television (CTV) in the data acquisition room. The magnetic scanner (that can sweep the beam by 15mm in y-direction and 15mm in x-direction) ensures the uniform irradiation of samples. A cylindrical enclosure of stainless steel surrounds the sample ladder, which is kept at a negative potential of 120V. This enclosure suppresses the secondary electrons coming out of the sample during the irradiation. An opening in the suppressor allows the ion beam to fall on the sample. The total number of particles/charges falling on the sample can be estimated by a combination of the current integrator and the pulse counter (Faraday cup) from which the irradiation fluence/dose can be measured.

The counts for the desired fluence for each sample can be calculated using the following relation:

$$numberofcounts = \frac{fluence \times q \times 1.6 \times 10^{-19}}{pulseheight} \quad (2.12)$$

and

$$Time(T) = \frac{Dose \times ChargeState \times Area}{Current \times 6.25 \times 10^9} \quad (2.13)$$



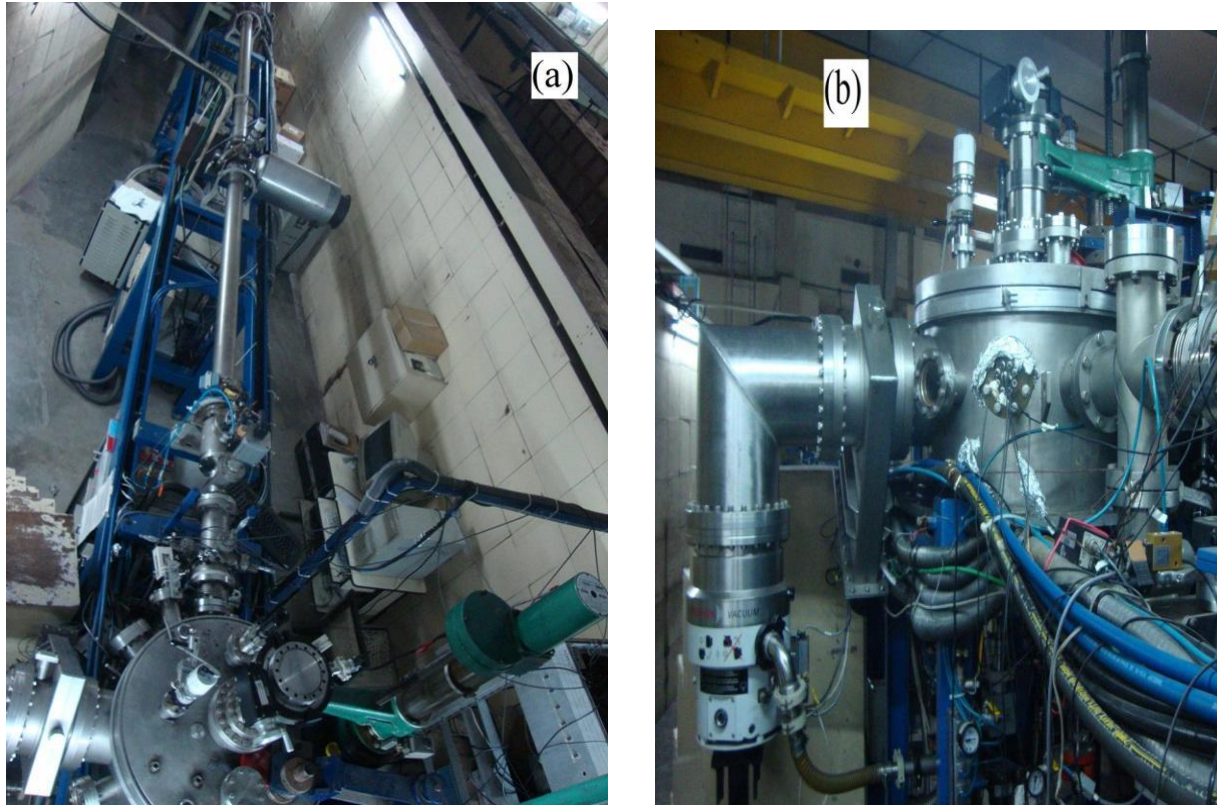


*Figure 2.12* An overview of (a) Experimental chamber and (b) materials science beam line at Inter-University Accelerator Center, New Delhi, India.

### 2.4.3 Ion Solid Interaction

When an energetic ion passes through the matter, it experiences a series of elastic and inelastic collisions with the atoms which lie in its path. These collisions occur because of the electrical forces between the nucleus and electrons of the projectile and those of the atoms which constitute the solid target. During this collision the energetic ions transfer its energy to nuclei (by elastic atomic collision) and electronic (by ionization and excitation) of the target material by two processes:

1. Elastic collision with the target atoms leading to displacement of atoms from their regular lattice sites. This mode of energy transfer is known as nuclear energy loss denoted by  $(dE/dX)_n$  or  $S_n$ . It is well known mechanism of defect creation in the low energy regime and it has negligible contribution.



2. Inelastic collision with the target electrons causing their excitation/ionization. This mode of energy transfer is referred to as electronic energy loss  $(dE/dX)_e$  or  $S_e$ .

It is well known fact that when a material is bombarded by the heavy ion irradiation, it creates damage zones in the material, when swift heavy ion passes through the material then material in the vicinity of the ions trajectory may be transformed into a disordered state, giving rise to the so called latent track (damage zone created along the path of the swift heavy ion). In case of SHI irradiation, electronic energy loss is the most considerable energy loss process. The emergence of these traces is the result of local electronic energy deposition along the ion path. Therefore, a number of experimental results have shown that the higher electronic excitations can induce the structural modifications. This implies that all the  $S_e$  dependent effects induced in different materials are probably related to the basic energy transfer between the incident ions and the target atoms. Two basic models of microscopic energy transfer mechanism, namely thermal spike and the coulomb explosion have been used to establish the relevant parameters governing the basic energy transfer process.

### 2.4.3.1 Thermal Spike Model

Thermal Spike model is based on the transient thermal process. This model was developed to explain the phase transformation after the SHI irradiation. According to this model the heavy ion irradiation may increase the lattice temperature that induces solid to liquid phase transformations into a localized zone of few nanometer (nm), which is followed by the thermal quenching ( $10^{13}$ K/s) of a cylindrical molten liquid along the ion track. This results in the formation of amorphized latent track. The threshold value for the creation of the latent tracks is associated with the energy needed to induce a liquid phase along the ion path [31, 32].

In this process, the incoming ion gives its energy to the electron gas in  $\sim 10^{17}$ s which is calculated from the collision time of ion with electron. The local thermalization in electronic system will take  $10^{-15}$ s to complete. Heat transfer from the electronic to atomic subsystem becomes substantial between  $10^{-14}$  to  $10^{-12}$  s depending on the magnitude of the coupling (electron-electron coupling and electron-phonon coupling) between the sub systems. The electron-phonon coupling implies the ability of electrons to transfer their energy to the lattice.

### 2.4.3.2 Coulomb Explosion Model

In the Coulomb Explosion Model [33, 34], it is assumed that the ionizing ions scatter the target electrons and create a column/cylinder of ionized atoms and the excited electrons are ejected by the coulomb repulsion. The electron excitation is rapidly shared with other electrons via electron phonon interaction. The mutual Coulomb repulsion of the ions produces atomic displacements leading to a dense cloud of interstitial atoms and vacancies along the original ion trajectory. This model seems to be well suited for the insulating materials. In metals, which have large electronic mean free path, the free electrons carry away the excitation energy so efficiently that the sample warms up as a whole without considerable atomic motion.

In the present work, the thin films of the BMN or SMN dielectric or ferroelectric samples deposited on ITO substrates have been irradiated with 100 MeV  $O^{7+}$  and 200 MeV  $Ag^{15+}$  ions. The Ag ions were selected to create the columnar defects. In fact, the defect morphology depends upon threshold value of the particular materials to be irradiated [35]. The electronic energy loss,  $(dE/dX)_e$  should be larger than the  $S_{eth}$ . Therefore, there is a possibility of creation of columnar defects/tracks in the materials.

### References

- [1] *Pulsed laser Deposition of Thin Films*, edited by D. B. Chrisey and G. H. Hubler (Wiley Interscience, New York, 1994).
- [2] S. Jin, T. H. Tiefel, M. McCromark, R. A. Fastnatch, R. Ramesh and L. H. Chen, *Science* **264**, 413, 1994.
- [3] S. Jin, M. McCromark, T. H. Tiefel and R. Ramesh, *J. Appl. Phys.* **76**, 6929, 1994.
- [4] N. D. Mathur, G. Burnell, S. P. Isaac, T. J. Jackson, B. S. Teo, J. L. MacManus-Dricoll, L. F. Cohen, J. E. Evetts and M. G. Blamire, *Nature* **387**, 266, 1997.
- [5] Ravi Bathe, S. K. Date, S. R. Shinde, L.V. Saraf, S. B. Ogale, S. I. Patil, Ravi Kumar, S. K. Arora and G. K. Mehta, *J. Appl. Phys.* **83**, 7174, 1998.
- [6] R. Shreekala, M. Rajeswari, K. Ghosh, A. Goyal, J. Y. Gu, C. Kwon, Z. Trazanovic, T. Boettcher, R. L. Green and T. Venkatesan, *Appl. Phys. Lett.* **71**, 282, 1997.

- 
- [7] J. Q. Guo, H. Takeda, N. S. Kazama, K. Fukamichi and M. Tachiki, *J. Appl. Phys.* **81**, 7445, 1997.
  - [8] Wei Zhang, Xiaoru Wang and Ian W. Boyd, *Appl. Phys. Lett* **73**, 2745, 1998.
  - [9] S. I. Patil, R. Shreekala, U. Lanke, A. Bhagwat, and S. B. Ogale, *Nucl. Instrum. Methods Phys. Res B* **114**, 42, 1996.
  - [10] P. K. Boyer, G. A. Roche, W. H. Ritchie and G. J. Collins, *Appl. Phys. Lett.* **40**, 716 1982.
  - [11] G. H. Snyder, R. Hiskes, S. Dicarolis, M. R. Beasley and T. H. Geballe, *Phys. Rev. B* **53**, 14434, 1996.
  - [12] E. S. Gillman, M. Li and K. H. Dahmen, *J. Appl. Phys.* **84**, 6217, 1998.
  - [13] J. J. Hermans, M. Carris, S. Watts, X. Yu, L. H. Dahmen and S. Von Molnar, *J. Appl. Phys.* **81**, 4967, 1997.
  - [14] S. Pignard, H. Vincent, J. P. Senatuer, J. Pierre and A. Abrutis, *J. Appl. Phys.* **82**, 44, 1997.
  - [15] K. B. Sundaram and G. K. Bhagavat, *Thin Solid Films* **78**, 35, 1981.
  - [16] D. Liu, Q. Wang, H. L. M. Chang and h. Chen, *J. Mater. Res.* **10**, 1516, 1995.
  - [17] *Thin Film Processes*, ed. By J. L. Vossen and W. Kern Academic Press, New York, 1982.
  - [18] K. Chahara, T. Ohno, M. Kasai and Y. Kosono, *Appl. Phys. Lett.* **63**, 1990, 1993.
  - [19] X. T. Zeng and H. K. Wong, *Appl. Phys. Lett.* **66**, 3371, 1995.
  - [20] E. Leja, T. Pisarkiewicz, and A. Kolodziej, *Thin Solid Films* **67**, 45, 1980.
  - [21] K. Choi and Y. Yamazaki, *Jpn. J. Appl. Phys.* **38**, 56, 1999.
  - [22] M. Leskela, J. K. Truman, C. H. Mueller and P. H. Holloway, *J. Vac. Sc. Tech.* **A7**, 3147 1989.
  - [23] R. B. Labowitz, R. H. Koch, P. Chaudhuri, R. H. Gambino, *Phys. Rev. B* **35**, 1996.
  - [24] G. Critchlow and T. M. Racheva, *Thin Solid Films* **292**, 299, 1997.
  - [25] *Hand Book of Thin Film Materials* Volume 1 (Deposition and processing of Thin Films) edited by Hari singh Nalwa Academic Press P 164 USA 2002.
  - [26] *Elements of X-ray Diffraction*, ed. By B. D. Cullity (Addison Wesley Publ. Co., 1978)
  - [27] C. Dong, *J. Appl. Cryst.* **32**, 838, 1999.
  - [28] *Hand Book of Microscopy for NanoTechnology* by NanYao and Zhong Lin Wang)

- [29] *Characterization of Materials*, edited by John B. Wachtman (Butterworth- Heinemann, 1993).
- [30] Y. Martin and H. K. Wickramasinghe, *Appl. Phys. Lett.* **50**, 1455, 1987.
- [31] M. Toulemonde, *Nucl. Instr. And Meth. B***156**, 1, 1999.
- [32] Z. G. Wang, Ch. Dufour, E. Paumier, M. Toulemonde, *J. Phys. Condens. Matter* **6**, 6733 1994.
- [33] R. L. Fleischer, P. B. Price and R. M. Walker, *Phys. Rev.* **156**, 2353, 1967.
- [34] D. Leseur and A. Dunlap, *Radia. Eff. And Def. Solids*, **126**, 163, 1993.
- [35] F. Studer, H. Pascard, D. Groult, Ch.Houpert, N. Nguyen and M. Toulemonde, *Nucl. Instr. And Meth. B* **32**, 389 1988.

## Chapter 3

### Effect of A- site substitution on the complex perovskites

#### $[\text{Ba}(\text{Mg}_{1/3}\text{Nb}_{2/3})\text{O}_3]$ bulk samples

In this chapter we have reported the effect of A-site substitution on the complex perovskite  $\text{Ba}(\text{Mg}_{0.33}\text{Nb}_{0.67})\text{O}_3$  [BMN] by different divalent ( $\text{Sr}^{2+}$ ,  $\text{Ca}^{2+}$ ) ionic substitution at Barium site on its structure, microstructure, dielectric, conductivity, and optical properties prepared by standard solid-state reaction technique. The structure of BMN, SMN, CMN is free from impurities. On replacing Barium by Strontium or Calcium, structure moves towards lower symmetry side and its dielectric properties are affected. The polar dielectric [BMN] moves to become a relaxor ferroelectric material. The observed findings are explained on the basis of cole-cole analysis. Further, the band gaps of these compounds are found to be shifting within wide band gap semiconductor region.

### 3.1 Introduction

Perovskites have been extensively investigated for use as microwave dielectric materials because of the outstanding and tuneable dielectric properties present in a number of compositions. In the perovskite structure ( $\text{ABO}_3$ ) the A-site cation is located in the cavity formed by the corner-sharing network of  $[\text{BO}_6]$  octahedra. The fit of the A-site cation is described by the tolerance factor [1]. If the tolerance factor is greater than unity, often no octahedral tilting is observed, whereas compositions with a tolerance factor less than unity typically undergo octahedral tilting distortions [2, 3]. The series of  $[\text{Ba}(\text{M}'_{1/3}\text{M}''_{2/3})\text{O}_3]$  or  $\text{Ba}_3\text{MM}'_2\text{O}_9$  ( $\text{M} = \text{Mg, Ni, Zn}$ ;  $\text{M}' = \text{Nb, Ta}$ ) perovskites that do not undergo an octahedral tilting distortion exhibit optimal dielectric properties. It is to be noted here that the origins of the dielectric property differences between the isostructural compounds are still not understood well. Entanglement of synthetic variables (e.g., chemical composition, reagent purity, annealing and sintering temperatures and times, initial particle size, processing conditions, and partial  $\text{O}_2$  pressure) and experimental observables (e.g., crystal structure, density, cation order inside of a domain, ordered domain size, domain boundaries, defects, and impurity phases) that influence the dielectric properties (i.e.,  $\epsilon$ ,  $\tau_f$ , and  $Q$ ) complicate formation of structure-property relationships. Substituting smaller A-site cations (i.e.,  $\text{A} = \text{Sr}^{2+}, \text{Ca}^{2+}$ ) in place of  $\text{Ba}^{2+}$  in  $\text{Ba}_3\text{MM}'_2\text{O}_9$  perovskites is one approach to adjust the octahedral tilting and consequently the  $\tau_f$ . The  $\epsilon$  of dielectrics originates from the superposition of ionic and electronic polarization [4]. Electronic polarization is considered a constant for a particular ion, whereas ionic polarization occurs because of lattice vibrations related to the crystal structure and is a particularly important contribution in high  $\epsilon$  ( $>20$ ) materials [5,6]. Relationships between the crystal structure, dielectric properties, and crystal chemistry are prone to be complex; however, the elucidation of the structural differences between  $\text{M}' = \text{Ta}$  and  $\text{M}' = \text{Nb}$  compounds is a starting point in understanding the dielectric property differences. Ceramics of the general formula  $\text{Ba}(\text{B}'_{1/3}\text{B}''_{2/3})\text{O}_3$  ( $\text{B}' = \text{Mg, Zn, Ni or Co}$ ;  $\text{B}'' = \text{Ta and Nb}$ ) have attracted a great deal of attention because of their interesting microwave properties in the wireless microwave communications community for their usage in low-loss dielectric resonators. Unfortunately, the cost of  $\text{Ta}_2\text{O}_5$  is very high. Therefore, a large number of Nb-based complex perovskite materials have been reported in the scientific literature because

$\text{Nb}_2\text{O}_5$  is comparatively cheap. Ta-based complex perovskite materials such as  $\text{Ba}(\text{Mg}_{1/3}\text{Ta}_{2/3})\text{O}_3$  and  $\text{Ba}(\text{Zn}_{1/3}\text{Ta}_{2/3})\text{O}_3$  were candidate materials used commercially and showed the highest Q values ( $Q = 1/\tan \delta$ ) of all the microwave perovskites (e.g.,  $Q > 12000$  at 10 GHz) and are used extensively in commercial applications [7-13].

Oxides with  $A = \text{Ba}, \text{Sr}$ ;  $B' = \text{Zn}, \text{Mg}$  and  $B'' = \text{Nb}$  and Ta have been found to have appropriate dielectric properties.  $\text{Ba}_3\text{ZnTa}_2\text{O}_9$  was first reported to show extremely low dielectric loss at microwave frequencies [14]. Several studies on related oxides have been carried out on other tantalates.  $\text{Ba}_3\text{MgTa}_2\text{O}_9$  has been studied extensively for its microwave properties [15-17]. The  $A(B'_{1/3}B''_{2/3})\text{O}_3$  or  $A_3B'B''_2\text{O}_9$  type of perovskite oxides were first prepared by [18,19]. Previous research has demonstrated that the dielectric properties of these ceramics are closely tied to a number of factors including variations in density, component volatilization (in the ZnO-containing systems), and the degree of cation ordering on the B-site positions [20-22]. Most research has focused on substituent's that enter the B-site sub lattice; A-site additives, other than the obvious replacement of Ba by other alkaline earths (Ca, Sr), have received less attention.

This gives rise to an attractive proposition: whether the near-zero  $\tau_f$  value can be attained in BMN-BNN system [23]. The ordering behaviour of  $\text{Ba}(\text{Mg}_{1/3}\text{Nb}_{2/3})\text{O}_3$  ceramics (BMN) substituted by  $\text{La}^{3+}$ ,  $\text{Na}^+$ ,  $\text{K}^+$  was investigated [24]. The 1:2 ordered structure of BMN can be transformed to 1:1 ordered structure by substituting a small amount of La cation ion into the A-site. Moreover, the degree of ordering was increased with La content in the compound, and reached almost unity at  $[\text{La}] = 50$  mol%. When the La ion in  $(\text{Ba}_{1-x}\text{La}_x)(\text{Mg}_{(1+x)/3}\text{Nb}_{(2-x)/3})\text{O}_3$  (BLMN) was substituted by Na or K ions, the 1:1 ordered structure of BLMN was transformed into the 1:2 ordered structure. The degree of 1:2 ordering was found to be influenced by the sintering temperature and the size difference between the A and B site ions.

BMN [25] reported to have hexagonally ordered perovskites structures and its dielectric properties showed comparatively higher loss than BMT [26]. Further, Ganguli and Thirumunal [27] investigated the influence of A-site partial substitution of Sr in place of Ba and found that the B-site ordering has improved along with lower sintering temperatures ( $1300^\circ\text{C}$ ).

The effects of Mg deficiency on the microwave dielectric properties of  $\text{Ba}(\text{Mg}_{1/3}\text{Nb}_{2/3})\text{O}_3$  ceramics were also been reported [28]. It is observed that 1:2 ordering as well as relative density of specimens increase with small Mg deficiency. Maximum values of ordering parameter and relative density were obtained for the  $\text{Ba}(\text{Mg}_{1/3-0.02}\text{Nb}_{2/3})\text{O}_3$  specimen. The increase of ordering

and relative density was explained on the basis of existence of vacancies which promote cation movement.

In addition to above the Relaxor behaviour has been found in the solid solutions between complex perovskite  $\text{Ba}(\text{Mg}_{1/3}\text{Nb}_{2/3})\text{O}_3$  (BMN) and ferroelectric  $\text{PbTiO}_3$  (PT), 0.4BMN-0.6PT, prepared by solid state reactions. The solid solution between the dielectric complex perovskite BMN and ferroelectric PT, 0.4BMN- 0.6PT, exhibits the typical characteristics of relaxor ferroelectrics, with broad and dispersive permittivity maxima. The frequency dependence of the temperature of the dielectric maxima ( $T_m$ ) follows the Volger-Fulcher relationship, like in the canonical relaxors. All these features indicate that 0.4BMN- 0.6PT is a lead-reduced relaxor ferroelectrics with an enhanced dielectric properties at around room temperature, potentially useful for applications as microwave dielectrics and high power density capacitors [29].

Relaxor-like dielectric behaviour, analogous to that found in lead magnesium niobate, has also been induced in the polar dielectric barium magnesium niobate (BMN). In BMN, the dielectric constant was increased and the temperature of the maximum dielectric constant was shifted to a lower temperature with a decrease in measurement frequency with increasing A-site vacancy concentrations. Relaxor-like dielectric characteristics have been induced in the polar dielectric BMN by creating A-site vacancies. Activation energy of 0.15 eV, a pre exponential factor  $10^{14}\text{s}^{-1}$ , a fictitious freezing temperature near 0 K, and a Curie constant of  $1.773 \times 10^5$  were calculated for BMN-10. A linear P–E curve was observed at room temperature and the polarization was found to increase with increasing A-site vacancy concentration. The origin of the relaxational polarization in BMN is explained using the Skanavi model [30].

The  $\text{Ba}(\text{Mg}_{1/3}\text{Nb}_{2/3})\text{O}_3$ , barium magnesium niobate (BMN) synthesized by the solid state reaction technique shows monoclinic structure at room temperature. The frequency- dependent dielectric dispersion of BMN is investigated in the temperature range from 300 to 503K. An analysis of the real and imaginary parts of dielectric constant with frequency is performed assuming a distribution of relaxation times. The most probable relaxation times obtained from the frequency dependence of the loss peak were found to obey an Arrhenius law with activation energy of 0.72eV [31].

Detailed Crystal structural analysis with Reitveld Refinement of BMN has been studied and it exhibits hexagonal symmetry [32]. Raman and Far- Infrared Spectroscopy studies were



carried out and found that the B-site ordering drastically affects the microwave dielectric properties [33].

As discussed above work carried out on these compositions have lots of contradictory results for the same compositions in terms of reported structure and value of activation energies. It also lack of understanding regarding A- and /or B-site elements role in the observed dielectric behaviour. Therefore in the present work the effect of A-site substitution in the  $\text{Ba}(\text{Mg}_{1/3}\text{Nb}_{2/3})\text{O}_3$ [BMN] complex perovskites has been studied in details. Samples are analysed with help of different techniques like X-ray diffraction analysis, micro structural analysis, Dielectric properties, UV-absorption studies and results of the same is correlated with one and another.

We have studied complete replacement of A-site by different divalent ions of lower ionic radii. We have prepared the basic composition of  $\text{Ba}(\text{Mg}_{1/3}\text{Nb}_{2/3})\text{O}_3$ [BMN] by standard solid state reaction technique. Synthesis parameters (as explained in Chapter 2) were similar. The structural analysis of BMN has been studied by POWDER X program [34]. The impedance spectroscopy measurement has been carried out in the department. The temperature-dependent dielectric measurements were carried out using an LCR meter (1260 Solartron) having frequency range of  $10\text{-}10^7$  Hz. The  $\text{A}(\text{Mg}_{0.33}\text{Nb}_{0.67})\text{O}_3$  samples (thickness 1.18 mm and diameter of 12 mm) were polished with silver paste and heat-treated at  $200^\circ\text{C}$  in order to remove micro-cracks (if any). Polished discs were placed between two electrodes connected to an LCR meter and measurements were performed from room temperature to  $350^\circ\text{C}$ ; the results were found to be reproducible. The dc conductivity was calculated using the Cole-Cole plot. The UV/VIS Spectroscopy was measured by Perkin Elmer Precisely Lambda 950 instrument. Its range was from 300-1500nm. All the measurement was carried out in Reflectance mode. The microstructures of the samples were studied by Scanning Electron Microscopy (JEOL JSM 5600).

## 3.2 Results and Discussions

### 3.2.1 X-ray Diffraction (XRD) Measurements

X-ray diffraction technique was employed to understand the structural phase identification of the  $A(\text{Mg}_{0.33}\text{Nb}_{0.67})\text{O}_3$  materials. Further, it also helps us to understand the effect of A site replacement of  $\text{Ba}^{2+}$  by smaller ionic radii  $\text{Sr}^{2+}$ , and  $\text{Ca}^{2+}$ .

Figure 3.1 shows the powder X-ray diffraction pattern of  $A(\text{Mg}_{0.33}\text{Nb}_{0.67})\text{O}_3$  samples. The measurements were carried out at room temperature with  $\text{Cu-K}\alpha$  radiation using high resolution Shimadzu X-ray diffractometer 6000 with ( $\lambda = 1.5402\text{\AA}$ ). The diffraction patterns were recorded from  $2\theta = 10^\circ$  to  $110^\circ$  with a step of  $0.02^\circ$ . The X-ray diffraction pattern was analyzed by using Powder X program [34]. From the analysis, it is observed that all the samples exhibit a single phase nature with structural transformation from hexagonal [BMN] to monoclinic [SMN, CMN] after the replacement by  $\text{Sr}^{2+}$  and  $\text{Ca}^{2+}$  at A- site. The system therefore moves from higher symmetry side to lower symmetry side on substitution of ion with lower ionic radii. The increase in asymmetry was accompanied by the simultaneous increase in the cell volume [30]. In earlier work researchers have observed an anti-phase tilting of the oxygen octahedral in SMN and an anti-phase/in-phase tilting of the oxygen octahedral accompanied by an anti-parallel shift of A-site cations in CMN compounds [35]. The observed enhancement in distortions can have correlated variations in the dielectric properties of these compounds.. The Lattice Constant with volume is shown in table 3.1 for all the samples. It is evident that the XRD peaks shifted toward higher  $2\theta$  angle on replacement of  $\text{Ba}^{2+}$  by  $\text{Sr}^{2+}$  or  $\text{Ca}^{2+}$  at the A-site.

**Table 3.1** Structure, lattice Constant and Unit cell Volume for  $A(\text{Mg}_{0.33}\text{Nb}_{0.67})\text{O}_3$ 

Composition	Structure	Lattice Constant	Volume of Unit Cell
$\text{Ba}(\text{Mg}_{1/3}\text{Nb}_{2/3})\text{O}_3$ BMN	Hexagonal	$a = 5.766 \text{ \AA}$ $b = 5.766 \text{ \AA}$ $c = 7.077 \text{ \AA}$	$236.45 \text{ \AA}^3$
$\text{Sr}(\text{Mg}_{1/3}\text{Nb}_{2/3})\text{O}_3$ SMN	Monoclinic	$a = 8.956 \text{ \AA}$ $b = 13.461 \text{ \AA}$ $c = 5.778 \text{ \AA}$ $\beta = 93.33$	$696.64 \text{ \AA}^3$
$\text{Ca}(\text{Mg}_{1/3}\text{Nb}_{2/3})\text{O}_3$ CMN	Monoclinic	$a = 10.965 \text{ \AA}$ $b = 13.463 \text{ \AA}$ $c = 5.875 \text{ \AA}$ $\beta = 125$	$867.65 \text{ \AA}^3$

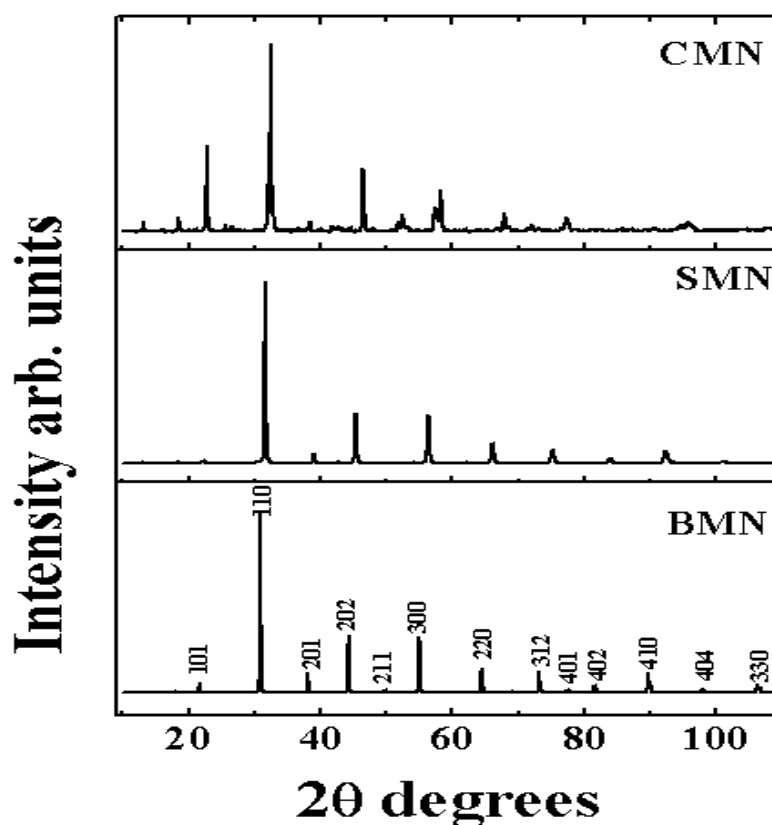


Figure 3.1 X- ray powder diffraction patterns of BMN, SMN, and CMN samples.

### 3.2.2 Scanning Electron Microscopy Analysis

In order to understand the morphology, grain size and shape of compounds BMN, SMN and CMN, SEM study has been carried out. The SEM micrographs were taken at 2500 magnification at different parts of the samples. The SEM images of BMN, SMN, CMN samples are shown in Figure 3.2 (a-c).

Figure 3.2 shows the micrograph of [BMN], [SMN], [CMN] ceramic. As it can be seen in this micrograph, the ceramic is composed of small grains with an average size of approximately 1-2  $\mu\text{m}$ . We believe that these morphological characteristics are governed by the matter transport mechanism between the grains during the sintering process. In principle, in the initial stages of small solid state reaction route, the carbonates and oxides ( $\text{BaCO}_3$ ,  $\text{SrCO}_3$ ,  $\text{CaCO}_3$ ,  $\text{MgO}$ ,  $\text{Co}_2\text{O}_3$  and  $\text{Nb}_2\text{O}_5$ ) used to form the BMN, SMN, CMN phases were well mixed and constantly milled in order to reduce the powder particle sizes. The heat treatments were performed at  $1200^\circ\text{C}$  for

12, 24, 36 hrs in order to promotes good grain formation. It has been observed that in case of BMN we observe intragranular and well defined grains. The average grain size is approximately  $\sim 1\mu\text{m}$  reported earlier [30]. But as we move towards to Sr and Ca we observe little porosity in the composition and agglomeration. Therefore, it is clear from these micrographs that with the substitution of smaller ionic radii, numbers of pores are increased as well as resulted in enhanced agglomeration. This in turn likely to enhance grain boundary induced inter grain effects such as conductivity and dipolar mobility. System can move towards relaxor/ferroelectricity from normal dielectrics.

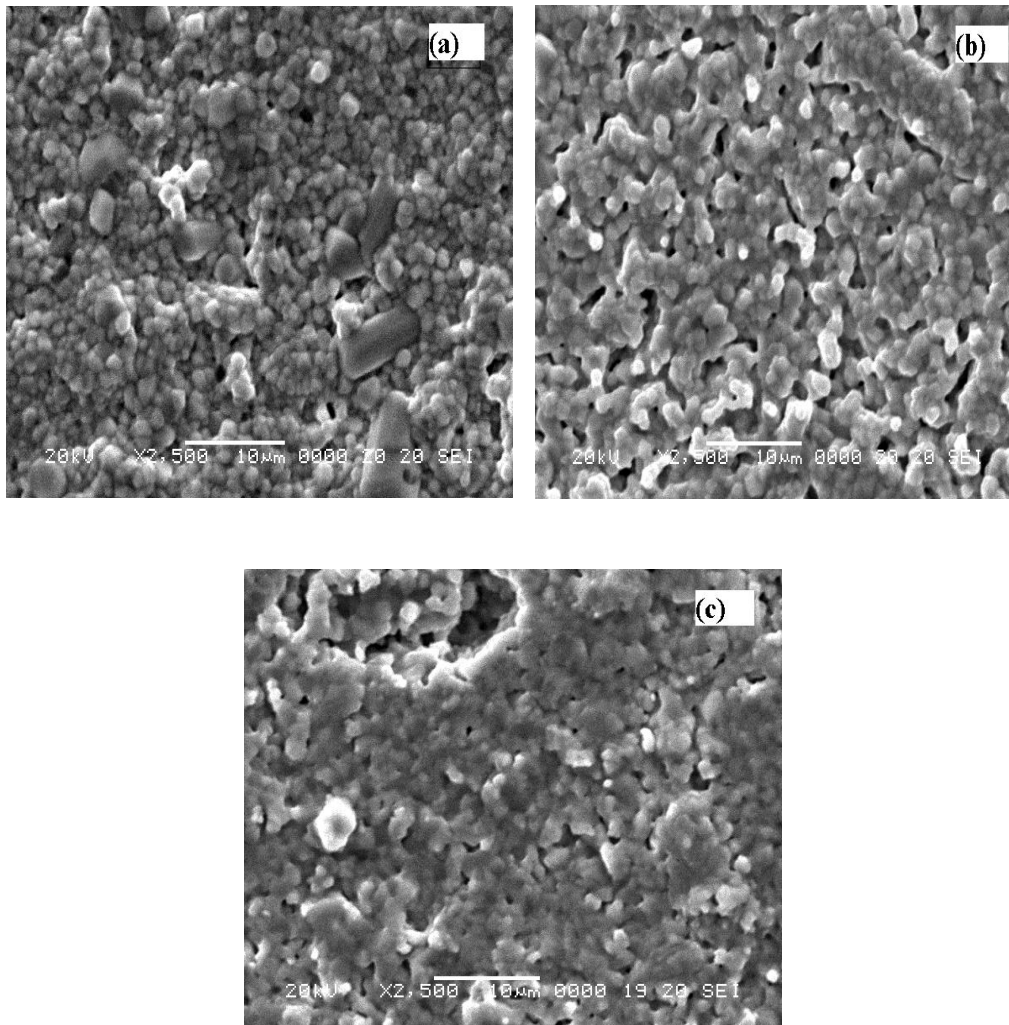


*Figure 3.2* SEM Micrograph of (a) BMN, (b) SMN, (c) CMN.

### 3.2.3 Dielectric Measurement

#### 3.2.3.1 Frequency dependence Dielectric Properties

Figure 3.3 (a-c) shows the frequency dependence dielectric permittivity of BMN, SMN and CMN ceramic samples in temperature range (room temperature -180<sup>0</sup>C). It is observed that all studied samples shows the dispersion behaviour i.e., the dielectric constant decreases with increase in frequency except BMN which is polar dielectric materials as reported [30]. This is the general dielectric behaviour observed in most of the ferroelectric materials, which can be explained with interfacial polarization predicted by the Maxwell-Wagner model [36] in agreement with Koop's phenomenological theory [37]. According to these models, the dielectric materials can be imagined as a heterogeneous structure consisting of well conducting grains separated by thin layer of poorly conducting substances (grain boundaries). These grain boundaries could be formed during the sintering process, either by superficial reduction or oxidation of crystallites in the porous materials as a result of their direct contact with the firing atmosphere [38].

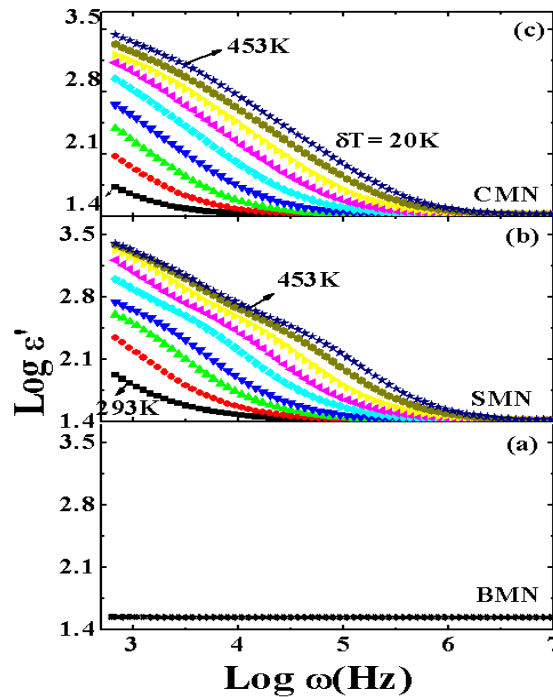


Figure 3.3 (a-c) Angular Frequency dependence of the real part ( $\epsilon'$ ) of the electrical permittivity for different compositions.

The observed variation in the values of dielectric constant in BMN, SMN and CMN is likely to be due to the fact that as we replace the total A-site by lower ionic radii i.e  $Ba^{2+}$ ,  $Sr^{2+}$ ,  $Ca^{2+}$  the unit cell get relaxed and the atomic positions of B' and B'' site gets some movements. This in turn changes the polarization activities occurring in the unit cell. We have seen that BMN does not shows any variation in the  $\epsilon'$  vs. frequency plots while SMN and CMN shows clear dispersions.

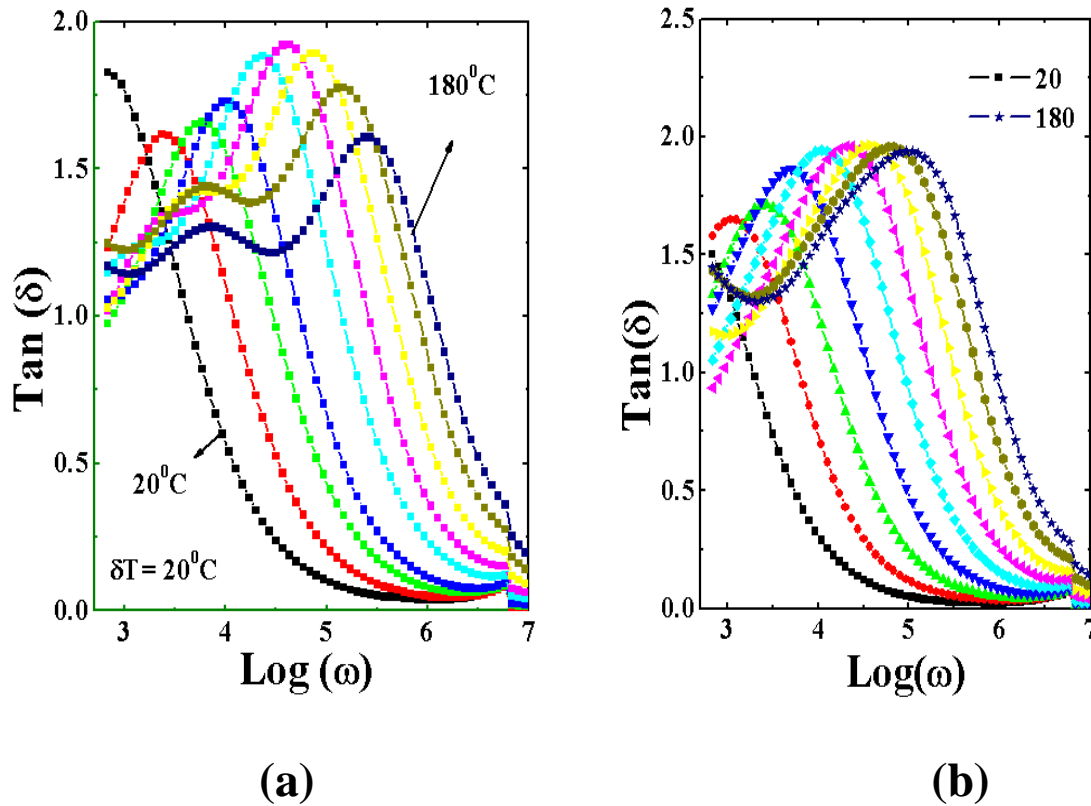


Figure 3.4 Dielectric losses ( $\tan\delta$ ) versus frequency plots (a) for SMN and (b) for CMN.

The variation of dielectric loss ( $\tan\delta$ ) versus frequency is shown in the Figure 3.4 in full temperature range (room temperature -180°C). It shows that as we move from polar system [BMN] towards non-polar system [SMN], [CMN] relaxation mechanism is introduced in the system. It shows characteristic peaks for different temperatures in full frequency ranges. From the above graph we have taken  $\log \omega_{max}$  corresponding to particular temperature and it has been plotted against inverse of temperatures, Figure 3.5. The graph follows the Arrhenius relations and from this we obtain the activation energies corresponding to SMN and CMN.

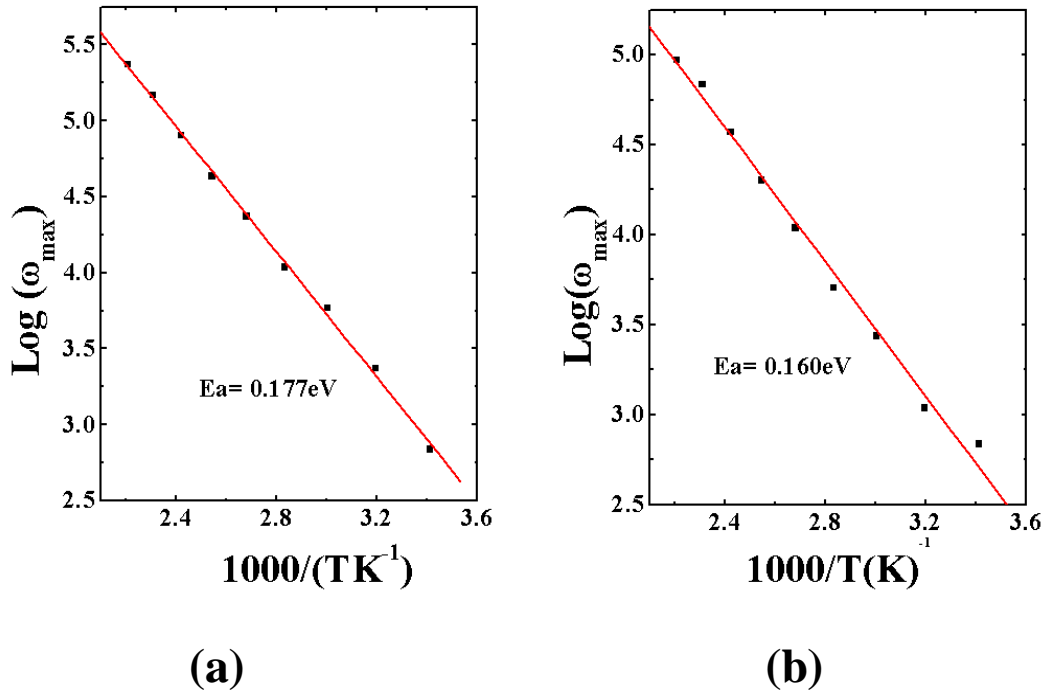


Figure 3.5 The Arrhenius plot for the  $\tan \delta_{\max}$  with inverse of temperature.

### 3.2.3.2 Temperature dependence of Dielectric Properties

Figure 3.6 shows the temperature-dependence of the dielectric constant  $\epsilon'$  measured at various frequencies (100Hz to 32 MHz). We have observed a transition in dielectric properties from normal to colossal values ( $\sim 10^3$ ) as well as occurrence of dielectric relaxation due to A-site modification in  $\text{Ba}(\text{Mg}_{0.33}\text{Nb}_{0.67})\text{O}_3$ . It is noted here that there is no variation in BMN dielectric constant values with change in temperature and frequency. On replacement of Barium by Strontium or Cobalt at A- site we observe drastic enhancement in dielectric constant values and relaxation mechanism is introduced in the system. This probably is due to the observed expansion of the unit cell volume which in turn increases the polarization mechanism in the system. The present results indicate strong correlation between the dielectric properties and the structural modifications around the A-site in  $\text{A}(\text{Mg}_{0.32}\text{Nb}_{0.67})\text{O}_3$  compounds. We are unable to see the transition temperature of the above system within our temperature range of measurement.



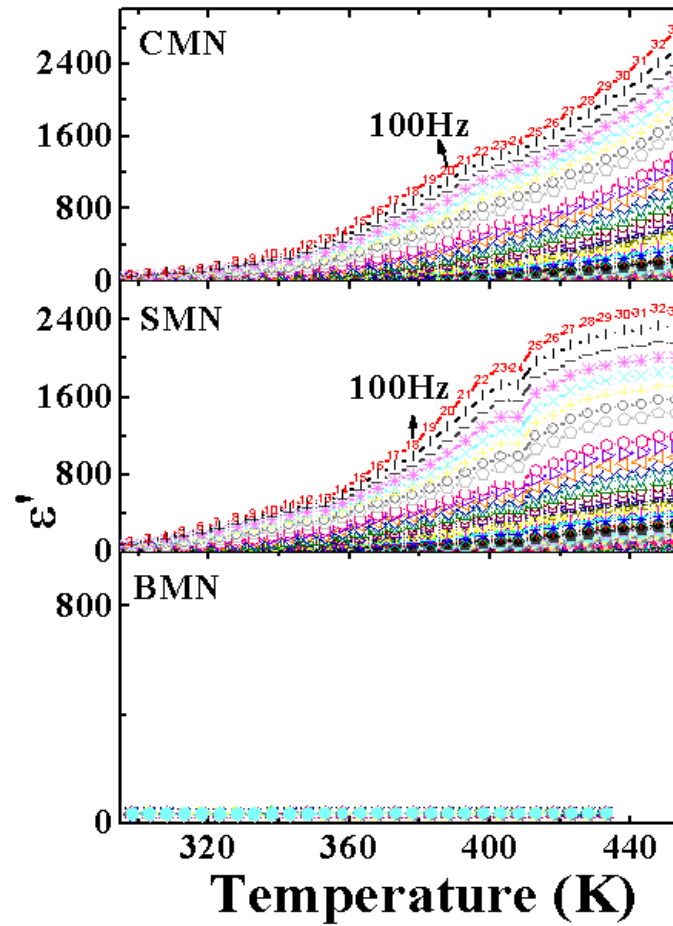


Figure 3.6 Temperature dependence of the real part ( $\epsilon'$ ) of the electrical permittivity for different frequencies.

### 3.2.4 Modulus Spectroscopy Analysis

The electric modulus formalism is expressed as

$$Z^*(\omega) = Z' - jZ'' \quad (3.1)$$

$$M^*(\omega) = M'(\omega) + jM''(\omega) \quad (3.2)$$

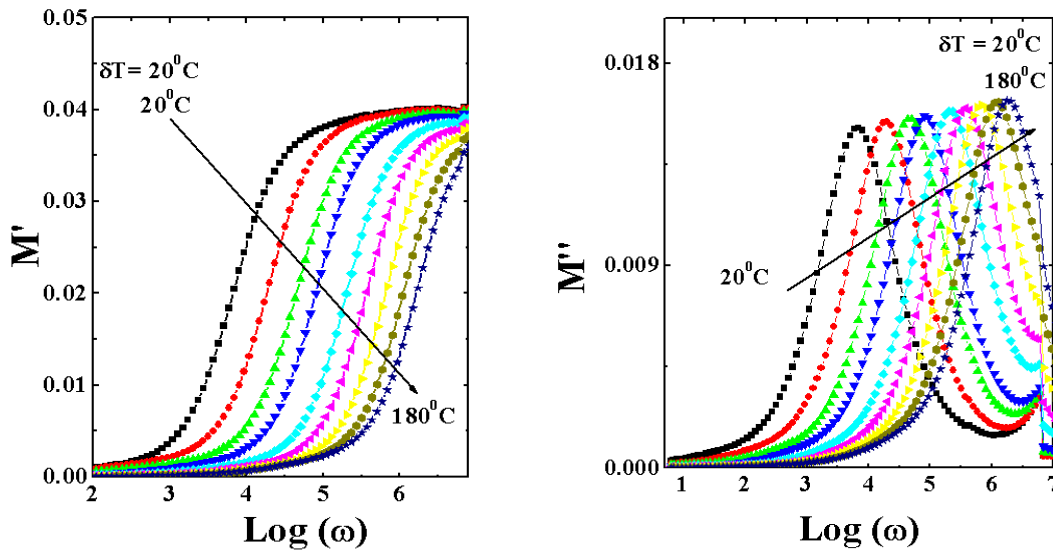
$$M^*(\omega) = j\omega C_0 Z^*(\omega) \quad (3.3)$$

From Equation (3.1), (3.2) and Equation (3.3) one can get the following Equations (3.4) and (3.5)

$$M' = \omega C_0 Z'' \quad (3.4)$$

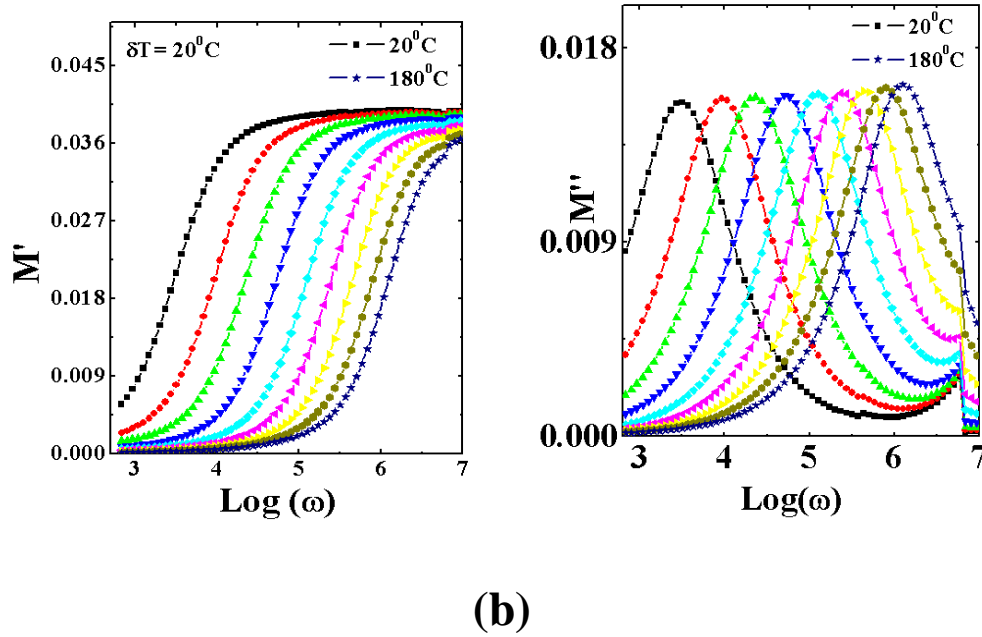
$$M'' = \omega C_0 Z' \quad (3.5)$$

Where  $C_0$  is given by  $C_0 = \epsilon_0 A / L$ ,  $L$  is the thickness, and  $A$  is the area of the sample,  $\epsilon_0 = 8.854 \times 10^{-14} \text{ F/cm}$  is the permittivity of the free space. The modulus analysis has an advantage that it suppresses the space charge/electrode effects from the experimental data [39-42]. This can also be used to study the conductivity relaxation time [42,43]. The complex modulus is defined as inverse of the complex permittivity and in the present work, the impedance data were converted into electrical modulus using the equations (3.1-3.5).



(a)

**Figure 3.7(a) Variation of real part of modulus, and imaginary part of modulus of SMN with different frequency at different temperatures.**



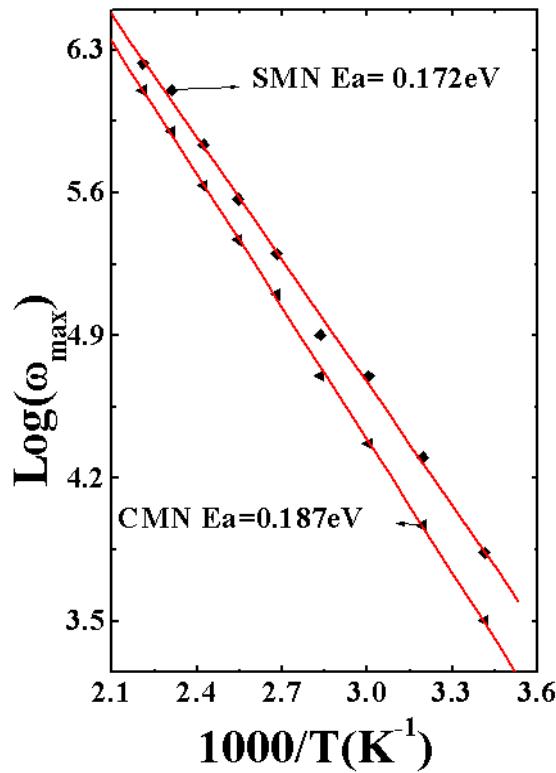
**Figure 3.7(b) Variation of real part of modulus, and imaginary part of modulus of CMN with different frequency at different temperatures.**

Figure 3.7 (a) and (b) shows the real and imaginary part of electrical modulus for [SMN], [CMN] as a function of frequency at different temperatures, respectively. At lower frequencies,  $M'$  tends to be very small, confirming that the contribution from the electrode effect is negligible and hence can be ignored when the data are analysed in modulus formalism [44]. The observed dispersion in  $M'$  at higher frequencies may be due to conductivity relaxation. It may be noted from Figure 3.7(a) and (b) that the position of the peak  $M''_{max}$  shifts to higher frequencies as the temperature is increased. The asymmetric broadening of the peak indicates the spread of relaxation with different time constant, and relaxation in the material is of non-Debye type. The frequency region below peak maximum  $M''$  determines the range in which charge carriers are mobile on long distances. At frequency above peak maximum  $M''$ , the carriers are confined to potential wells, being mobile on short distances. The frequency  $\omega_m$  (corresponding to  $M''_{max}$ ) gives the most probable relaxation time  $\tau_m$ . Each peak attains a maximum value  $M''_{max}$  at frequency  $\omega_{max}$  called conductivity relaxation frequency and it obeys the Arrhenius relation.

The most probable relaxation time follows the Arrhenius law, given by

$$\omega_m = \omega_0 \exp\left(\frac{-E_a}{K_B T}\right) \quad (3.6)$$

where  $\omega_0$  is the pre-exponential factor and  $E_a$  is the activation energy. Figure 3.8 shows a plot of the  $\log \omega_m$  versus  $1/T$ , for SMN and CMN where the circles are the experimental data and the solid line is the least-squares straight-line fit.



**Figure 3.8** The Arrhenius plots of relaxation frequency ( $\omega_{max}$ ) for SMN and CMN as a function of temperature where the crosses are the experimental points and the solid line is the least- square straight line-fit.

The activation energy  $E_a$  calculated from the least-squares fit to the points. From Figure 3.8 SMN (a) and CMN (b) it can be seen that the activation energy calculated from Arrhenius relation  $E_a = 0.172\text{eV}$  [SMN] and  $0.187\text{eV}$  [CMN] for relaxation of  $M''$  is found to be close to

the activation energy  $E_a = 0.180$  eV [SMN] and  $0.185$  eV [CMN] for dc conductivity plots shown in Figure 3.9.

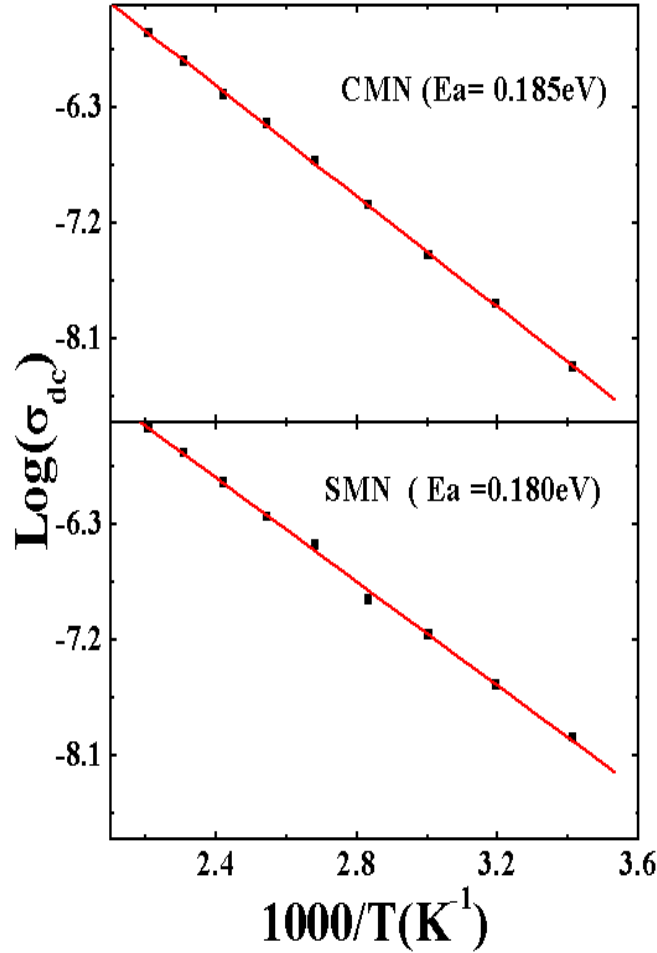


**Figure 3.9** The Arrhenius plots of dc conductivity ( $\sigma_{dc}$ ) for SMN and CMN as a function of temperature where the crosses are the experimental points and the solid line is the least-square straight line-fit.

The dc bulk conductivity  $\sigma_{dc}$ , of the sample was evaluated from the impedance spectrum by using the relation

$$\sigma_{dc} = \frac{t}{R_b A} \quad (3.7)$$

Where  $R_b$  is the bulk resistance,  $t$  is the thickness and  $A$  the surface area of the sample. Figure 3.9 shows the variation of  $\sigma_{dc}$  with  $1000/T(K^{-1})$ . The nature of the variation is linear and follows the Arrhenius relationship

$$\sigma_{dc} = \sigma_0 \exp\left(-\frac{E_{dc}}{K_B T}\right) \quad (3.8)$$

Where  $E_{dc}$  is the activation energy of the conduction,  $K_b$  is the Boltzmann Constant and  $T$  is the absolute temperature. This shows that there is similar hopping mechanism. It should be noted that Surya et. al., [30] had earlier reported the activation energy of the order of 0.150eV for [BMN].

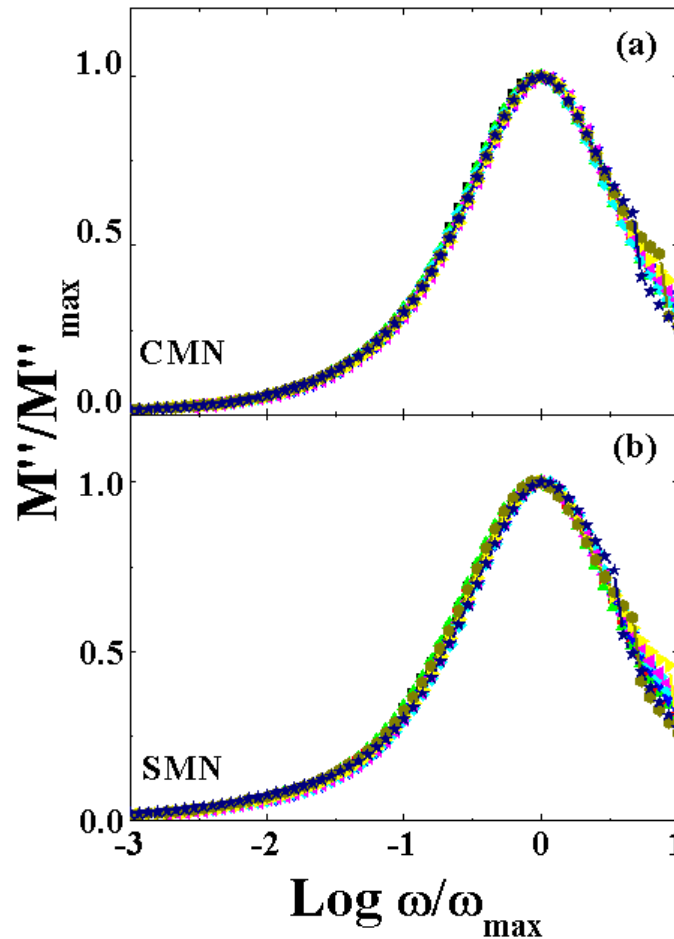


**Figure 3.10** The Scaling behaviour of  $M''_{max}$  for SMN and CMN as a function of temperatures.

Figure 3.10 (a) [SMN] and (b) [CMN] shows the Scaling plot of  $M''/M''_{max}$  versus  $\log (\omega/\omega_{max})$  and at various temperatures. We have scaled each  $M''$  by  $M''_{max}$  and each frequency by  $\omega_{max}$  for different temperatures in Figure 3.10 (a) and (b). The coincidence of all curves/peaks at different temperatures exhibits temperature independent behavior of the dynamic processes [45] occurring in the material. This might be due to the ion migration that takes place via hopping mechanism for (a) CMN and (b) SMN, Figure 3.10.

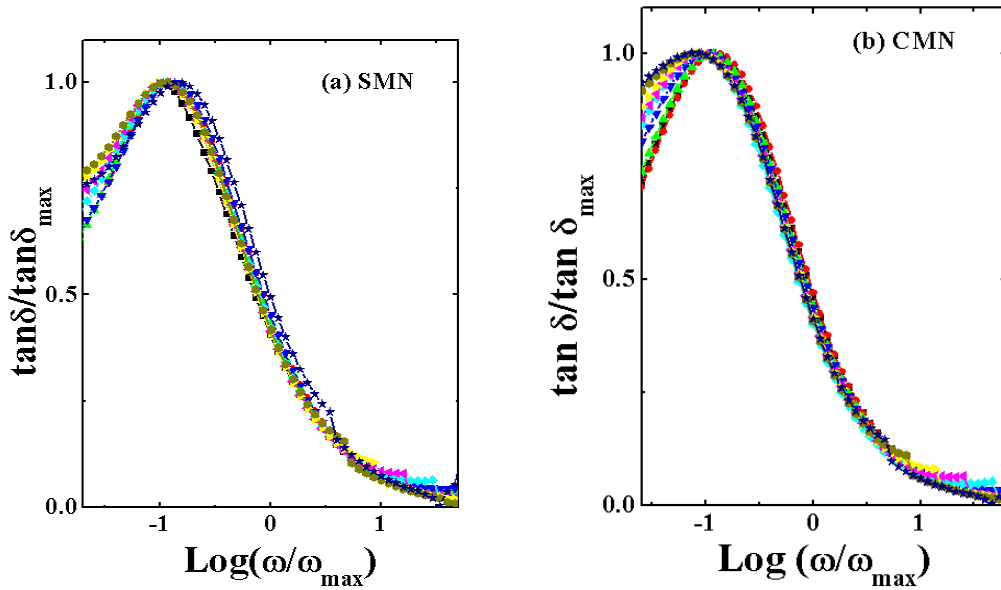


**Figure 3.11 The Scaling behaviour of  $\tan \delta_{max}$  for SMN and CMN as a function of temperatures.**

Same mechanism is followed by  $\tan \delta / \tan \delta_{max}$  versus  $\log (\omega/\omega_{max})$  and at various temperatures. We have scaled each  $\tan \delta$  by  $\tan \delta_{max}$  and each frequency by  $\omega_{max}$  for different temperatures in Figure 3.11. The coincidence of all curves/peaks reconfirms our above stated findings that temperature independent behavior of the dynamic processes [45] occurring in the materials and the ion migration must be taking place via hopping mechanism.

### 3.2.5 Conductivity Studies

The ac conductivity ( $\sigma_{ac}$ ) was studied over a frequency range of 100 Hz to 32MHz as well as varying the temperature from room temperature to 180°C is shown in Figure 3.12(a) and (b) for SMN and CMN. The  $\sigma_{ac}$  calculated from the dielectric data, using the following equation

$$\sigma_{ac} = \varepsilon' \varepsilon_0 \omega \tan \delta \quad (3.8)$$

increases for  $A(\text{Mg}_{0.33}\text{Nb}_{0.67})\text{O}_3$  samples and is distinct in the high frequency region. This indicates that the hopping frequency of the charge carriers is influenced by the neighbors of  $\text{Sr}^{2+}$  or  $\text{Ca}^{2+}$  ions. Further, it is noted that at higher frequencies ( $\sim 2$  MHz),  $\sigma_{ac}$  decreases for all compositions indicating the inability of hopping of charges to follow the high frequency of the applied field.

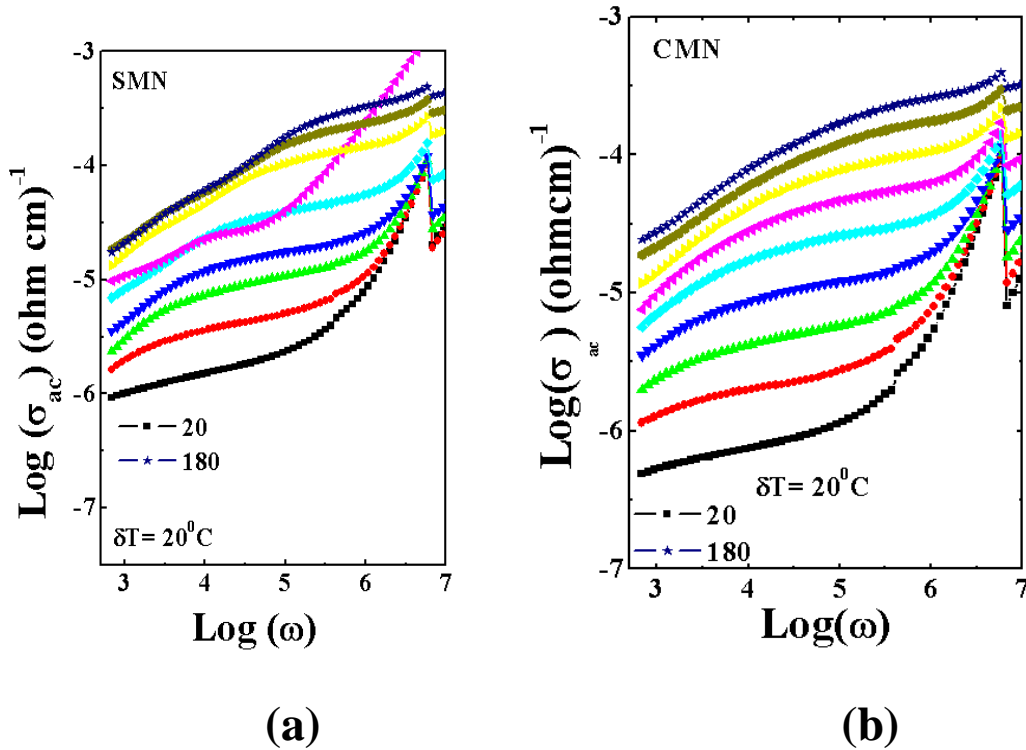


**Figure 3.12** (a) Frequency dependence of ac conductivity of SMN at different temperatures.  
(b) Frequency dependence of ac conductivity of CMN at different temperatures.

The total conductivity of the material at a given frequency is given by,



$$\sigma_{total}(\omega) = \sigma_{dc}(\omega) + \sigma_{ac}(\omega) \quad (3.9)$$

where, hopping-induced conduction arising from A-site substitutions is responsible for the enhancement of both dc and ac conductivities. The dc conductivity is the  $\omega \rightarrow 0$  limit of  $\sigma_{total}(\omega)$ . For semiconductors and disordered systems, the ac conductivity follows the power law behavior:

$$\sigma_{ac}(\omega) = A\omega^s \quad (3.10)$$

Where A is a temperature-dependent constant and  $s$  is the frequency exponent ( $s \leq 1$ ). From the slope of log-log plots drawn for  $\sigma_{ac}$  vs.  $\omega$  (Figure 3.12(a) SMN and 3.13(b) CMN), for the different compositions at different temperature, the slope directly provides the value of dimensionless frequency exponent  $s$ . The ac conductivity shows frequency-dependent dispersion similar to the dielectric behavior discussed earlier.

### 3.2.6 UV-Vis Spectroscopy Analysis

Figure 3.13 (a-c) shows the UV-vis absorption spectra of [BMN], [SMN], [CMN]. The optical band gap energy ( $E_{gap}$ ) was estimated by the method proposed by [46]. According to the author optical band gap is associated with the absorbance and photon energy by the following equation:

$$h\nu \propto (h\nu - E_{gap})^n \quad (3.11)$$

(where  $\alpha$  is the absorbance,  $h$  is the Planck constant,  $\nu$  is the frequency,  $E_{gap}$  is the optical band gap and  $n$  is a constant associated to the different types of electronic transitions ( $n = 0.5, 2, 1.5$  or  $3$  for direct allowed, indirect allowed, direct forbidden and indirect forbidden transitions, respectively). Thus, the  $E_{gap}$  values of [BMN], [SMN], [CMN] were evaluated extrapolating the linear portion of the curve or tail. In our work, the UV-vis absorbance spectra indicated an indirect allowed transition and, therefore, the value of  $n = 2$  is used in equation 3.11 [47].

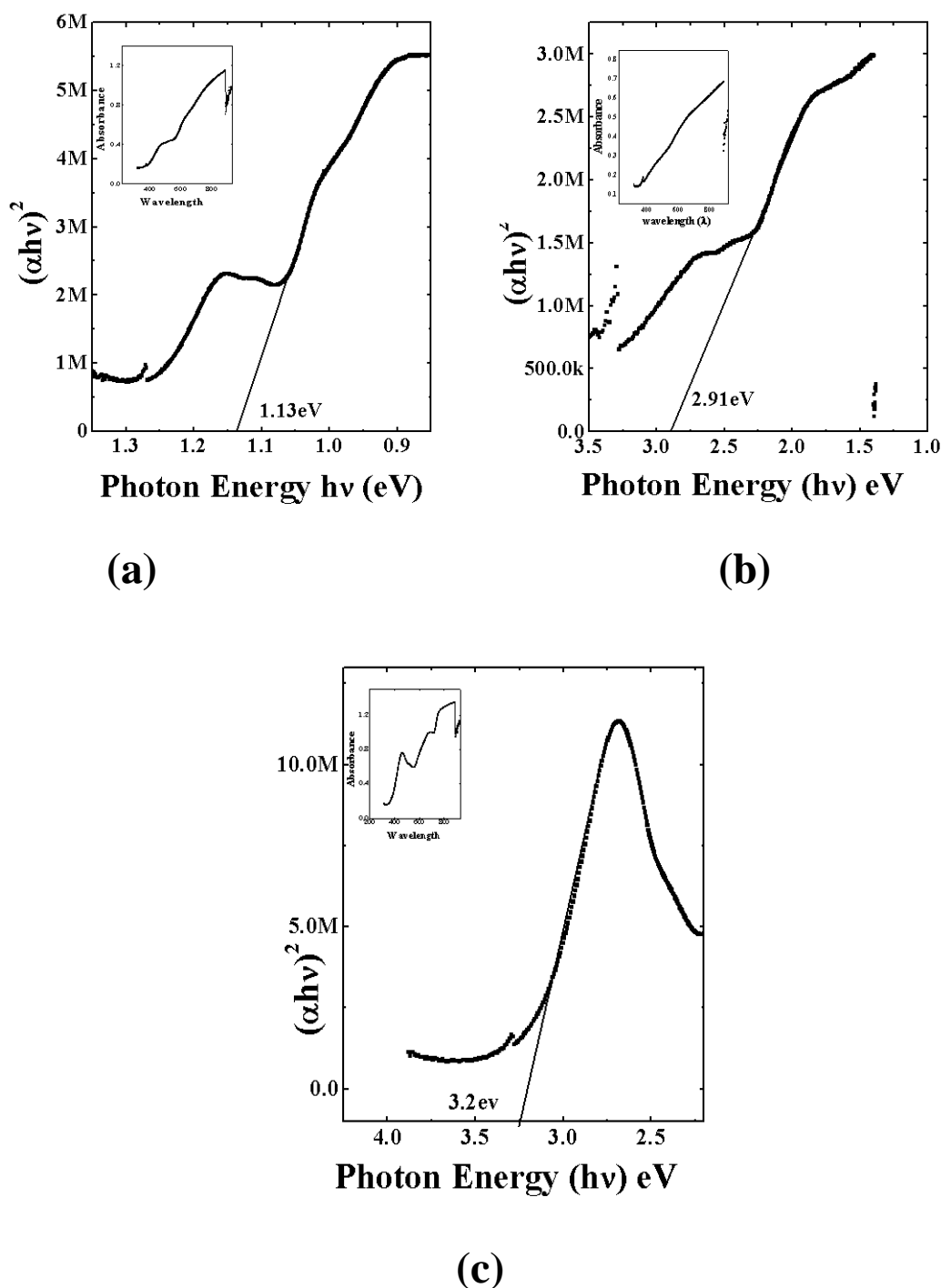


Figure 3.13 (a-c) UV- Vis Absorption Spectra of (a) BMN, (b) SMN, (c) CMN samples

The indirect band gap values are tabulated in Table 3.2 It is reported in the literature [48] that the band gap energy is indirect when the electronic transitions occur from maximum-energy states

located near or in the valence band (VB) to minimum-energy states below or in the conduction band (CB).

**Table 3.2 The observed indirect band Gap values of BMN, SMN and CMN**

Composition	Band Gap
BMN	1.13eV
SMN	2.91eV
CMN	3.24eV

### 3.3 Conclusions

In summary, we have successfully synthesized polycrystalline bulk samples of  $A(\text{Mg}_{0.33}\text{b}_{0.67})\text{O}_3$  where  $A = (\text{Ba}^{2+}, \text{Sr}^{2+}, \text{Ca}^{2+})$  [BMN], [SMN], [CMN] by standard solid state reaction technique. The effect of replacement of A site in  $A(\text{Mg}_{0.33}\text{b}_{0.67})\text{O}_3$  was studied by means of structural, micro structural, electrical, Conductivity and Optical studies. The following observations have been made on the basis of several experiments performed on the bulk samples.

- (i) The XRD analysis of  $A(\text{Mg}_{0.33}\text{b}_{0.67})\text{O}_3$  where  $A = (\text{Ba}^{2+}, \text{Sr}^{2+}, \text{Ca}^{2+})$  [BMN], [SMN], [CMN] indicates that all samples exhibit a single phase nature with [BMN] exhibit hexagonal symmetry and on replacement of Barium by Strontium and Calcium which have lower ionic radii the structure shifts to the lower symmetry side i.e Monoclinic side. This is also confirmed from the increase in unit cell volume. Increase in structural asymmetry gradually enhances the unit cell leading to correlated enhancement in dielectric constant  $\epsilon'$ .
- (ii) The dispersion behavior observed in dielectric constant as a function of frequency has been explained according to interfacial polarization as predicted by the Maxwell-Wagner and Koop's phenomenological theory. Increase in structural asymmetry gradually enhances the unit cell leading to correlated enhancement in dielectric constant  $\epsilon'$ . Dielectric loss  $\tan \delta$  is nearly same for Sr and Ca substituted compounds, but  $\text{Tm}$  gradually increases ( $\text{Ba} \rightarrow \text{Sr} \rightarrow \text{Ca}$ ). Both SMN and CMN exhibits enhancement in relaxation time with temperature suggesting systematic softening of dipolar coupling.

- (iii) Thus above niobate system possessing wide semi- conducting band gap region and conductivity mechanism based switching behavior is an ideal candidate for sensor, optoelectronic, and electrical switching device applications.

## References

- [1] V M Goldschmidt, *Naturwissenschaften*, **14**, 477, 1926.
- [2] A M Glazer, *Acta Crystallogr., Sect. B*, **28**, 3384, 1972.
- [3] P M Woodward, *Acta Crystallog., Sect. B*, **53**, 32, 1997.
- [4] R D Shannon, *J. Appl. Phys.*, **73**, 348, 1993.
- [5] H Tamura, D A Sagala, K Wakino, *Jpn. J. Appl. Phys.* 1, **25**, 787, 1986.
- [6] I M Reaney, I Qazi, W E Lee, *J. Appl. Phys.*, **88**, 6708, 2000.
- [7] W. Wersing, *Curr. Opin Solid State Mater. Sci*, **1**, 715, 1996.
- [8] W. A. Lan, M. H. Liang, C. T. Hu, K. S. Liu and I .N. Lin, *Mater. Chem. Phys.* **79**, 266, 2003.
- [9] J. I. Yang, S. Nahm, C .H. Choi, H. J. Lee and H .M. Park, *J. Amer. Ceram. Soc.* **85** 165, 2002.
- [10] H. Hughes, D. M. Iddles and I. M. Reaney, *Appl. Phys. Lett.* **79**, 2952, 2001.
- [11] I. Molodetsky and. K. Davies, *J. Eur. Ceram. Soc.* **21**, 2587, 2001.
- [12] I .T. Kim, Y .H. Kim and S .J. Chung, *J. Mater. Res.* **12**, 518, 1997.
- [13] S. Nomura, *Ferroelectrics* **49**, 61, 1983.
- [14] S Kawashima, M Nishida, I Ueda and H Ouchi *J. Am. Ceram. Soc.* **66**, 421, 1983.
- [15] S Nomura, K Toyama and K Kaneta *Jpn J. Appl. Phys.* **21**, L624, 1982.
- [16] S. B. Desu and H. M. O'Bryan *J. Am. Ceram. Soc.* **68**, 546, 1985.
- [17] Vincent H, Perrier C, Theritier P and Labeyrie M *Mater. Res. Bull.* **28**, 951, 1993.
- [18] Roy R *J. Am. Ceram. Soc.* **27**, 581, 1954.
- [19] F Galasso, L Katz and L R Ward *J. Am. Chem. Soc.* **81** 820, 1959.
- [20] S. B. Desu and H. M. O'Bryan, *J. Am. Ceram. Soc.*, **68** [10], 546, 1985.

- 
- [21] K. Matsumoto, T. Hiuga, K. Takada, and H. Ichimura, pp 118–21 in Proceedings of the 6th IEEE International Symposium on Application of Ferroelectrics (June 1986). Institute of Electrical and Electronic Engineers, New York, 1986.
  - [22] P. K. Davies, J. Tong, and T. Negas, *J. Am. Ceram. Soc.*, **80** [7], 1727, 1997.
  - [23] H. X. Liu, Z. Q. Tian, H. Wang, H. T. Yu, S. X. Ouyang *Journal Mat Sci Lett* **39**, 4319, 2004.
  - [24] Jong-Hoo Paik, Sei-Ki Kim, Mi-Jae Lee, Byung-Hyun Choi, Eun-Kyeong Lim, Sahn Nahm *J of the Europ Ceramic Society* **26**, 2885, 2006.
  - [25] F Galasso and J Pyle *J. Phys. Chem.* **67** 1561, 1963.
  - [26] S Nomura *Ferroelectrics* **49**, 61, 1983.
  - [27] M Thirumal and A K Ganguli *Bull. Mater. Sci.*, **23**, 495, 2000.
  - [28] J. H. Paik, S. Nahm, J. D. Bylin, M. H. Kim, H. J. Lee *Journal Mat Sci Lett*, **17**, 1777, 1998.
  - [29] Xifa Long and Zuo-Guang Ye *App Phy Lett*, **90**, 112905, 2007.
  - [30] Surya M. Gupta, E. Furman, E. Colla, and Z. Xu, Dwight Viehland *J of App Phy*, **88**, 2836, 2000.
  - [31] Alo Dutta, T.P.Sinha *Physica B* **405**, 1475, 2010.
  - [32] Michael W. Lufaso *Chem. Mater.*, **16**, 2148, 2004.
  - [33] A. Dias, V.S.T. Ciminelli, F.M. Matinaga, R.L. Moreira *J of the European Ceramic Society* **21**, 2739, 2001.
  - [34] Dong Cheng, Powder, X, Window-95 program for powder x-ray diffraction data processing, *J. Appl. Cryst.* **32**, 838, 1999.
  - [35] C. S. Park, J. H. Paik, S Nahm, H.J Lee, H. M. Park, Y. K. Kim *J Mat Sci letters* **18**, 691 1999.
  - [36] J Maxwell, Electricity and Magnetism (Vol.1, Section 328, Oxford University Press, London) 1873.
  - [37] C. Koops. *Phys. Rev.* **83**, 121, 1951.
  - [38] J Smit H Wijn *Ferrites*, Wiley, New York, p. 369, 1959.
  - [39] I M Hodge, M D Ingram and A R West, *J. Electroanal. Chem* **74**, 125, 1976.
  - [40] K C Sobha, and K Rao., *Solid State Ionics*, **81**, 145, 1995.
  - [41] M Ganguli, H M Bhat and K Rao *J, Phys. Chem. Glasses*, **40**, 297, 1999.

- [42] S Lanfredi, S P Saia, R Lebullenger and C A Hernandes. *Solid State Ionics*, **146**, 329, 2002.
- [43] S Ghosh, and A Ghosh. *Solid State Ionics*, **149**, 67. 2002.
- [44] S F Howell, A R Bose. B P Macedo.and T C Moynihan, *J. Phys. Chem.*,**78**, 639, 1974.
- [45] S Saha, T P Sinha, *Phys. Rev. B* **65**, 134103, 2002.
- [46] D L Wood, J Tauc, *Physical Review B*, **5**, 3144, 1972.
- [47] Bhagwati Bishnoi, P.K. Mehta, C.J. Panchal, M.S. Desai, Ravi Kumar *J. Nano. Electron. Phys* .**3(1)**, 698, 2010.
- [48] Cavalcante. L.S, Gurgel. M.F.C, Paris. E.C, Simoes. A.Z, Joya. M.R, Varela. J.A, Pizani. P. S, Longo. E, *Acta Materialia*, **55**, 6416, 2007.

## Chapter 4

### **Replacement at B'-site by divalent ions in Strontium Series and its impacts on Structural, microstructure, dielectric, complex impedance, Conductivity and Optical studies.**

In this chapter we have reported the effect of B'-site substitution on the complex perovskite  $\text{Sr}(\text{B}'_{0.33}\text{Nb}_{0.67})\text{O}_3$  by different divalent ion ( $\text{Mg}^{2+}$ ,  $\text{Co}^{2+}$ ,  $\text{Cu}^{2+}$ ). The effects probed are its structure, microstructure, dielectric, conductivity and optical properties. The structure of SMN, SCoN, SCuN are found to be free from impurities. On replacing Magnesium by Cobalt or Copper structure moves towards lower symmetry side and its dielectric properties are drastically enhanced but maintaining low losses. All the compositions are relaxor ferroelectrics. All the observed findings are explained on the basis of cole-cole analysis. The band gap of these is found to be shifting within wide band gap semiconductor region. Overall impact of Jahn-Teller effect is positive on the properties of Strontium Niobates.

#### 4.1 Introduction

In recent years, significant efforts have been focused on reducing the size and weight of power electronic modules. To achieve these goals in high-power capacitors, microwave devices and memory devices, alternative materials and fabrication processes are needed. Ferroelectric/dielectric oxides in bulk form proved to be a robust and reliable solution for device applications. Efforts are being put in the search of suitable ferroelectric/dielectric materials having reasonably high remnant polarization, low coercive field, and high fatigue lifetime to ensure the reliability of a non volatile random access memory. Materials studied so far are predominantly lead based defects Perovskites, such as  $\text{BaTiO}_3$ ,  $\text{PbTiO}_3$ ,  $\text{Pb}(\text{Zr}_x\text{Ti}_{1-x})\text{O}_3$ ,  $\text{Pb}(\text{Mg}_{1/3}\text{Nb}_{2/3})\text{O}_3$ ,  $\text{Pb}(\text{Zr}_{0.5}\text{Ti}_{0.47})\text{O}_3$  (PZT) and  $(\text{Ba}_{1-x}\text{Sr}_x)\text{TiO}_3$  (denoted as BST) etc. Lead based oxides show good ferroelectric properties but they suffer from severe fatigue problems under operating conditions [1-3]. Materials which overcome such problems are Barium, Bismuth and Strontium based layered Perovskite oxides. They offer the advantage of relative ease of fabrication due to the absence of volatile Lead and good ferroelectric/dielectric properties along with higher fatigue endurance [4]. These barium based compositions show limited variations in the crystal symmetry with most of them exhibiting cubic or hexagonal symmetry [5-7]. On the other hand replacing Barium by Strontium at the A-site in above compound, distorts the structure towards lower symmetry [8, 9], i.e. Monoclinic, and at the same time dielectric properties were also drastically affected. The dielectric properties are known to be linked to the structural variations within tolerance limit. Reany et al. [10] based on analysis of tolerance factor had suggested that atoms with lower ionic radii decreases the lattice strain and reduces the dielectric loss in the samples.

The tolerance factor is given by the formula

$$t = \frac{r_a + r_o}{\sqrt{2} (r_b + r_o)} \quad (4.1)$$

Where  $r_a$  is the average radius of the A-site ions,  $r_b$  is the average radius of B-site ions and  $r_o$  is the average ionic radii of Oxygen ions.



In this chapter, we report the effect of replacing the B'site ions in the  $\text{Sr}(\text{B}'_{1/3}\text{Nb}_{2/3})\text{O}_3$  by different divalent atoms such as  $\text{Mg}^{2+}$ ,  $\text{Co}^{2+}$  and  $\text{Cu}^{2+}$ . These compounds are analysed on the basis of their crystal structure, microstructure, dielectric, ferroelectric properties as well as ac conductivity behaviour. It is to be noted that  $\text{Mg}^{2+}(2p^6)$  possess filled 2p orbitals where as  $\text{Co}^{2+}(3d^7)$  has unevenly filled  $t_{2g}$  levels and can exhibit weak Jahn-Teller Effect in comparison to  $\text{Cu}^{2+}(3d^9)$  having doubly degenerate  $e_g$  levels capable of producing very strong Jahn-Teller distortions within oxygen octahedral. We have prepared the above strontium series by standard solid state reaction technique. The final product comes out to be  $\text{Sr}(\text{Mg}_{1/3}\text{Nb}_{2/3})\text{O}_3$  [SMN],  $\text{Sr}(\text{Co}_{1/3}\text{Nb}_{2/3})\text{O}_3$ , [SCoN],  $\text{Sr}(\text{Cu}_{1/3}\text{Nb}_{2/3})\text{O}_3$  [SCuN]. Here we have discussed the effect of total replacement of B'-ste where  $\text{B}' = (\text{Mg}^{2+}, \text{Co}^{2+}, \text{Cu}^{2+})$  on structural, micro structural, dielectric properties, complex impedance studies, conductivity studies, and optical studies.

## 4.2 Results and Discussions

### 4.2.1 X-ray Diffraction (XRD) Measurements

Figure 4.1 shows the XRD patterns of  $\text{Sr}(\text{Mg}_{1/3}\text{Nb}_{2/3})\text{O}_3$  [SMN],  $\text{Sr}(\text{Co}_{1/3}\text{Nb}_{2/3})\text{O}_3$  [SCoN],  $\text{Sr}(\text{Cu}_{1/3}\text{Nb}_{2/3})\text{O}_3$  [SCuN] compounds. Each composition exhibits single phase formation with no trace of impurities. Lattice parameters of the samples were calculated from X-ray diffractograms using the least square refinement method based computer program package POWDER X [11]. The calculated lattice parameters along with respective structures are listed in Table 4.1.

We find that the lattice parameters and unit cell volume decreased when  $\text{Mg}^{2+}$  is replaced by  $\text{Co}^{2+}$ , but they rather increase when it is replaced by  $\text{Cu}^{2+}$ . It is to be noted here that the lattice parameters of SMN reasonably matched well with the published data [12]. Now the decrease in volume on incorporating  $\text{Co}^{2+}$  at the  $\text{Mg}^{2+}$  site purely follow ionic radii size dependent behavior [13]. But substitution of  $\text{Cu}^{2+}$  instead of  $\text{Mg}^{2+}/\text{Co}^{2+}$  completely changed the crystal symmetry from Monoclinic to Tetragonal as well as also resulted into abrupt increase in the unit cell volume. This may be due to  $\text{Cu}^{2+}(3d^9)$  configuration induced Jahn-Teller effect in the unit cell [14]. It is worth noting that when Mg having filled 2p orbital is replaced by  $\text{Co}^{2+}(3d^7)$ , possessing

unevenly filled  $t^{2g}$  levels, produces weak Jahn-Teller effect resulting  $90^\circ$  cyclically rotated crystallographic structure (Table 4.1) though the type of structure remaining unchanged.

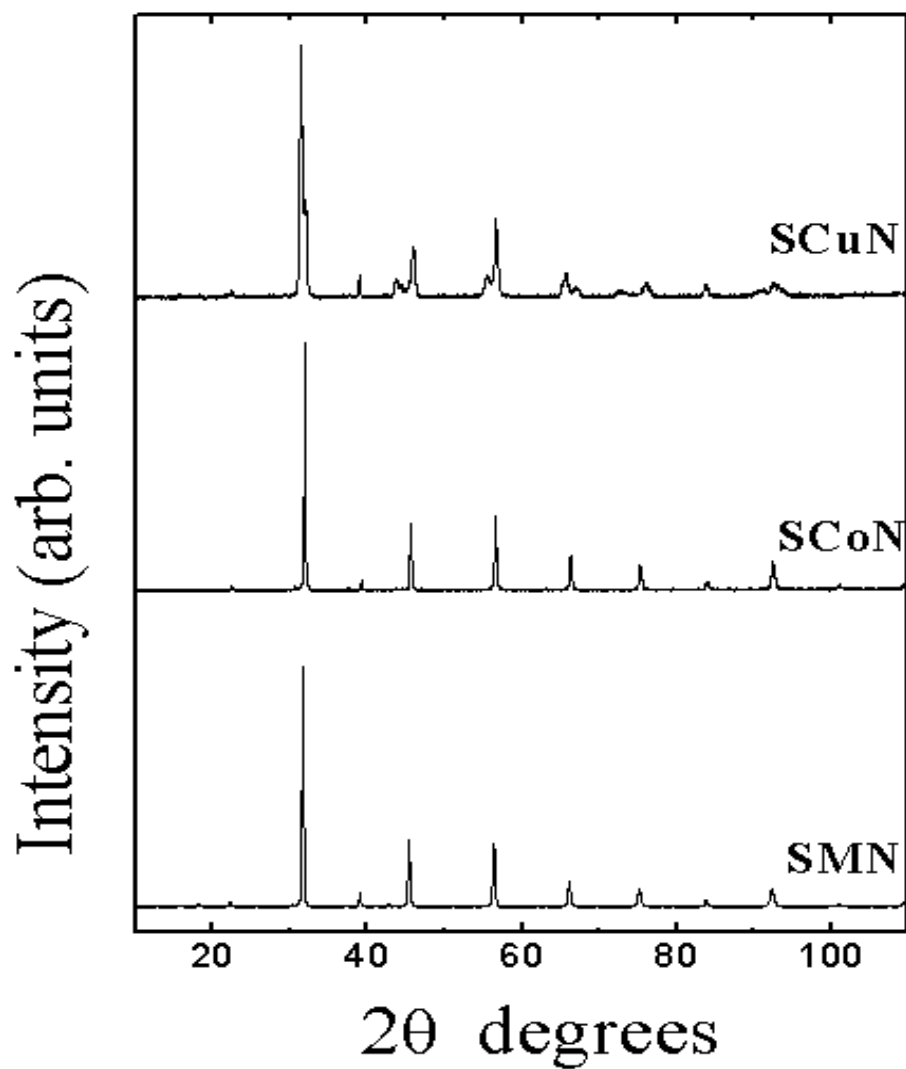


*Figure 4.1* X-ray powder diffraction pattern of SMN, SCoN, SCuN samples

**Table 4.1 Structure, Lattice parameters and Tolerance of  $\text{Sr}(\text{B}'_{1/3}\text{Nb}_{2/3})\text{O}_3$  ( $\text{B}'=\text{Mg}^{2+}$ ,  $\text{Co}^{2+}$ ,  $\text{Cu}^{2+}$ )**

Composition	Tolerance	Structure	Lattice Parameter	Volume
$\text{Sr}(\text{Mg}_{1/3}\text{Nb}_{2/3})\text{O}_3$ SMN	0.971	Monoclinic	$a=8.95625 \text{ \AA}$ $b=13.46112 \text{ \AA}$ $c=5.77833 \text{ \AA}$ $\beta=93.33$	$696.64 \text{ \AA}^3$
$\text{Sr}(\text{Co}_{1/3}\text{Nb}_{2/3})\text{O}_3$ SCoN	0.984	Monoclinic	$a=5.79909 \text{ \AA}$ $b=8.57682 \text{ \AA}$ $c=13.45582 \text{ \AA}$ $\beta=95.45$	$669.26 \text{ \AA}^3$
$\text{Sr}(\text{Cu}_{1/3}\text{Nb}_{2/3})\text{O}_3$ SCuN	0.972	Tetragonal	$a=10.9567 \text{ \AA}$ $c=11.7908 \text{ \AA}$	$1415.47 \text{ \AA}^3$

#### 4.2.2 Scanning Electron Microscopy Analysis

In order to understand the morphology, grain size and shape of the B'-site variation in  $\text{Sr}(\text{B}'_{1/3}\text{Nb}_{2/3})\text{O}_3$ , SEM study has been carried out. The SEM micrographs were taken at 2500 magnification at different parts of the samples. The SEM images of all samples are shown in Figure 4.2 (a-c). It is clear from the SEM micrograph that the micro-structure gets modified with different divalent ion substitution. On a closer look of these micro-structures, it reveals conglomerated structures with noticeable porosity in SMN as well as SCoN samples. The conglomeration is probably due to trapping of moisture during crystallization producing semi liquid phase at grain boundaries. The microstructure altogether changed to elongated grain type structures in Cu substituted SCuN sample. These rods like elongated grains are randomly oriented. Correlating observed changes in crystal structure as well as microstructure in  $\text{Mg}^{2+}$ ,  $\text{Co}^{2+}$  or  $\text{Cu}^{2+}$  substituted strontium niobates suggests the possibilities of drastic changes in

respective dielectric/ferroelectric behaviours. We do observe that microstructure behaviour does affect their dielectric properties like dielectric constant ( $\epsilon'$ ) and dielectric loss ( $\tan\delta$ ).

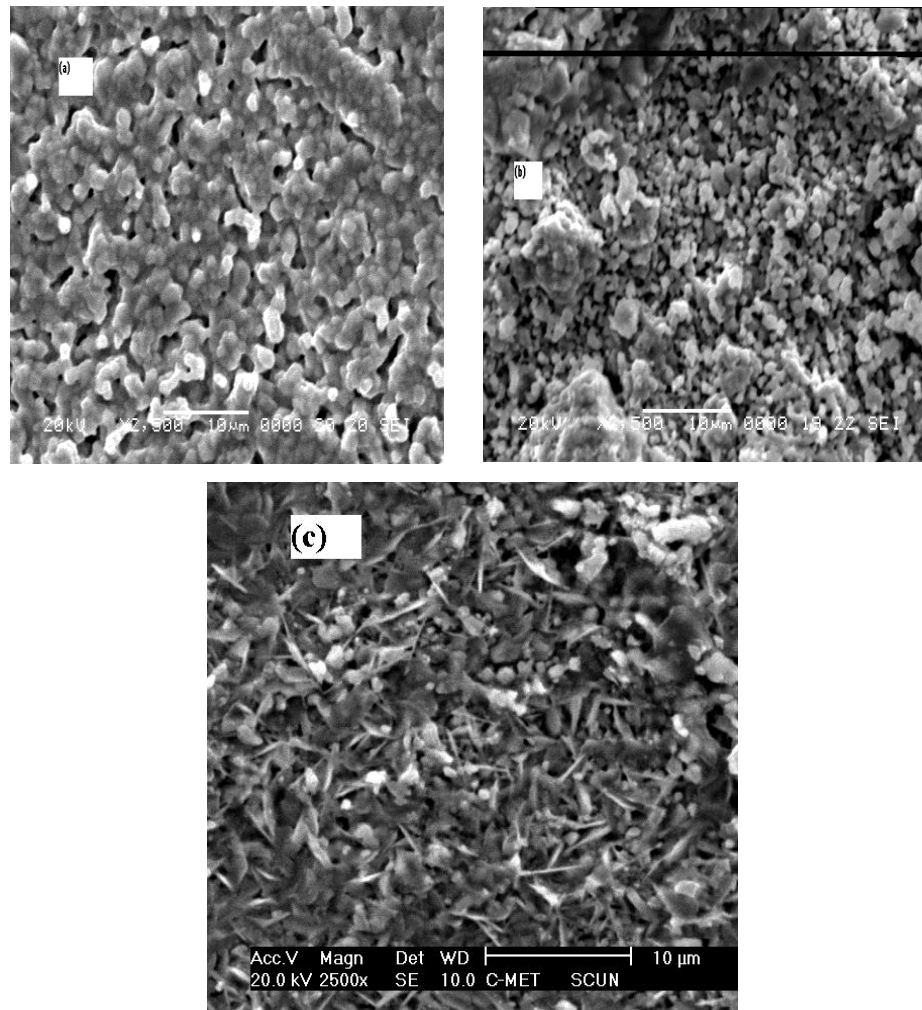


*Figure 4.2* SEM Micrograph of (a) SMN (b)SCoN, (c) SCuN samples.

### 4.2.3 Dielectric Measurement

#### 4.2.3.1 Frequency Dependence Dielectric Properties

Figure 4.3 shows the frequency dependence of relative real part of dielectric permittivity performed in the temperature range (room temperature to 350<sup>0</sup>C) and the frequencies range of 100Hz-3.2MHz for  $\text{Sr}(\text{B}'_{1/3}\text{Nb}_{2/3})\text{O}_3$  samples, where ( $\text{B}' = \text{Mg}^{2+}, \text{Co}^{2+}, \text{Cu}^{2+}$ ). It is observed that

all studied samples exhibit dispersion behaviour, i.e., the dielectric constant decreases with increase in the frequency. This is the general dielectric behaviour observed in most of the oxide materials, which can be explained with interfacial polarization predicted by the Maxwell-Wagner model [15] in agreement with Koop's phenomenological theory [16]. According to these models, the dielectric materials can be imagined as a heterogeneous structure consisting of well conducting grains separated by thin layer of poorly conducting substances (grain boundaries). These grain boundaries could be formed during the sintering process, either by superficial reduction or oxidation of crystallites in the porous materials as a result of their direct contact with the firing atmosphere [17]. In  $\text{Sr}(\text{Mg}_{1/3}\text{Nb}_{2/3})\text{O}_3$  [SMN] the value of dielectric constant ( $\epsilon'$ ) varies in the order of  $(10-10^3)$  as well as it shows distinct dispersion behaviour. On the replacement of  $\text{Mg}^{2+}$  by  $\text{Co}^{2+}$  ( $3d^7$ ) the dielectric constant ( $\epsilon'$ ) value drastically increase in order  $(10-10^4)$ . This is likely to be due to the fact that Mg ( $2p$ ) orbital state are completely filled state and on replacing it with Co ( $3d^7$ ) which have partially filled  $t_{2g}$  levels which in turn results in weak Jahn Teller distortions in the compound. This composition also shows the dispersion behavior. On the other hand on further replacement of  $\text{Co}^{2+}$  by  $\text{Cu}^{2+}$ , having  $3d^9$  configurations, there is further enhancement in the dielectric constant values ( $10^2-10^5$ ).

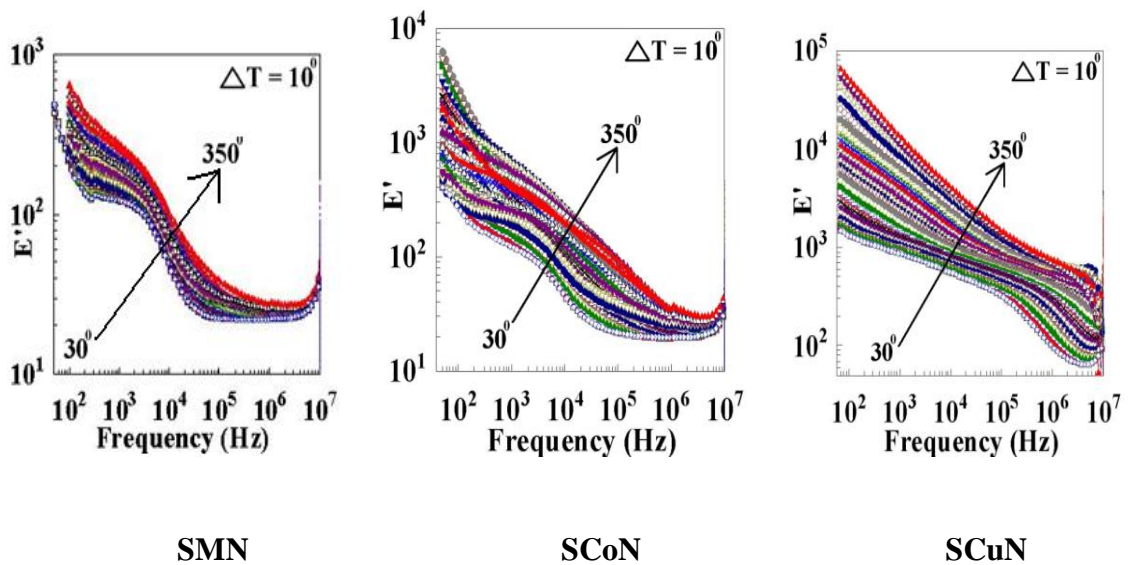


**Figure 4.3 Dielectric Constant as a function of Frequency of SMN, SCoN, SCuN samples from (RT – 350°C)**

Figure 4.4 shows the frequency dependence of dielectric loss ( $\tan\delta$ ) for SMN, SCoN and SCuN in full temperature range (RT- 350°C). In case of SMN the loss are less in comparison to SCoN but as we replace  $\text{Co}^{2+}$  by  $\text{Cu}^{2+}$  we found that losses are very less. In Co based composition we have higher losses which are likely to be due to the presence of liquid phase along with smaller grain size inducing mobile oxygen vacancies at grain boundaries Figure 4.2 (b).

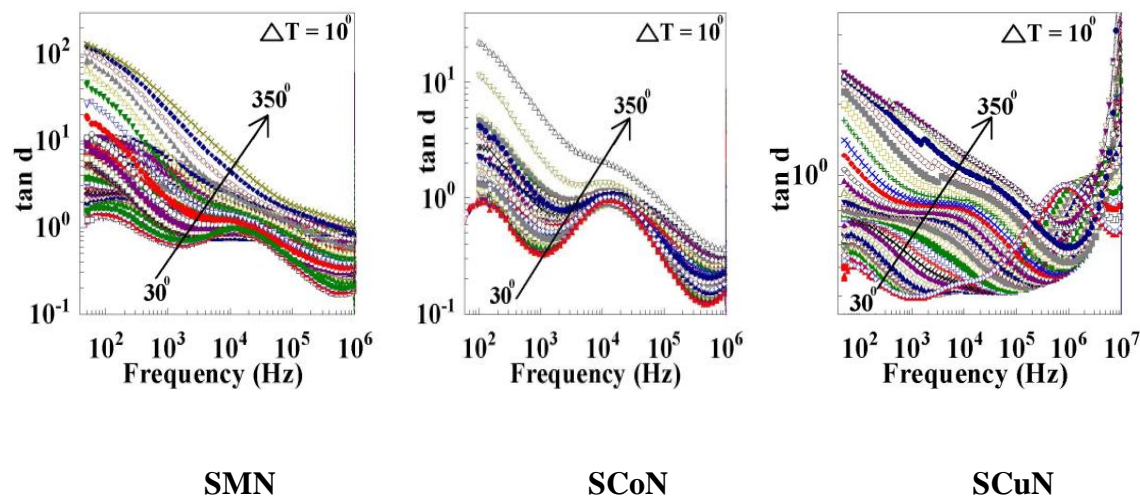


**Figure 4.4 Dielectric Loss ( $\tan\delta$ ) vs. Frequency of SMN, SCoN, SCuN samples from (RT – 350°C)**

As we move towards the  $\text{Sr}(\text{Cu}_{1/3}\text{Nb}_{2/3})\text{O}_3$  where  $\text{Cu}^{2+}$  ( $3d^9$ ) configurations with possible strong Jahn-Teller effect give rise to very low losses, compared to  $\text{Mg}^{2+}$  and  $\text{Co}^{2+}$ , and in turn have excellent dielectric constant values. This composition also happens to show better grain formation, Figure 4.2 (c).

#### 4.2.3.2 Temperature Dependent Dielectric Properties

Figure 4.5 shows the dielectric constant for B'-site substituted divalent ions in  $\text{Sr}(\text{B}'_{1/3}\text{Nb}_{2/3})\text{O}_3$  series as a function of temperature in frequency range (100-32MHz). The real permittivity ( $\epsilon'$ ) value gradually increases up to a maximum value ( $\epsilon_m$ ) with the increase of temperature, and then it smoothly decreases, suggesting a phase transition. The maximum relative permittivity ( $\epsilon_m$ ) as well as its corresponding temperature ( $T_m$ ) is dependent on the frequency. In this case, the relative dielectric permittivity magnitude decreases with the increase



in the frequency, shifting the maximum value ( $\epsilon_m$ ) to higher temperatures. Hence, this result indicates that the dielectric polarization has relaxation-type behaviour. We know that according to CFS theory  $\text{Co}^{2+}$  with  $3d^7$  electronic configurations the  $t_{2g}$  orbitales are unevenly occupied producing weak Jahn-Teller effects. The Jahn-Teller Effect distorts the octahedral along one of its crystallographic direction and hence enhances the polarization in the system. This effect is strongest in  $3d^9$  configurations but weak in  $3d^7$  configurations. Figure 4.5 clearly illustrates such a correlated variations in the dielectric constant ( $\epsilon'$ ) strengthening our argument. Strong Jahn-Teller effect in  $\text{Cu}^{2+}$  ( $3d^9$ ) produces large polarization in unit cell enhancing dipole moment dependent dielectric constant ( $\epsilon'$ ) the most. Whereas,  $\text{Co}^{2+}$  ( $3d^7$ ) possessing weak Jahn-Teller effect give intermediate values and  $\text{Mg}^{2+}$  ( $2p^6$ ) with no Jahn-Teller effect the least dielectric constant values. Further, localized change in bond strength due to partially filled orbital in  $\text{Co}^{2+}$  compared to filled  $\text{Mg}$  ( $2p^6$ ) orbital decreases Curie temperature in  $\text{SCoN}$ . Such behaviour was also observed earlier in doped  $\text{BaTiO}_3$  compound [18]. On replacing  $\text{Co}^{2+}$  by  $\text{Cu}^{2+}$  we observe abrupt rise in transition temperature ( $T_m$ ) again due to doubly degenerate unevenly filled  $e_g$  orbitales's. Earlier a ferroelectric phase transition at  $T_m = 663\text{K}$  in  $\text{SCuN}$  is reported to be connected to electron-phonon type interaction in the presence of Jahn-Teller Effect [14, 19].

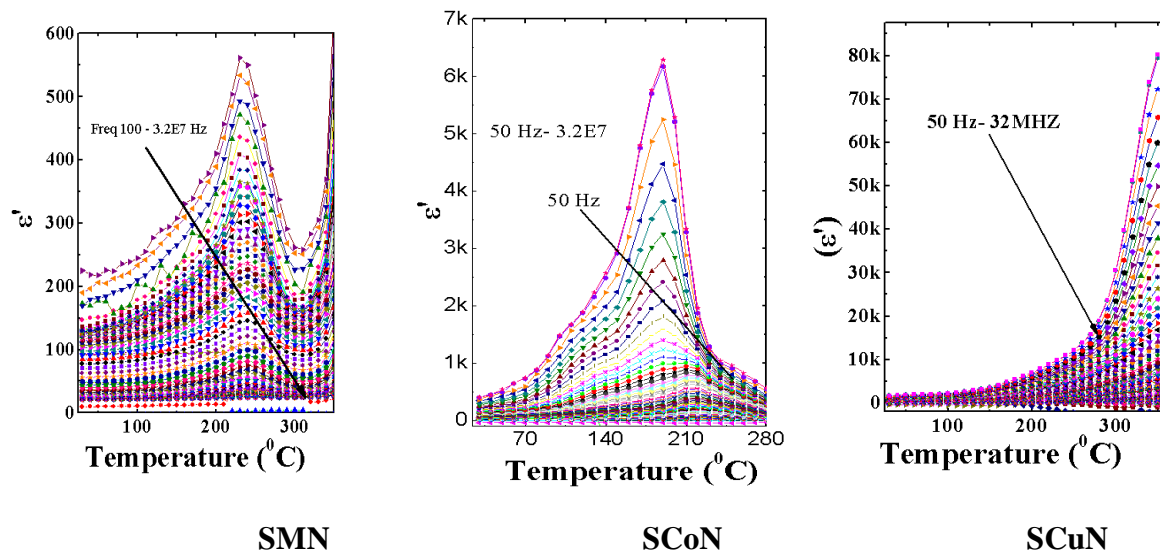


**Figure 4.5** Temperature dependence of Dielectric Constant for SMN, SCoN and SCuN ceramics in full frequency range (100-32MHz).

Figure 4.6 shows the variation of dielectric loss as a function of temperature. It is observed that due to relaxor nature of samples dielectric loss ( $\tan\delta$ ) increases with increase in temperatures. The large enhancement of dielectric loss ( $\tan\delta$ ) in SCoN can be correlated to enhanced mobility of charges in unevenly filled orbitals of  $\text{Co}^{2+}$  ( $3d^7$ ). Dielectric loss as a function of temperature is lower for SMN and further reduces in SCuN due to localization of conduction electrons either by the presence of completely filled orbitals ( $\text{Mg}^{2+}$ ) or Jahn-Teller effect, in  $\text{Cu}^{2+}$ . Further, reduction in grain size of SCoN also leads to increase in the grain boundary induced space charge polarization [20], this additionally can result in enhancement of loss parameter and reduction in  $Q \times f$  values [21]. In the case of SCoN room temperature dielectric loss is around 1.43, while in the case of SCuN room temperature dielectric loss is only around 0.16. It is known that  $e_g$  orbitals involved in degeneracy are rigidly directed towards ligand orbitals leading to pinning of conduction electrons. That is why loss in SCuN is lowest among present series of Sr based compounds.

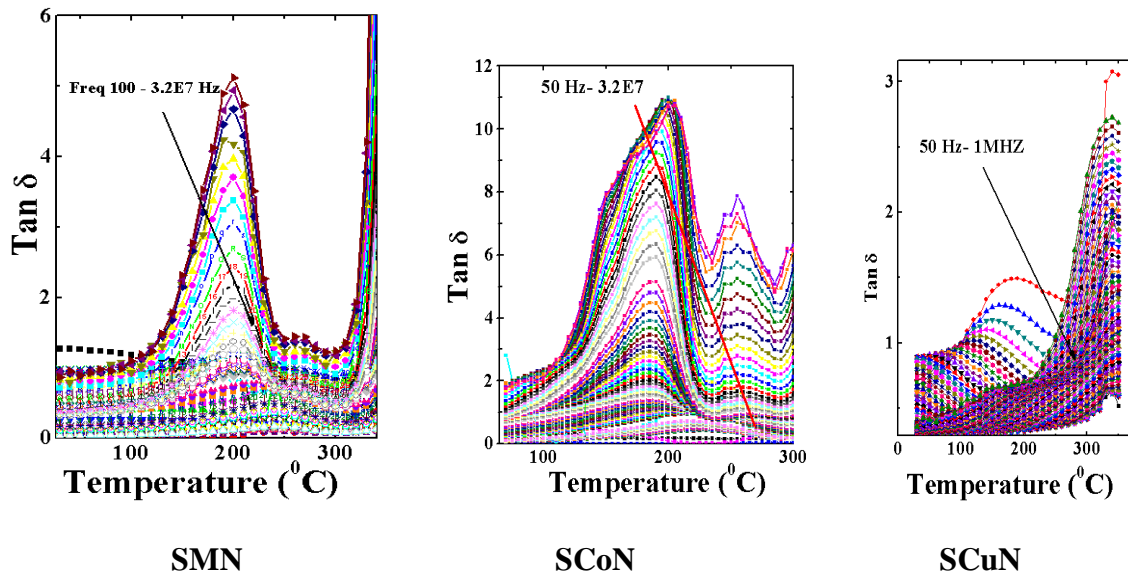


**Figure 4.6** Temperature dependence of Dielectric loss ( $\tan\delta$ ) for SMN, SCoN and SCuN ceramics in full frequency range (100-32MHz).

#### 4.2.4 Diffuse Phase Transition

A diffuse phase transition is commonly observed by the broadening of the dielectric constant ( $\epsilon'$ ) as a function of temperature ( $T$ ). The large separation (in temperature) between the maximum real (dielectric constant) and imaginary (dielectric loss) points from the dielectric



constant curve, deviation from the Curie–Weiss law near  $T_m$ , frequency dispersion of both dielectric and dielectric loss in the transition region imply a frequency dependence with  $T_m$  [22, 23]. A deviation from the Curie–Weiss law can be observed for all frequencies (Figure 4.7). This deviation is a typical behavior of ferroelectric materials with diffuse phase transition. A modified Curie–Weiss law has been proposed to describe the diffuseness in a phase transition (Uchino and Nomura 1986) [24]

$$\ln \left( \frac{1}{\epsilon} - \frac{1}{\epsilon_m} \right) = \ln (T - T_m)^\gamma / C' \quad (4.1)$$

where both  $\gamma$  and  $C'$  are constants. The parameter  $\gamma$  gives information on the phase transition character ( $\gamma = 1 \rightarrow$  a normal Curie–Weiss law behaviour is obtained and  $\gamma = 2 \rightarrow$  it exhibits the quadratic dependence, a signature of complete diffuse phase transition).

The plot of  $\ln (1/\epsilon - 1/\epsilon_{max})$  versus  $\ln (T - T_m)$  at 10 kHz for [SMN] and [SCoN] ceramics are shown in Figure 4.7. Linear relationships are observed. The slopes of the fitting curve are used to determine the parameter  $\gamma$  value. The  $\gamma$  value was found to be 1.03 for [SMN] and 1.40 for [SCoN] at frequency 10 kHz.

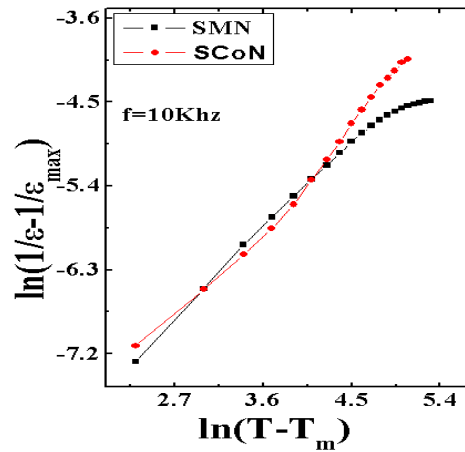


Figure 4.7 Variation of  $\ln (1/\epsilon - 1/\epsilon_{max})$  with  $\ln (T - T_m)$  at 10 kHz

While in case of SCoN we do not observe the transition temperature within our temperature range of measurement therefore the value of diffusivity is not determined. Further,

we observed that in the case of SMN diffusivity nearly obey the Curie- Weiss law but as we move towards Co based composition, SCoN, it move towards the diffuse phase transition region. An important observation on the fit performed in our experimental data by means of equation (4.1) indicates that a universal  $\gamma$  value was not obtained in the temperature range above  $T_m$ . The  $\gamma$  value continuously approaches unity when it departs from  $T_m$ . This value suggests that the material has structural order-disorder and diffuse phase transition. The observed broadness or diffusiveness occurs mainly due to the either compositional fluctuation and/or due to the structural disorder in the lattice. It points toward a microscopic heterogeneity in SMN, SCoN structures leading to differing local Curie points. The nature and variation of the dielectric constant indicate that the material has a ferroelectric-relaxor phase transition.

#### 4.2.5 Impedance Spectroscopy Studies

The detail studies of impedance spectroscopy of  $\text{Sr}(\text{B}'_{1/3}\text{Nb}_{2/3})\text{O}_3$  where ( $\text{B}' = \text{Mg}^{2+}, \text{Co}^{2+}, \text{Cu}^{2+}$ ) ceramics are discussed. Figure 4.8 shows the Nyquist plots (complex impedance spectrum) of [SMN], [SCoN], [SCuN] at different temperatures. Characteristically, two semicircular arcs have been observed. The complex impedance plot (Figure 4.8) shows two semicircular arcs with their centers lying below the real axis rather than on the real axis. The angle by which the semicircle is depressed below the real axis and the amount of inclination of the straight line are related to the width of the distribution of the relaxation time. This suggests the poly-dispersive nature of the sample. One obtains it by fitting the Cole-Cole equation,

$$\epsilon^* = \epsilon' + i\epsilon'' = \epsilon_\infty + \frac{\Delta\epsilon}{1 + (i\omega\tau)^{1-\alpha}} - i \frac{\sigma_d}{\epsilon_0\omega} \quad (4.2)$$

Here,  $\tau$  is the mean relaxation time instead of the single relaxation time of pure Debye process while the Cole-Cole parameter  $\alpha$  indicates the width of the relaxation time distribution and provides a measure of the poly-dispersive nature. The fitting of the Cole-Cole equation was performed to study the dispersive and the conducting nature of the samples. It is seen from Figure 4.9 ( $\alpha$  is plotted versus temperature) that the observed non-zero values of the Cole-Cole

parameter  $\alpha$  indicates non-Debye type poly-dispersive nature of these samples. While in the case of [SCuN] we do not observe any semi circular arc forming in the frequency range.

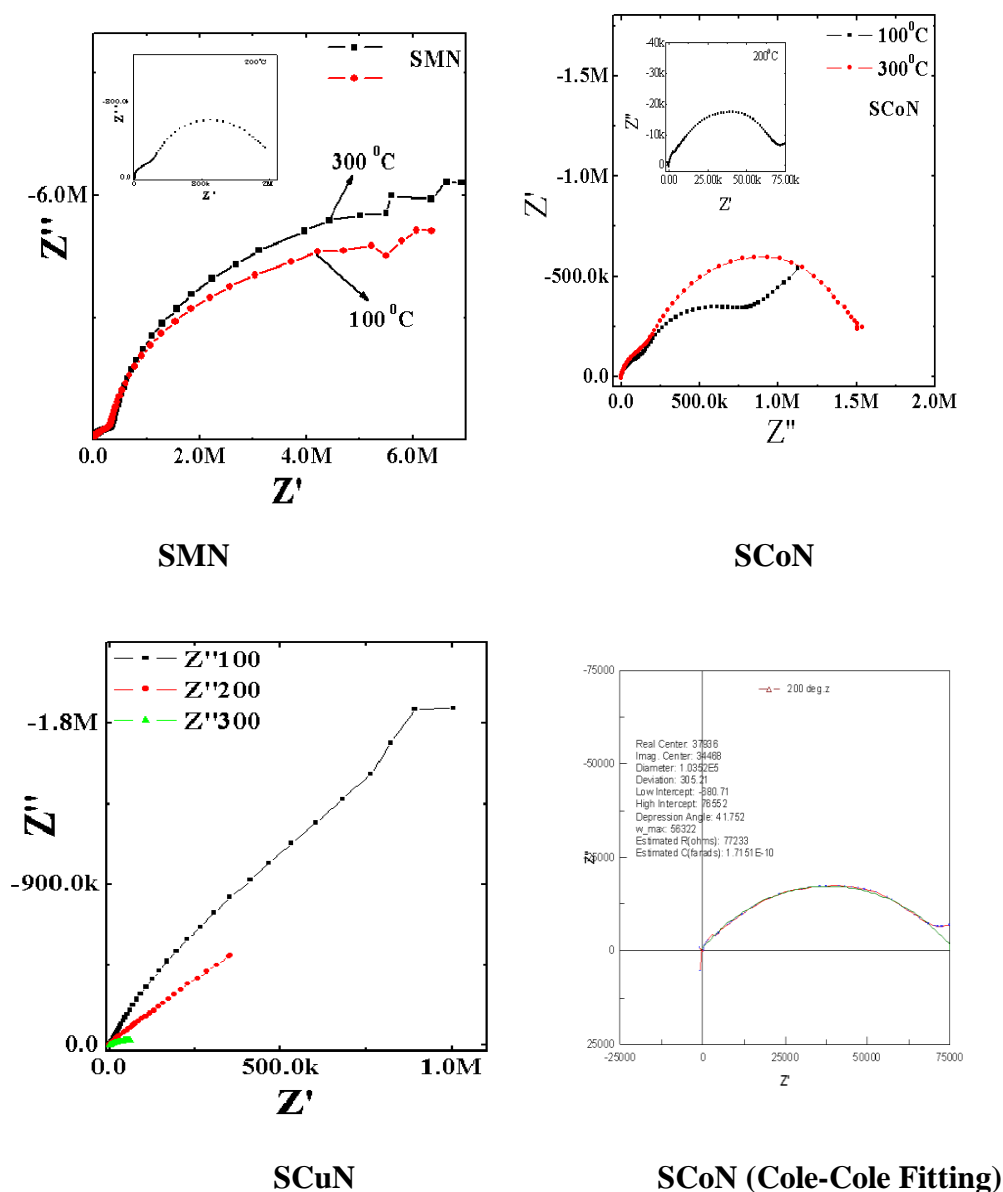
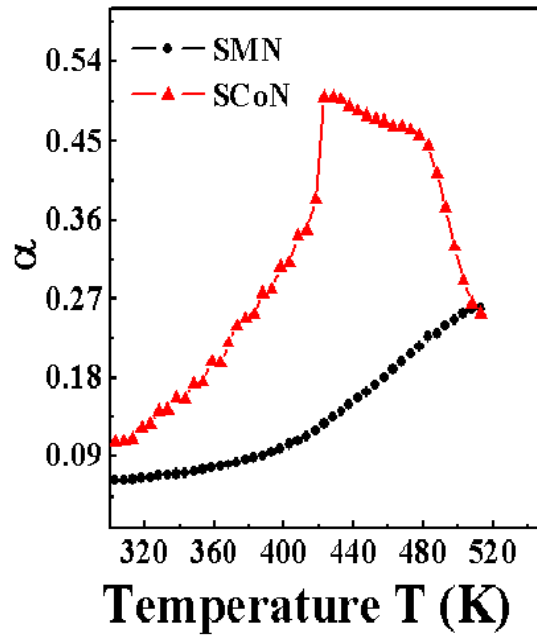
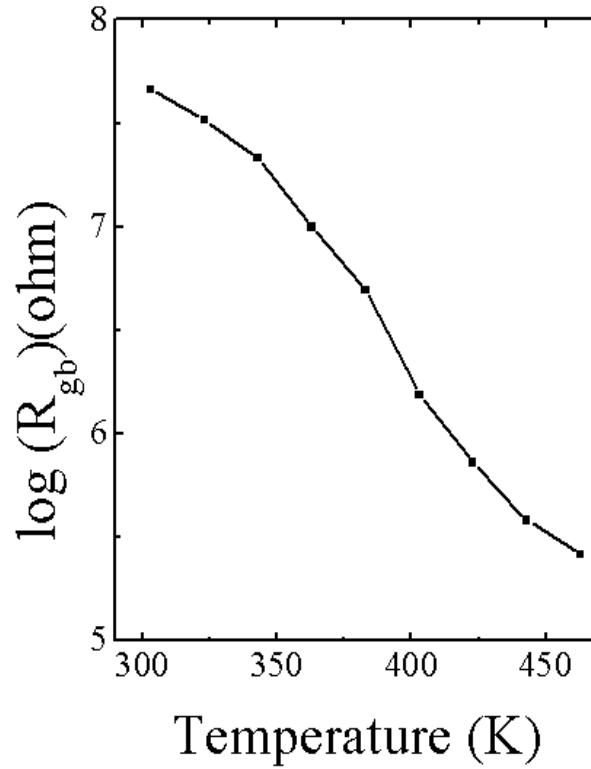


Figure 4.8 Cole-Cole graphs of SMN, SCoN and SCuN at three different temperatures 100, 200, 300 deg.



**Figure 4.9** The Temperature dependence of the Cole-Cole parameter, which indicates the width of the relaxation time distribution.

Using the ZView commercial software, the impedance data were analyzed in order to obtain the bulk resistance ( $R_g$ ) and grain boundary resistance ( $R_{gb}$ ). The observed features the low frequency semicircle is considered due to the grain boundary (blocking core) whereas the higher frequency semicircle depicts the bulk effect. The bulk effect arising due to the parallel combination of bulk resistance ( $R_b$ ) and capacitance ( $C_b$ ) for SMN, SCoN are shown in the equivalent circuit (Figure 4.8 (inset)). Using the ZView commercial software, the impedance data were analyzed to obtain the value of bulk resistance ( $R_b$ ) and grain boundary resistance ( $R_{gb}$ ) at different temperatures from the intercept of the semicircular arc on the real axis ( $Z'$ ). As the temperature increases, the radius of the arc corresponding to the bulk resistance of the sample decreases indicating an activated conduction mechanism. Figure 4.10 shows the variation of grain boundary resistance with temperature.



**Figure 4.10** Variation of grain boundary resistance ( $R_{gb}$ ) as a function of temperature for SCoN sample.

The values of Resistance and Capacitance are given in Table 4.2 and the conductivity values are shown in Table 4.4. The plot of grain and grain boundary conductivity for SCoN is shown in Figure 4.11. Here the activation energies are calculated using equation 4.3.

$$\sigma = \sigma_0 \exp \left[ - \frac{E_a}{k_B T} \right] \quad (4.3)$$

Where,  $\sigma$  is the conductivity,  $\sigma_0$  is the exponential component,  $E_a$  is the activation energy,  $k_B$  is the Boltzmann constant and  $T$  is the temperature. The experimental data of  $\sigma_g$  and  $\sigma_{gb}$  were fitted with equation 4.1 and a linear nature is obtained. The activation energy is calculated from the slope and is tabulated in Table 4.3.

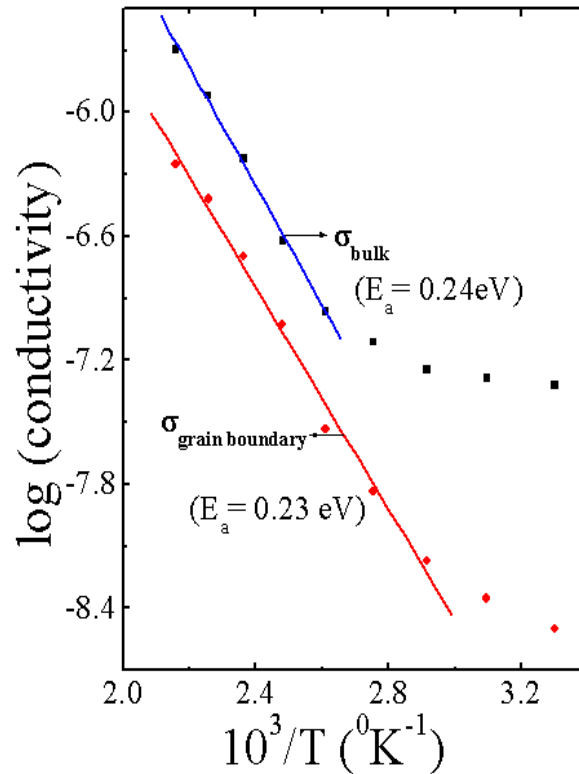


**Figure 4.11** Variation of frequency independent conductivity due to grain (bulk) and grain boundary effects as a function of temperature for SCoN sample.

The graph indicates that the changes in grain boundary resistance at elevated temperatures representing the role of grain boundaries in electrical conduction process of the material. The decrease in grain boundary resistance with rise in temperature may be due to the lowering of barrier favoring the increase of mobility of charge carriers that adds to the conduction process. The activation energy due to grain and grain boundary for SMN and SCoN is tabulated in Table 4.3. The conduction mechanism for grains and grain boundaries are different.

**Table 4.2** Variations of electrical parameters (bulk and grain boundary) as a function of temperature.

Composition	Temperature	( $R_g$ )	( $C_g$ )	( $R_{gb}$ )	( $C_{gb}$ )
<b>SMN</b>	30	398700	1.285E-11	1.80E7	6.80E-11
	50	393440	1.264E-11	1.53E7	6.54E-11
	70	388610	1.269E-11	1.43E7	6.74E-11
	90	377960	1.280E-11	1.24E7	7.11E-11
	110	361410	1.296E-11	1.00E7	7.64E-11
	130	334260	1.317E-11	6.94E6	8.30E-11
	150	296720	1.345E-11	4.10E6	9.16E-11
	170	255610	1.384E-11	2.38E6	1.02E-10
	190	215230	1.437E-11	1.48E6	1.15E-10
<b>SCoN</b>	30	250000	3.97E-11	3.78E6	1.85E-10
	50	230000	4.97E-11	2.68E6	2.50E-10
	70	210000	5.97E-11	1.76E6	2.90E-10
	90	154590	6.97E-11	816300	4.11E-10
	110	109960	7.97E-11	406300	4.91E-10
	130	49900	8.37E-11	126300	3.91E-10
	150	19900	9.17E-11	59300	3.11E-10
	170	9900	9.97E-11	31300	3.00E-10
	190	5900	1.01E-10	21300	2.98E-10

Table 4.3 Calculated Activation energies from different formalisms.

<i>Composition</i>	<i>Activation energies <math>E_a</math> (<math>\sigma_g</math>)</i>	<i>Activation energies <math>E_a</math> (<math>\sigma_{gb}</math>)</i>	<i>Activation energies <math>E_a</math> (<math>Z''</math>)</i>	<i>Activation energies <math>E_a</math> (<math>M''</math>)</i>
<b>SMN</b>	0.12eV	0.20eV	0.19eV	0.17eV
<b>SCoN</b>	0.24eV	0.23eV	0.20eV	0.22eV

Table 4.4 Conductivity values for grain and grain boundary calculated from Table 4.2

<b>Composition</b>	<b>Temp</b>	<b>Dc (<math>\sigma_g</math>)</b>	<b>Dc (<math>\sigma_{gb}</math>)</b>	<b>Composition</b>	<b>Dc (<math>\sigma_g</math>)</b>	<b>Dc (<math>\sigma_{gb}</math>)</b>
<b>SMN</b>	30	4.75E-8	1.05E-9	<b>SCoN</b>	4.75E-8	3.14E-9
	50	4.81 E-8	1.23 E-9		5.17 E-8	4.43 E-9
	70	4.87 E-8	1.32 E-9		5.66 E-8	6.76 E-9
	90	5.01 E-8	1.52 E-9		7.69 E-8	1.45 E-8
	110	5.24 E-8	1.89 E-9		1.08 E-7	2.92 E-8
	130	5.66 E-8	2.72 E-9		2.38 E-7	9.42 E-8
	150	6.38 E-8	4.61 E-9		5.97 E-7	2.00 E-7
	170	7.40 E-8	7.95 E-9		1.20 E-6	3.80 E-7
	190	8.79 E-8	1.27 E-8		2.01 E-6	5.58 E-7



#### 4.2.6 Modulus Spectroscopy Analysis

The electric modulus formalism is expressed as

$$Z^*(\omega) = Z' - jZ'' \quad (4.4)$$

$$M^*(\omega) = M'(\omega) + jM''(\omega) \quad (4.5)$$

$$M^*(\omega) = j\omega C_0 Z^*(\omega) \quad (4.6)$$

From Equation (4.4), (4.5) and Equation (4.6) one can get the following Equations (4.7) and (4.8)

$$M' = \omega C_0 Z'' \quad (4.7)$$

$$M'' = \omega C_0 Z' \quad (4.8)$$

where  $C_0$  is given by  $C_0 = \epsilon_0 A/L$ ,  $L$  is the thickness, and  $A$  is the area of the sample,  $\epsilon_0 = 8.854 \times 10^{-14} \text{ F/cm}$  is the permittivity of the free space. The modulus analysis has an advantage that it suppresses the information about electrode effects [25-28]. This can also be used to study the conductivity relaxation times [28, 29]. The complex modulus is defined as inverse of the complex permittivity and in the present work, the impedance data were converted into electrical modulus using the above equations (4.4-4.8).

Figure 4.12 (a) and (b) shows the real and imaginary part of electrical modulus for [SMN], [SCoN] as a function of frequency at different temperatures, respectively. At lower frequencies,  $M'$  tends to be very small, confirming that the contribution from the electrode effect is negligible and hence can be ignored when the data are analysed in modulus formalism [30]. The observed dispersion in  $M'$  at higher frequencies may be due to conductivity relaxation. It may be noted from Figure 4.12(a) and (b) that the position of the peak  $M''_{max}$  shifts to higher frequencies as the temperature is increased. The asymmetric broadening of the peak indicates the spread of relaxation with different time constant, and relaxation in the material is of non-Debye

type. The frequency region below peak maximum  $M''$  determines the range in which charge carriers are mobile on long distances. At frequency above peak maximum  $M''$ , the carriers are confined to potential wells, being mobile on short distances. The frequency  $\omega_m$  (corresponding to  $M''_{max}$ ) gives the most probable relaxation time  $\tau_m$ . Each peak attains a maximum value  $M''_{max}$  at frequency  $\omega_{max}$  called conductivity relaxation frequency and it obeys the Arrhenius relation.

The most probable relaxation time follows the Arrhenius law, given by

$$\omega_m = \omega_0 \exp \left( \frac{-E_a}{K_B T} \right) \quad (4.9)$$

Where  $\omega_0$  is the pre-exponential factor and  $E_a$  is the activation energy. Figure 4.12 (a) and 4.12 (b) inset shows a plot of the  $\log \omega_m$  versus  $1000/T(K^{-1})$ , where the circles are the experimental data and the solid line is the least-squares straight-line fit. The activation energy  $E_a$  calculated from the least-squares fit to the points. From Figure 4.12 (a) and (b) it can be seen that the activation energy calculated from Arrhenius relation  $E_a = 0.17\text{eV}$  [SMN] and  $0.22\text{eV}$  [SCoN] for relaxation of  $M''$  is found to be close to the activation energy  $E_a = 0.19\text{eV}$  [SMN] and  $0.20\text{eV}$  [SCoN] for  $Z''$ . Figure 4.12 (c) shows the plots of SCoN sample. It is observed from the figure that resonance peak show dispersion on the lower frequency side of the peak but merges in to one on higher frequency side.

Figure 4.13 (a) [SMN] and (b) [SCoN] shows the Scaling plot of  $M''/M''_{max}$  versus  $\log(\omega/\omega_{max})$  and at various temperatures. We have scaled each  $M''$  by  $M''_{max}$  and each frequency by  $\omega_{max}$  for different temperatures in Figure 4.13 (a) and (b). The coincidence of all curves/peaks at different temperatures exhibits temperature independent behavior of the dynamic processes [31] occurring in the material. This might be due to the ion migration that takes place via hopping mechanism for Figure 4.13(a) [SMN]. While for the case Figure 4.13 (b) [SCoN] the plots shows that  $\omega_{max}$  shifts towards higher frequencies with increasing temperature. This suggests that conductivity relaxation mechanisms occurring at different frequencies exhibit different thermal energy and the dynamical processes are temperature dependent. This is mainly due to the existence of Polar Regions around this temperature range, where the system shows Diffuse Phase transition (DPT) in the dielectric response in case of [SCoN].

Going further in the description of experimental data, the variation of normalized parameters  $M''/M''_{max}$  and  $Z''/Z''_{max}$  as a function of logarithmic frequency measured at  $190^\circ\text{C}$  for

[SMN] and 150°C for [SCoN] are shown in Figure 4.14 (a) and (b). Comparison of impedance and electrical modulus data allows the determination of the bulk response in terms of localized (i.e. defect relaxation) or non-localized conduction (i.e. ionic or electronic conductivity) [32]. The Debye model is related to an ideal frequency response of localized relaxation. In reality the non-localized process is dominated at low frequencies. In the absence of interfacial effects, the non-localized conductivity is known as the dc conductivity. Thus, the high dielectric loss,  $\tan\delta$ , is usually accompanied by rising  $\epsilon'(\omega)$  at low frequencies. It is possible to determine the type of dielectric response. It involves inspecting the magnitude of overlap between peaks of parameters  $Z''(\omega)$  and  $M''(\omega)$ [32]. The overlapping of peak positions of  $M''/M''_{max}$  and  $Z''/Z''_{max}$  curves gives an evidence of delocalized or long-range relaxation [32]. However, for the present system the  $M''/M''_{max}$  and  $Z''/Z''_{max}$  peaks do overlap but in very narrow region suggesting contributions of both long-range as well as localized relaxation exits. In order to mobilize the localized electron, the aid of lattice oscillation is required. In these circumstances electrons are considered not to move by them but by hopping motion activated by lattice oscillation. In addition, the magnitude of the activation energy suggests that the carrier transport is due to the hopping conduction.

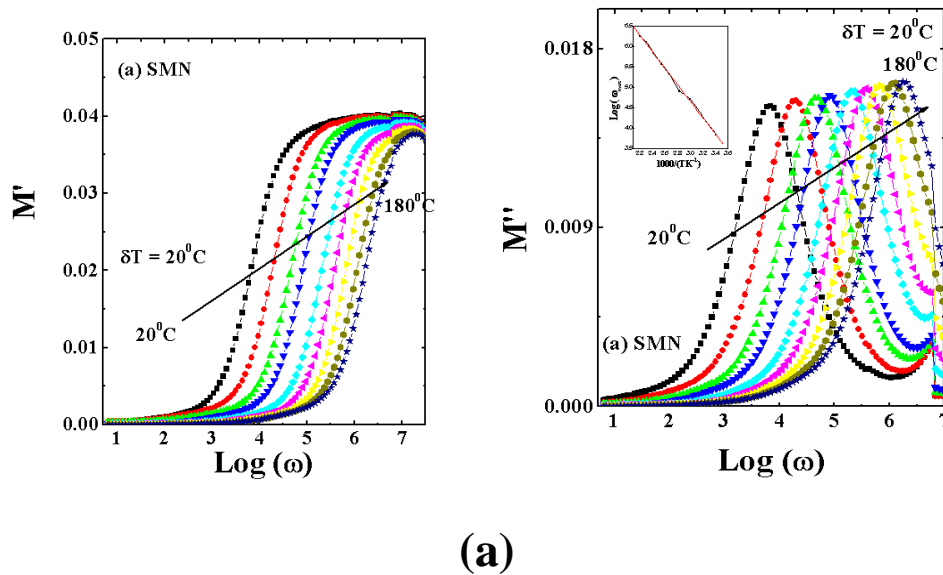
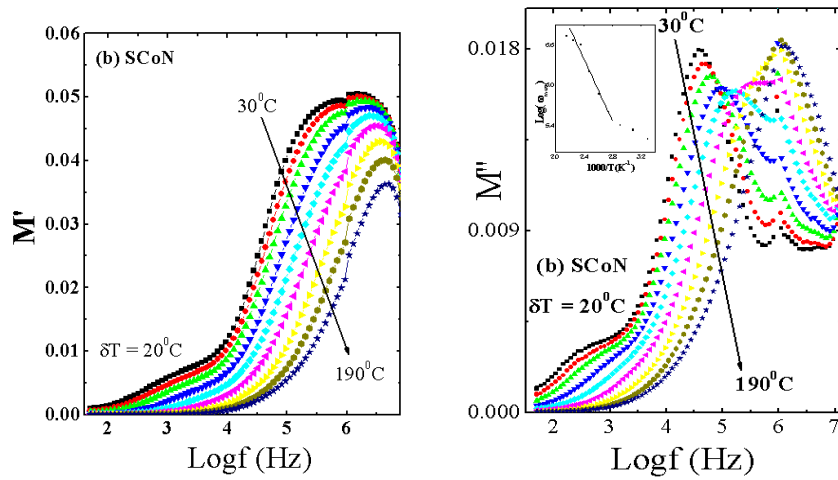
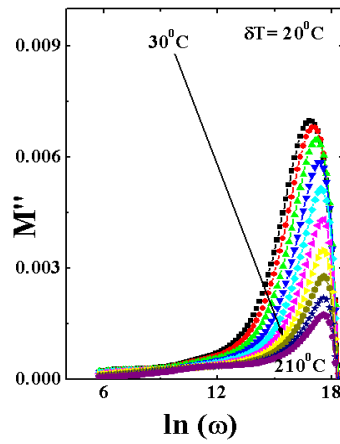


Figure 4.12 (a) Variation of real part of modulus, and imaginary part of modulus of SMN with different frequency at different temperatures and (inset) is the Arrhenius plot of  $\log \omega_{max}$  with inverse temperature.



(b)

Figure 4.12 (b) Variation of real part of modulus, and imaginary part of modulus of SCoN with different frequency at different temperatures and (inset) is the Arrhenius plot of  $\log \omega_{max}$  with inverse temperature.



(c)

Figure 4.12 (c) Variation of imaginary part of modulus of SCoN with different frequency at different temperatures.

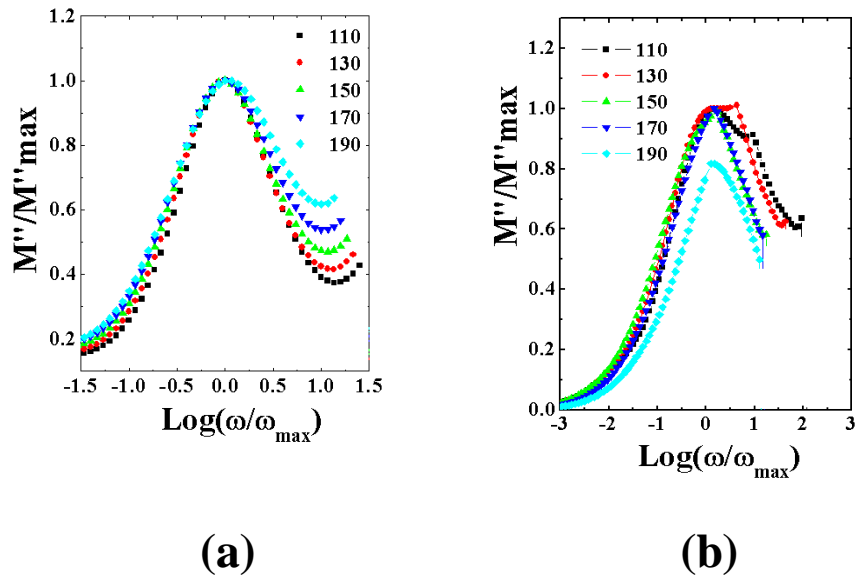


Figure 4.13 (a) Scaling behaviour of  $M''_{\max}$  at various temperatures for [SMN]  
 (b) Scaling behaviour of  $M''_{\max}$  at various temperatures for [SCon]

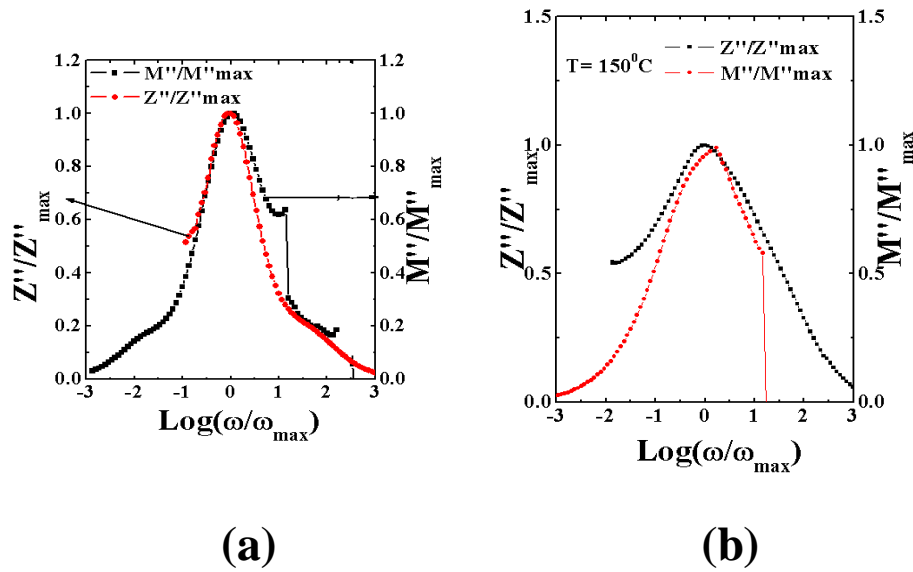


Figure 4.14 (a) Frequency dependence of normalized peaks,  $Z''/Z''_{\max}$  and  $M''/M''_{\max}$  for SMN ceramic at 190 °C

Figure 4.14 (b) Frequency dependence of normalized peaks,  $Z''/Z''_{\max}$  and  $M''/M''_{\max}$  for SCon ceramic at 150 °C

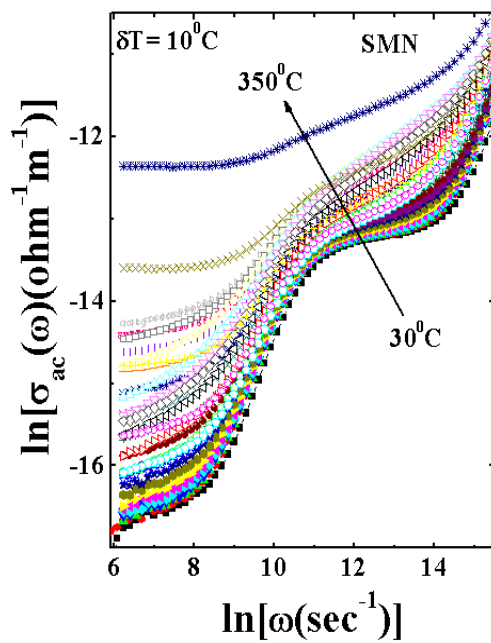
### 4.2.7 Conductivity Studies

#### 4.2.7.1 Frequency dependent conductivity

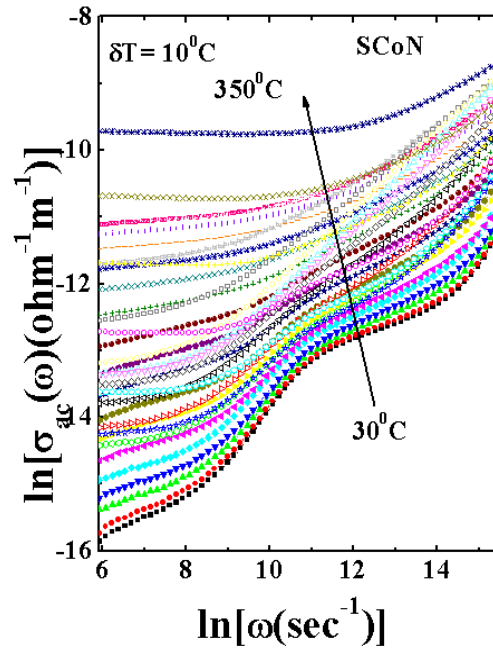
Figure 4.15 shows the variation of the conductivity with frequency at different temperatures. The ac conductivity in most of the previous studied on iso-morphous perovskite materials [33-36] and by A.R Long and R S Eliot [37,38], found to follow a universal power law

$$\sigma_{ac} = A(T)\omega^{s(T)} \quad (4.10)$$

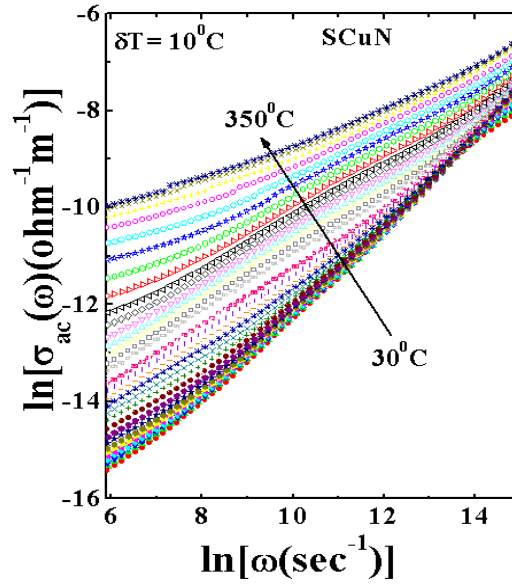
where  $0 < s < 1$ . The relation between  $\sigma$  and  $\omega$  is usually fall linear in the double-logarithmic presentation, and the slopes of the lines, varying with temperature, are related to the conduction mechanism [38].



(a)



(b)



(c)

**Figure 4.15** The frequency response of the conductivity for (a) SMN, (b) SCoN, and (c) SCoN at different temperatures ranges from 30°C to 350°C with an interval of 10°C.

It is clear from the Figure 4.15 that the results do not follow the simple power law relation given by (4.15). The low frequency ac conductivity (region I) is characterized by a linear response with nearly equal slopes at different temperatures. The onset of the characteristic dispersion (region II), at the high frequency end of region I shifts towards higher frequencies with increasing temperature.

The values of the  $s$  parameter are obtained using the derivative equation:

$$s = \frac{d \ln \sigma}{d \ln \omega} \quad (4.11)$$

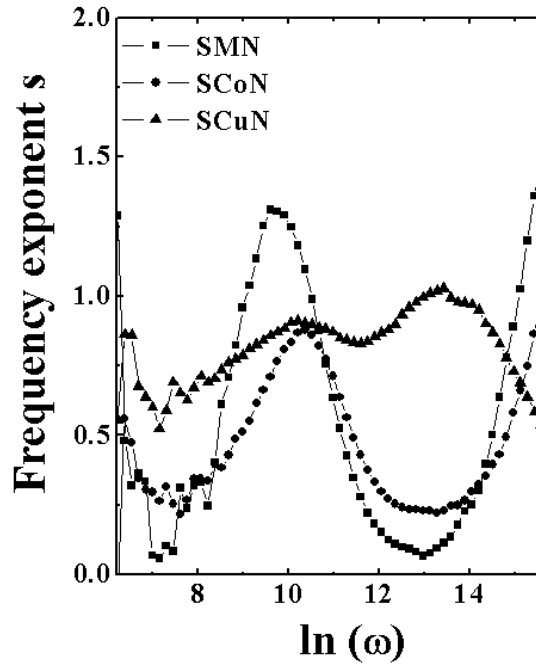


**Figure 4.16** The room temperature values of the frequency exponent  $s$  as a function of the frequency, obtained using the derivative curves.

Figure 4.16 shows the frequency dependence of the  $s$  parameter at room temperature. As pointed we observe a peak in  $s$  versus  $\ln\omega$  curve (Figure 4.16). At low frequencies we observe non-zero values of the  $s$  parameter for SMN, SCoN, SCuN samples. In mid-frequency region, the  $s$  parameter increases rapidly and after showing a peak, it becomes nearly linear at higher frequencies. The observed nature of  $s$  in various frequency regions can be explained using the JRM of Funke [39], who successfully used it to explain the hopping of ions. The slopes of the  $\ln\sigma - \ln\omega$  plots in the dispersion region II are strongly temperature dependent. In the jump relaxation model (JRM), introduced by Funke, during ionic conduction in solids there is a high probability for a jumping ion to have unsuccessful hop. However, if the neighborhood becomes relaxed with respect to the ion's position, the ion stays in the new site. The conductivity in the low frequency region is associated with successful hops. But beyond the low frequency region many hops are unsuccessful and its probability increases as the frequency increases. The change in the ratio of successful to unsuccessful hops results in the dispersive conductivity. The JRM suggests that different activation energies are associated with unsuccessful and successful



hopping processes. Applying the JRM to the frequency response of the conductivity for the present material, it was possible to fit the data to a double power law:

$$\sigma_{ac} = A1 (T) \omega^{s1(T)} + A2 (T) \omega^{s2(T)} \quad (4.12)$$

where  $s < 1$  corresponds to the translational hopping motion. Similar nature was also observed in 1:1 system by our group [40].

#### 4.2.7.2 Temperature dependent conductivity

The temperature dependence of the  $s$  parameter for the critical mid-frequency region is shown in Figure 4.17. The values of  $s$  obtained from the slopes of the  $\ln\sigma - \ln\omega$  plots (Figure 4.15) are plotted as a function of temperature in Figure 4.17.

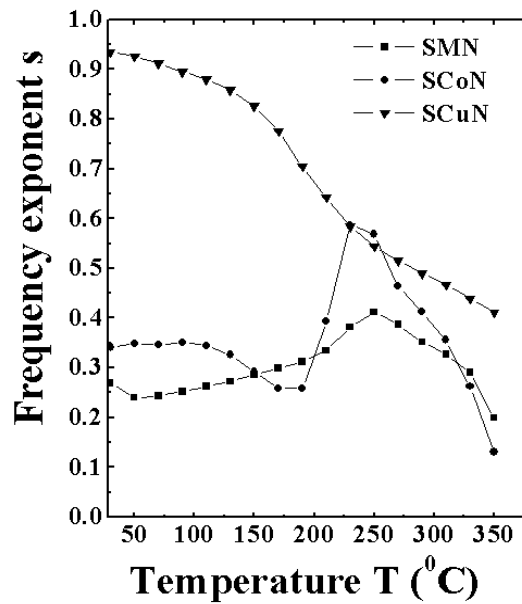


Figure 4.17 The peak values of the frequency exponent  $s$  vs. the absolute temperature  $T$ .

It shows a nonlinear nature of the frequency exponent with temperature. According to the correlated barrier hopping (CBH) model [38, 41], the parameter  $s$  has the form:

$$s = 1 - \frac{6kT}{[W_M - kT \ln(1 / \omega \tau_0)]} \quad (4.13)$$

Here,  $W_M$  is the energy required to cross the barrier height. The model predicts downward nature of  $s$  parameter for small values of  $W_M/kT$ . On the other hand, the increasing nature of  $s$  at high temperatures can be explained using the small polaron tunnelling (SPT) [38, 41] model given by:

$$s = 1 - \frac{4}{\ln(1 / \omega \tau_0) - W_H / kT} \quad (4.14)$$

Here,  $W_H$  is the activation energy required for polaron transfer. Small polarons are generally assumed to be so localized that their distortion clouds do not overlap. Therefore, the ac conductivity only in the high temperature limit is expected to be due to tunnelling of randomly distributed carriers trapped at structural defects [38]. Now for our SCuN and SMN samples nearly identical downward variation of the frequency exponent  $s$  indicates that the conduction process is predominantly due to the correlated barrier hopping (CBH) of electrons. In the SCoN, up to 180 deg, CBH mechanism is dominating, but above (180-240) deg temperature, due to disruption of long-range lattice disorder, the contribution of localized electron induced small polaron tunnelling appears to be involved in the conduction process.

#### 4.2.8 UV-Vis Spectroscopy Analysis

Figure 4.18 (a-c) shows the UV-vis absorption spectra of [SMN], [SCoN], [SCuN]. The optical band gap energy ( $E_{gap}$ ) was estimated by the method proposed by [42]. According to the author optical band gap is associated with the absorbance and photon energy by the following equation:

$$h\nu \propto (h\nu - E_{gap})^n \quad (4.15)$$

(where  $\alpha$  is the absorbance,  $h$  is the Planck constant,  $\nu$  is the frequency,  $E_{gap}$  is the optical band gap and  $n$  is a constant associated to the different types of electronic transitions ( $n = 0.5, 2, 1.5$  or  $3$  for direct allowed, indirect allowed, direct forbidden and indirect forbidden transitions, respectively). Thus, the  $E_{gap}$  values of [SMN], [SCoN], [SCuN] were evaluated extrapolating the linear portion of the curve or tail. In our work, the UV-vis absorbance spectra indicated an indirect allowed transition and, therefore, the value of  $n = 2$  is used in equation 4.15.

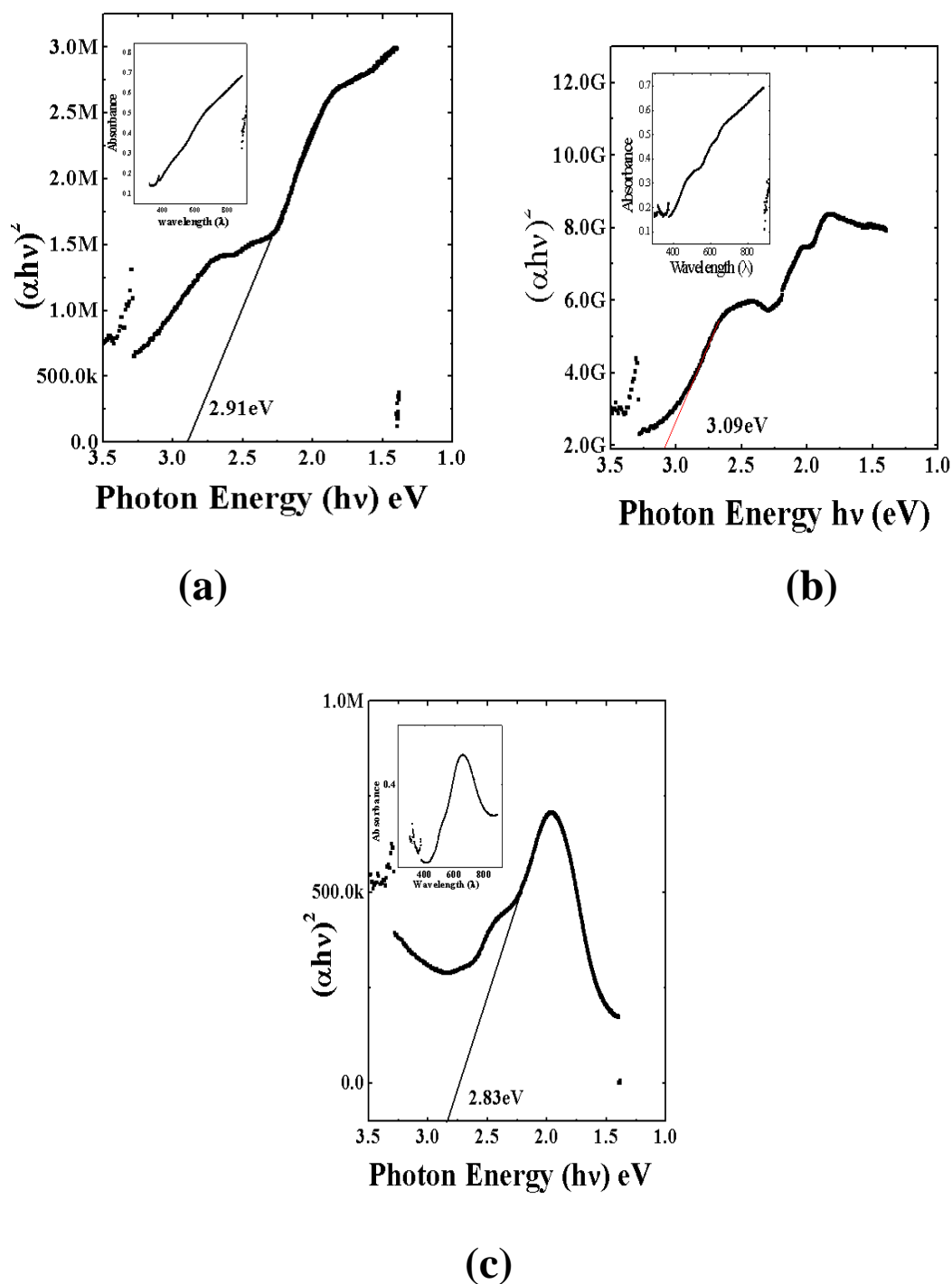


Figure 4.18 (a-c) UV- Vis Absorption Spectra of (a) SMN, (b) SCoN, (c) SCuN samples

The indirect band gap values are tabulated in table 4.5. The literature [43] describes that the band gap energy is indirect when the electronic transitions occur from maximum-energy states located

near or in the valence band (VB) to minimum-energy states below or in the conduction band (CB), but of different regions in the Brillouin zone. The distinct  $E_{gap}$  calculated from the UV-vis absorption spectra indicates the existence of intermediary energy levels within the optical band gap (Figure 4.18(a-c)). This is due to the fact that observed excitation energy ( $\lambda = 350 \text{ nm}$  or  $3.54 \text{ eV}$ ) for all ceramic powders is higher than our  $E_{gap}$ . The highest Band Gap  $E_{gap}$  value was verified for the SCoN compositions.

**Table 4.5 The Indirect band Gap values of SMN, SCoN and SCuN**

Composition	Band Gap
SMN	2.91eV
ScoN	3.09eV
ScuN	2.83eV

### 4.3 Conclusions

In summary, we have successfully synthesized polycrystalline bulk samples of  $\text{Sr}(\text{B}'_{0.33}\text{Nb}_{0.67})\text{O}_3$  where  $\text{B}' = (\text{Mg}^{2+}, \text{Co}^{2+}, \text{Cu}^{2+})$  [SMN], [SCoN], [SCuN] by standard solid state reaction technique. The effect of replacement of B'-site in  $\text{Sr}(\text{B}'_{0.33}\text{Nb}_{0.67})\text{O}_3$  was studied by means of structural, micro structural, electrical, Conductivity and Optical studies. The following observations have been made on the basis of above analysis performed on the bulk samples;

- (i) The XRD analysis of  $\text{Sr}(\text{B}'_{0.33}\text{Nb}_{0.67})\text{O}_3$ , where  $\text{B}' = (\text{Mg}^{2+}, \text{Co}^{2+}, \text{Cu}^{2+})$  [SMN], [SCoN], [SCuN], indicates that all samples exhibit a single phase nature. The [SMN] and [SCoN] exhibit monoclinic symmetry where as on replacement of Cobalt by Copper which have  $3d^9$  configurations shifting the structure to the higher symmetry side i.e tetragonal side. Decrease in structural asymmetry has led to the observed enhancement in dielectric constant  $\epsilon'$  values and decrease in dielectric loss ( $\tan\delta$ ) values.
- (ii) The dispersion behavior observed in dielectric constant as a function of frequency has been explained according to interfacial polarization as predicted by the Maxwell-Wagner and Koop's phenomenological theory. As we move from monoclinic to tetragonal side it

drastically enhances the unit cell dimension leading to correlated enhancement in dielectric constant  $\epsilon'$  and lower losses Dielectric loss  $\tan \delta$  is very low in case of SCuN sample as compared to SCoN and SMN. It is likely to be due to the Strong Jahn- Teller Distortion in SCuN as compared to SCoN.

- (iii) The dielectric constant is highest in SCuN samples about 80K while that for SCoN and SMN is 6K and 600 only. This shows that this effect is strongly related to the Jahn Teller distortion of Cobalt and Copper based compositions. In case of SCoN where  $\text{Co}^{2+}$  is in  $3d^7$  electronic configurations and  $\text{Cu}^{2+}$  is in  $3d^9$  configurations. We observe strong distortion in case of SCuN sample. This distortion has led to very enhancing properties (dielectric const and lower losses).
- (iv) The Cole- Cole analysis of the SMN, SCoN and SCuN gave the non-zero values of alpha ( $\alpha$ ) parameter suggesting that the compositions are poly-dispersive in nature.
- (v) The activation energies using the Arrhenius relations and co-related it with the impedance analysis and found that the activation are in close appromixation to the impedance data. Further the scaling of electric modulus  $M''/M''_{max}$  vs  $\text{Log} (\omega/\omega_{max})$  shows that coincidence of all curves/peaks at different temperatures exhibits temperature independent behavior of the dynamic processes. This further suggests that conductivity relaxation mechanisms occurring at different frequencies exhibit different thermal energy and the dynamical processes are temperature dependent. This is mainly due to the existence of Polar Regions within this temperature range, where the system shows Diffuse Phase transition (DPT) in the dielectric response particularly in the case of [SCoN].
- (vi) The observed nature of  $s$  in various frequency regions can be explained using the JRM of Funke [39]. SCuN and SMN samples nearly identical downward variation of the frequency exponent  $s$  indicates that the conduction process is predominantly due to the correlated barrier hopping (CBH) of electrons. But in the SCoN, up to 180 deg temperature, CBH mechanism is dominating, but above (180-240) deg temperature, due to disruption of long-range lattice disorder the contribution of localized electron induced small polaron tunnelling appears to be involved in the conduction process.
- (vii) Thus above Niobate system possessing wide semi- conducting band gap region and due to observed conductivity mechanism based switching behavior, SCoN can be a candidate for sensor, optoelectronic, and electrical switching device applications.

## References

- [1] B Angadi, P Victor, V.M. Jali, M. T. Lagare, Ravi Kumar, S. B. Krupanidhi, *Mat. Science Engg.* **B100**, 93, 2003.
- [2] J.T. Evans, R. Womak, *IEEE J. Solid-State Circuits* **23**, 1171, 1988.
- [3] G.A.C.M. Spierings, M.J.E. Ulenaers, G.L.M. Kampschoer, H.A.M. van hal, P. K. Larsen, *J.Appl. Phys.***70**, 2290, 1991.
- [4] K. Amanuma, T. Hase, Y. Miyasaka, *Appl. Phys. Le* **t66**, 221, 1995.
- [5] X. H. Liu, Q. Z. Tian, H.Wang, T. H. Yu, and X. S. Ouyang *J. Mat. Sci.* **39**, 4319, 2004.
- [6] M. S. Gupta, E. Furman, E. Colla, Z. Xu, and D. Viehland, *J. App. Phys.* **88**, 2836, 2000.
- [7] W. C. Ahn, J. H. Jang, S. Nahm, M. H. Park, and J. H. Lee *J. Eur. Cer. Soc.* **23**, 2473, 2003.
- [8] J. H. Lee, M. H. Park, C. K. Yang, and S. W. Yong, *J. Am. Cer. Soc.* **84**, 3032, 2001.
- [9] S. C. Park, H. J. Paik, S. Nahm, J. H. Lee, M. H. Park, and Y. K. Kim, *J. Mat. Sci. Letters* **18**, 691, 1999.
- [10] I. M. Reaney, *American Ceram. Soc. Meeting AMA* 1-B-01 2002.
- [11] Dong Cheng, Powder, X, Window-95 program for powder x-ray diffraction data processing, *J. Appl. Cryst.* **32**, 838, 1999.
- [12] C S Park, H J Paik, S Nahm, H J Lee, H M Park, Y K Kim *J Mat Sci letters*; **18**, 691, 1999.
- [13] R D Shannon and T C Prewitt *Acta Crystallographica.* **B25**, 925, 1969.
- [14] K Sambasiva Rao, S P Jagga Rao, K Rama Rao,V A Rao Prasada. A I Robin, R P Tandon, *Ferroelectrics Letters*; **16**, 195, 1993.
- [15] J Maxwell, *Electricity and Magnetics* (Vol.1, Section 328, Oxford University Press, London) (1873).
- [16] C. Koops. *Phys. Rev.* **83**, 121, 1951.
- [17] J Smit H Wijn *Ferrites*, Wiley, New York, 369, 1959.
- [18] Cao Wanqiang, Junwen Xiong and Juanpin Sun, *Materials Chemistry and Physics*, **106** (2-3), 338, 2007.
- [19] Yu N Venevtsev, *Mat. Res. Bull*, **6**, 1085, 1971.
- [20] I S Zheludev, *Physics of Crystalline Dielectrics. vol 1: crystallography spontaneous polarization.* New York: Plenum Press; 1971.

- 
- [21] X M Chen, D Liu, Z R Ho, X Hu, and X Q Liu, *J. Am. Cer. Soc.* **87**, 2208, 2004.
- [22] A Dixit, S B Majumder, R S Katiyar, A S Bhalla, *Appl. Phys. Lett.* **82**, 2679, 2003.
- [23] T Maiti, R Guo, A S Bhalla, *Appl. Phys. Lett.* **90**, 182901, 2007.
- [24] K Uchino, and S. Nomura, *Ferroelectrics Lett. Sect.* **44**, 55, 1982.
- [25] I M Hodge, M D Ingram and A R West, *J. Electroanal. Chem* **74**, 125, 1976.
- [26] K C Sobha, and K Rao. *J. Solid State Ionics*, **81**, 145, 1995.
- [27] M Ganguli, H M Bhat and K Rao *J. Phys. Chem. Glasses*, **40**, 297, 1999.
- [28] S Lanfredi, S P Saia, R Lebullenger and A C Hernandez. *Solid State Ionics*, **146**, 329, 2002.
- [29] S Ghosh, and A Ghosh. *Solid State Ionics*, **149**, 67, 2002.
- [30] S F Howell, A R Bose, B P Macedo and T C Moynihan, *J. Phys. Chem*, **78**, 639, 1974.
- [31] S Saha, T P Sinha, *Phys. Rev.* **B65**, 134103, 2002.
- [32] R Gerhardt. *J. Phys. Chem. Solids* **55**, 1491, 1994.
- [33] M. F. Mostafa, M. El Nimer, and F. Richa, *Phys. Scr.* **43**, 541 1991.
- [34] M. F. Mostafa, A. S. Atallah, and M. Elessawi, *Phase Transitions* **64**, 215, 1998.
- [35] M. F. Mostafa and A. S. Atallah, *Phys. Lett.* **A264**, 242, 1999.
- [36] M. F. Mostafa, M. M. Abdel-Kadar, A. S. Atallah, and M. El-Nimer, *Phys. Stat. Sol.* **135(a)**, 549, 1993.
- [37] A. R. Long, *Adv. Phys.* **31**, 553, 1982.
- [38] R. S. Elliot, *Adv. Phys.* **36**, 135, 1987.
- [39] K. Funke, *Prog. Solid St. Chem.* **22**, 111, 1993.
- [40] Devang D Shah, P. K. Mehta, M. S. Desai, C. J. Panchal *Jour of alloys and Compounds* **509**, 1800, 2011.
- [41] R. Gangopadhyay, A. De, S. Das, *J. Appl. Phys.* **87**, 2363, 2000.
- [42] D L Wood, J Tauc, *Phys Review* **B5**, 3144, 1972.
- [43] Cavalcante. L.S, Gurgel. M.F.C, Paris. E.C, Simoes. A.Z, Joya. M.R, Varela. J.A, Pizani. P.S, Longo. E, *Acta Materialia*, **55**, 6416, 2007.

## Chapter 5

### **Effect of replacement at B'-site by divalent ions in Barium Niobates and its impact on Structural, microstructure, dielectric and complex impedance, Conductivity properties.**

The chapter presents effect of replacement of  $\text{Mg}^{2+}$  by divalent ions from transition elements ( $\text{Co}^{2+}, \text{Cu}^{2+}$ ) in  $\text{Ba}(\text{Mg}_{0.33}\text{Nb}_{0.67})\text{O}_3$ . Impacts on Structural, micro-structure, dielectric, complex impedance and Conductivity properties are analyzed here. The present study is carried out in order to understand the ion size effect at the B-site as well as possible Jahn Teller effect on structure and dielectric properties. We observed that substitution effect is negative on Barium Niobates unlike positive effect observed in Strontium Niobates (chapter-4).



## 5.1 Introduction

Complex perovskite oxides based on  $\text{Ba}(\text{B}'_{1/3}\text{B}''_{2/3})\text{O}_3$  ( $\text{B}' = \text{Zn, Co, Ni and Mg}$ ;  $\text{B}'' = \text{Ta and Nb}$ ) are suitable materials for dielectric resonator (DR) applications due to their high dielectric constant, high quality factor, and temperature stability of the resonant frequency [1–4]. Recently, due to the high cost of  $\text{Ta}_2\text{O}_5$ , niobium based complex perovskites have attracted considerable attention. For example, BCoN has a relative permittivity of 32, a quality factor ( $Q \times f$ ) greater than 50,000 GHz and negative temperature coefficient of resonant frequency ( $\tau_f$ ) which can be adjusted to zero by Zn substitution [5–8]. BCN crystallizes in either a disordered cubic structure or in an ordered hexagonal structure. Ordered structure results from 1:2 ordering of  $\text{B}'$  and  $\text{B}''$  cations along the  $\langle 111 \rangle$  directions of a cubic unit cell. It is well established that B-site cation ordering in complex perovskites has a significant influence on the dielectric losses at microwave frequencies [9, 10]. Stoichiometry of the B-site may also affect the rate of 1:2 ordering. Twenty years ago, Desu and O'Bryan [11] made the first attempt to correlate the excellent microwave quality factor of  $\text{Ba}(\text{Zn}_{1/3}\text{Ta}_{2/3})\text{O}_3$  (BZT) with B-site cation stoichiometry. In the related materials,  $\text{Ba}(\text{Mg}_{1/3}\text{Nb}_{2/3})\text{O}_3$ , Paik et al. [12] found that Mg deficiency had a significant effect on the microwave dielectric properties. They reported an improvement in both density and the dielectric  $Q$  value when  $x = 0.02$  in  $\text{Ba}(\text{Mg}_{1/3-x}\text{Nb}_{2/3})\text{O}_3$ . The densification was explained in terms of enhanced grain boundary mass transport because of the formation of additional lattice defects. Lu and Tsai [13] examined the effect of Ba-deficiency in the analogous  $\text{Ba}(\text{Mg}_{1/3}\text{Ta}_{2/3})\text{O}_3$  (BMT) ceramics and found an improvement in the degree of 1:2 order, sinterability and microwave dielectric properties.

In this chapter, we report the effect of replacing the  $\text{B}'$ -site ions in the  $\text{Ba}(\text{B}'_{1/3}\text{Nb}_{2/3})\text{O}_3$  by different divalent atoms such as Mg, Co and Cu. These compounds are analysed on the basis of their crystal structure, microstructure, dielectric, as well as ac conductivity behaviour. We have prepared the above Barium series by standard solid state reaction technique. The final compositions are  $\text{Ba}(\text{Mg}_{1/3}\text{Nb}_{2/3})\text{O}_3$  [BMN],  $\text{Ba}(\text{Co}_{1/3}\text{Nb}_{2/3})\text{O}_3$ , [BCoN],  $\text{Ba}(\text{Cu}_{1/3}\text{Nb}_{2/3})\text{O}_3$  [BCuN]. Here we have discussed the effect of total replacement of  $\text{B}'$ -site, where  $\text{B}' = (\text{Mg}^{2+}, \text{Co}^{2+}, \text{Cu}^{2+})$  on structural, micro structural, dielectric properties, complex impedance, conductivity properties.

## 5.2 Results and Discussions

### 5.2.1 X-ray Diffraction (XRD) Measurements

Figure 5.1 shows the XRD patterns of  $\text{Ba}(\text{Mg}_{1/3}\text{Nb}_{2/3})\text{O}_3$  [BMN],  $\text{Ba}(\text{Co}_{1/3}\text{Nb}_{2/3})\text{O}_3$  [BCoN],  $\text{Ba}(\text{Cu}_{1/3}\text{Nb}_{2/3})\text{O}_3$  [BCuN] compounds. The measurements were carried out at room temperature with  $\text{Cu-K}\alpha$  radiation using high resolution Shimadzu X-ray diffractometer 6000 with ( $\lambda = 1.5402 \text{ \AA}$ ). The diffraction patterns were recorded from  $2\theta = 10^\circ$  to  $110^\circ$  with a step of  $0.02^\circ$ . The X-ray diffraction pattern was analyzed by using Powder X program [14]. From the analysis, it is observed that all the samples exhibit a single phase nature with structural transformation from hexagonal [BMN], [BCoN] to tetragonal [BCuN]. The calculated lattice parameters along with respective structures are listed in Table 5.1.

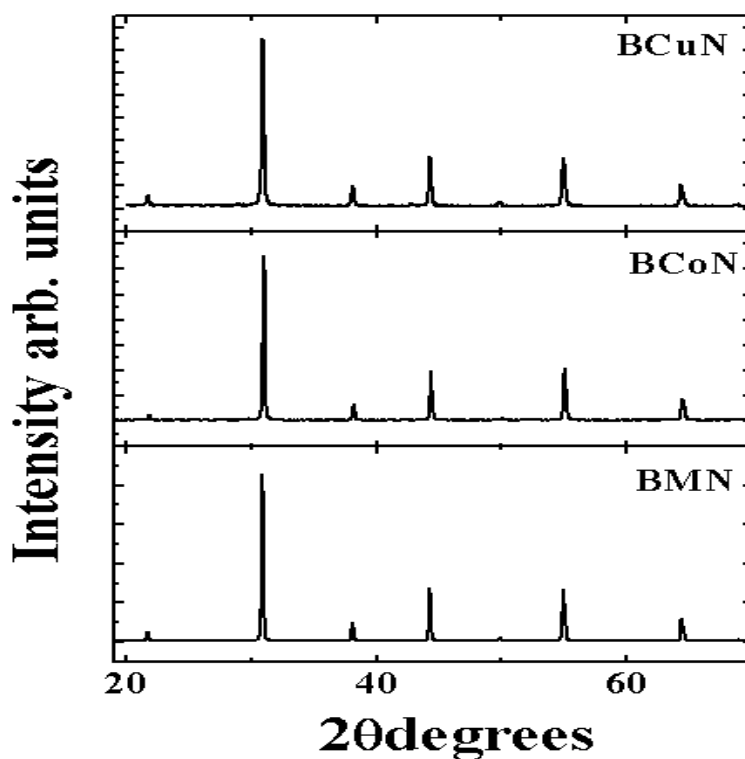


Figure 5.1 X-ray powder diffraction pattern of BMN, BCoN, BCuN samples.

**Table 5.1 Structure and lattice parameters for  $\text{Ba}(\text{B}'_{1/3}\text{Nb}_{2/3})\text{O}_3$  ( $\text{B}'=\text{Mg}^{2+}, \text{Co}^{2+}, \text{Cu}^{2+}$ ).**

Composition	Structure	Lattice Parameters
$\text{Ba}(\text{Mg}_{1/3}\text{Nb}_{2/3})\text{O}_3$ BMN	Hexagonal	$a=5.766 \text{ \AA}$ $b=5.766 \text{ \AA}$ $c=7.077 \text{ \AA}$
$\text{Ba}(\text{Co}_{1/3}\text{Nb}_{2/3})\text{O}_3$ BcoN	Hexagonal	$a=5.7737 \text{ \AA}$ $b=5.7737 \text{ \AA}$ $c=7.0852 \text{ \AA}$
$\text{Ba}(\text{Cu}_{1/3}\text{Nb}_{2/3})\text{O}_3$ BCuN	Tetragonal	$a=4.0464 \text{ \AA}$ $b=4.0464 \text{ \AA}$ $c=4.199 \text{ \AA}$

### 5.2.2 Scanning Electron Microscopy Analysis

In order to understand the morphology, grain size and shape of the B'-site variation in  $\text{Ba}(\text{B}'_{1/3}\text{Nb}_{2/3})\text{O}_3$ , SEM study has been carried out. The SEM micrographs were taken at 2500 magnification at different parts of the samples. The SEM images of all samples are shown in Figure. 5.2 (a-c). It is clear from the SEM micrograph that the micro-structure gets modified with different divalent ion substitution. It has been observed that in case of BMN we observed granular microstructure with average grain size is  $\sim 1\mu\text{m}$  [15] but it changes to elongated grain type structures in Cu substituted BCuN. It is to be noted that similar microstructure is also been observed in SCuN sample (Chapter-4). These rods like elongated grains are randomly oriented. Presence of Co at the B'-site resulted in agglomerated grains similar to SCoN case. Observed changes in crystal structure as well as microstructure in  $\text{Mg}^{2+}$ ,  $\text{Co}^{2+}$  or  $\text{Cu}^{2+}$  substituted barium niobates suggests the possibilities of changes in respective dielectric behaviour of Barium Series. We do observe that randomly oriented microstructure behaviour of BCuN does affect their dielectric properties like dielectric constant ( $\epsilon'$ ) and dielectric loss ( $\tan\delta$ ).

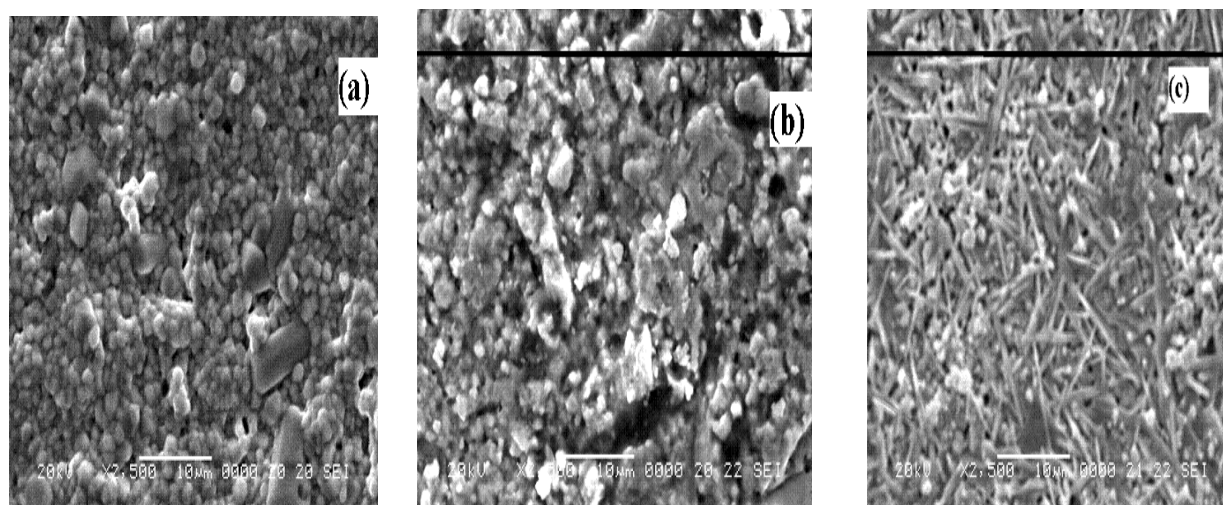


Figure 5.2 SEM Micrograph of (a) BMN (b) BCoN, (c) BCuN

### 5.2.3 Dielectric Measurement

#### 5.2.3.1 Frequency Dependence Dielectric Properties

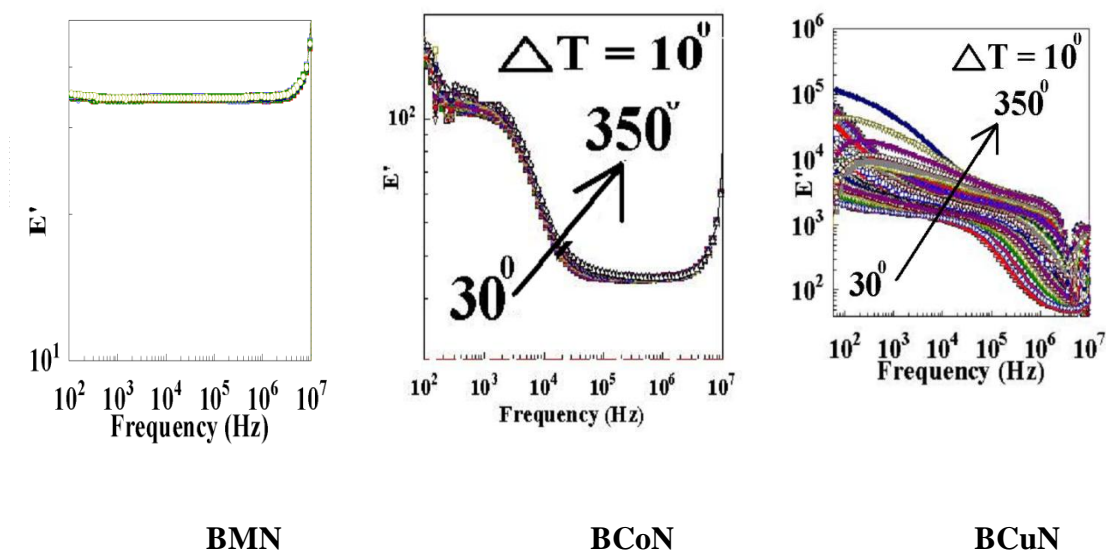
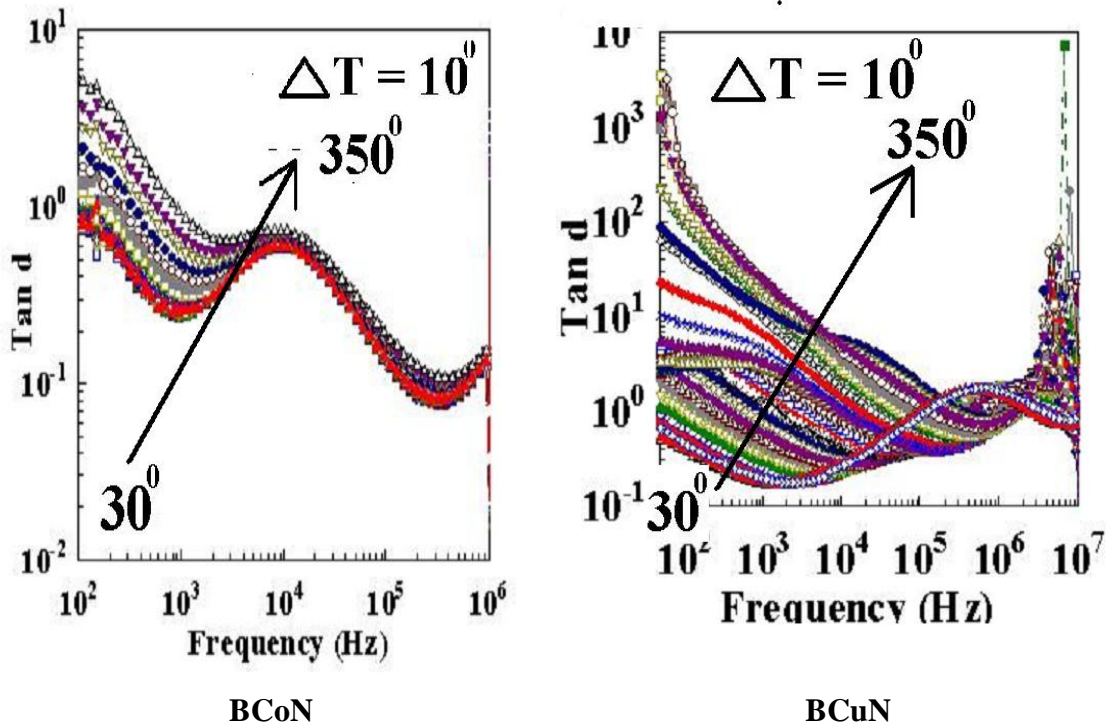


Figure 5.3 Dielectric Constant as a function of Frequency of BMN, BCoN, BCuN samples from (RT – 350°C)

Figure 5.3 shows the frequency dependence of relative real part of dielectric permittivity performed in the temperature range (room temperature to 350<sup>0</sup>C) except for BMN (room temperature – 160<sup>0</sup>C) and the frequencies range of 100Hz-3.2MHz for Ba(B'<sub>1/3</sub>Nb<sub>2/3</sub>)O<sub>3</sub> samples, where (B'= Mg<sup>2+</sup>, Co<sup>2+</sup>, Cu<sup>2+</sup>). It is observed that except BMN which is a polar dielectric material [15] all studied samples exhibit dispersion behaviour, i.e., the dielectric constant decreases with increase in the frequency. This is the general dielectric behaviour observed in most of the oxide materials, which can be explained with interfacial polarization predicted by the Maxwell-Wagner model [16] in agreement with Koop's phenomenological theory [17]. According to these models, the dielectric materials can be imagined as a heterogeneous structure consisting of well conducting grains separated by thin layer of poorly conducting substances (grain boundaries). These grain boundaries could be formed during the sintering process, either by superficial reduction or oxidation of crystallites in the porous materials as a result of their direct contact with the firing atmosphere [18]. In Ba(Mg<sub>1/3</sub>Nb<sub>2/3</sub>)O<sub>3</sub> [BMN] the value of dielectric constant ( $\epsilon'$ ) normally remains constant i.e  $\sim 34$ . It shows linear behavior. It does not have any effect of frequency. On the replacement of Mg<sup>2+</sup> by Co<sup>2+</sup> (3d<sup>7</sup>) the dielectric constant ( $\epsilon'$ ) value doubles that of BMN. It shows the dispersion behavior but as such Co<sup>2+</sup> (3d<sup>7</sup>) which has weak Jahn-Teller distortion effects it has not produced as such drastic increase in values in BCoN. On the other hand on further replacement of Co<sup>2+</sup> by Cu<sup>2+</sup>, having 3d<sup>9</sup> configurations, there is further enhancement in the dielectric constant values (10<sup>3</sup>-10<sup>5</sup>). Here we can say that strong Jahn- Teller effect distortion have more prominent effect as compared to weak Jahn- Teller effect on dielectric properties.



**Figure 5.4 Dielectric Loss ( $\tan\delta$ ) vs. Frequency of BCoN, BCuN samples from (RT – 350°C)**

Figure 5.4 shows the frequency dependence of dielectric loss ( $\tan\delta$ ) for BCoN and BCuN in full temperature range (RT- 350°C). In case of BMN the loss shows the irregular behaviour so it has not been shown here. While in case of BCoN the dielectric loss ( $\tan\delta$ ) is high i.e. in order of (10-15) which is likely to be due to the agglomerations of grains which is shown in Figure 5.2 (b) while on fully replacing it with  $\text{Cu}^{2+}$  the losses drastically increased in the range of ( $10^0$ -  $10^3$ ) which is very high. May be it has been somewhat correlations with the grains which are elongated type. But as in previous chapter we have seen that same type of elongated grains is observed in SCuN samples also. But over there the losses were low in comparison to BCuN samples. We can say that it is the simultaneous presence of large ions both at the A-site (Ba,  $r=1.35\text{\AA}$ ) and at B'-site (Cu,  $r=0.69\text{\AA}$ ) reduces the flexibility of dipole motion leading to higher losses. The loss reduces when the Barium is replaced by smaller ion Sr ( $r=1.13\text{\AA}$ ) providing greater flexibility to dipole motion in the unit cell.

### 5.2.3.2 Temperature Dependent Dielectric Properties

Figure 5.5 shows the dielectric constant for B'-site substituted divalent ions in Ba ( $B'_{1/3}Nb_{2/3}$ )O<sub>3</sub> series as a function of temperature in the frequency range (100-32MHz). The real permittivity ( $\epsilon'$ ) in BMN is constant as it did not vary with frequency or temperature. While of replacing  $Mg^{2+}$  with  $Co^{2+}$  we did not find any behavior change but the dielectric constant value abruptly rises. It is 5 times higher than that of BMN. We know that according to CFS theory  $Co^{2+}$  with  $3d^7$  electronic configurations the  $t_{2g}$  orbitals are unevenly occupied producing weak Jahn-Teller effects. The Jahn-Teller Effect distorts the octahedral along one of its crystallographic direction and hence enhances the polarization in the system. This effect is strongest in  $3d^9$  configurations but weak in  $3d^7$  configurations. In case of BCuN the real permittivity ( $\epsilon'$ ) value gradually increases up to a maximum value ( $\epsilon_m$ ) with the increase of temperature, and then it smoothly decreases, suggesting a phase transition. The maximum relative permittivity ( $\epsilon_m$ ) as well as its corresponding temperature ( $T_m$ ) is dependent on the frequency. In this case, the relative dielectric permittivity magnitude decreases with the increase in the frequency, shifting the maximum value ( $\epsilon_m$ ) to higher temperatures. Hence, this result indicates that the dielectric polarization has relaxation-type behaviour. Strong Jahn-Teller effect in  $Cu^{2+}$  ( $3d^9$ ) produces large polarization in unit cell enhancing dipole moment dependent dielectric constant ( $\epsilon'$ ) the most. Whereas,  $Co^{2+}$  ( $3d^7$ ) possessing weak Jahn-Teller effect gave

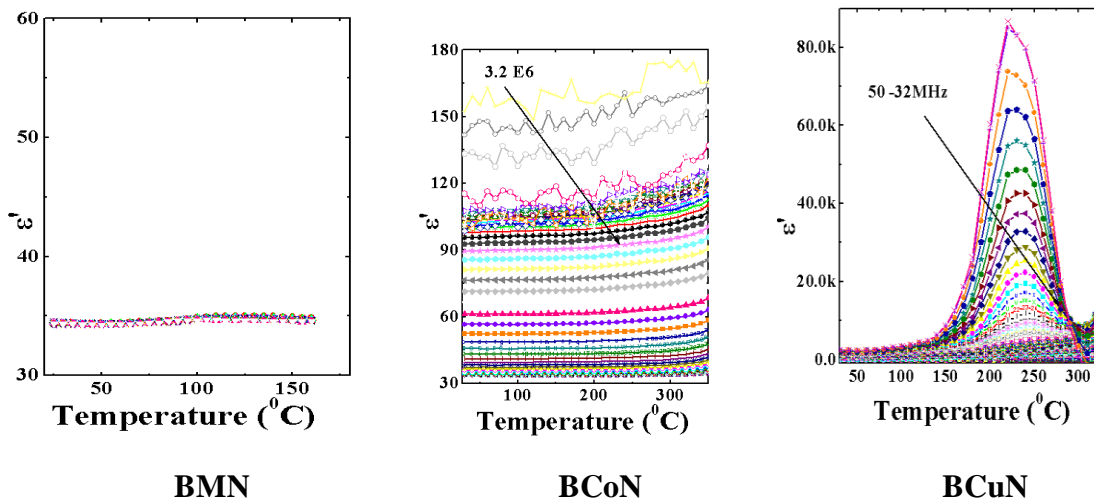


Figure 5.5 Temperature dependence of Dielectric Constant for BMN, BCoN and BCuN ceramics.



intermediate values and  $\text{Mg}^{2+}$  ( $2p^6$ ) with no Jahn-Teller effect the least dielectric constant values. In case of BCuN at 50 Hz the maximum  $\epsilon_m = 85037$  is observed at  $T_m = 220$ , while at 1Khz we observe shift in  $T_m$  to 250 and the  $\epsilon_m$  is around 7040.

Figure 5.6 shows the variation of dielectric loss as a function of temperature. It is observed that in case of BMN which is a polar dielectric the loss is linear with no effect of temperature. Losses are very low in order of (0.0-0.5) in comparison to BCoN and BCuN samples. While moving towards BCoN we observe that the loss characteristic is different from that of dielectric constant. In dielectric constant part it was showing linear behaviour with temperature while in loss parameter we observe that with increase in frequency the losses values goes on reducing it shows dispersion behaviour in comparison to BMN. While the losses values are high than that of BMN in range of (0-4.0) for BCoN On further switching towards  $\text{Cu}^{2+}$  based composition (BCuN) we observe the  $T_m$  above  $300^\circ\text{C}$  and the losses are very high ( $\sim 330$ ). We observe large enhancement of dielectric loss ( $\tan\delta$ ) in BCuN composition as compared to other BMN and BCoN samples.

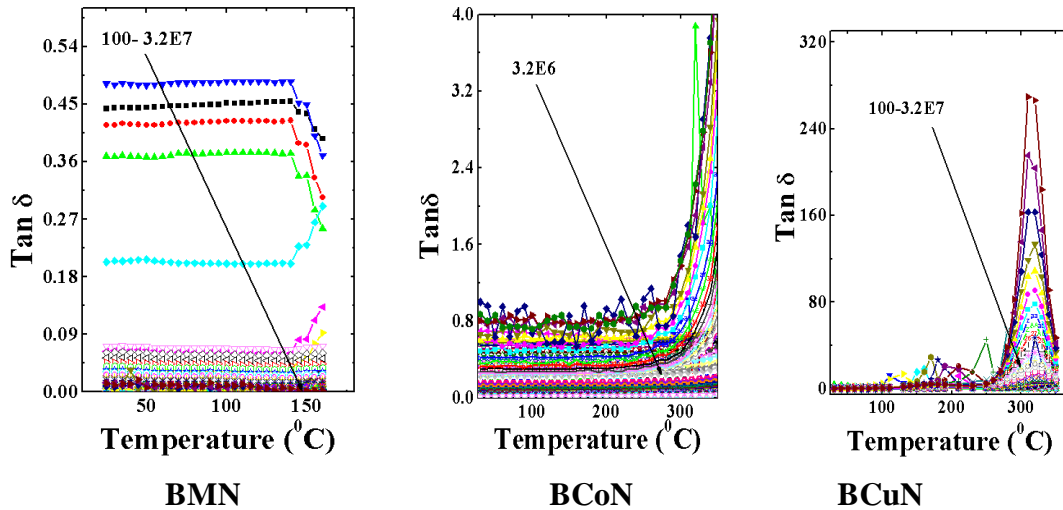


Figure 5.6 Temperature dependence of Dielectric loss ( $\tan\delta$ ) for BMN, BCoN and BCuN ceramics.

#### 5.2.4 Diffuse Phase Transition

A diffuse phase transition is commonly observed the signature broadening of the dielectric constant ( $\epsilon$ ) as a function of temperature ( $T$ ). The deviation from the Curie–Weiss law



near  $T_m$ , i.e. frequency dispersion of both dielectric and dielectric loss in the transition region, imply frequency dependence with  $T_m$  [23, 24]. A deviation from the Curie–Weiss law is observed for all frequencies (Figure 5.7). This deviation is a typical behavior of ferroelectric materials with diffuse phase transition. A modified Curie–Weiss law has been proposed to describe the diffuseness in a phase transition (Uchino and Nomura 1986) [25]

$$\frac{1}{\epsilon} - \frac{1}{\epsilon_m} = (T - T_m)^{\gamma}/C' \quad (5.1)$$

Where both  $\gamma$  and  $C'$  are constants. The parameter  $\gamma$  gives information on the phase transition character ( $\gamma = 1 \rightarrow$  a normal Curie–Weiss law behaviour is obtained and  $\gamma = 2 \rightarrow$  it exhibits the quadratic dependence, a signature of complete diffuse phase transition).

The plot of  $\ln(1/\epsilon - 1/\epsilon_{\max})$  versus  $\ln(T - T_m)$  at 10 kHz [BCuN] ceramic is shown in Figure 5.7. Linear relationship is observed. The slope of the fitting curve is used to determine the parameter  $\gamma$  value. The  $\gamma$  value was found to be 1.08 for [BCuN] at frequency 10 kHz.

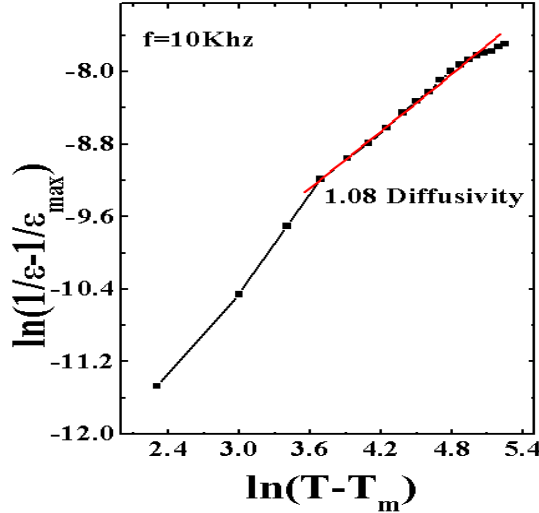


**Figure 5.7** Variation of  $\ln(1/\epsilon - 1/\epsilon_{\max})$  with  $\ln(T - T_m)$  at 10 kHz

As in case of BMN and BCoN we did not observe any transition temperature within our temperature range of measurement, we have not determined diffusivity for these samples.

Further, we have observed that in the case of BCuN diffusivity nearly obey the Curie- Weiss law. An important observation on the fit performed in our experimental data by means of equation (5.1) indicates that a universal  $\gamma$  value was not obtained in the temperature range above  $T_m$ . The  $\gamma$  value continuously approaches unity where it departs from  $T_m$ . This value suggests that the material has structural order–disorder and diffuse phase transition.

### 5.2.5 Impedance Spectroscopy studies

Figure 5.8 shows the Nyquist plots (complex impedance spectrum) of [BCoN], [BCuN] at different temperatures. BMN sample does not form the Cole-Cole Curve. Therefore it has not been shown here. Characteristically, two semicircular arcs have been observed. The complex impedance plot (Figure 5.8) shows two semicircular arcs with their centers lying below the real axis rather than on the real axis. The angle by which the semicircle is depressed below the real axis and the amount of inclination of the straight line are related to the width of the distribution of the relaxation time. This suggests the poly-dispersive nature of the sample. One obtains it by fitting the Cole-Cole equation,

$$\epsilon^* = \epsilon' + i\epsilon'' = \epsilon_\infty + \frac{\Delta\epsilon}{1 + (i\omega\tau)^{1-\alpha}} - i \frac{\sigma_{dc}}{\epsilon_0\omega} \quad (5.2)$$

Here,  $\tau$  is the mean relaxation time instead of the single relaxation time of pure Debye process while the Cole-Cole parameter  $\alpha$  indicates the width of the relaxation time distribution and provides a measure of the poly-dispersive nature.

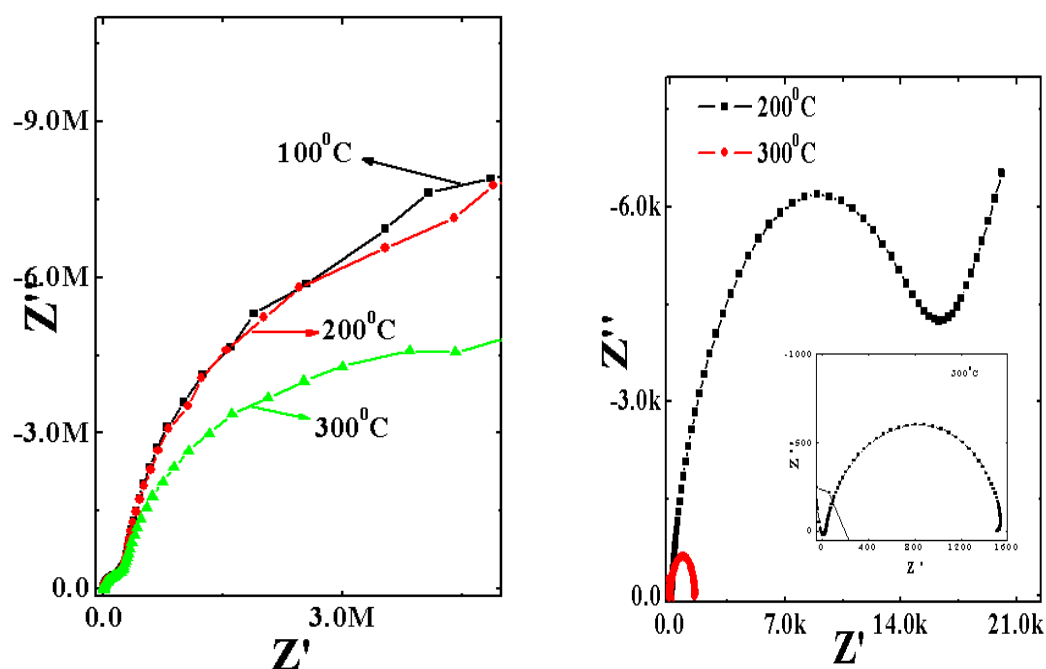


*Figure 5.8* Cole-Cole graphs of BCoN and BCuN at two different temperatures 200, 300 deg.

The fitting of the Cole-Cole equation was performed to study the dispersive and the conducting nature of the samples. It is seen from Figure 5.9 ( $\alpha$  is plotted versus temperature) that the observed non-zero values of the Cole-Cole parameter  $\alpha$  indicates non-Debye type poly-dispersive nature of these samples. While in the case of [SCuN] we do not observe any semi circular arc forming in the frequency range.

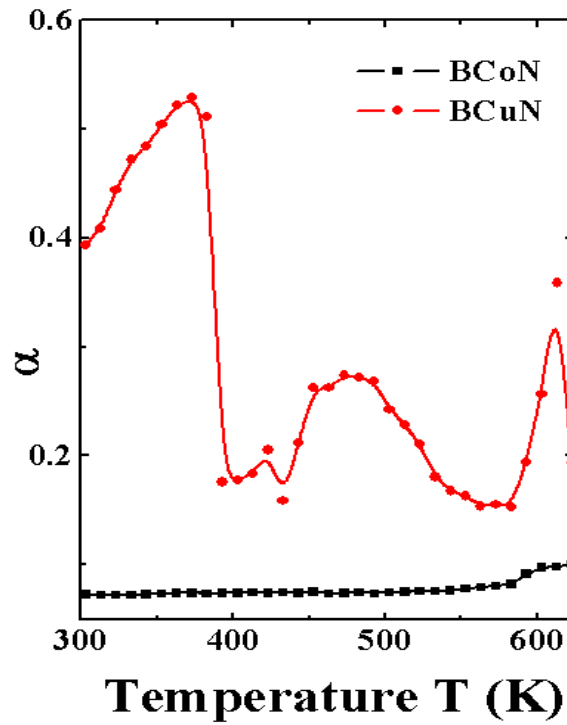


*Figure 5.9* The Temperature dependence of the Cole-Cole parameter, which indicates the width of the relaxation time distribution.

### 5.2.6 Modulus Spectroscopy Analysis

The electric modulus formalism is expressed as

$$Z^*(\omega) = Z' - jZ'' \quad (5.3)$$

$$M^*(\omega) = M'(\omega) + jM''(\omega) \quad (5.4)$$

$$M^*(\omega) = j\omega C_0 Z^*(\omega) \quad (5.5)$$

From Equation (5.3), (5.4) and Equation (5.5) one can get the following Equations (5.6) and

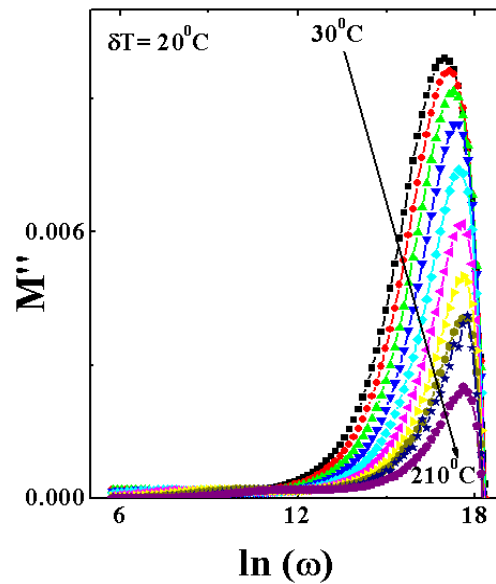
(5.7)

$$M' = \omega C_0 Z'' \quad (5.6)$$

$$M'' = \omega C_0 Z' \quad (5.7)$$

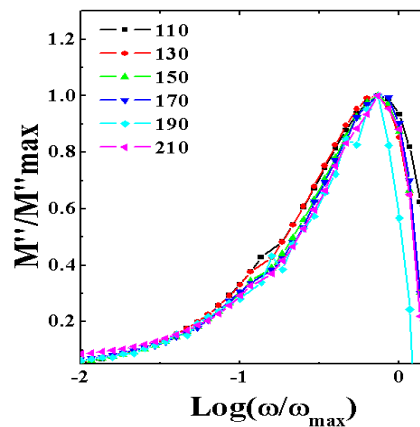
where  $C_0$  is given by  $C_0 = \epsilon_0 A/L$ ,  $L$  is the thickness, and  $A$  is the area of the sample,  $\epsilon_0 = 8.854 \times 10^{-14} \text{ F/cm}$  is the permittivity of the free space. The modulus analysis has an advantage that it suppresses the information about electrode effects [20-23]. This can also be used to study the conductivity relaxation times [23, 24]. The complex modulus is defined as inverse of the complex permittivity and in the present work, the impedance data were converted into electrical modulus using the above equations (5.3-5.7).

Figure 5.10 shows the plot of imaginary part of modulus for BCuN sample. In case of BMN and BCoN since we did not observe any variation with the temperature and frequency the plots of BMN and BCoN are not shown here. The modulus formalism gives the information about the conductivity relaxation mechanism. In case of BCuN sample there is no variation of conductivity with temperature and frequency after 200 deg as BCuN has the transition temperature around  $\sim 220$  deg (which is shown in Figure 5.5). Above 200 deg the modulus formalism shows temperature and frequency independent behaviour predicting that the composition is going into phase transition above 200 deg.



**Figure 5.10** Variation of imaginary part of modulus at different frequencies and at different temperatures.

Figure 5.11 shows the Scaling plot of  $M''/M''_{\max}$  versus  $\log(\omega/\omega_{\max})$  and at various temperatures. We have scaled each  $M''$  by  $M''_{\max}$  and each frequency by  $\omega_{\max}$  for different temperatures in Figure 5.11. The coincidence of all curves/peaks at different temperatures exhibits temperature independent behavior of the dynamic processes [25] occurring in the material.



**Figure 5.11** Scaling behavior of  $M''$  at various temperatures for [BCuN]

This might be due to the ion migration that takes place via hopping mechanism.

### 5.2.7 Conductivity Studies

#### 5.2.7.1 Frequency dependent conductivity

Figure 5.12 shows the variation of the conductivity with frequency at different temperatures. The ac conductivity in most of the previous studied on iso-morphous perovskite materials [26-29] and by A.R Long and R S Eliot [30, 31], found to follow a universal power law

$$\sigma_{ac} = A(T)\omega^{s(T)} \quad (5.8)$$

where  $0 < s < 1$ . The relation between  $\sigma$  and  $\omega$  is usually fall linear in the double-logarithmic presentation, and the slopes of the lines, varying with temperature, are related to the conduction mechanism [31].

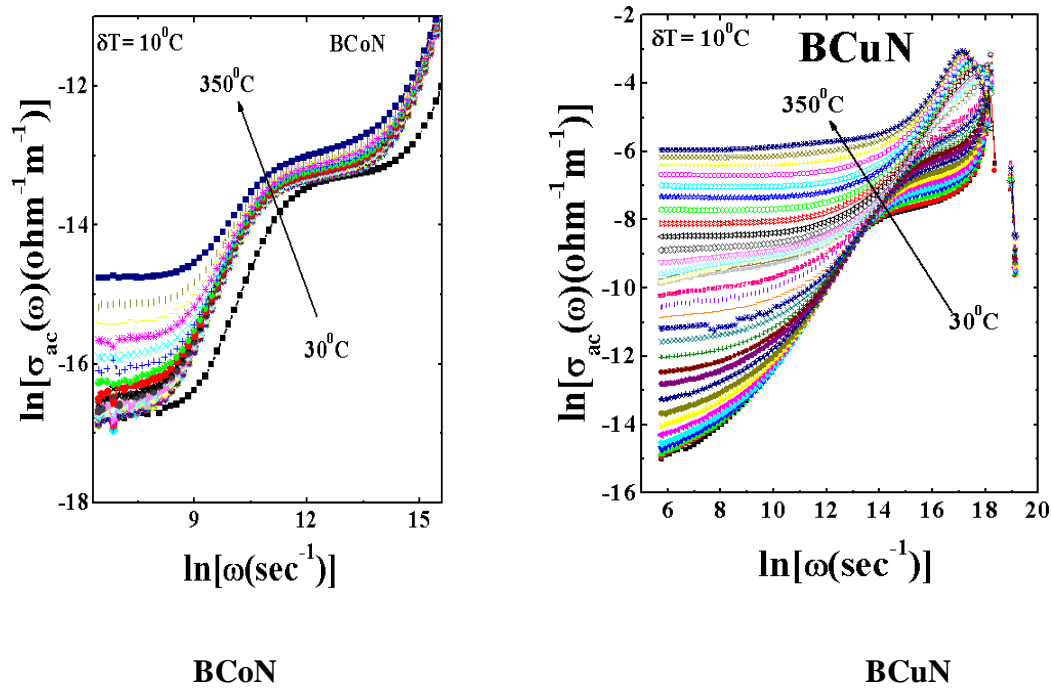
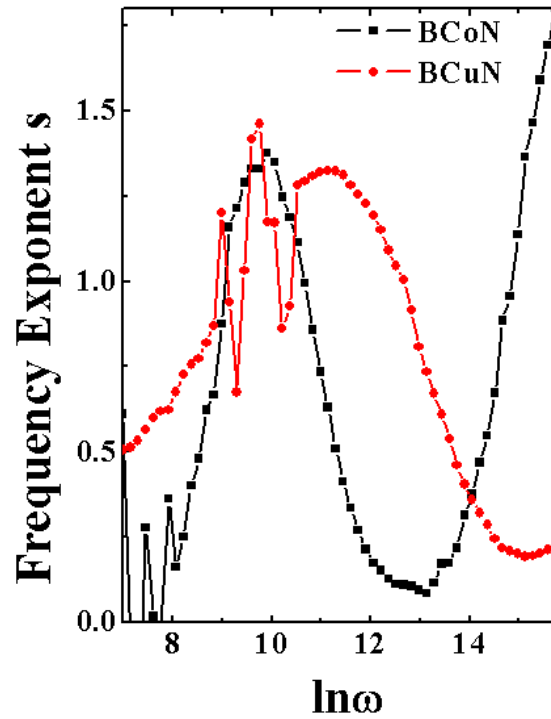


Figure 5.12 The frequency response of the conductivity for BCoN and BCuN at different temperatures ranges from 30°C to 350°C with an interval of 10°C.

It is clear from the Figure 5.12 that the results do not follow the simple power law relation given by (5.8). The low frequency ac conductivity (region I) is characterized by a linear response with nearly equal slopes at different temperatures. The onset of the characteristic dispersion (region II), at the high frequency end of region I shifts towards higher frequencies with increasing temperature.

The values of the  $s$  parameter are obtained using the derivative equation:

$$s = \frac{d \ln \sigma'}{d \ln \omega} \quad (5.9)$$



**Figure 5.13** The room temperature values of the frequency exponent  $s$  as a function of the frequency, obtained using the derivative curves.

Figure 5.13 shows the frequency dependence of the  $s$  parameter at room temperature. At low frequencies we observe non-zero values of the  $s$  parameter for BCuN sample. In mid-frequency region, the  $s$  parameter increases rapidly and after showing a peak, it becomes nearly linear at



higher frequencies. The observed nature of  $s$  in various frequency regions can be explained using the JRM of Funke [32], who successfully used it to explain the hopping of ions. The slopes of the  $\ln\sigma - \ln\omega$  plots in the dispersion region II are strongly temperature dependent. In the jump relaxation model (JRM), introduced by Funke, during ionic conduction in solids there is a high probability for a jumping ion to have unsuccessful hop. However, if the neighborhood becomes relaxed with respect to the ion's position, the ion stays in the new site. The conductivity in the low frequency region is associated with successful hops. But beyond the low frequency region many hops are unsuccessful and its probability increases as the frequency increases. The change in the ratio of successful to unsuccessful hops results in the dispersive conductivity. The JRM suggests that different activation energies are associated with unsuccessful and successful hopping processes. Applying the JRM to the frequency response of the conductivity for the present material, it was possible to fit the data to a double power law:

$$\sigma_{ac} = A1(T) \omega^{s1(T)} + A2(T) \omega^{s2(T)} \quad (5.10)$$

Where,  $s < 1$  corresponds to the translational hopping motion.

### 5.2.7.2 Temperature dependent conductivity

The temperature dependence of the  $s$  parameter for the critical mid-frequency region is shown in Figure 5.14. The values of  $s$  obtained from the slopes of the  $\ln\sigma - \ln\omega$  plots (Figure 5.12) are plotted as a function of temperature in Figure 5.14.

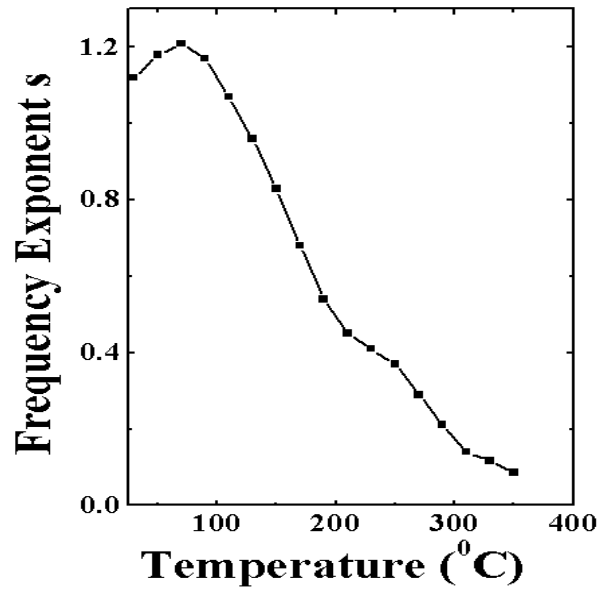


Figure 5.14 The peak values of the frequency exponent  $s$  vs. the absolute temperature  $T$ .

It shows a nonlinear nature of the frequency exponent with temperature. According to the correlated barrier hopping (CBH) model [31, 33], the parameter  $s$  has the form:

$$s = 1 - \frac{6kT}{[W_M - kT \ln(1 / \omega \tau_0)]} \quad (5.11)$$

Here,  $W_M$  is the energy required to cross the barrier height. The model predicts downward nature of  $s$  parameter for small values of  $W_M/kT$ . Now BCuN sample nearly identical downward variation of the frequency exponent  $s$  indicates that the conduction process is predominantly due to the correlated barrier hopping (CBH) of electrons.

### 5.3 Conclusion

In summary, we have successfully synthesized polycrystalline bulk samples of  $\text{Ba}(\text{B}'_{0.33}\text{b}_{0.67})\text{O}_3$  where  $\text{B}' = (\text{Mg}^{2+}, \text{Co}^{2+}, \text{Cu}^{2+})$  [BMN], [BCoN], [BCuN] by standard solid state reaction technique. The effect of replacement of B'-site in  $\text{Ba}(\text{B}'_{0.33}\text{b}_{0.67})\text{O}_3$  is studied by means

of structural, micro structural, electrical, Conductivity behaviour studies. The following observations have been made on the basis of several experiments performed on the bulk samples.

- (i) The XRD analysis of  $\text{Ba}(\text{B}'_{0.33}\text{b}_{0.67})\text{O}_3$  where  $\text{B}' = (\text{Mg}^{2+}, \text{Co}^{2+}, \text{Cu}^{2+})$  [BMN], [BCoN], [BCuN] indicates that all samples exhibit a single phase nature with [BMN] exhibiting hexagonal symmetry. On replacement of Magnesium by Cobalt and Copper which have  $3d^9$  configurations shifting the structure to the higher symmetry side i.e tetragonal side. Decrease in structural asymmetry has led to the observed enhancement in dielectric constant  $\epsilon'$  values and increase in dielectric loss ( $\tan\delta$ ) values in case of BCuN and BCoN samples.
- (ii) The dispersion behavior observed in dielectric constant as a function of frequency has been explained according to interfacial polarization as predicted by the Maxwell-Wagner and Koop's phenomenological theory.
- (iii) The dielectric constant is highest in BCuN samples  $\sim 80\text{K}$ , while for BCoN and BMN it is, respectively,  $\sim 180$  and  $\sim 35$  only. As both BMN and BCoN does not show any effect of temperature or frequency. We observe strong distortion in case of BCuN sample which has led to enhanced effect on dielectric properties (dielectric const and higher losses).
- (iv) The Cole- Cole analysis of the BCoN and BCuN gave the non-zero values of alpha ( $\alpha$ ) parameter suggesting that the compositions are poly-dispersive in nature.
- (v) The observed nature of  $s$  in various frequency regions can be explained using the JRM of Funke [32]. In BCuN sample nearly identical downward variation of the frequency exponent  $s$  indicates that the conduction process is predominantly due to the correlated barrier hopping (CBH) of electrons.

## References

- [1] H Matsumoto, H Tamura and K Wakino, *Jpn. J. Appl. Phys.*, **30** (9B), 2347, 1991.
- [2] I M Reaney, P L Wise, I Qazi, C A Miller, T J Price, D S Cannell *J.Eur Ceram. Soc.***23**, 3021, 2003.
- [3] T Fukui, C Sakurai and M Okuyama,*J. Mater. Res*, **7**(7), 1883, 1992.
- [4] F Azough, C Leach, and R Freer, *Key Eng. Mater*, **264–268**, 1153, 2002.
- [5] K Endo, K Fujimoto, and K Murakawa, *J. Am. Ceram.Soc.*, **70**(9), C-215, 1987.
- [6] W C Ahn, J H Jang, S Nahm, H M Park, and J H Lee,. *J. Eur. Ceram. Soc*, **23**, 2473, 2003.
- [7] F Azough, C Leach, and R Freer, *J. Eur. Ceram. Soc*,**25**, 2839, 2005.
- [8] H Hughes, M D Iddles, and I M Reaney, *Appl.Phys. Lett.*, **79**(18), 2952, 2001.
- [9] P K Davis,J Tong, and T Negas, *J. Am. Ceram. Soc*, **80**(7), 1724, 1997.
- [10] I T Kim, Y H Kim and S J Chung, *Jpn. J.Appl. Phys*, **34** (Part 1, No. 8A), 4096,1995.
- [11] S Desu, and H M O’Bryan, *J. Am. Ceram. Soc.*, **68**(10), 546, 1985.
- [12] J H Paik, I T Kim,J D Byun, H M Kim and J Lee, *J. Mater. Sci. Lett.*,**17**, 1777,1998.
- [13] C H Lu, and C CTsai, *J. Mater. Res*. **5**, 1219, 1996.
- [14] Dong Cheng, Powder, X, Window-95 program for powder x-ray diffraction data processing, *J. Appl. Cryst.* **32**, 838, 1999.
- [15] Surya M. Gupta, E. Furman, E. Colla, and Z. Xu, Dwight Viehland*J of App Phy*,**88**, 2836, 2000.
- [16] J Maxwell, Electricity and Magnetics (Vol.1, Section 328, Oxford University Press, London) (1873).
- [17] C. Koops. *Phys. Rev.* **83**, 121, 1951.
- [18] J Smit H Wijn *Ferrites*, Wiley, New York, p. 369, 1959.
- [19] S. Nomura, *Ferroelectrics* **49**, 61,1 983.
- [20] I M Hodge, M D Ingram and A R West, *J. Electroanal. Chem* **74**, 125, 1976.
- [21] K C Sobha. and K J Rao , *Solid State Ionics*, **81**,145, 1995.
- [22] M Ganguli, H M Bhat and K Rao *J, Phys. Chem. Glasses*, **40**, 297, 1999.
- [23] S Lanfredi, P S Saia, R Lebullenger and A C Hernandez *Solid State Ionics*,**146**, 329, 2002.
- [24] S Ghosh,and A Ghosh, *Solid State Ionics*, **149**, 67, 2002.

- [25] S Saha, T P Sinha, *Phys. Rev.***B65**, 134103, 2002.
- [26] M. F. Mostafa, M. El Nimer, and F. Richa, *Phys. Scr.* **43**, 541 1991.
- [27] M. F. Mostafa, A. S. Atallah, and M. Elessawi, *Phase Transitions* **64**, 215, 1998.
- [28] M. F. Mostafa and A. S. Atallah, *Phys. Lett.* **A264**, 242, 1999.
- [29] M. F. Mostafa, M. M. Abdel-Kadar, A. S. Atallah, and M.El-Nimer, *Phys. Stat. Sol.* **135(a)**, 549, 1993.
- [30] A. R. Long, *Adv. Phys.***31**, 553, 1982.
- [31] R. S. Elliot, *Adv. Phys.* **36**, 135, 1987.
- [32] K. Funke, *Prog. Solid St. Chem.* **22**, 111, 1993.
- [33] R. Gangopadhyay, A. De, S. Das, *J. Appl. Phys.* **87**, 2363, 2000.

## Chapter 6

### **A comparative Study of Crystal Structure, Microstructure, Dielectric and Conductivity properties of bulk and thin films of $\text{Ba}(\text{B}'_{0.33}\text{Nb}_{0.67})\text{O}_3$ , where B' stands for $(\text{Mg}^{2+}, \text{Co}^{2+})$**

#### **PART -A**

##### **i) Studies on un-irradiated thin films**

This chapter presents a comparative study of structural and dielectric properties of  $\text{Ba}(\text{B}'_{0.33}\text{Nb}_{0.67})\text{O}_3$ , where B' stands for  $(\text{Mg}^{2+}, \text{Co}^{2+})$ , in the form of bulk and thin films deposited on various substrates. Films for both the compositions show higher dielectric constant and dielectric loss. Relaxor behaviour is introduced in BCoN thin films not observed in its bulk sample. We observed significant increase in dielectric constant with low loss on  $\text{O}^{7+}$  as well as  $\text{Ag}^{15+}$  ion irradiation, may enhance the electro-optical properties which in turn increase compounds tuneability for device applications.

## 6.1 Introduction

Ferroelectric materials - in particular ceramics - have been commercially important to the electronics industry for more than 50 years. Prominent examples include lead zirconium titanate ceramic, the ultrasonic transducer in virtually all sonar and depth-sounding systems; and modified barium titanate, which is the dielectric multilayer ceramic capacitor. Until very recently, ferroelectrics have been used in the form of bulk ceramics and, where available, single crystals. Whilst these materials have proved a robust and reliable solution, producing thin layers (less than 10 nm) or dimensional tolerances better than a few microns has proved impractical [1,2].

Since the 1980s, various methods have been developed [3] to fabricate ferroelectrics in the form of thin films. The availability of thin-film ferroelectrics has encouraged the re-examination of previously unrealizable designs, resulting in the integration of ferroelectrics with semiconductor circuits, and architectures combining the excellent properties of ferroelectrics with micro machined silicon structures. The future appears promising for the development of a new generation of ferroelectric devices, some of which will profoundly affect the evolution of the electronics industry over the next 50 years.

Relaxor ferroelectric thin films attract much attention of scientists in the last few years. Bulk relaxor ferroelectrics possess excellent dielectric, electromechanical and electro optical properties which found number of technical applications as stated above. The experimental study of relaxor ferroelectric thin films are aimed to investigate possible variations or improvement in physical properties by the changing film thickness, substrate material and growth conditions. Because of the complexity of the problem there are no answers about the influence of the aforementioned external and internal factors, e.g. chemical disorder, on the relaxor ferroelectric films properties.

Several methods are in current use for depositing thin films, each of which has its merits and disadvantages. The methods can be classified into three groups:

- *Physical vapour deposition (PVD)*, e.g. RF sputtering and pulsed laser deposition
- *Chemical vapour deposition (CVD)*, e.g. metal-organic chemical vapour deposition
- *Chemical solution deposition (CSD)*, e.g. sol-gel.

Although PVD and CVD techniques are currently favored by the semiconductor industry partly because of their existing investment and experience in using these techniques - CSD is a useful research and development tool requiring very little capital expenditure. The quality of the films is comparable across all three methods.

Among these deposition techniques, pulsed laser deposition (PLD) is widely used method for the thin film growth. In the present work PLD technique is used for thin film due to its versatility (see details in chapter 2). In PLD, the films are deposited with flowing oxygen onto heated substrate, which produce polycrystalline thin films without any subsequent heat treatments. In addition, the stoichiometry of the target is faithfully reproduced in the film, if the conditions of the PLD are judiciously set, which has been found difficult for other conventional techniques such as sputtering, evaporation etc. Another advantage is the deposition of the multilayer thin films carried out by varying the gas pressure or the substrate temperature or the target.

Several research groups have used pulsed laser deposition technique for deposition of polycrystalline thin films. R.S Katiyar et. al., [4] fabricated PSNT thin films by PLD technique to study the dielectric relaxation mechanism. Cheng-Ji Xian et. al., [5] fabricated  $\text{Bi}_2\text{Mg}_{2/3}\text{Nb}_{4/3}\text{O}_7$  (BMN) pyrochlore thin films on PT and Cu metal at low temperatures by PLD technique for embedded capacitors applications. D. Miu et. al., [6] fabricated the  $\text{SrBi}_2\text{Ta}_2\text{O}_9$  [SBT] thin films by PLD technique and studied its dielectric properties on different substrates.

In general, we can say that the physical properties of the thin films are highly dependent upon the deposition technique and parameters. Therefore, from the application point of view, it is important to synthesize a single-phase structure and correlation of its micro structural and dielectric properties. During the last few years, a lot of efforts have been made on oxides thin films, but there is no report available on the thin films of  $\text{Ba}(\text{B}'_{0.33}\text{Nb}_{0.67})\text{O}_3$  where ( $\text{B}' = \text{Mg}^{2+}$  and  $\text{Co}^{2+}$ ) oxides thin films. In this chapter, we have reported a growth characteristic of [BMN] on different substrates namely platinum coated silicon (Pt-Si), MgO (001) and Si (111) and indium tin oxide coated glass (ITO) and its effects on structures, microstructures, dielectric properties. After finding the suitability of ITO as substrate we deposited [BMN] and [BCoN] thin films by (PLD) technique and then characterized it through various techniques.



## 6.2 Deposition Conditions for the Pulsed Laser Depositions (PLD) Thin Films

$\text{Ba}(\text{B}'_{0.33}\text{Nb}_{0.67})\text{O}_3$  where  $\text{B}' = (\text{Mg}^{2+}, \text{Co}^{2+})$  thin films were prepared by pulsed laser deposition (PLD) method on ITO coated glass substrates. But [BMN] thin film was prepared on Pt-Si, MgO (001), Si (111) and ITO substrate also for the purpose of studying growth characteristic of different substrates. These thin films were prepared from a single phase polycrystalline bulk targets of [BMN] or [BCoN]. The polycrystalline bulk target of [BMN], [BCoN] was synthesized by conventional solid-state reaction technique (for details see Ref. [7]). The KrF excimer laser (Lambda Physik model COMPEX-201) of wavelength 248 nm and pulse duration of 20 ns was employed for the deposition. During the deposition laser energy density at the target surface was kept at 220mJ/cm<sup>2</sup> and repetition rate at 10 Hz. Substrate temperatures was maintained at 300°C for indium tin oxide coated glass (ITO) and 450°C for platinum coated silicon (Pt-Si), MgO (001) and Si (111) substrates respectively and the oxygen pressure was 200mTorr during the deposition. The focused laser beam was incident on the target surface at an angle of 45°. The target was rotated at about 10 rpm and the substrate was mounted opposite to the target at a distance of 4 cm. The substrate was mounted on a heater plate using a silver paint. The deposition was performed for 20 minutes. The film thickness was found to be ~200-300 nm for the film deposited on ITO for [BMN] and [BCoN]. On the other hand thickness of ~100-200 nm was achieved for film deposited on Pt-Si, MgO (001) and Si (111) as per the measurement by Stylus profilometer.

## 6.3 Results and Discussions

### 6.3.1 X-ray Diffraction (XRD) Measurements

X-ray diffraction measurements have been carried out for the structural analysis of [BMN], [BCoN] thin films. Figures 6.1 illustrate the x-ray diffraction pattern of [BMN] bulk, thin films deposited at Pt-Si, MgO (001), Si (111) and ITO using the PLD respectively.  $\theta$ -2 $\theta$  geometry was used to get the XRD pattern of the thin film deposited on different substrates whereas glancing mode was used for film deposited on different substrate. In glancing mode tube was fixed at 5° and detector was scanned from 20 – 60 degrees. Experimentally observed XRD patterns for polycrystalline film and bulk sample have been indexed using

PowderXsoftware developed by C. Dong [8]. From the XRD analysis, it is observed that all the diffraction peaks represent polycrystalline single phase hexagonal structure.

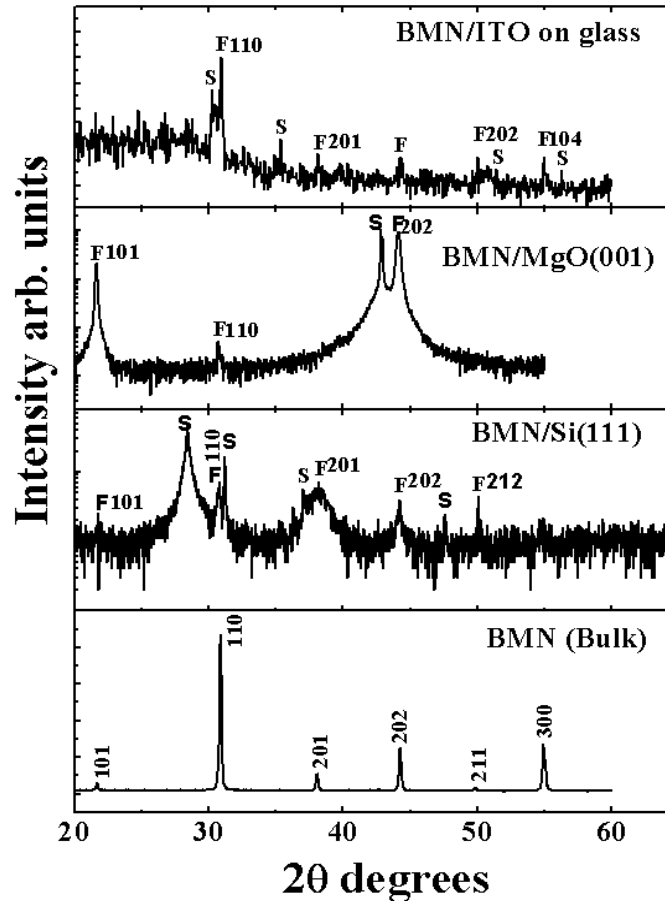


**Figure 6.1** X-ray diffraction pattern of un-irradiated BMN bulk, Si, MgO and ITO coated glass substrates.

No impurity phase is detected in the films. It is to be noted that the substrates Si, MgO and ITO coated glass all are single crystals with cubic lattice but films of our sample have hexagonal symmetry. Further, different symmetries do not preclude epitaxy to occur. The lattice parameters calculated from the standard Powder X Program [8] shows that there is a marginal increase in the lattice constant values of films compared to bulk. The XRD peaks shift by a small increment towards lower  $2\theta$  side in the case of films grown on Si and MgO substrates but on ITO substrates, peaks shift towards higher  $2\theta$  side. Additionally, it can be clearly seen from the

diffraction pattern that the reflection lines in the films are quite broad in comparison to the bulk sample (see Figure 6.1) which indicates that the grain size of the films is smaller than that of bulk material. The grain size is given by

$$D = 0.94 \times \lambda / (B \cos \theta) \quad (6.1)$$

Here  $\lambda$  is the wavelength of the x-ray source and  $B$  the full width at half maximum (FWHM) of an individual peak at  $2\theta$  (where  $\theta$  is the Bragg angle).

The lattice strain ( $T$ ) in the material causes broadening of diffraction peak, which can be represented by the relationship

$$T \tan \theta = (\lambda / D \cos \theta) - B \quad (6.2)$$

These calculated parameters are tabulated in Table 6.1. It is clear from table 1 that the film deposited on ITO coated glass substrate, has maximum FWHM values (lowest  $D$ ). We observe maximum strain in the film deposited on ITO. Previous literature study reveals that strain/stress has pronounced effects on the electrical properties of the films. The value of the lattice parameter for the film deposited on ITO is almost same as in case of the bulk ( $a=0.578\text{nm}$ ,  $c=0.707\text{nm}$ ) and ( $a=0.579\text{nm}$ ,  $c=0.708\text{nm}$ ), whereas it is higher for the film deposited on MgO and Si. This indicate that lattice is expanding in case of MgO and Si, while remains constant for film deposited on ITO.

**Table 6.1 XRD peak and AFM analysis of BMN films on Si, MgO and ITO coated glass substrates.**

<i>Compositions</i>	<i>Grain Size(nm)</i>	<i>Strain</i>	<i>Lattice Constant (nm)</i>	<i>Roughness(nm)</i>
BMN-Bulk	425	$1.1 \times 10^{-3}$	$a=0.578$ $c=0.707$	-
BMN-MgO	459	$7.5 \times 10^{-4}$	$a=0.581$ $c=0.708$	27.81nm
BMN-Si	344	$9.0 \times 10^{-4}$	$a=0.581$ $c=0.708$	2.89nm
BMN-ITO	74	$4.7 \times 10^{-3}$	$a=0.579$ $c=0.708$	2.56nm

Figure 6.2 shows the XRD pattern of BCoN films deposited on indium tin oxide coated glass (ITO) substrate along with the bulk. No impurity phase is detected in the films. It confirms the single hexagonal phase of the films and matches well with the bulk targets. The substrate

ITO is cubic in nature, while the BCoN films grown are polycrystalline with Hexagonal symmetry. The lattice parameters are calculated from the standard Powder X Program [8].

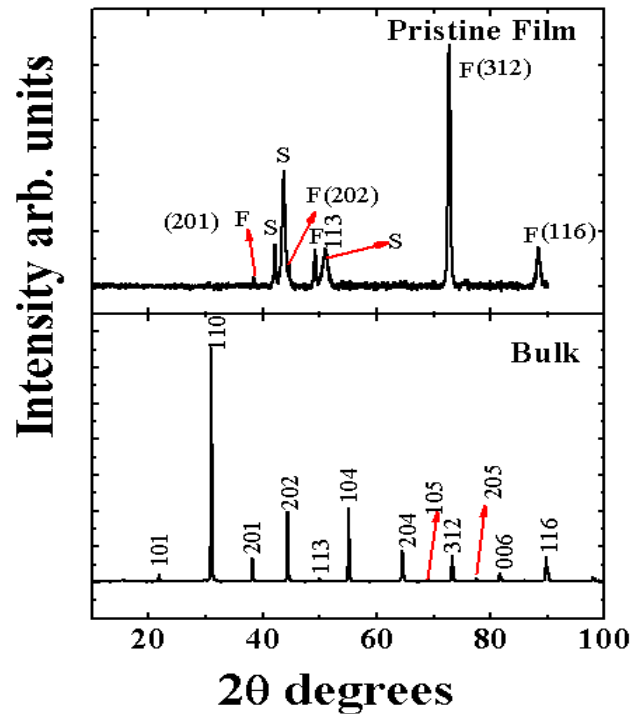
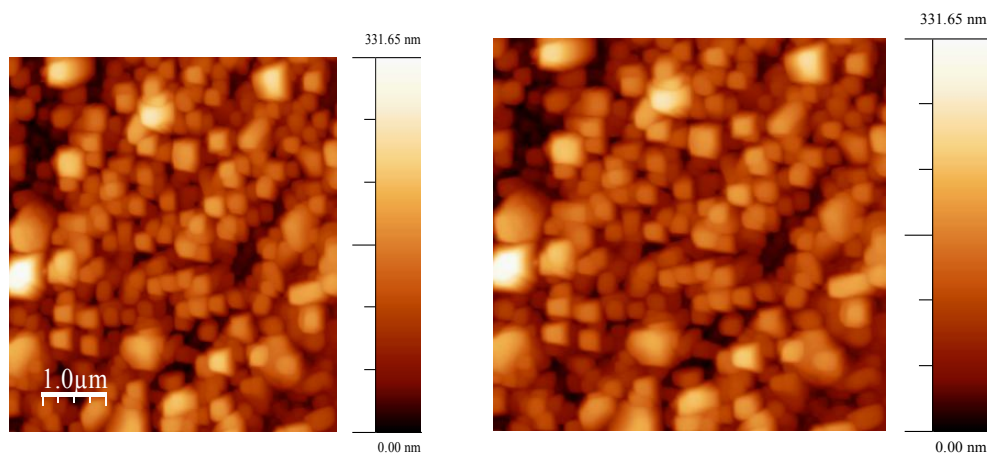


**Figure 6.2** X-ray diffraction patterns of BCoN bulk, and un-irradiated thin film on ITO coated glass.

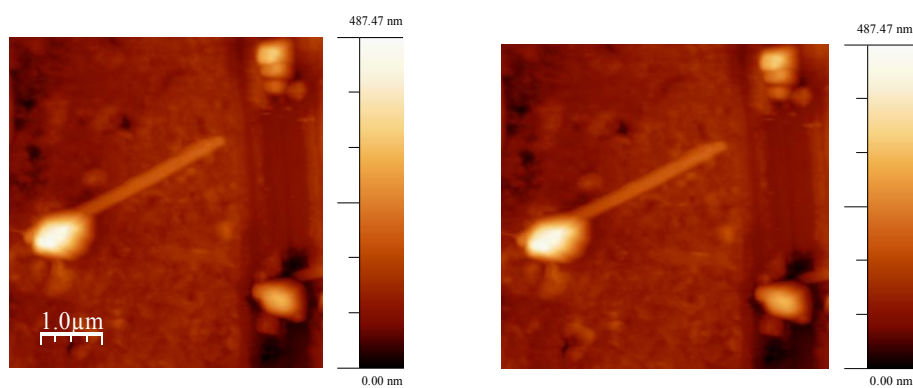
### 6.3.2 Atomic Force Microscopy Analysis

Surface morphology of the thin films is characterized by the atomic force microscopy (AFM). Figure 6.3(a-d) and Figure 6.4 show the AFM images of BMN on different substrates (Pt-Si, MgO, Si deposited at substrate temperatures  $450^{\circ}\text{C}$  and ITO coated glass deposited at  $300^{\circ}\text{C}$ ) and BCoN thin films deposited on ITO at  $300^{\circ}\text{C}$  respectively, in a oxygen pressure of 200mTorr. The AFM used in the present work is a commercial optical deflection microscope (Nanoscope, Digital Instruments) operating in air. The samples were mounted on a piezo ceramic which controls the motion in the three directions. The deflection of the laser beam on the cantilever is used to monitor the height displacement via a photodiode and a feedback loop. Using this technique one can measure the height variations of the order of 0.1 nm. For all these

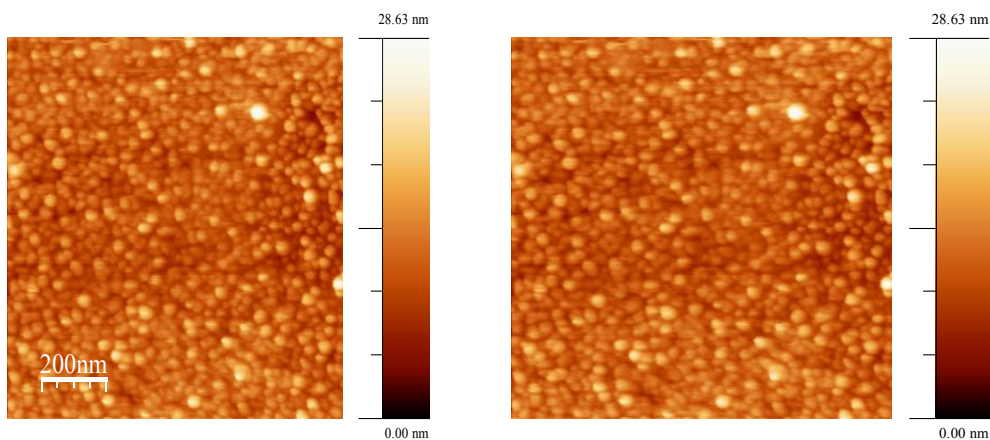
measurements the data have been acquired in the tapping mode with  $512 \times 512$  data points in the length of  $5\mu\text{m}$ , which gives a sampling rate of  $5\mu\text{m} / 512 \approx 9.76\text{ nm}$ .



(a)



(b)



(c)

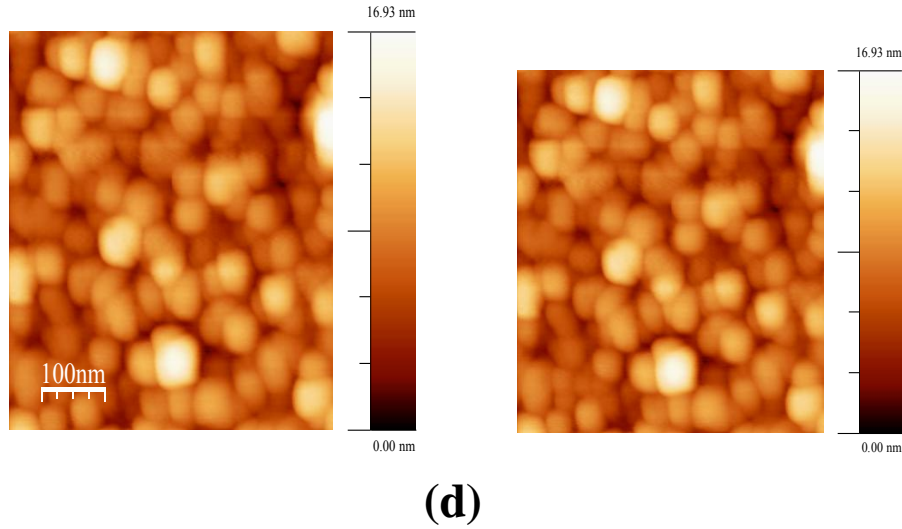


**Figure 6.3 AFM images of BMN on different substrates (a) Pt-Si (1.0 $\mu$ m), (b) MgO (001) (1.0 $\mu$ m, (c) Si (111) (100nm) (d) ITO (100nm).**

Figure 6.3 (a-d) shows the AFM images growth characteristics of the BMN films on different substrates. We observe uniform columnar grain formation on Si, Pt-Si and ITO films, while on MgO we do not notice any grain formation. Average tip size on each substrates are found to be  $\sim 100$ nm (Pt-Si), 20-25nm in Si and  $\sim 50$ nm in case of ITO coated on glass substrate films. From the XRD analysis it is observed that films grown on ITO has higher strain compared to other substrates. The grain size calculated from XRD pattern roughly matches with the AFM images. MgO substrates show poor grain formation. Although Pt-Si shows large grains but they have arbitrary orientation and absence of any columnar packing of grains. The Si substrate shows good grain growth but with moderate strain and roughness. Analysis of growth characteristics from AFM and XRD measurement reveal that the films grown on ITO are relatively better compared to Si, MgO or Pt-Si for electrical parameters studies and device applications. The roughness results are tabulated in Table 6.1. The AFM images of the BCoN films deposited on ITO coated glass substrates is shown Figure 6.4. Here also we observe columnar type of grain growth.

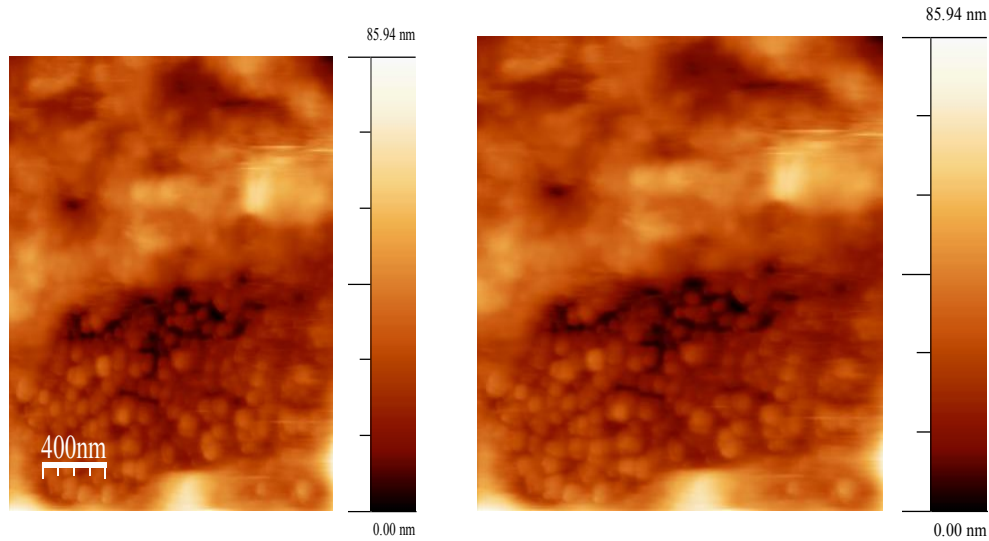
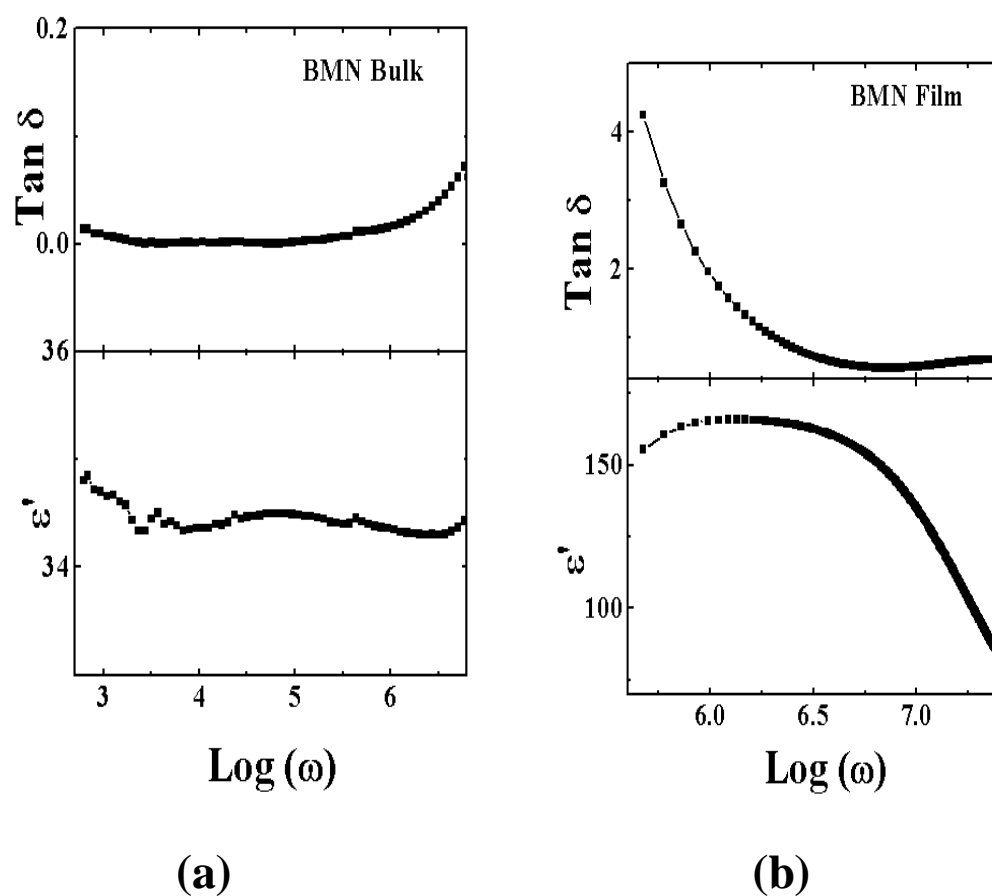


*Figure 6.4* AFM images of BCoN pristine thin films.

### 6.3.3 Dielectric Measurements

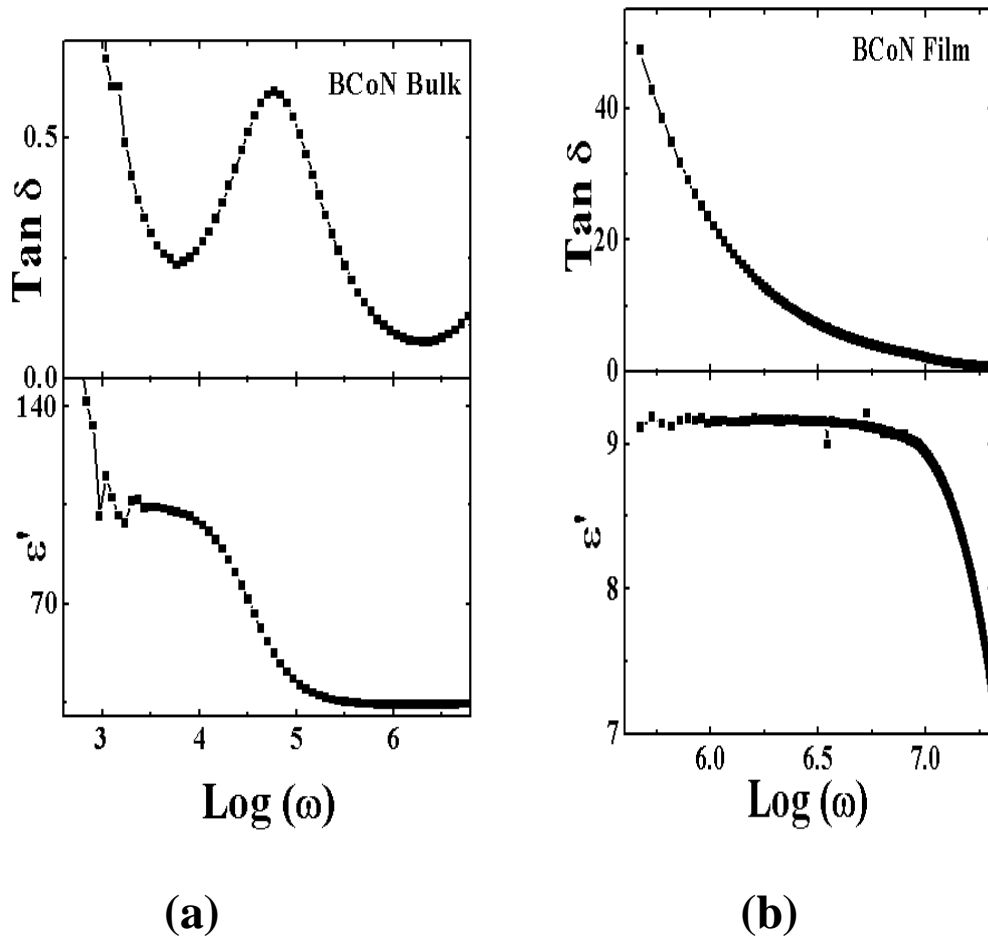
#### 6.3.3.1 Frequency dependence Dielectric Properties.

Figure 6.5(a) and (b) shows the variation of dielectric constant and dielectric loss ( $\tan \delta$ ) vs. frequency at room temperature for the BMN bulk sample and thin film. It exhibits frequency independent behaviour of dielectric constant and loss. While in case of thin films the dielectric constant and loss shows dispersion behavior i.e., the dielectric constant and loss decreases with increase in the frequency. This is the general dielectric behaviour observed in most of the oxide materials, which can be explained with interfacial polarization predicted by the Maxwell-Wagner model [9] in agreement with Koop's phenomenological theory [10].



*Figure 6.5* Variation of Dielectric Constant and Dielectric loss vs Frequency at room temperature of BMN(a) Bulk sample and (b) thin film sample.





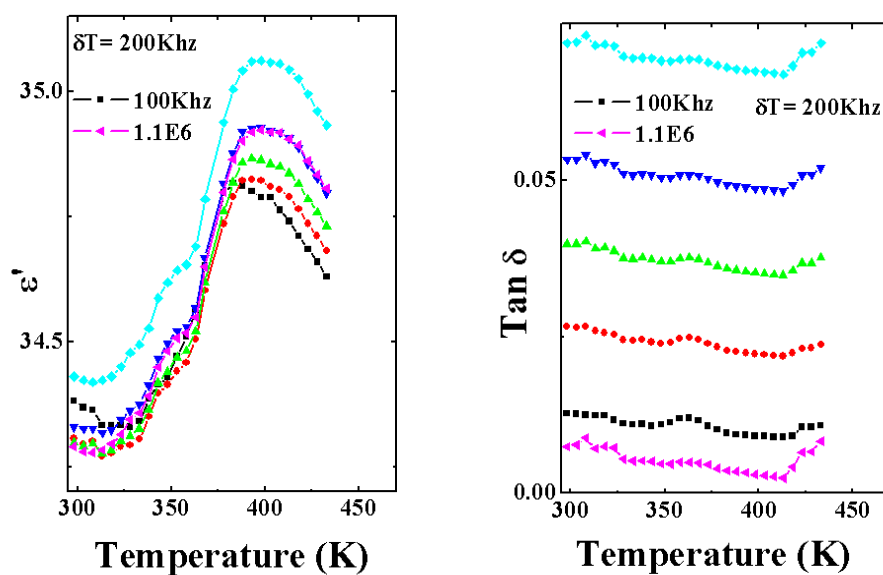
**Figure 6.6** Variation of Dielectric Constant and Dielectric loss vs Frequency at room temperature of BCoN(a) Bulk sample and (b) thin film sample.

Figure 6.6(a) and (b) shows the variation of dielectric constant and dielectric loss ( $\text{tan } \delta$ ) vs. frequency at room temperature for the BCoN bulk sample and thin film. In BCoN, unlike BMN samples, we observe frequency dependent dielectric constant and loss. They show clearly dispersion behavior. Further, we observe the characteristic distinct peak in dielectric loss values. The losses are very low in case of bulk BCoN, a nature similar to BMN. But in case of thin films the dielectric constant and loss shows dispersion behavior as well as enhanced values of both the dielectric parameters.

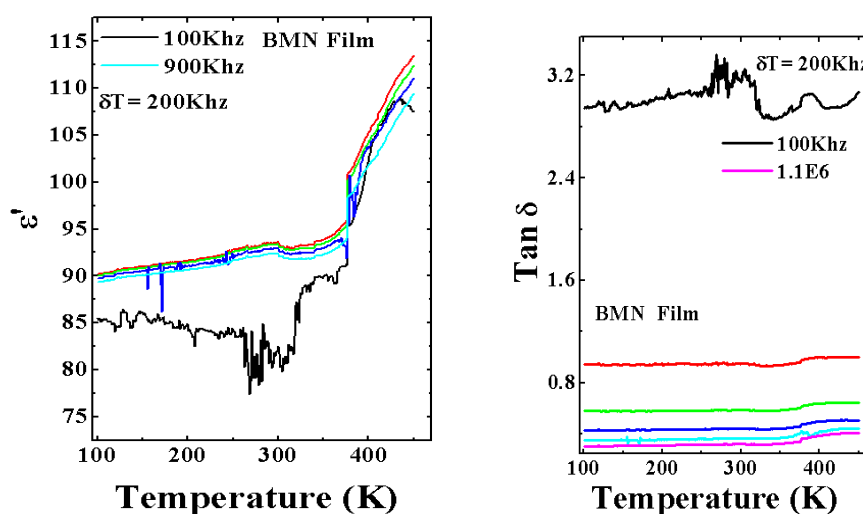
### 6.3.3.2 Temperature dependence Dielectric Properties

Dielectric constant for thin films were measured using an Agilent 4285A (LCR) bridge in the frequency range of 75 KHz to 30 MHz and a temperature range of 100 K to 450 K and Dielectric constant for bulk were measured using the LCR 1260 Solatron in the frequency range of 100 Hz- 3.2MHz and a temperature range of Room temperature to 350<sup>0</sup>C. Figure 6.7 (a) and (b) shows the plot of bulk and Thin Films of BMN at different frequencies. It is seen from the Figures 6.7 (a) that the dielectric constant shows peak at around 400K and loss shows almost linear behavior. It is temperature and frequency independent. Further, it has been observed that the losses are very low in case of bulk. As we switch from bulk materials to the thin films of the same samples we observe drastic variation in the behavior and properties. We observe reverse behavior in the loss parameter with the frequency. In Figure 6.7 (b) we see that the dielectric constant values are suddenly increased to double of the bulk values. Then on increasing the frequency the dielectric constant values are increasing. Further, we observe that the loss values are high in comparison to bulk values. The thin films grown by Pulsed Laser Deposition technique are polycrystalline in nature and sizes are in few Nano meter range. The observed size reduction might be playing a role in the change of dielectric response between bulk and thin film. Till now we haven't observed any study of thin films on Indium coated glass (ITO) for BMN and BCoN.

Figure 6.8 (a) and (b) shows the plot of bulk and Thin Films of BCoN at different frequencies. It is clear from the Figure 6.8 (a) that the BCoN bulk sample does not show any variation with the temperature and frequency. It shows almost linear behavior as in the case of BMN. It is likely to be due to the fact that the barium based Niobates are polar dielectrics it does not show any effect of temperature and frequency on the sample.

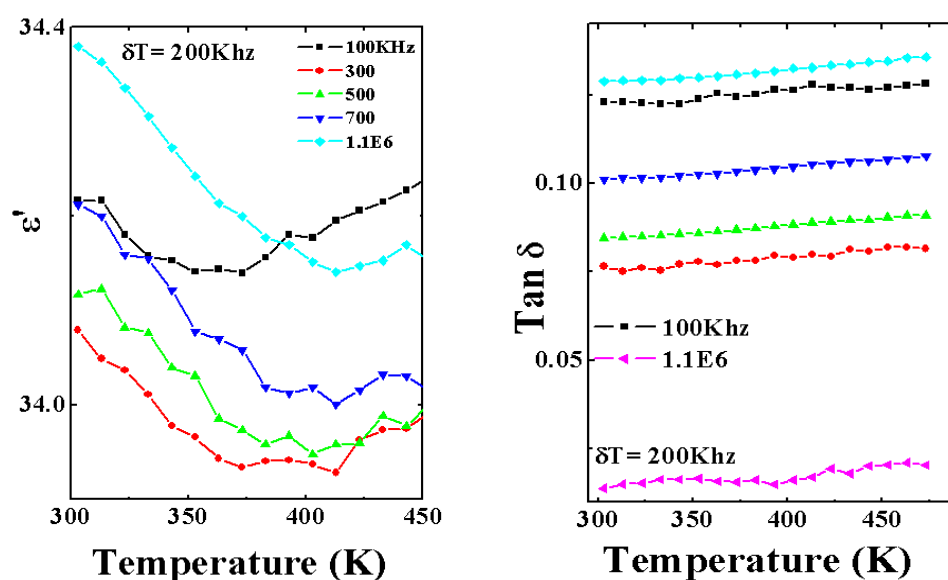


(a)

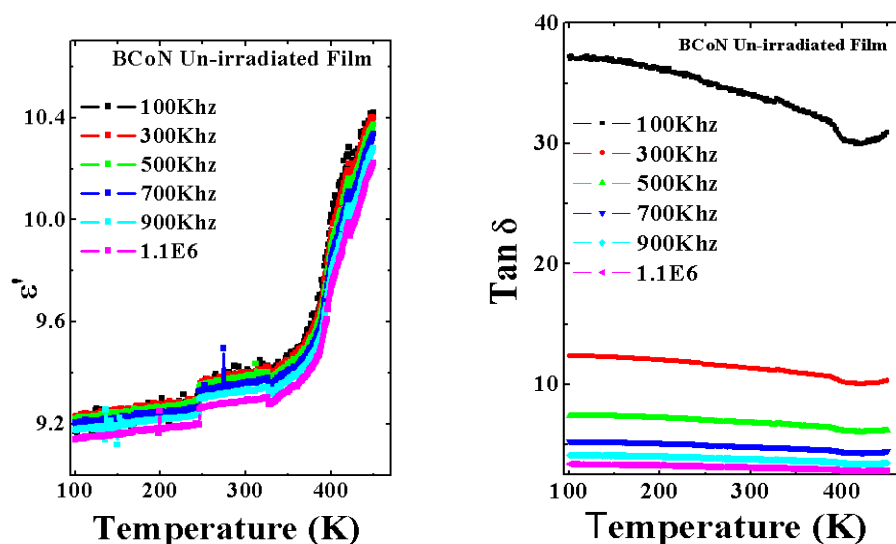


(b)

Figure 6.7 (a) Dielectric Constant and Loss of BMN-Bulk sample  
(b) Dielectric Constant and Loss of BMN- Pristine Film.



(a)



(b)

Figure 6.8 (a) Dielectric Constant and loss for the BCoN-Bulk sample.  
 (b) Dielectric Constant and loss for the BCoN-Thin Film.

## ii) Studies on irradiated thin films

### 6.4 Introduction

Swift heavy-ion irradiation (SHI) is a tool for the control or modification of some specific properties of the material. SHI penetrates deep into the materials and produces a long and narrow disordered zone along its trajectory resulting in localized changes to size, shape, and structure [11]. The degree of defects can range from point defect to a continuous amorphized zone along the ion's path, commonly called the latent track. The effect of the energetic ion beam depends on ion energy, fluence and ion species. It is evident that the electronic energy loss,  $S_e$ , due to inelastic collision is able to generate the point/clusters defects, if the  $S_e$  is less than the threshold value of the electronic energy loss. But it produces columnar or amorphization of materials, if  $S_e$  is higher than the  $S_{th}$ [12]. In addition, it is known that SHI produces the strain/stress in the oxides films [13, 14]. When a swift heavy ion passes through materials, a thermal spike is produced by individual heavy ion, which generates the local temperature far above than their melting temperature; this phenomenon is highly localized both in space as well as in time. These thermal spikes are known to construct craters and holes in the films during ion irradiation [15].

In the present study, we have studied the irradiation effects of the 200MeV  $Ag^{15+}$  and 100MeV  $O^{7+}$  ion beams on BMN and  $Ba(Co_{0.33}Nb_{0.67})O_3$  (BCoN) thin films and its effect on dielectric properties as a function of temperature and frequency are presented here.

The thin films of  $Ba(Mg_{0.33}Nb_{0.67})O_3$  [BMN], and  $Ba(Co_{0.33}Nb_{0.67})O_3$  [BCoN] on ITO substrates were cut into pieces, each of 5 mm  $\times$  1 cm size. This set of pieces was used for irradiation and further study in order to keep the growth conditions uniform for all the samples. One piece of film was kept pristine while the other pieces of the thin film were irradiated at the room temperature with 200 MeV  $Ag^{15+}$  and 100 MeV  $O^{7+}$  ion beam using the 15 UD tandem accelerator at the Inter-University Accelerator Centre, New Delhi, INDIA, with different fluence value such as  $1 \times 10^{11}$ ,  $1 \times 10^{12}$  and  $1 \times 10^{13}$  ions/cm<sup>2</sup>. The irradiation was performed under high vacuum condition (base pressure  $2 \times 10^{-6}$  Torr). The incident angle of the ion beam was kept slightly away from the surface normal to the sample to avoid the channeling effects and also the beam current was kept 0.5-1pA to avoid the heating. The ion beam was focused to a spot of 1 mm diameter and scanned over the entire area of the film using a magnetic scanner. The fluence values were determined by measuring the charge falling over the sample surface under the

secondary electron suppressed geometry. The ladder current was measured with a digital current integrator and a scalar counter.

## **6.5 Irradiation Effects of 200 MeV $\text{Ag}^{15+}$ and 100 MeV $\text{O}^{7+}$ on $\text{Ba}(\text{Mg}_{0.33}\text{Nb}_{0.67})\text{O}_3$ [BMN] and $\text{Ba}(\text{Co}_{0.33}\text{Nb}_{0.67})\text{O}_3$ [BCoN] thin films on dielectric properties.**

### **6.5.1 Dielectric Properties of BMN irradiated thin film.**

Figure 6.9 (a) shows the temperature dependence of the dielectric constant of un-irradiated,  $\text{Ag}^{15+}$  and  $\text{O}^{7+}$  irradiated films at 300 KHz frequency. Growth parameters can be directly tested on the dielectric response of the films. Further, SHI irradiation can help in modulating lattice strain which can alter dielectric loss as well as dielectric constant of the film. In the present study the dielectric constant ( $\epsilon'$ ) and dielectric loss ( $\tan\delta$ ) are investigated as a function of temperature for BMN films. The samples irradiation results are reported only for the highest fluence. We observe linear temperature dependence of dielectric constant for un-irradiated and irradiated samples. The un-irradiated film shows abrupt rise in the magnitude of dielectric constant compared to that of bulk which on correlating with our XRD results indicate that the drastic rise in dielectric constant in the film is mainly due to strain rather than lattice mismatch as there is marginal increase in the value of lattice constant of film compared to bulk.

The present studies indicate that in these materials irradiating the films with either of the beams exhibit reduction in the magnitude of dielectric constant. Values decrease much more drastically for  $\text{O}^{7+}$  irradiated films compared to  $\text{Ag}^{15+}$ . The drastic fall in values is dictated by the type of defects created in the films along the latent tracks. Normally silver ion beam produces points/columnar defects while  $\text{O}^{7+}$  beams produces amorphization of materials during its passage.

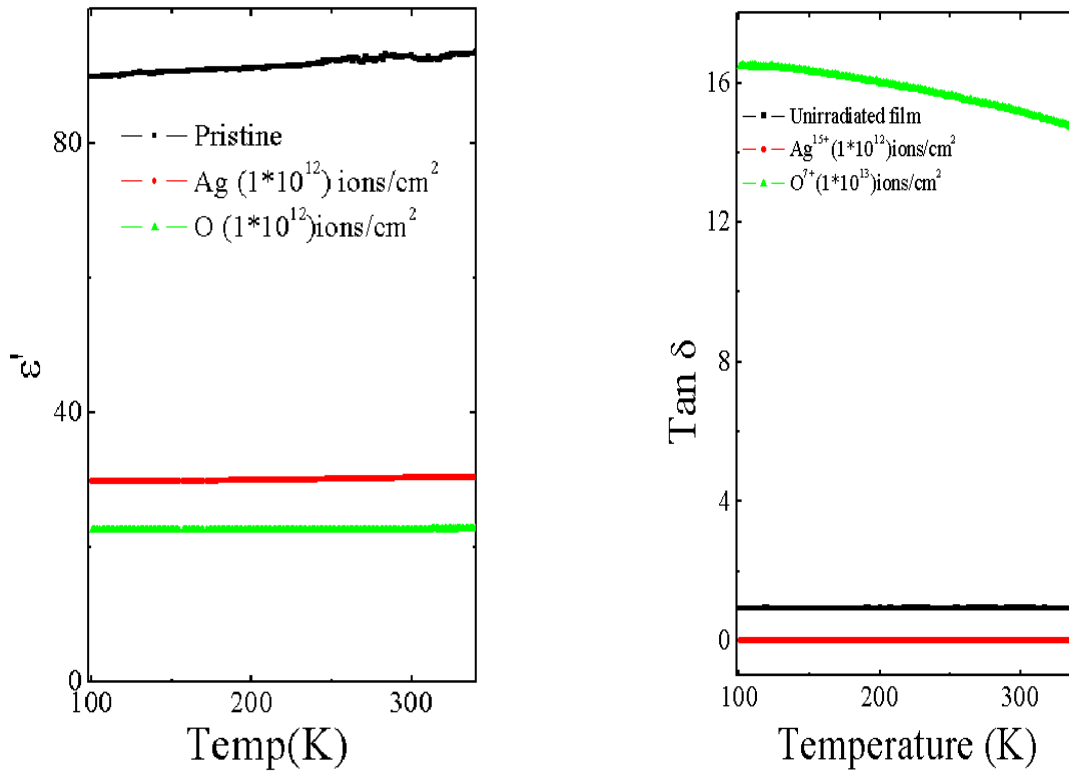


Figure 6.9 (a) Variation of dielectric constant vs. temperature at 300 KhZ for un-irradiated as well as Ag<sup>15+</sup> and O<sup>7+</sup> irradiated BMN films.

(b) Variation of  $\tan \delta$  vs. temp at 300 KHz for pristine as well as Ag<sup>15+</sup> and O<sup>7+</sup> irradiated BMN films.

Figure 6.9 (b) represents the dielectric loss parameter ( $\tan \delta$ ) for pristine, Ag<sup>15+</sup> and O<sup>7+</sup> irradiated films at 300 KHz with temperature. We observe nearly temperature independent dielectric loss for un-irradiated and Ag<sup>15+</sup> irradiated films while for O<sup>7+</sup> irradiated film it shows drastic rise. Ag<sup>15+</sup> ion irradiation reduces the dielectric loss to the order of  $10^{-3}$ .

## 6.5.2 Dielectric Measurement of BCoN irradiated thin film.

### 6.5.2.1 Frequency dependence of Dielectric Properties

In order to ascertain the frequency dependent response, variation of the dielectric loss for un-irradiated and Ag<sup>15+</sup> and O<sup>7+</sup> irradiated films is shown in Figure 6.10. The enhancement of dielectric constant for frequencies lower than 500 kHz is mainly due to the combined effects of

oxygen vacancy induced localized charges and increase of grain boundary–grain ratio. At higher frequencies, the response of oxygen vacancy induced dipoles decreases resulting in a gradual fall in dielectric values.

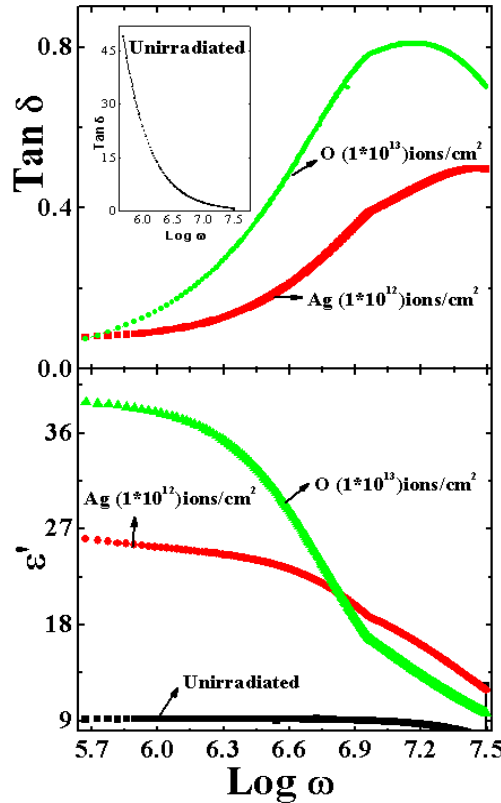


**Figure 6.10** Variation of dielectric constant and loss vs. frequencies for un-irradiated,  $\text{Ag}^{15+}$  and  $\text{O}^{7+}$  irradiated BCoN films at room temperature. Inset in (b) shows frequency dependence of dielectric loss in un-irradiated BCoN film.

### 6.5.2.2 Temperature dependence of Dielectric Properties

The temperature dependence of the dielectric constant ( $\epsilon'$ ) and the dielectric loss tangent ( $\tan \delta$ ) for  $\text{Ag}^{15+}$  and  $\text{O}^{7+}$  irradiated films are plotted in Figure 6.11 for different frequencies. Here we have presented results only for the highest irradiation fluence. The inset in Figure 6.11(b) shows, for reference only, the dielectric loss in un-irradiated film at 300 kHz. It is to be noted in Figure 6.11 (a) that we observe a peak formation for dielectric loss as a function of frequencies in irradiated films with overall lower values though it was missing in un-irradiated



film (inset Figure. 6.11 b). Further, the dielectric loss peak in  $O^{7+}$  irradiated films appears at lower temperatures compared to  $Ag^{15+}$  irradiated film. This peak may well be attributed to space charge related the Maxwell–Wagner interfacial polarization dependent matching of hopping frequency with frequency of an applied field [16]. Hence, the movement of hopping frequency tied to the peak towards the lower temperature in  $O^{7+}$  irradiated films suggests that point/cluster defects relaxes lattices the most. The overall dielectric constant in  $O^{7+}$  irradiated film (Figure 6.11(b)) is found to be higher compared to  $Ag^{15+}$  and un-irradiated films. This is probably due to the effectiveness of defects created along the ion tracks in reducing the disorderliness in the crystal [17,18]. The observed shift of dielectric loss peak to lower temperatures is complimented with the dielectric constant peak also shifting towards lower temperature on  $O^{7+}$  irradiation compared to  $Ag^{15+}$  and un-irradiated films. All these irradiated films show the dispersion behavior of dielectric constant with frequency, though it was absent in un-irradiated film and in the bulk. The enhancement of the dielectric constant and lowering of dielectric loss can be attributed to the reduction as well as pinning of the trapped charges within the aligned and well packed domains producing rise in net dipole moment. The correlated enhancement in columnar grain packing and reduction in roughness on irradiation in particular with  $Ag^{15+}$  ion irradiation points at its role in restricting the movement of mobile charges leading to increase in dielectric constant and lowering of dielectric loss. As the electro-optic co-efficient is directly proportional to the dielectric constant, hence, its enhancement on heavy ion irradiation is likely to increase their utility in various nonlinear optical applications [19].

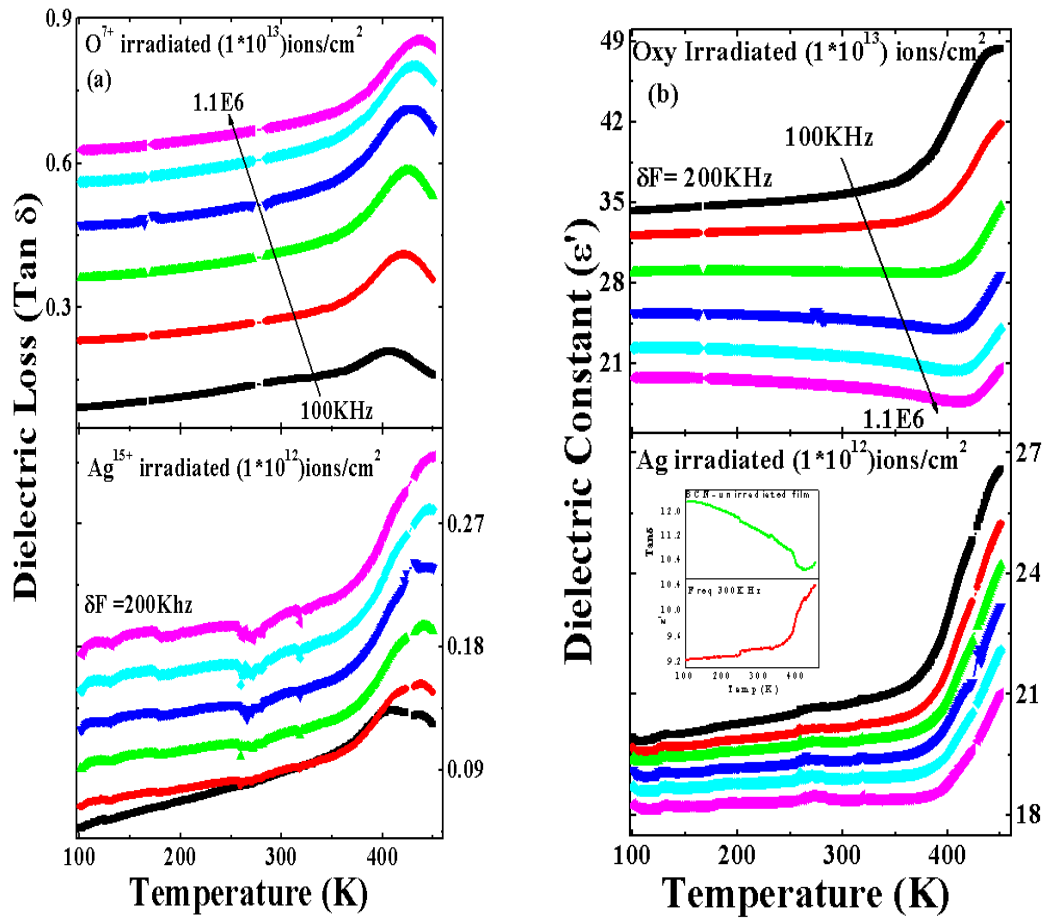
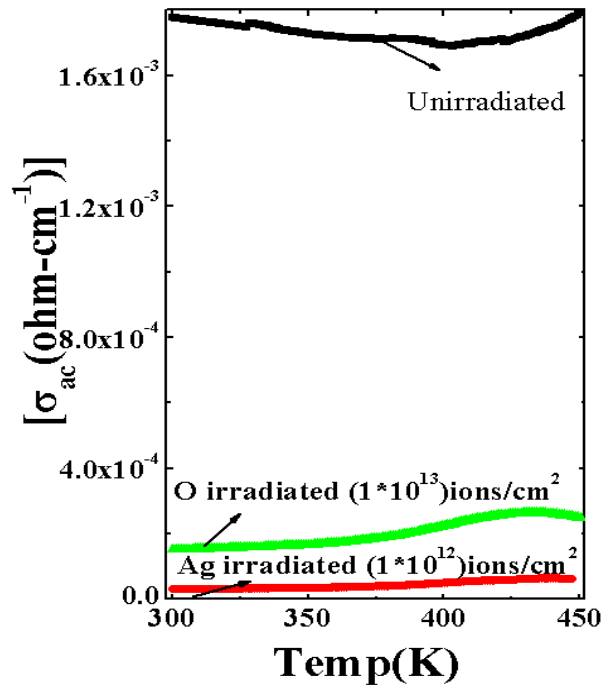


Figure 6.11

(a) Shows the temperature dependence of dielectric loss ( $\tan \delta$ ) of  $Ag^{15+}$  and  $O^{7+}$  irradiated BCoN films at highest fluence at different frequencies. (b) Shows the temperature dependence of dielectric constant ( $\epsilon'$ ) of  $Ag^{15+}$  and  $O^{7+}$  irradiated films at highest fluence. Inset in (b) shows temperature dependence of dielectric loss and dielectric constant in un-irradiated BCoN film.



**Figure 6.12** Variation of conductivity vs. temperature for un-irradiated, Ag irradiated and oxygen irradiated BCoN films at 300 kHz frequency.

Figure 6.12 shows the variation in ac conductivity for un-irradiated, Ag<sup>15+</sup> and O<sup>7+</sup> irradiated films. The un-irradiated films show higher values of conductivity as compared to that of the irradiated films. As discussed above on irradiating films with different beams and energies, we find that the oxygen beam gives higher values of conduction as compared to silver beam due to better reduction in the movement of induced or trapped charges. The conductivity in irradiated films is much less than in un-irradiated film. Further, the activation energy, as calculated by taking  $\ln$  vs.  $1/T$  of above graphs, is only marginally affected on irradiation.

## 6.6 Conclusions

In summary, we have successfully synthesized thin films of bulk samples of Ba[(B'<sub>0.33</sub>Nb<sub>0.67</sub>)]O<sub>3</sub> where B' = (Mg<sup>2+</sup>, Co<sup>2+</sup>)[BMN], [BCoN] by Pulsed Laser Deposition technique (PLD). The effect of replacement of B' site in Ba[(B'<sub>0.33</sub>Nb<sub>0.67</sub>)]O<sub>3</sub> was studied by means of structural, micro

structural, electrical. The following observations have been made on the basis of several experiments performed on the bulk samples.

- (i) The BMN thin films deposited on different substrates shows that the growth formation on the ITO coated on the glass substrates films is relatively better. We observe marginal shift in the lattice parameters, but large tensile strain in ITO films is the reason behind the larger values of dielectric constant in film compared to bulk.
- (ii) In comparison to BMN bulk samples its thin films are show higher values of dielectric constant as well as dielectric loss but over all nature are identical. Frequency and temperature independent behaviour is observed.
- (ii) The BCoN thin films deposited on ITO coated on the glass substrates shows good columnar grain growth formation. In bulk sample we do not see any effect of temperature or frequency on the sample. But in its thin film the frequency and temperature dependent behaviour is observed.
- (iii) Comparing the overall effects of irradiation on films dielectric response, it is inferred that  $\text{Ag}^{15+}$  irradiation is more helpful then  $\text{O}^{7+}$  irradiation. This is mainly due to the fact that  $\text{Ag}^{15+}$  irradiation due to type of defects it created is more effective in reducing lattice strain induced dielectric losses along with marginal loss of dielectric constant. Further, frequency independent dielectric nature of BCoN films changes to frequency dependent nature (relaxor like) on irradiation.
- (iii) Although, Lead based films compared to Barium based films show higher dielectric constants but along with high dielectric loss. Therefore significant increase in dielectric constant with low loss, on  $\text{O}^{7+}$  as well as  $\text{Ag}^{15+}$  ion irradiation, may enhance the electro-optical properties which in turn increase compounds tuneability for device applications.

**PART-B**

**A comparative Study of Crystal Structure, Microstructure,  
Dielectric and Conductivity properties of Bulk and thin films of  
 $\text{Sr}(\text{Mg}_{0.33}\text{Nb}_{0.67})\text{O}_3$**

This chapter presents a comparative study of structural and dielectric properties of  $\text{Sr}(\text{Mg}_{0.33}\text{Nb}_{0.67})\text{O}_3$  in the thin films deposited on indium tin oxide coated glass (ITO). In films the transition temperature ( $T_m$ ) shifts toward lower temperature suggesting larger flexibility of dipole movement in films as compared to bulk.

## 6.7 Introduction

Here we present dielectric response of  $\text{Sr}(\text{Mg}_{0.33}\text{Nb}_{0.67})\text{O}_3$ [SMN] thin films prepared by Pulsed Laser Deposition Technique (PLD) as a function of temperature and frequency. Dielectric constant  $\epsilon'(\omega)$  and  $\tan\delta$  values determined for the film are compared with Bulk. Further, we have calculated conductivity and activation energy in order to know its suitability as device. To the best of our knowledge, there are no reports on the study of dielectric and ac conductivity of  $\text{Sr}(\text{Mg}_{0.33}\text{Nb}_{0.67})\text{O}_3$ [SMN] thin films.

## 6.8 Deposition Conditions for the Pulsed Laser Depositions (PLD) Thin Films

$\text{Sr}(\text{Mg}_{0.33}\text{Nb}_{0.67})\text{O}_3$ [SMN] thin films were prepared by pulsed laser deposition (PLD) method on ITO substrates. The polycrystalline bulk target of [SMN] was synthesized by conventional solid-state reaction technique (for details see Ref. [7]). The KrF excimer laser (Lambda Physik model COMPEX-201) of wavelength 248 nm and pulse duration of 20 ns was employed for the deposition. During the deposition laser energy density at the target surface was kept at 220mJ/cm<sup>2</sup> and repetition rate was 10 Hz. During the deposition substrate temperatures was maintained at 300°C and the oxygen pressure was 200mTorr. The focused laser beam was incident on the target surface at an angle of 45°. The target was rotated at about 10 rpm and the substrate was mounted on a heater plate using a silver paint and kept opposite the target at a distance of 4 cm. The deposition was performed for 20 minutes. The film thickness is found to be about 250 nm when measured by Stylus profilometer.

## 6.9 Results and Discussions

### 6.9.1 X- Ray Diffraction (XRD) Measurements

Figure 6.13 shows the X ray diffraction pattern of SMN thin film. It shows single phase nature.

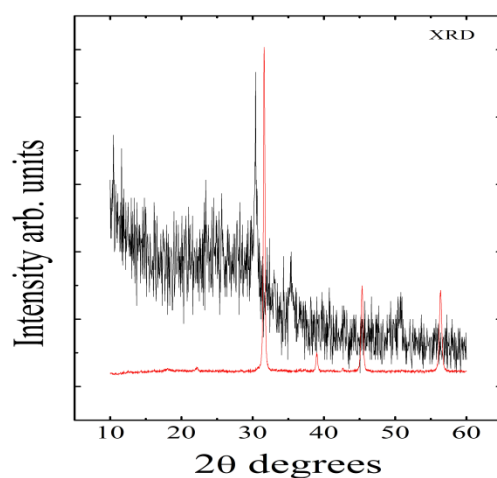


*Figure 6.13* X-ray diffraction pattern of Bulk (red) and thin film (black) of SMN.

### 6.9.2 Atomic Force Microscopy Analysis

The AFM images of SMN are shown in Figure 6.14. Here we observe agglomerated type of grain formation. The growths of the grains are columnar but agglomerated.

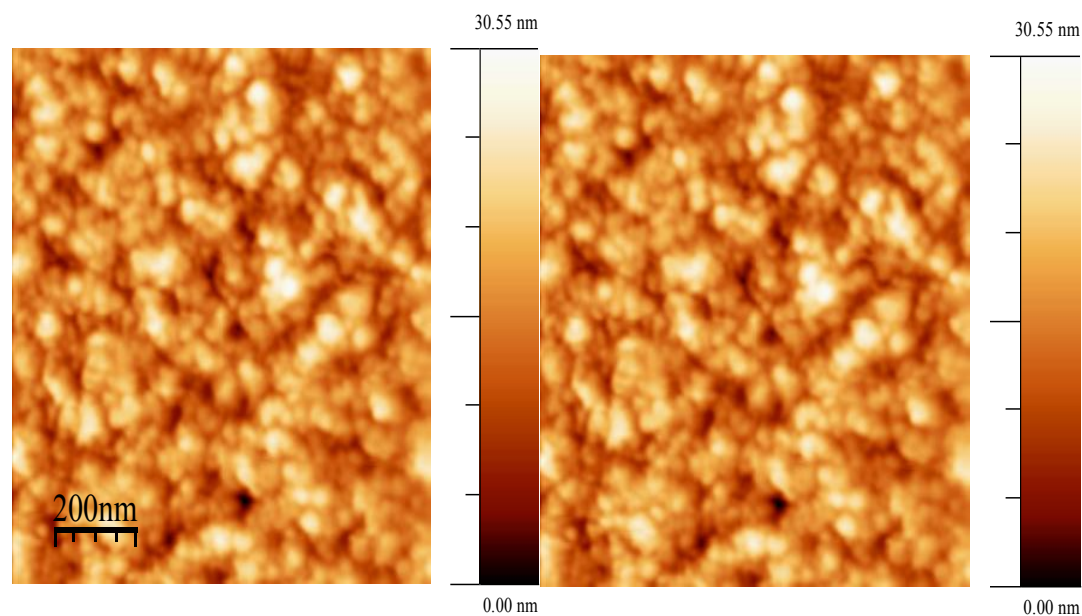


*Figure 6.14* AFM images of SMN pristine thin film.

### 6.9.3 Dielectric Measurement

Dielectric spectroscopy is used to investigate the dielectric and electrical properties of ceramic films. These properties of materials can be expressed in various ways, using different representations (Complex Permittivity  $\epsilon^*$ , Complex Modulus  $M^*$ , Complex Impedance  $Z^*$ , Complex Admittance  $Y^*$ ). The complex dielectric permittivity  $\epsilon^*(\omega)$  is defined as

$$\epsilon^*(\omega) = \epsilon'(\omega) + i\epsilon''(\omega) \quad (6.3)$$

The temperature dependence of dielectric constant  $\epsilon'(\omega)$  and  $\tan\delta$  are plotted in Figure 6.15, for different frequencies.

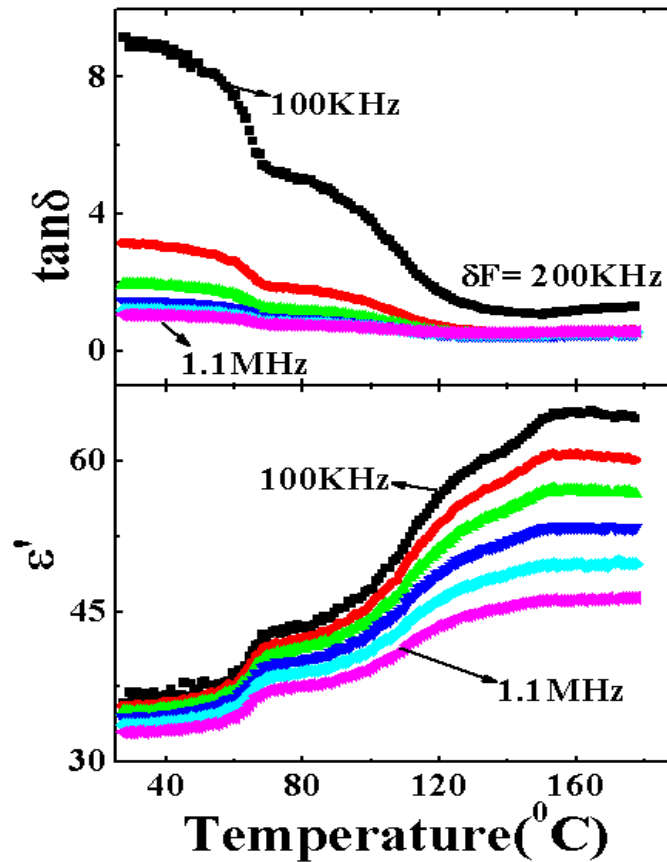
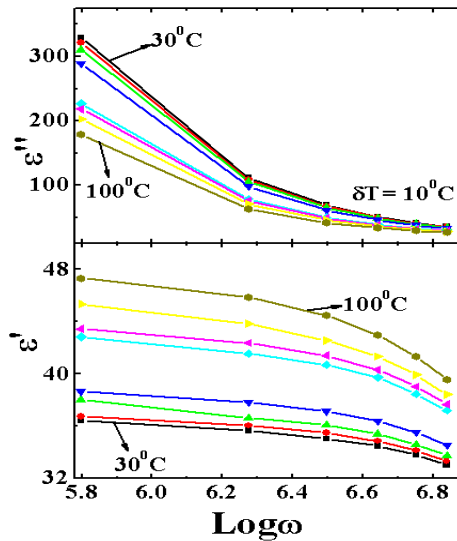


Figure 6.15 Variation of  $\epsilon'$  and  $\tan\delta$  with temperature at different frequencies.

It is seen that at higher frequencies  $\epsilon'$  becomes almost constant at  $\sim 160^\circ\text{C}$ . A step like anomaly is observed at  $70^\circ\text{C}$  in film but absent in bulk is attributed to the grain boundary, surface roughness or extrinsic effects. Further, in thin film it is observed that the transition temperature ( $T_m$ ) shifts to lower temperature in comparison to bulk, where  $T_m$  is above our measurement limit of  $180^\circ\text{C}$ .



This may be due to larger flexibility in dipole movement in films as compare to bulk. The loss factor ( $\tan\delta$ ) decreases with increase in temperature and shows pronounced effect at  $\sim$  (100 KHz). The observed behavior is likely to be due to reduction in effect of extrinsic factors on disordering of...B-O-B... chains at higher temperatures and frequency. Strong temperature dependence of  $\epsilon'$  at higher temperatures and at lower frequencies can be accounted for by assuming that the contribution of dipole orientation is insignificant [8]. The main contribution to the dielectric constant in the high frequency region is likely to be electronic polarization. Further, it can be inferred that at high temperatures the losses are dominated by thermally activated electron hopping where as in the low-temperature region such an activated process is frozen, resulting in a decrease of  $\epsilon''$  [9].



**Figure 6.16** Variation of the real ( $\epsilon'$ ) and complex part of permittivity ( $\epsilon''$ ) with frequencies at different temperatures.

The frequency dependence of  $\epsilon'(\omega)$  as well as  $\epsilon''(\omega)$  vs. frequency is plotted in Figure 6.16. The figure shows that  $\epsilon'$  decreases with frequency and temperature while  $\epsilon''$  is a decreasing with frequency but increases with temperature. As stated earlier, this may be due to the lack of ordering in B-O-B chain at lower frequencies.

### 6.9.4 Conductivity Studies

The total conductivity  $\zeta_{\text{tot}}$  of the material comprises of dc conductivity  $\zeta_{\text{dc}}$  and the ac conductivity  $\zeta_{\text{ac}}$ ,

$$\sigma_{\text{total}} = \sigma_{\text{dc}} + \sigma_{\text{ac}} \omega \quad (6.4)$$

Here,  $\zeta_{\text{dc}}$  accounts for the frequency independent free charges carriers resident in the material while the ac conductivity accounts for the frequency dependent bound charges. The  $\zeta_{\text{ac}}$  can be expressed in terms of the absolute permittivity  $\epsilon_0$  and the dissipation factor  $\tan\delta$ ,

$$\sigma_{\text{ac}} = \epsilon_0 \epsilon' \omega \tan\delta \quad (6.5)$$

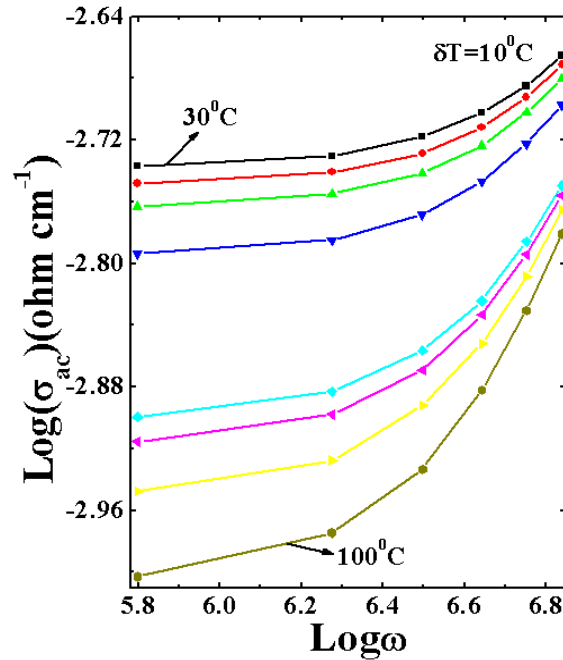


Figure 6.17 Variation of Ac Conductivity with frequency at measured temperatures.

The frequency dependence of the ac conductivity at different temperatures for the SMN film is shown in Figure 6.17. As  $\zeta_{\text{ac}}(\omega)$  is related to  $\epsilon'$  and  $\tan\delta$ , their contrasting behavior as a function of temperature and frequency produces net reduction in conductivity of thin film as temperature increases. The observed fall in conductivity at high temperatures together with lower  $T_m$  values make SMN thin film as promising material for switching devices.

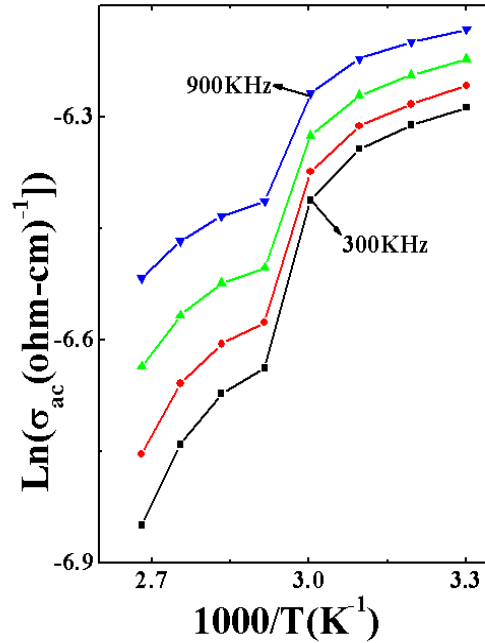


Figure 6.18 Arrhenius Plot of  $\text{Ln}\sigma_{\text{ac}}$  vs.  $1000/T$  (K) for SMN thin film.

The Arrhenius Plot ( $\text{Ln}\zeta_{\text{ac}}$  vs.  $1000/T$ ) of SMN thin film at four different frequencies is shown in Figure 6.18. The plots show two different regions for the activation energy. The activation energy, calculated at 300 KHz, in low temp region is found to be 0.02eV, which corresponds to the shallow traps. At temperatures above 70°C it enhances to 0.1eV may correspond to either formation or migration of oxygen vacancies [12]. The observed two step activation energy values are found to be lower than that of our bulk pellets (0.123eV).

## 6.10 Conclusions

- (i) Polycrystalline growth of films was observed. Dielectric measurements show the transition temperature( $T_m$ ) shifting toward lower temperature suggesting larger flexibility of dipole movement in films as compared to bulk.
- (ii) Two step activation energy observed in the SMN film corresponds to shallow traps at low temperatures while at high temperatures it is due to migration of oxygen vacancies.

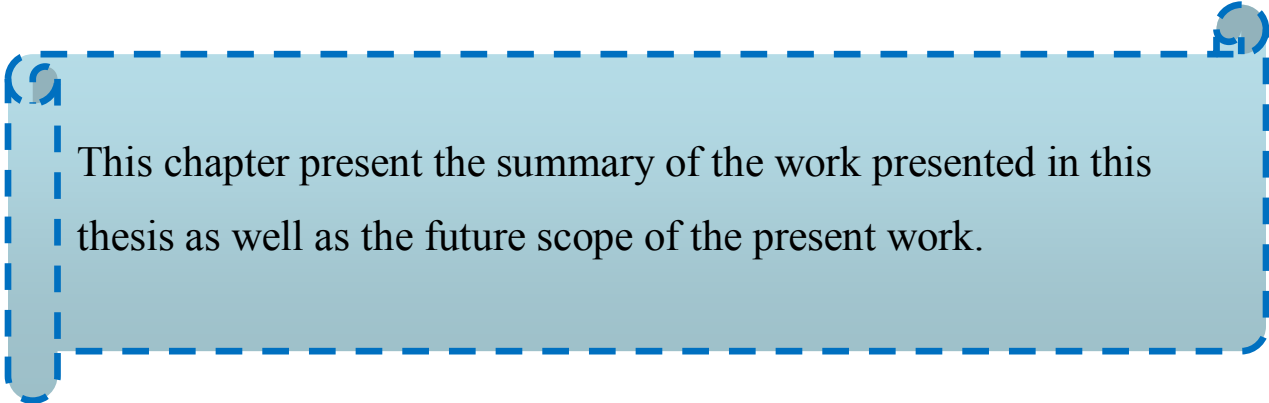
## References

- [1] A J Moulson, J M Herbert, *Electroceramics*. Chapman and Hall, London, 1990.
- [2] Y Xu North-Holland, Amsterdam, 1991.
- [3] De Araujo C Paz, J F Scott, G W Taylor, Gordon and Breach, Amsterdam, 1996.
- [4] Margarita Correa, Ashok Kumar, and R. S. Katiyar *App PhysLett* **91**,082905, 2007.
- [5] Cheng-Ji Xian, Jong-Hyun Park, Kyung-Chan Ahn, and Soon-Gil Yoon, Jeong-Won Lee, Woon-Chun Kim, Sung-Taek Lim, Seung-Hyun Sohn, Jin-Seok Moon, Hyung-Mi Jung, Seung-Eun Lee, In-Hyung Lee, and Yul-Kyo Chung, Min-Ku Jeon and Seong-Ihl Woo *App PhysLett* **90**, 052903 2007.
- [6] D. Miu *Jou of Opto electronics and advanced materials*. **8**, 1498, 2006.
- [7] Bhagwati Bishnoi, P.K. Mehta, C.J. Panchal, M.S. Desai, Ravi Kumar. *J of Nano Electron Phys* **3**, 698, 2010.
- [8] Dong C; Dong, Powder, X, Window-95 program for powder x-ray diffraction data processing, *J. Appl. Cryst*, **32**, 838, 1999.
- [9] J Maxwell, Electricity and Magnetics (Vol.1, Section 328, Oxford University Press, London) 1873.
- [10] C. Koops. *Phys. Rev.* **83**, 121, 1951.
- [11] D. Kanjilal, *Current Science*. **80**, 1560, 2001.
- [12] Basavaraj Angadi, P Victor V M Jali, M T Lagare, Ravi Kumar, S BKrupanidhi, *Materials Science and Engineering* **B100**, 93, 2003.
- [13] Basavaraj Angadi,V M Jali, M T Lagare, N S Kini, A M Umarji, Ravi Kumar, S K Arora, D Kanjilal *Nucl. Instr. And Meth.* **B187**, 87, 2002.
- [14] Deepthy K S, K Rao H L Bhat, Ravi Kumar, K Asokan *J. Appl. Phys.* **89** 6560, 2001.
- [15] F. Brochard Wyart and J. Daillant, *Can. J. Phys.* **68**, 1084 1990.
- [16] Anjana Dogra, M. Singh, Ravi Kumar, *Nucl. Instrum. Methods B* **207**, 296, 2003.
- [17] A.P. Bhat, P.S. Aithal, P.M. Rao, D.K. Avasthi, *Nucl. Instr Methods B* **166**, 964, 2000.
- [18] R. Varatharajan, P. Jayavel, J. Kumar, R. Jayavel, K. Asokan, *Nucl. Inst. Methods B* **170**, 145, 2000.
- [19] T. Kanagasekaran, P. Mythili, P. Srinivasan, N. Vijayan, G. Bhagavannarayana,P.K. Kulriya, D. Kanjilal, R. Gopalakrishnan, P. Ramasamy, *Cryst. Res. Technol.***42**,1376, 2007.

- [20] C.R. Dutta and K. Barua, *Thin Solid Films* **100**, 149, 1983.
- [21] A.R. Long and W.R. Hogg, *J. Non-Crystalline Solids* **59-60**, 1095, 1983.

## Chapter 7

### Summary and Future Scope



This chapter present the summary of the work presented in this thesis as well as the future scope of the present work.

## 7.1 Summary of the present work

We have successfully synthesized polycrystalline bulk samples of  $A(\text{Mg}_{0.33}\text{Nb}_{0.67})\text{O}_3$  where  $A = (\text{Ba}^{2+}, \text{Sr}^{2+}, \text{Ca}^{2+})[\text{BMN}], [\text{SMN}], [\text{CMN}]$ ,  $\text{Ba}(\text{B}'_{0.33}\text{Nb}_{0.67})\text{O}_3$  where  $\text{B}' = (\text{Mg}^{2+}, \text{Co}^{2+}, \text{Cu}^{2+})[\text{BMN}], [\text{BCoN}], [\text{BCuN}]$ , and  $\text{Sr}(\text{B}'_{0.33}\text{Nb}_{0.67})\text{O}_3$ , where  $\text{B}' = (\text{Mg}^{2+}, \text{Co}^{2+}, \text{Cu}^{2+}) [\text{SMN}], [\text{SCoN}], [\text{SCuN}]$ , by standard solid state reaction technique. The effect of replacement of A- site in  $A(\text{Mg}_{0.33}\text{Nb}_{0.67})\text{O}_3$ , B' site in  $\text{Ba}(\text{B}'_{0.33}\text{Nb}_{0.67})\text{O}_3$  and B' site in  $\text{Sr}(\text{B}'_{0.33}\text{Nb}_{0.67})\text{O}_3$  was studied by means of structural, micro structural, electrical, Conductivity and Optical studies. The following observations have been made on the basis of several experiments performed on the bulk samples.

Work presented in this thesis relates studies on structural, micro structural, dielectric properties (dielectric constant, dielectric loss), Modulus, Impedance studies, conductivity and optical studies of  $A(\text{Mg}_{0.33}\text{Nb}_{0.67})\text{O}_3$ , where A stands for  $(\text{Ba}^{2+}, \text{Sr}^{2+}, \text{Ca}^{2+})$ . In  $\text{Sr}(\text{B}'_{0.33}\text{Nb}_{0.67})\text{O}_3$  and  $\text{Ba}(\text{B}'_{0.33}\text{Nb}_{0.67})\text{O}_3$ , B' stands for  $(\text{Mg}^{2+}, \text{Co}^{2+}, \text{Cu}^{2+})$ . We have synthesized the single phase bulk samples of each of these samples. The thin films of some of the compositions were prepared, i.e.  $\text{Ba}(\text{B}'_{0.33}\text{Nb}_{0.67})\text{O}_3$ , B' stands for  $(\text{Mg}^{2+}, \text{Co}^{2+})$  and  $\text{Sr}(\text{Mg}_{0.33}\text{Nb}_{0.67})\text{O}_3$ . The thin films of above compositions are prepared by Pulsed laser Deposition (PLD) on ITO coated glass substrates. In addition to this, Swift heavy ion irradiation (SHI) has also been used for material modifications. Since it is well known that SHI irradiation generate different types of controlled defect states namely point defects ( $\text{Se} < \text{Seth}$ , Seth is the electronic threshold value of the material), extended point defects ( $\text{Se} \sim \text{Seth}$ ) and amorphized latent tracks ( $\text{Se} > \text{Seth}$ ), which modify the structural and magnetic properties. Beside these properties, SHI irradiation is also used for engineering the patterns of thin film surface.

Substituting the lower ionic radii at A-site in  $A(\text{Mg}_{0.33}\text{Nb}_{0.67})\text{O}_3$  the structure shifts from higher to lower symmetry, i.e. hexagonal symmetry to Monoclinic symmetry. This structural asymmetry has led to enhanced dielectric properties and introduced the dispersion phenomena but losses also increase as we move from polar (BMN) to non-polar systems (SMN and CMN). All the compositions show the poly dispersive nature. In addition when we replace at the B'-site in Barium series  $\text{Ba}(\text{B}'_{0.33}\text{Nb}_{0.67})\text{O}_3$  with 3d elements (Co or Cu), although the ionic radii marginally altered but the structural moves towards better symmetry by Hexagonal structure [BMN, BCoN] becoming Tetragonal [BCuN]. Here the changes in structural symmetry are likely

to be due to the complete Jahn-Teller Distortion in BCuN. Further, our analysis suggest that such a distortion has led to negative effects on dielectric properties as apart from dielectric constant dielectric loss also increased simultaneously. Here conductivity analysis shows the CBH mechanism in BCuN. Now when we carried out B'-site substitution with 3d elements (Co or Cu) in  $\text{Sr}(\text{B}'_{0.33}\text{Nb}_{0.67})\text{O}_3$ , it has led to positive effect of Jahn-Teller distortions. In this case apart from structure moving from lower symmetry to higher symmetry, i.e. from monoclinic to tetragonal, the dielectric constant increases drastically but keeping the dielectric losses low. Further, the relaxor phenomena are also introduced in the system. The conduction mechanism is still predominantly CBH type.

The BMN thin films deposited on different substrates shows that the growth formation on the ITO coated glass substrates is relatively better for film growth and it is also suitable for the dielectric measurements. In comparison to BMN bulk, its thin films show higher values of dielectric constant as well as dielectric loss but overall physical nature are identical to bulk. Frequency and temperature independent behaviour is observed in BCoN sample which was not visible in the bulk sample. All the films grown are of polycrystalline in nature and average grain size is  $\sim 50\text{nm}$ , much lower than respective bulk grains. Dielectric measurements show the transition temperature ( $T_m$ ) shifting toward lower temperature suggesting larger flexibility of dipole movements in films. Two step activation energy observed in the SMN film corresponds to shallow traps at low temperatures and at high temperatures it is due to migration of oxygen vacancies.

Analysing the overall effects of irradiation on films dielectric response, it is inferred that  $\text{Ag}^{15+}$  irradiation is more helpful than  $\text{O}^{7+}$  irradiation. This is mainly due to the fact that  $\text{Ag}^{15+}$  irradiation due to the type of defects it created is more effective in reducing lattice strain induced dielectric losses along with marginal loss of dielectric constant. Further, frequency independent dielectric nature of BCoN films changes to frequency dependent nature (relaxor like) on irradiation.



**Future scope of the Work**

It is expected that the Electric field vs. polarization (E-P) plots will give us better understanding regarding the ferroelectric nature of these compositions as well as its relaxor behaviour. The polycrystalline growth of thin films of these materials can be further optimized by optimizing the growth parameters in order to achieve improvement in dielectric parameters. Presently we have carried out irradiation studies on these films only by  $\text{Ag}^{15+}$ / $\text{O}^{7+}$  beams and with limited doses. The studies can be extended to other ion beams with multiple doses in order to get maximum enhancement in dielectric parameters. Further, attempts are on to achieve multi-layer growth of the films for composition which has given us better dielectric response among all the composition studied in the present work.

## List of Publications

1. “Ag<sup>15+</sup> and O<sup>7+</sup> ion irradiation induced improvement in dielectric properties of the Ba(Co<sub>1/3</sub>Nb<sub>2/3</sub>)O<sub>3</sub> thin films” **Bhagwati Bishnoi**, P.K. Mehta, C.J. Panchal, M.S. Desai, Ravi Kumar, V. Ganesan, *Materials Chemistry and Physics* **126**, 660-664, (2011)
2. “Structural, Optical and Dielectric Properties of A[(Mg<sub>0.32</sub>Co<sub>0.02</sub>)Nb<sub>0.66</sub>]O<sub>3</sub> Semiconductor where (A = Ba, Sr or Ca)”**Bhagwati. Bishnoi**, P.K. Mehta, C.J. Panchal, M.S. Desai, R. Kumar, *Journal of Nano Electron Phys.*,**3 (1)**, 698-708, (2011).
3. “Structure Correlated Enhancement in Dielectric and Electrical Properties of Strontium Based Niobates” **Bhagwati Bishnoi**; P. K. Mehta, Ravi Kumar, R. J. Choudhary, D. M. Phase *Integrated Ferroelectrics***122 (1)**, 1-11, (2010).
4. “Dielectric and Conductivity Studies of Sr[(Mg<sub>0.32</sub>Co<sub>0.02</sub>) Nb<sub>0.66</sub>]O<sub>3</sub>Thin Film” P.K.Mehta, **Bhagwati Bishnoi**, Ravi Kumar, R. J. Choudhary and D. M. Phase *Solid State Phenomena* **155**, 145-149, (2009).
5. “Study of dielectric Relaxation in Sr(Co<sub>1/3</sub>Nb<sub>2/3</sub>)O<sub>3</sub> Compound” **Bhagwati S Bishnoi**, P. K. Mehta and C. J. Panchal, to be Communicated.
6. “Irradiation Effects On Microstructure and Dielectric Properties of Ba[(Mg<sub>0.32</sub>Co<sub>0.02</sub>)Nb<sub>0.66</sub>]O<sub>3</sub> [BMCN] Thin Films” N V Patel, **Bhagwati Bishnoi**, P. K. Mehta, Ravi Kumar, R. J. Choudhary, D M Phase and V Ganesan, to be Communicated.
7. “High energy Oxygen ion irradiation effects on Sr[(Mg<sub>0.32</sub>Co<sub>0.02</sub>) Nb<sub>0.67</sub>]O<sub>3</sub> thin films”,**Bhagwati Bishnoi**, P. K. Mehta, Ravi Kumar, R .J. Choudhary, D. M.Phase and V. Ganesan, to be Communicated.

## List of Publications in Proceedings/Conferences

1. “Structure and Dielectric Study of  $\text{Ca}(\text{Co}_{1/3}\text{Nb}_{2/3})\text{O}_3$  [CCoN]” **Bhagwati Bishnoi** and P. K. Mehta, *55<sup>th</sup> DAE Solid State Symposium* (26<sup>th</sup> to 30<sup>th</sup> December 2010, Manipal University, Manipal, India) *AIP conference Proceedings* **1349**, 979-980 (2011).
2. “Structure and dielectric properties of BMCN thin films prepared by Pulse Laser ablation technique.” **Bhagwati Bishnoi**, P. K. Mehta, Ravi Kumar, R. J. Choudhary, D. M. Phase, V. Ganesan and A. Gupta, *54<sup>th</sup> DAE Solid State Symposium* (14<sup>th</sup> to 18<sup>th</sup> December 2009, The M. S. University of Baroda, Vadodara, Gujarat, India) *SSPS Proceedings* 543 (2009).
3. “SHI effect on the dielectric properties of  $\text{Ba}(\text{Co}_{1/3}\text{Nb}_{2/3})\text{O}_3$  [BCoN] thin films” P. K. Mehta, **Bhagwati Bishnoi** Ravi Kumar, R. J. Choudhary and D. M. Phase, *54<sup>th</sup> DAE Solid State Symposium* (14<sup>th</sup> to 18<sup>th</sup> December 2009, The M. S. University of Baroda, Vadodara, Gujarat, India) *SSPS Proceedings* 547 (2009).
4. “Effect of Substrate on growth Characteristics of BMCN films.” Patel N V, **Bhagwati Bishnoi**, P. K. Mehta, Ravi Kumar and R. J. Choudhary, *54<sup>th</sup> DAE Solid State Symposium* (14<sup>th</sup> to 18<sup>th</sup> December 2009, The M. S. University of Baroda, Vadodara, Gujarat, India) *SSPS Proceedings* 589 (2009).
5. “Effect of substitution of 3d element Cu at the B'-site on the dielectric properties of  $\text{Sr}(\text{B}'_{1/3}\text{Nb}_{2/3})\text{O}_3$ ” **Bhagwati Bishnoi** and P. K. Mehta, *53<sup>rd</sup> DAE Solid State Symposium* (16<sup>th</sup> to 20<sup>th</sup> December 2008, Bhabha Atomic Research Centre, Mumbai, India) *SSPS Proceedings* 987 (2008).
6. “Dielectric studies of  $\text{Ba}[(\text{Fe}_{1-x}\text{Co}_x)_{1/2}\text{Nb}_{1/2}]\text{O}_3$  Compounds” Devang Shah, **Bhagwati Bishnoi** and P. K. Mehta, *52<sup>nd</sup> DAE Solid State Symposium* (27<sup>th</sup> to 31<sup>st</sup> December 2007, Department of Studies in Physics, University of Mysore, Manasagnagotri, Mysore, India) *SSPS Proceedings* 867 (2007).

7. “Structural and dielectric properties of  $\text{Ba}[(\text{Mg}_{1-x}\text{Co}_x)_{1/3}\text{Nb}_{2/3}]\text{O}_3$  ( $x=0.05$ )” **Bhagwati Bishnoi**, Devang Shah, P. K. Mehta, Dinesh Shukla and Ravi Kumar, *52<sup>nd</sup> DAE Solid State Symposium* (27<sup>th</sup> to 31<sup>st</sup> December 2007, Department of Studies in Physics, University of Mysore, Manasagnagotri, Mysore, India) *SSPS Proceedings* 861 (2007).
8. “Dielectric Properties of  $\text{Sr}[(\text{Mg}_{0.32}\text{Co}_{0.02})\text{Nb}_{0.66}]\text{O}_3$  [SMCN] thin films” **Bhagwati Bishnoi**, P.K. Mehta, N.V. Patel and Ravi Kumar *3<sup>rd</sup> National Seminar on Advances in Material Science(NSAMS 2009)* (16<sup>th</sup> to 17<sup>th</sup> March 2009, Department of Physics, Manonmaniam Sundaranar University, Tirunelveli, Tamil Nadu, India) *NSAMS Proceedings* 154, (2009)
9. “Irradiation Effects On Microstructure and Dielectric Properties of  $\text{Ba}[(\text{Mg}_{0.32}\text{Co}_{0.02})\text{Nb}_{0.66}]\text{O}_3$  [BMCN] Thin Films”, **Bhagwati Bishnoi**, P. K. Mehta, N.V. Patel, Ravi Kumar, R. J. Choudhary, D M Phase and V Ganesan, *Swift Heavy Ion Multifunctional Engineering Conference* (6<sup>th</sup> to 9<sup>th</sup> October 2010, at Inter University of Accelerator Centre (IUAC), New Delhi, India)
10. “Structural and dielectric relaxation in  $\text{Sr}(\text{Co}_{1/3}\text{Nb}_{2/3})\text{O}_3$ ” **Bhagwati Bishnoi**, P. K. Mehta and Ravi Kumar *International Conference on Multifunctional Oxide Materials*(16<sup>th</sup> to 18<sup>th</sup> April 2009, H. P. University, Shimla, India).